DESIGN, ASSEMBLY AND CHARACTERIZATION OF COMPOSITE STRUCTURES OF BARIUM TITANATE AND NICKEL

By

JIAN XU

Master of Science in Chemical Engineering

Oklahoma State University

Stillwater, OK

2004

Submitted to the Faculty of the
Graduate College of the
Oklahoma State University
in partial fulfillment of
the requirements for
the Degree of
DOCTOR OF PHILOSOPHY
May, 2010

DESIGN, ASSEMBLY AND CHARACTERIZATION

OF COMPOSITE STRUCTURES OF BARIUM

TITANATE AND NICKEL

Dissertation Approved:

Dr. James E. Smay

Dissertation Adviser

Dr. R. Russell Rhinehart

Dr. AJ Johannes

Dr. Martin S. High

Dr. Jay C. Hanan

Dr. A. Gordon Emslie

Dean of the Graduate College

ACKNOWLEDGEMENTS

First and foremost, I would like to thank my parents for all the care and love I have received from them over the years. Also, I would like to thank my great uncle for inspiration and encouragement he gives me on my journey of intellectual pursuit. Second, I am grateful to my advisor, Dr. Jim Smay, for his guidance and support during my stay at OSU. I have really enjoyed the open and friendly atmosphere that he has maintained in the group. I would like to thank my committee for their time and help. For this I owe deep gratitude to Dr. AJ Johannes and Dr. Russell Rhinehart for their guidance on my writing and presentation skills. I was also fortunate to have worked on a project with Dr. Jay Hanan and was inspired by his working ethics and organization. For this study, I received help from some of the finest technical experts in their various fields. I would like to express my appreciation to Dr. Paul Clem and Dr. Geoffrey Brennecka at Sandia National Laboratories for their help on the dielectric and piezoelectric characterization work. I would also like to thank Dr. Alan Apblett for the help on thermogravimetric analysis involved in this work. I would like to thank staff member Genny, Melissa, Eileen, Carolyn, Shelley, and Mindy for all the help and assistance that they have given me over the years. Finally, I would like to thank all my friends at OSU. Without their friendship, I would not have had such a great experience in Stillwater.

TABLE OF CONTENTS

LIST OF TABLES

LIST OF FIGURES

CHAPTER 1 INTRODUCTION

1.1. Motivation

Solid freeform fabrication (SFF) refers to the collection of techniques that build solid objects directly from computer aided designs to near net shape through "stacking" of build materials layer-by-layer on the micrometer to millimeter scale. SFF is most often used either for rapid production of prototypes or for low throughput, small volume, but high value-added parts that are either uneconomical or impossible to fabricate by other methods. The insight gained by holding a three-dimensional prototype produced by SFF is often enough to justify the relatively high production cost. Recent trends in direct SFF production of high value, functional devices can also drive the use of SFF methods. A broad spectrum of build materials are available in SFF, including high strength alloys,[1-3] performance plastics,[4] and functional ceramics.[5, 6] These materials combined with the SFF approach also promise novel structures and functions in the form of composites.

To date, functionally graded or composite parts are rare. Fabrication of functional composites, especially ceramic-metal composites face several technical hurdles to become feasible, however, progress has been made toward composites in several of the SFF areas. Techniques such as Selective Laser Sintering (SLS)[2] and Electron Beam Melting (EBM)[1] may directly fuse ceramic and metal particles, but have lacked the

ability to manipulate composition variations due to the use of powder bed platforms. Laser Engineered Net Shaping (LENS)[3] could produce composition variations in space, but it uses of focused high power radiation, as also seen in SLS and EBM, creates high thermal stress and may cause cracks in ceramic-metal composites. Methods like Three-Dimensional Printing (3DP)[7] and Fused Deposition Modeling (FDM)[4] use high binder content and face a significant binder removal issue in the finishing steps. New methods and material systems have to be developed for SFF to overcome the inherent difficulties and limitations in the context of ceramic-metal composites.

1.2. Thesis Objective

The overarching objective of the work described in this thesis is assembly of a complex, three-dimensional structure of ferroelectric $BaTiO_3$ ceramic along with Ni metal. This dissertation details the evolution of a SFF technique called Robocasting to assemble functional, ceramic-metal composites with controlled structure on a sub-millimeter length scale. The Robocasting method was originally developed at Sandia National Laboratories and is similar to other extrusion-based SFF methods in print strategy. The extruded filament, however, is unique. The printing ink requires colloidal processing of materials in a concentrated, aqueous-gel form. The ink is robotically patterned by controlled extrusion followed by drying, binder burnout, and co-sintering of composite green compacts. To realize the goal of SFF of functional metal-ceramic composites requires building upon an existing knowledge-base of colloidal processing of polyelectrolyte stabilized ceramic and metallic sols, co-sintering of base metal electrodes with ferroelectric ceramics and the diverse field of functionally graded materials. The intersection of these fields generates new knowledge about the importance of controlling

and characterizing rheological properties to facilitate assembly of complex heterogeneous structures. Likewise, exploring the impact of process variations, such as liquid phase sintering to enable successful co-sintering of devices while maintaining the overall properties of the metal and ceramic phases, is a new area for SFF. Insights from this work reveal several key requirements for metal-ceramic composite SFF, namely: formulation of the appropriate colloidal gels of fugitive, ceramic, metal, and flux-containing materials, successful co-sintering of composite structures, and understanding of the limitations of the chosen materials system and processes.

1.3. Thesis Scope

The major task of this project is to develop aqueous colloidal inks for fabrication of ceramic-metal composite structures, focusing on the following aspects: 1) to formulate an aqueous colloidal fugitive ink with appropriate rheological properties and chemistries based on carbonaceous materials so that long-spanning and cantilevered features may be created by SFF; 2) to develop compatible aqueous colloidal ceramic and metal inks and evaluate their relevant chemistries and material properties; 3) to produce ceramic-metal composite powder preforms through serial printing of colloidal inks; 4) to consolidate these preforms and study the effects of process variables including ink composition, temperature profile, and sintering strategy. Finally, fabrication of disparate, heterogeneous, geometrically complex ceramic-metal composites is demonstrated.

1.4. Thesis Organization

This thesis is organized into seven chapters. Chapter one states the motivation of this work, thesis objectives, thesis scope, and thesis organization. Chapter two provides

basic information underlying the selection of materials, potential biomedical significance of this project, and a targeted literature survey of relevant fields including solid freeform fabrication, solid state sintering, liquid phase sintering, composite materials, and functional graded materials. The challenges faced when processing metals-ceramic composites is discussed in the context of traditional forming techniques. In chapter three, the development of an aqueous colloidal fugitive ink with carbon black nanoparticles is described. Chapter four investigates the formulation of an aqueous colloidal nickel (Ni) ink and its processing conditions. In chapter five, a composite ink of mixed colloidal barium titanate (BT) and Ni particles is developed for solid state sintering with a pure component BT ink. Chapter six examines the fabrication of BT-Ni composites through liquid phase sintering. Finally, the conclusions of this research and future directions to improve Robocasting ceramic-metal composites are provided in chapter seven.

Supplementary materials are provided in the Appendix section: 1) a mathematical model for describing oxidation of carbon black fugitive material in a complex ceramic green structure is provided; 2) the development of a fugitive ink based on rice starch powder is described; 3) fabrication of Ni-Cr alloys lattice using Ni and Cr particles is described; 4) an engineering chart of standard free energy of formation of oxides as a function of temperature is provided; 5) the binary phase diagram for ZnO-B_2O_3 system is provided; and 6) an optical image of the tube furnace for sintering process is provided.

CHAPTER 2 BACKGROUND

2.1. Materials System

Barium titanate (BT) and nickel (Ni) powders with particle size around 1 μm are the chosen materials for the fabrication of composite structures. The material selection is based on their commercial availability and practical applications, and processing requirements of the Robocasting technique. Some basic information for these two materials is provided in the following paragraphs.

BT is a solid solution of BaO and TiO_2 with a chemical formula $BaTiO_3$ and a perovskite structure, as illustrated in Figure 2.1. The Ba^{2+} and O^{2-} ions together form a face-centered cubic lattice, with Ti^{4+} ions sitting in the octahedral interstices. Below Curie temperature of around 125 °C, spontaneous alignment of the electric dipoles resulting from off-centered Ti^{4+} ions causes ferroelectricity. BT is primarily used as a dielectric material in ceramic capacitors. As a piezoelectric material, it has been largely replaced by lead zirconate titanate (PZT) in sensor and actuator applications. In the biomedical field, it is considered a biocompatible material and has been studied both *in vitro* and *in vivo* as implants. Colloidal processing of BT powder has been widely practiced in non-aqueous tape casting and screen printing of multilayer ceramic capacitors (MLCCs).

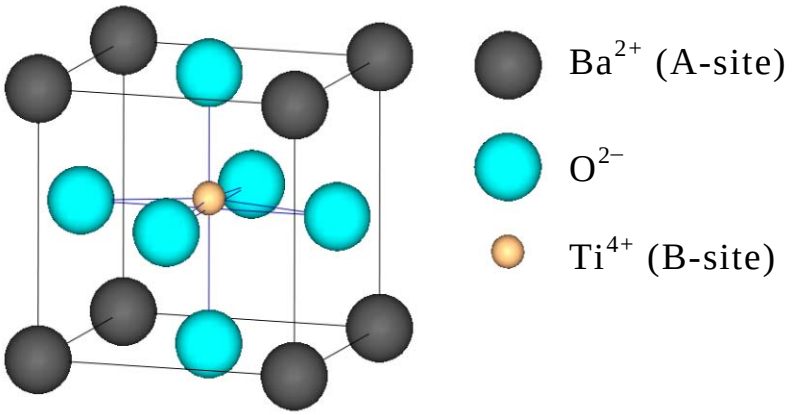

Figure 2.1 Schematic illustration of the BT unit cell (shown with tetragonal symmetry) demonstrating the offset B-site cation.

Ni is a ferromagnetic metal under normal temperatures and pressures, and is relatively corrosion resistant both in bulk and in particle form, due to the formation of a protective oxide surface. At high temperatures, Ni alloys may exhibit excellent mechanical strength, creep resistance, and corrosion resistance through a similarly passivated oxide surface. Primarily used as an alloy metal, Ni finds various uses in various applications such as alloys, steels, magnets, catalysts, biomedical implants, batteries, and fuel cells. In the electronics industry, Ni is used as a base metal electrode (BME) material to replace precious metals such as Au/Pd and Pt in MLCCs.

2.2. Reentrant Structures and Ceramic-Metal Composites

The primary funding for this dissertation work is in support of a collaborative effort with Dr. Lisa Friis' group in the Mechanical Engineering Department at the University of Kansas. The broad objective of the project is to create a biomedical scaffold with properties that mimic natural bone. That is, the scaffold should have porosity on the order of 50%, should be a non-linear elastic material and should display slight piezoelectric behavior. The following describes the biomedical significance in greater detail.

Non-linear elastic behavior is displayed by negative Poisson's ratio (NPR) structures while piezoelectricity can provide a self-sustaining electrical signal. Combined, these are hypothesized to mimic biologic bone to promote cell development through a combination of mechanical stress, electrical, and ionic fluid flow environments. Poisson's ratio v, as illustrated in Figure 2.2, is the ratio of transverse strain to the axial strain, when an object is stretched or compressed. Most materials have a positive Poisson's ratio, i.e. expanding in transverse direction when compressed in axial direction. A NPR indicates the reverse trend, i.e., a negative transverse strain along with a negative axial strain. Few materials in nature exhibit NPR behavior and natural cork is a good example of a zero Poisson’s ratio material. Usually NPR behavior is induced in a material as a result of structural modification. The term "reentrant" refers to one type of cellular NPR structure, where struts defining the unit cell of the structure point inward. The reentrant structure has many unique mechanical properties, including nonlinear load-deformation response and good vibration damping.

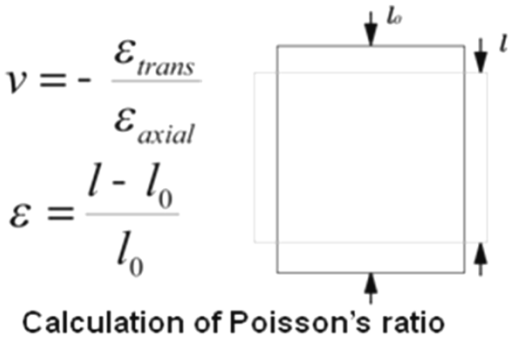

Figure 2.2 A schematic illustration of the Poisson's ratio.

The hypothesis is "a nonlinear electromechanical response that is unobtainable with bulk materials will be generated and such a response will lead to highly deformable structures with mechanical robustness and numerous applications",[8] and the objective is "to design, assemble, and characterize a metal-ceramic composite material consisting of a metallic NPR scaffold with integral piezoelectric ceramic nodes by direct writing of colloidal gel based ink".[8]

The use of reentrant structural material for orthopedic implants has been described by Dr. Friis.[9] The rationale for using the reentrant structure as a biological scaffold material focuses on its controllable nonlinear elastic behavior and possible superior fatigue resistance. Experimental evidence has suggested that mechanical signals play a crucial role in regulating stem cell fate.[9] They affect the differentiation process of stem cells, the recruitment of undifferentiated progenitor cells, and the cell differentiation into a particular phenotype.[10, 11] Applied load and electrical responses also impact on healing and maintenance of tissues, such as bones, cartilage, and tendons.[12-24] BT as biocompatible piezoelectric implants has already been investigated.[25] It is hypothesized that the use of the ceramic-metal NPR structural composite as a biomaterial in medical

devices would provide self-sustaining electrical signals to cells in or adjacent to the scaffold when the device is dynamically loaded. It provides a potential route to replicate the relevant mechanical and electrical environment in implanted medical device, and could be used to promote anisotropic tissue regeneration within one implant. Figure 2.3 demonstrates the fabrication concept for local Ni structures. Figure 2.4 illustrates proposed NPR BT-Ni composite structure.

The responsibilities for the joint project are assigned in such a way that the materials processing and composite fabrication are solely undertaken at OSU, the mechanical and electro-mechanical characterizations for the fabricated composites are primarily carried out at KU, and the design of composite materials is determined with inputs from both sides. In this context, this dissertation largely focuses on the materials processing and pertinent materials characterizations; and in-depth characterizations for the proposed mechanical and electro-mechanical properties fell on the shoulder of Dr. Friis' graduate student Nicolas V. Jaumard.

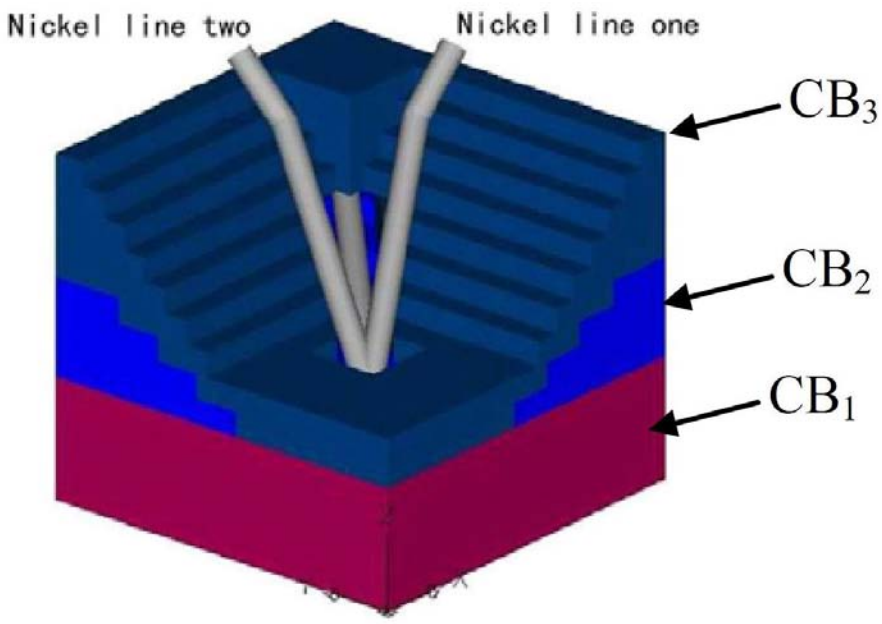

Figure 2.3 Schematic illustrations of fabrication concept for local Ni structures. The dark red, blue, and marine colored layers indicate the strata of fugitive support in the sequence of printing, and the grey filaments are Ni.

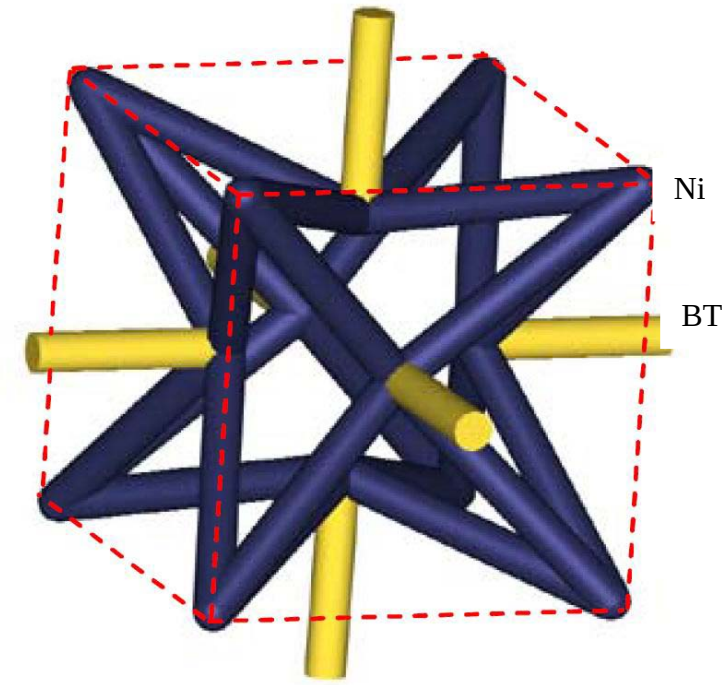

a)

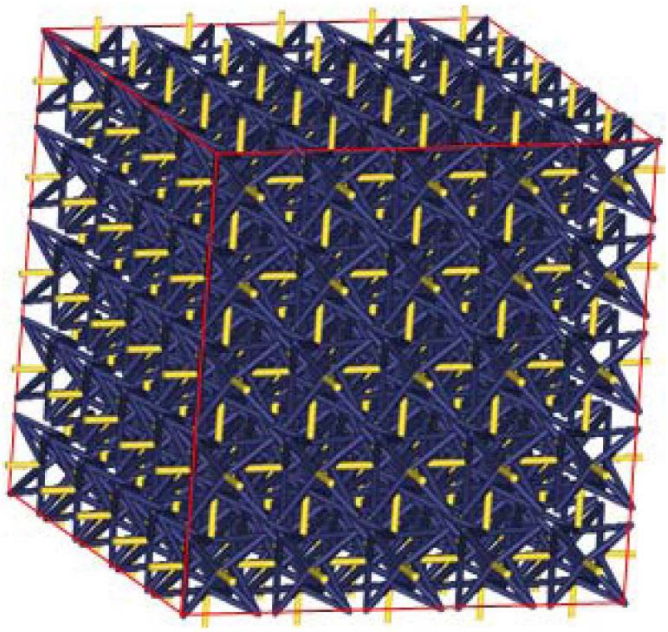

b)

Figure 2.4 Schematic illustrations of a) a reentrant unit cell and b) a reentrant structure composed of repeating unit cells in 3D. The yellow colored struts are BT, and blue colored ones are Ni. The red lines indicate the 3D space these two structures occupy.

2.3. Solid Freeform Fabrication

In this section, a brief overview for solid freeform fabrication (SFF) is first provided, followed by descriptions of major relevant SFF techniques. Finally, a comparison of process characteristics among these techniques is given. A more detailed introduction to the Robocasting process is provided separately in the next section.

2.3.1 Overview

SFF uses an additive approach to assemble solid objects layer by layer. Although this additive concept is not new, the use of computer aided design and automation to assist digitized placement of materials has created a field of active research and development since the 1990's. SFF enables much freedom for fabricating objects with customized shape, complex structure, and compositional gradients.

The overall concept of SFF is similar for all the techniques, but specifics of material delivery and post processing vary. The similar features include: 1) preparation of feedstock materials, 2) generation of machine code from CAD model, 3) assembly of 3D object through layer-by-layer addition of materials, and 4) finishing the assembled object, if necessary. There is an underlying requirement that each formed layer have enough mechanical strength for shape retention and structure evolution.

The SFF techniques are not in competition with current methods for mass production of inexpensive everyday consumables. Rather, SFF focuses on low throughput, small volume, but high value added parts that are either uneconomical or impossible to fabricate by other means. Those unusual but highly demanding needs may justify the high unit cost and low productivity in SFF. Currently, SFF has benefited the commercial

production of concept models, injection molds, and medical devices. Another major play field is in the aerospace field. SFF has been envisioned to fabricate parts and structural materials in a futuristic context, such as on expeditionary space shuttles, extraterrestrial planets, and moons.

The ongoing efforts to advance SFF are in three directions: 1) to identify new build materials and their functions, 2) to manufacture high precision, quality parts using these materials, and 3) to shorten production time and lower cost for these parts. While the last two objectives are inherently difficult to reconcile, new material functions are continuously being explored. Future SFF applications to a large extent lie in the creation of new functionalities from smart engineering of materials system while balancing structural resolution and production efficiency.

2.3.2 Major SFF Techniques

Stereolithography (STL) was created by 3D systems, Inc. to build polymeric prototypes by selective curing of resin.[26] In the process shown in Figure 2.5, STL uses a UV laser beam to trace a cross-section pattern at the surface of a bath of liquid UV-curable photopolymer a layer at a time. Exposure to the UV laser cures the traced planar pattern and bonds it to the layer below. The spot size of laser and details of photon interaction with the resin determine the width and thickness of the region cured and the rate of building. After a layer is cured, an elevator platform descends by a single layer thickness and a further layer of monomer is swept across the newly formed surface. The process repeats until a complete 3D part is formed. After building, parts are cleaned of excess resin by immersion in a chemical bath and then post-cured in a UV oven.

Stereolithography is one of the first and most popular of the SFF techniques. It can produce nearly any shape since the resin bath acts as a liquid support for overhanging features. Incorporation of solids into the resin bath is problematic because of the increased scattering of the laser beam. An enduring legacy of the STL technique is the .stl file format, which defines three-dimensional volumes in terms of a triangular tessellated surface. The tessellation is without much structure, save the fact that facet normals must point toward the exterior of the part. There is no connectivity data concerning the facets. Most SFF techniques use the .stl file as a standard description of the data because the triangular data is easily sliced into layers.

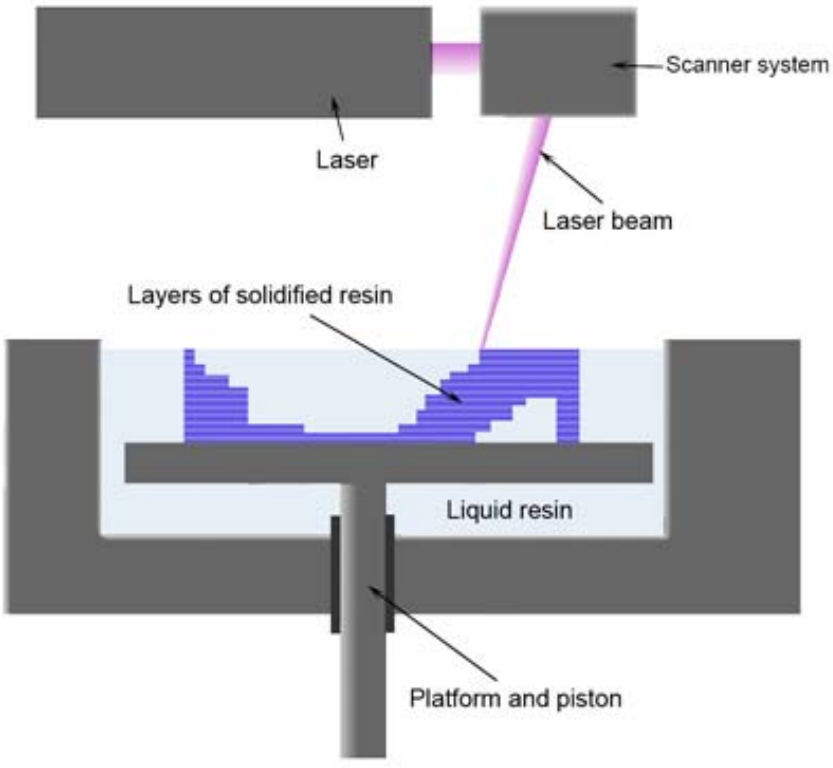

Figure 2.5 Schematic of the stereolithography process (Materialgeeza on wikipedia).

Fused Deposition Modeling (FDM) was developed by S. Scott Crump[4] in the late 1980s and was commercialized in 1990 by Stratasys Inc. As shown in Figure 2.6, a filament of thermoplastic build material is unwound from a coil and supplied to an extrusion nozzle. The nozzle is heated to melt the plastic and can turn the flow on and off. The extruded plastic solidifies and bonds to the layer below. For complex geometries, a filament of fugitive material is extruded from a separate nozzle to form support structures for the build material. As the extrusion nozzles can move in horizontal directions and the build platform can descend vertical by a numerically controlled mechanism, the 3D objects can then be constructed layer-by-layer.

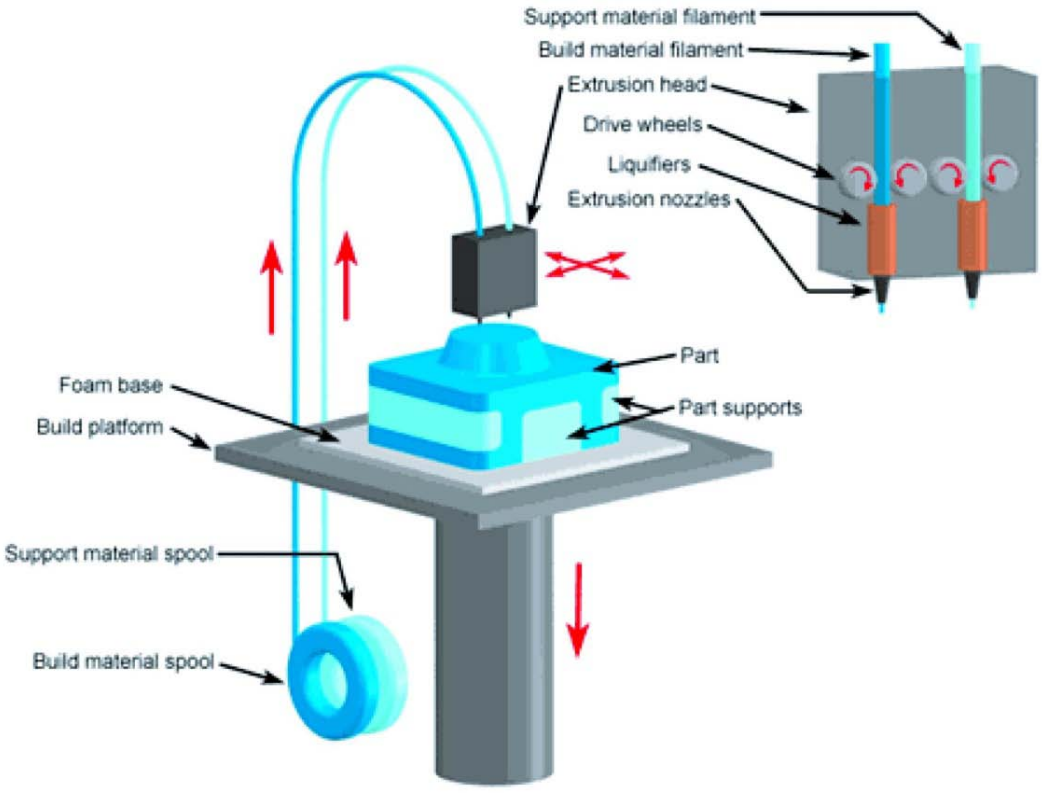

Figure 2.6 Schematic of the fused deposition modeling process (custompartnet.com).

Selective laser sintering (SLS) uses a high power CO_2 or YAG laser to fuse small particles layer-by-layer into 3D object.[2] As illustrated in Figure 2.7, a thin layer of powdered material is spread across a build platform where the laser selectively fuses the powdered material by tracing a cross-section pattern of the part. The platform then descends by one layer thickness and a new layer of material is applied on top, and the next cross-section is sintered to bond to the previous. This process continues until the part is completed.

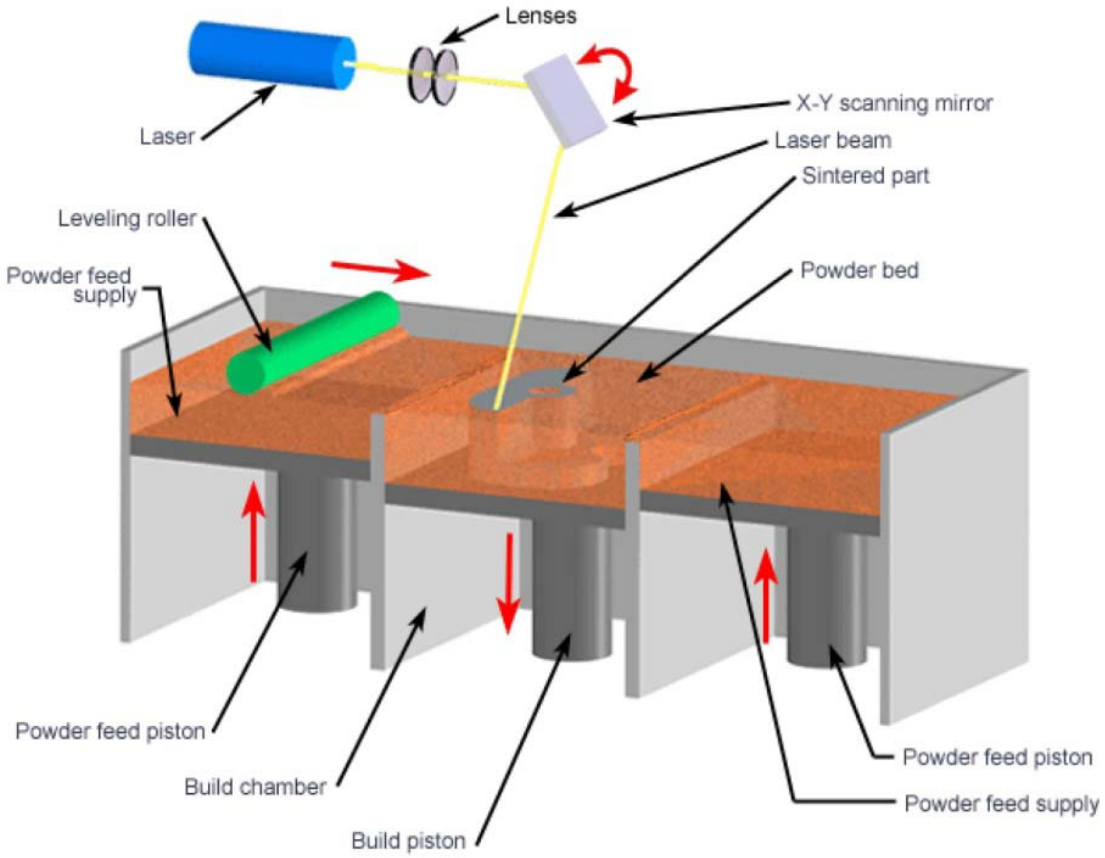

Figure 2.7 Schematic of the selective laser sintering process (custompartnet.com).

Laser Engineered Net Shaping (LENS)[3] is a technology developed by Sandia National Laboratories. As illustrated in Figure 2.8, a high power laser travels through the center of a deposition head and is focused to a small spot by one or more lenses. Powdered material supplied coaxially to the focus is melted by the laser beam. The X-Y table is moved in raster fashion to fabricate each layer of the object. As each layer is completed, the deposition head moves up vertically by one layer thickness relative to the X-Y table to let the structure evolve.

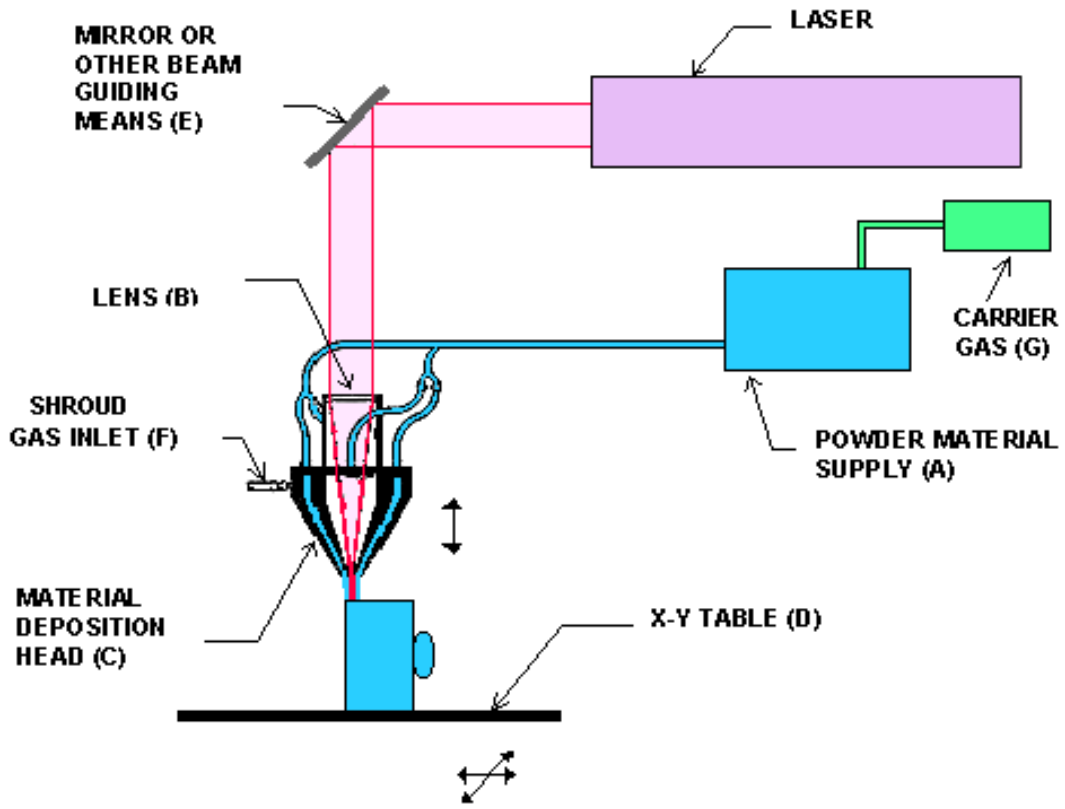

Figure 2.8 Schematic of the laser engineered net shaping (custompartnet.com).

Three-Dimensional Printing (3DP)[7] technology was developed at the Massachusetts Institute of Technology and is similar to the Selective Laser Sintering (SLS) process in many ways. But instead of using a laser to sinter the material, a multi-channel ink-jet printing head deposits a liquid adhesive to bind the material. 3D printed parts are typically infiltrated with a sealant to improve strength and surface finish. A schematic illustration for 3DP is shown in Figure 2.9.

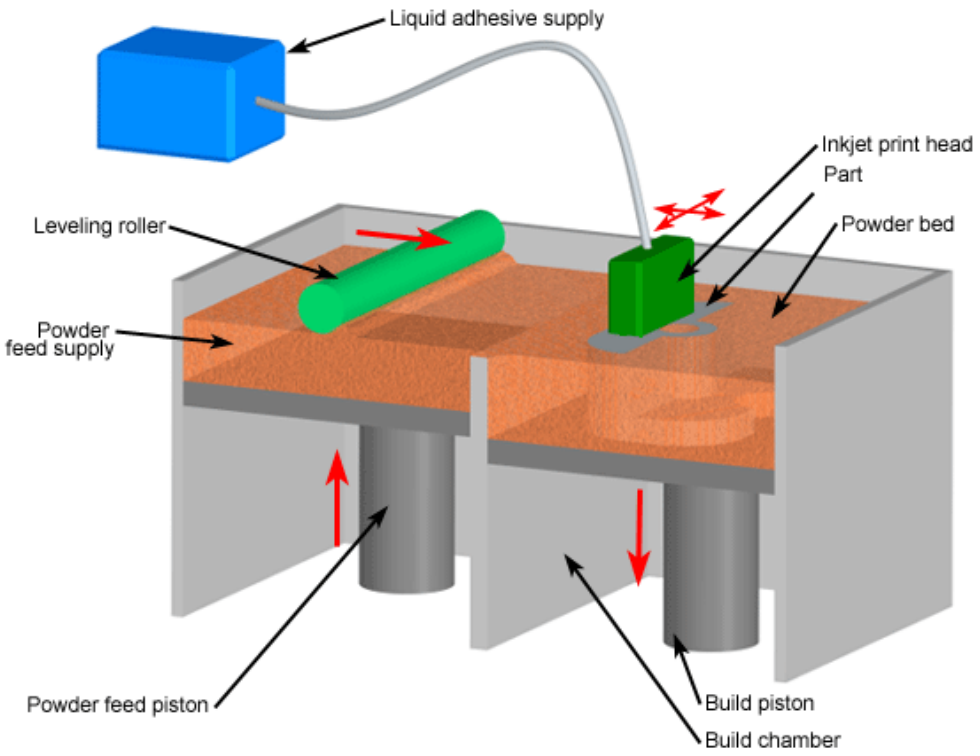

Figure 2.9 Schematic of the three dimensional printing (custompartnet.com).

Inkjet printing (IP)[27] is based on the 2D inkjet printer technique of depositing tiny ink drops onto a substrate. In this process, as shown in Figure 2.10, the ink is replaced with thermoplastic build material and waxy support material that are melted and held in separate heated reservoirs. These materials are each fed to an inkjet printing head that can move in the X-Y plane and squirt tiny droplets of material to required locations. The printed materials instantly cool and solidify to bond to layer underneath. After each layer is printed, a milling head is used to smooth the surface. Particles resulting from this cutting operation are vacuumed away. The elevator then lowers the build platform and the part so that the next layer can be built. After this process is complete, the part can be removed and the waxy support material may be melted away.

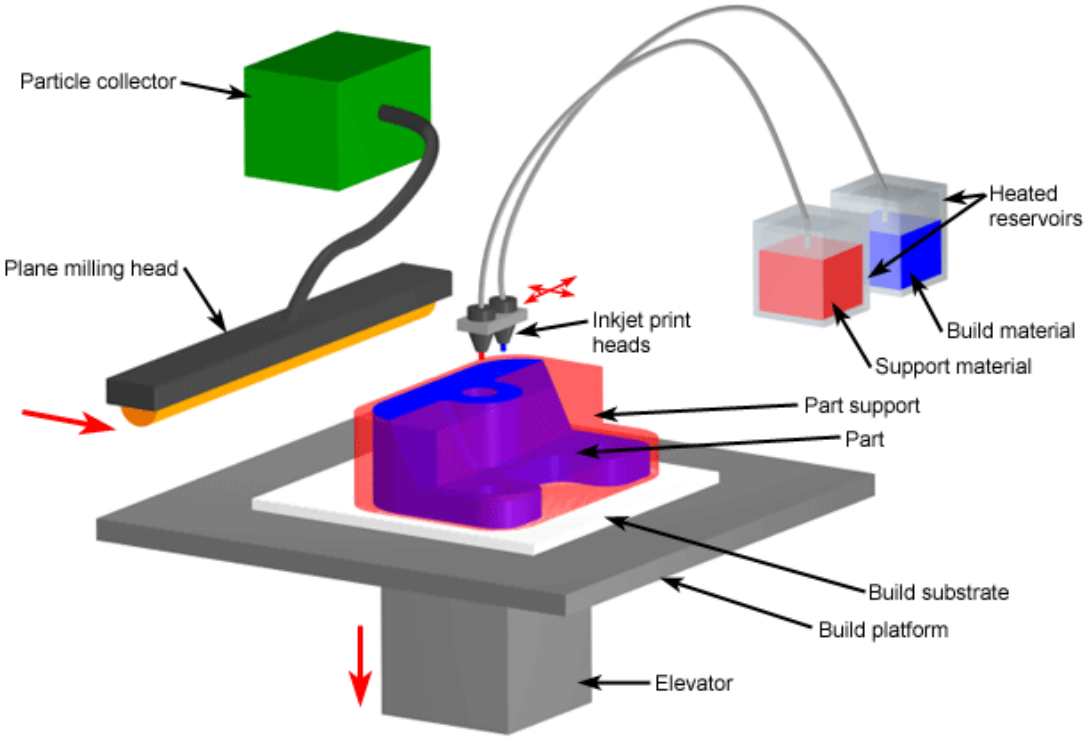

Figure 2.10 Schematic of the ink-jet printing (custompartnet.com).

Other techniques such as Electron Beam Melting (EBM)[1] and Direct Metal Laser Sintering (DMLS)[28, 29] are also available. However, their differences from those described above are usually marginal. Hence, an exhaustive description of all current SFF techniques is not given here.

2.3.3 Comparison of SFF Techniques

The characteristics of relevant SFF techniques are compared in Table 2.1. All these methods are able to fabricate objects with complex geometries. Only those employing high power radiation to directly sinter or melt powders have the potential to build high quality ceramic-metal composites; however, the equipment cost is usually high and thermal stress is a significant issue for these techniques. The rest of the techniques involve the use of high organic content build materials which, if required, may contain particulate fillers of various nature. With common metallic powders, however, these techniques will encounter a binder removal problem. Unless properly solved, this issue will jeopardize product properties after densification.

Table 2.1 Comparisons of various SFF techniques.

Classification	Technique	Characteristics	Materials	Advantage
High power radiation enabled direct powder consolidation	EBM	Electron beam; full build density; superior build rate	Primarily metals; ceramics and polymers possible but less concerned	High accuracy; good mechanical strength for high demanding applications
	DMLS	Laser; up to 100% build density; may require thermal treatment after build		
	LENS			
	SLS			
High organic (binder) content	STL*	Laser and photopolymer	Polymers and/or waxes; particulate fillers	High accuracy
	3DP	Weak bonding between particles		Low cost; primarily for rapid prototyping
	IP	Fast build rate		
	FDM	Extrusion		
	LOM*	Adhesive coated laminates	Paper, plastic and metal	

* SL=Stereolithography, LOM= Laminated Object Manufacturing

2.4. Robocasting

Developed by Sandia National Laboratory, Robocasting[5, 30] is the key technique employed in this research. It assembles 3D structures by a sequence of steps: first, a 3D model of the object is generated in a computer aided drafting (CAD) program or captured by scanning a real object. Next, the 3D model is sliced into a series of parallel planes, and tool paths are calculated for filling the resulting perimeters in each plane. Finally, the 3D object is assembled by printing each planar pattern directly atop the previous one on a flat substrate. The printing action is accomplished by extruding a colloidal ink through a deposition nozzle as it traces through the pre-calculated tool path. The ink possesses a yield stress such that after extrusion it maintains a finite thickness. After each planar pattern is printed, the deposition nozzle must be raised by a predefined distance to let the structure evolve. Due to the high concentration of the colloidal ink and the small diameter (c.a. $\leq$0.2 mm) of the filament extrudate, the printing process is usually performed with the substrate and printing nozzle submerged in a low-viscosity oil bath. Only after printing is completed, the structure is removed from the oil bath and then dried in air.

The subsequent finishing process for as-printed ceramic and metal structures includes three steps: drying, binder burnout, and sintering. The drying step is necessary to remove water and oil trapped within the green structure, followed by a binder burnout step for removal of the polymer additives. Finally, a sintering step is employed to consolidate the green structure so as to reach desired material properties. The processing steps involved in Robocasting are described in Figure 2.11. And a schematic illustration of the Robocasting apparatus is provided in Figure 2.12a.

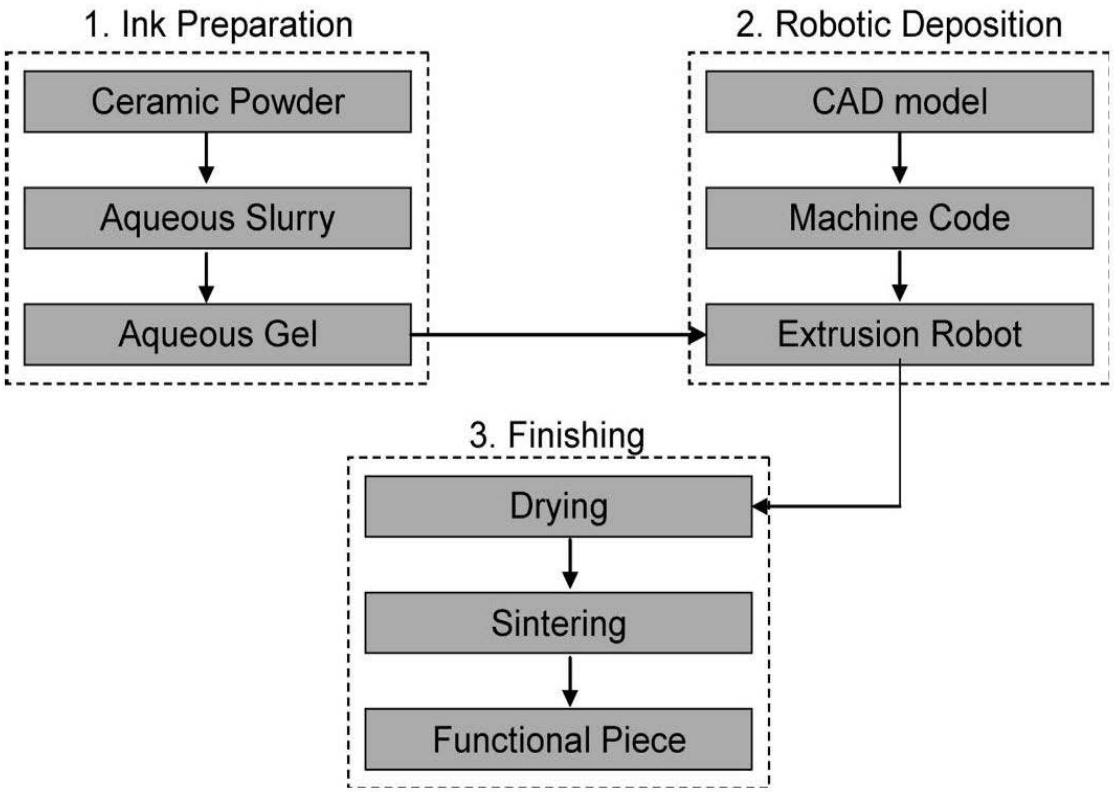

Figure 2.11 Processing steps involved in Robocasting.[31]

Robocasting of composite materials requires printing multiple ink compositions. Such printing may be achieved in several ways: 1) serial extrusion through a nozzle array, Figure 2.12b, 2) parallel extrusion through a mixing nozzle, Figure 2.12c, and 3) one that combines these two extrusion features. Preliminary success in parallel extrusion has been demonstrated in recent study;[31] but serial extrusion is used for fabrication of the composite structures in this work.

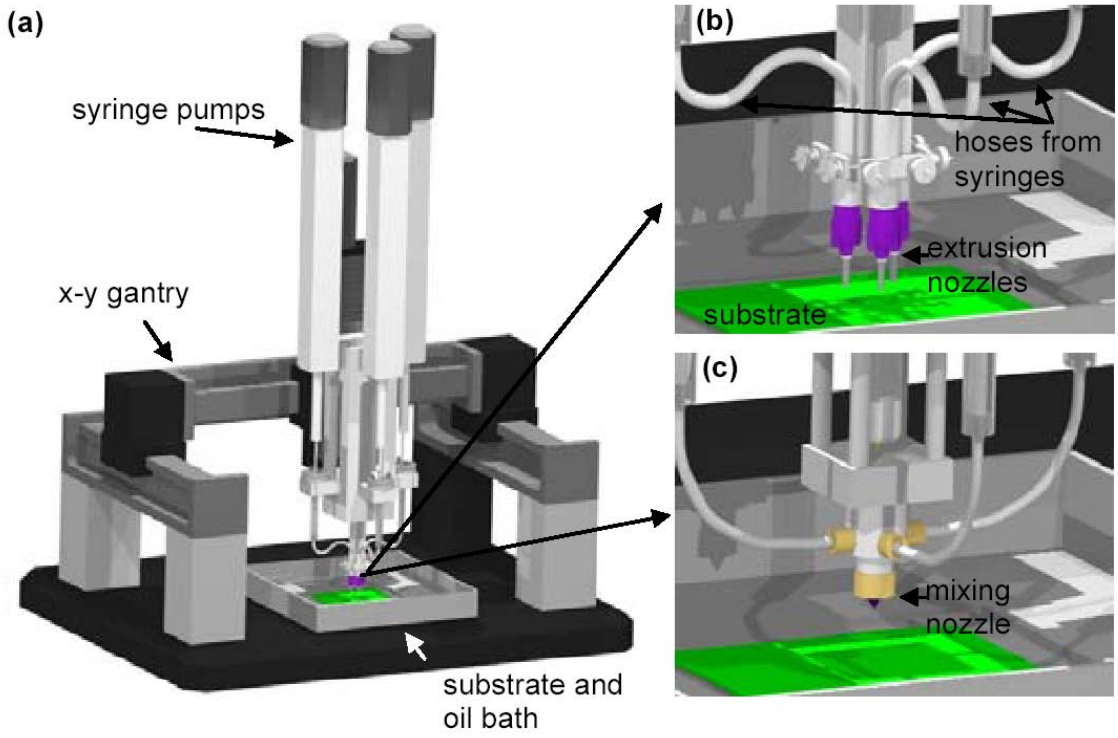

Figure 2.12 Schematic illustrations of multi-ink printing: a) the robotic gantry system used by robocasting, b) the arrayed nozzle assembly for serial extrusion, and c) the mixing nozzle assembly for parallel extrusion.[32]

2.4.1 Colloidal Inks

The printing ink for Robocasting consists of high solids fraction, low binder concentration aqueous colloidal gels. To formulate these inks, a two step process of dispersion followed by controlled flocculation is typical. The resulting ink exhibits Herschel-Bulkley (shear-thinning with yield stress) flow behavior. The controlled flocculation step is achieved by pH change, bridging flocculation through addition of oppositely charged polyelectrolyte, and salt addition or a combination of these. A schematic illustration of the concept of ink formulation is provided in Figure 2.13. All these methods induce a systematic change to the colloidal dispersion by diminishing the repulsive energy between stabilized particles, such that flocculation of the particles yields an interconnecting particle network.

Various particulate materials, including ceramics,[5, 6, 30, 32-34] metals,[35] and polymer,[36] have been employed for the ink preparation. With these inks, complex structures have been assembled, such as space-filling solids, high aspect-ratio walls, and periodic lattices.[6, 30, 34] Applications for these novel materials include sensors,[6] photonic materials,[30] tissue engineering scaffolds,[33] composites,[35] and catalyst supports. To allow extrusion through small diameter nozzles (~Ø0.1-1 mm), these inks have weak mechanical strength and low yield stress: shear elastic modulus on the order of 0.1 MPa, and yield stress around 100 Pa (measured by oscillatory rheometry at 1Hz).[31] Fabrication of structural features such as long spanning beams or extensive internal voids requires a support structure of fugitive material.

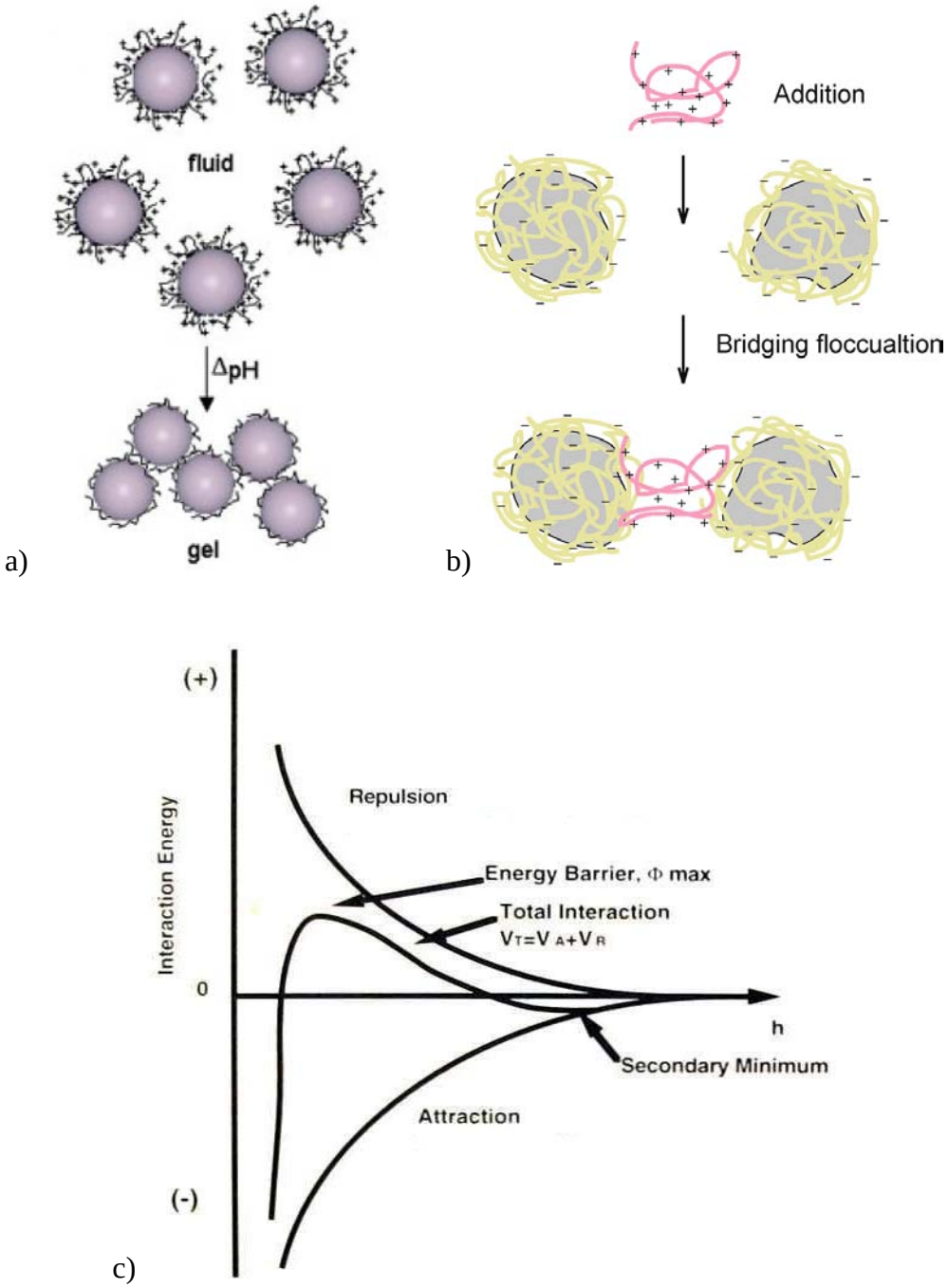

Figure 2.13 Schematic illustrations to the concept of ink formulation induced by a) pH change,[34] b) bridging flocculation, c) the total potential energy of interaction by two particles with electrical double layers is shown in Figure 2.9c.[37] Flocculation is achieved by diminishing the energy barrier, h is the separation distance.

Robocasting has lacked a well-designed fugitive ink since its invention. Hence, one of the objectives in this research is to develop a fugitive ink to facilitate building of cantilevered structures in Robocasting. A successful fugitive ink should be chemically compatible with the ceramic and metal inks. It should allow compatible printing and easy removal after assembly of powder preforms. The same concept of fugitive material is seen in other SFF techniques, e.g., the plastic fugitive ink in Figure 2.6, the unconsolidated powders in Figure 2.7 and 2.9, and the waxy ink in Figure 2.10.

2.5. Binder Removal

Organic processing aids, such as polyacrylic acid (PAA), polyethylenimine (PEI), and hydroxypropyl methylcellulose (HPMC), are used in Robocasting to control the rheology of the printing ink. The term "binder" refers to the collection of additives that remain in the as-formed particle compacts after drying. After the water is removed by drying, these organic additives are thermally removed prior to sintering of the metal or ceramic particles. This process is called binder removal. In Robocasting, binder removal is achieved by oxidation of the polymer in air (typically). The products of the oxidation are primarily CO_2, H_2O and NO_x (i.e., combustion products of the polymeric species). The polymer degrades along many possible pathways. The major concern relates to reaction of the main chain: the main chain can either break by chain scission or cross-linking to another chain. Scission leads to a decrease in molecular weight and volatile formation. Cross-linking causes an increase in molecular weight and leads to a series steps to eventual carbon formation. A list of polymers that depolymerize during thermal degradation is given in Table 2.2. The general mechanisms of main chain and side chain reactions are as outlined in Figure 2.14. For complete removal of carbon, a temperature at >600 °C is required.

Detailed analysis of the binder burnout process is beyond the scope of this work. For the purpose of this work, it is sufficient to observe the reduction in weight that occurs as the binder burnout occurs and note the temperatures required. Of key importance is that the gaseous combustion products are able to escape from the particle compact without causing structural damage. This is easy to achieve with a relatively slow ramp of temperature.

Table 2.2 Example polymers that depolymerize during thermal degradation[37] (EI=end initiation, WLS=weak link scission, RI=random initiation, CS=chain scission).

Polymer	Volatile Monomers (%)	T (°C)	Mechanism
Methylmethacrylate	100	275+340	EI+CS
Methyl-α-phenylacrylate	45	N/A	RI+CS
n-Butylmethacrylate	50	250	EI+CS
Styene	45	>300	WLS
α-Methylstyrene	45	N/A	RI+CS
Acrylic acid	45	350	RI+CS

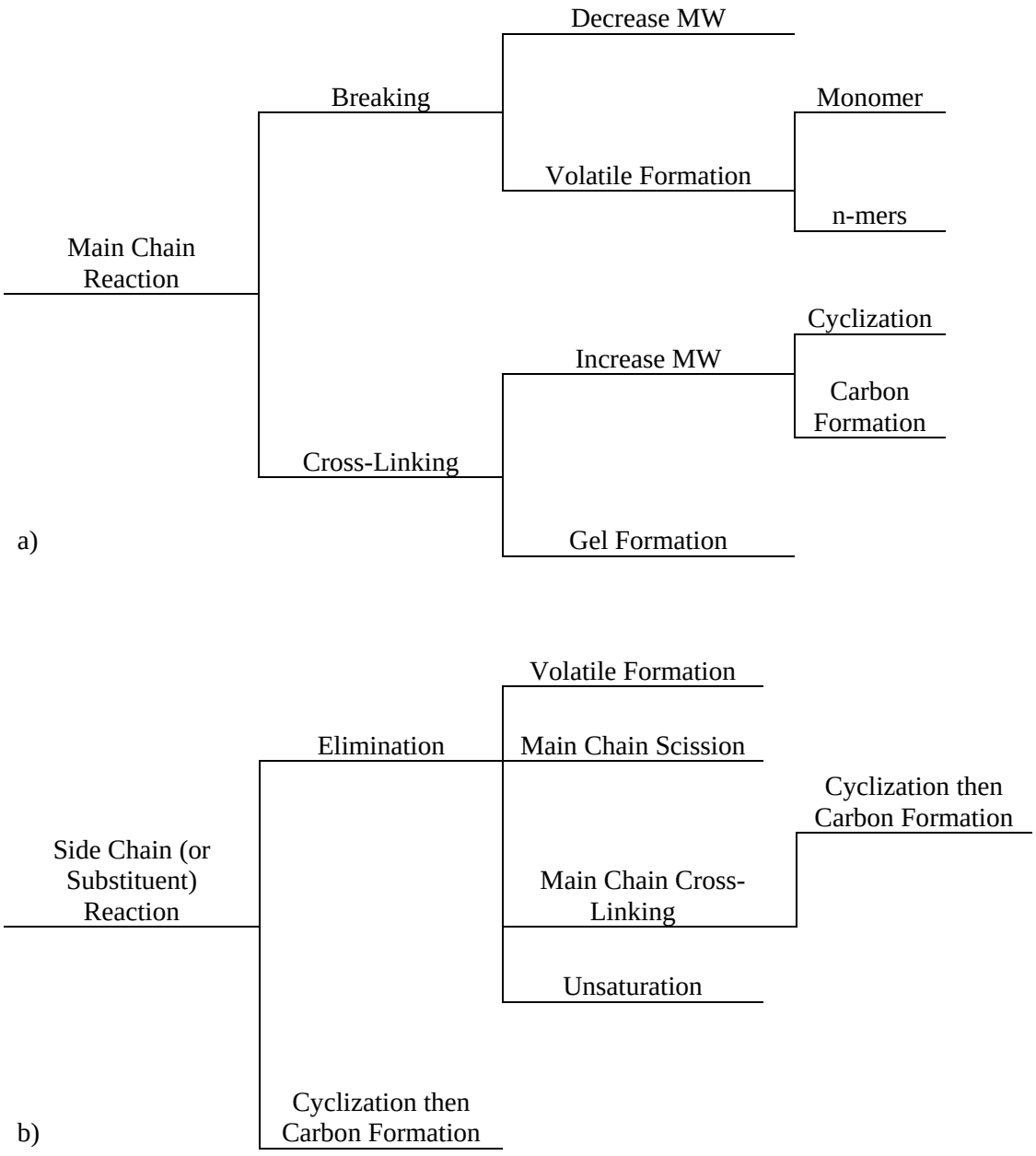

Figure 2.14 Pathway outlines for a) main chain reactions and 2) side chain reactions.[37]

2.6. Sintering

In robocasting, sintering is used after binder burnout to reduce porosity in the particle compact and enhance the strength of the material. Both solid state sintering and liquid phase sintering are explored in this research for co-sintering of heterogeneous composite structures of $BaTiO_3$ and Ni. Single component sintering is complex process where the main thermodynamic driving force is reduction of the surface area to volume ratio in the particle compact. The rate and extent of sintering are dependent on time, temperature and chemical environment. When more than one material is sintered in the same structure, the process is termed co-sintering and extra variables become important. For instance, the rate of sintering of the two materials may differ at a given temperature, which often leads to differential shrinkage, warping, and cracking of the overall structure. In the case that one material needs an oxidizing environment while the other needs a reducing environment, a compromise must be made. The following gives some basic knowledge of sintering to assist the understanding of the complexity of co-sintering.

2.5.1 Definition

Sintering uses thermal treatment to bond compacted particles into a coherent, predominantly solid structure via mass transport events occurring at the atomic level[38]. Sintering processes are categorized in many ways: solid state sintering, liquid phase sintering, pressure assisted sintering, and novel sintering techniques such as reactive sintering, microwave sintering, and spark plasma sintering. Despite these variations, the common characteristics of sintering processes are: 1) reduction of total surface energy

through particle bonding and grain formation, 2) evolution of grain size and shape, and 3) exclusion of internal porosity of the compact accompanied with its size shrinkage.

2.5.2 General Mechanism

For a powder compact, the total free energy ΔG_T is the driving force for sintering and may be described as

$$\Delta G_T = \Delta G_v + \Delta G_{gb} + \Delta G_s$$

where ΔG_v, ΔG_{gb}, and ΔG_s represent the change in free energy associated with the volume, boundaries and surface of particles, respectively.[37]

For simplicity in modeling, a spherical particle in the proximity of a flat surface of the same material is shown in Figure 2.15. Only the effect of change in surface energy is considered here. The spherical particle of diameter D has a volume of V and surface area A,

$$V = \frac{\pi}{6} D^3$$

$$A = \pi D^2$$

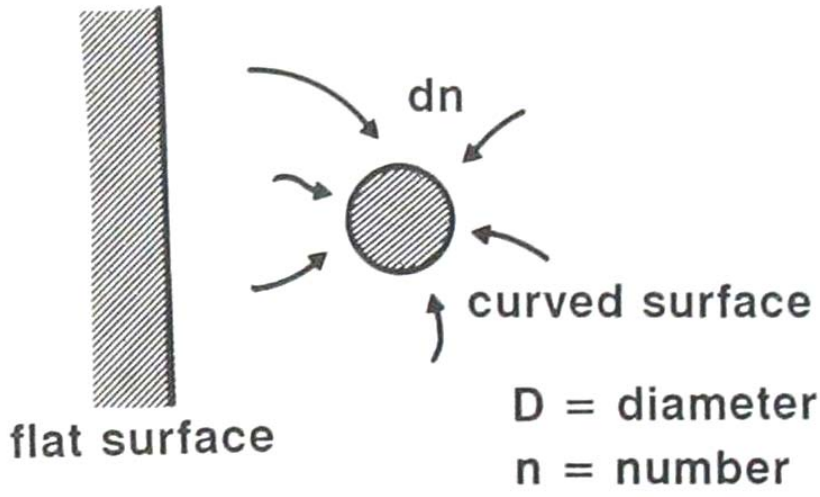

Figure 2.15 Sphere and plate model for examining the energy difference associated with a curved surface.[38]

The volume of the particle represents a collection of n atoms, each with a volume of Ω ($V = n\Omega$). At constant temperature and pressure, a change in number of atoms dn for the particle has corresponding change in diameter dD and volume dV:

$$dV = \Omega dn = \frac{\pi D^2 dD}{2} \tag{2.1}$$

and chemical potential difference ΔU

$$\Delta U = \gamma \frac{dA}{dn} = 2\gamma\pi D \frac{dD}{dn} \tag{2.2}$$

where γ is the surface energy density. Combining Equation 2.1 and 2.2, the chemical potential difference for the particle becomes

$$\Delta U = \frac{4\gamma\Omega}{D} \tag{2.3}$$

Equation 2.3 indicates that the excessive energy per atom in the spherical particle depends on the inverse of the particle size. Small particles are more energetic. For the flat surface, however, the chemical potential difference is zero as the surface area remains the same. In this sense, a concave solid surface tends to fill and a convex surface tends to flatten, Figure 2.16. In a powder compact consisting of particles and interstitial pores, sintering eliminates surface curvature. The particles are convex surfaces acting as the mass sources to fill the interstitial pores that have concave curvature.

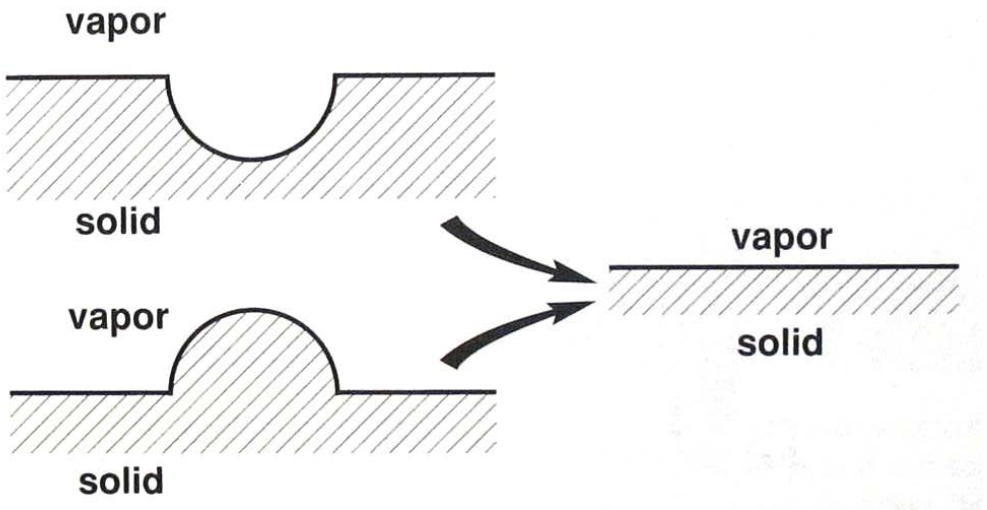

Figure 2.16 Effective curvature changes for both convex and concave surfaces with convergence toward a flat surface.[38]

Such mass flow requires high atom mobility, and only becomes significant at an adequately high temperature, which means that sintering processes are thermally activated. The Arrhenius equation applies to this process as

$$\frac{N}{N_0} = \exp(-\frac{Q}{RT})$$

where N is the population of vacant atomic sites or activated atoms, N_0 is the number of total atoms, Q is the activation energy, R is the gas constant, and T is the absolute temperature. Sintering rate is higher at higher temperatures because of increased number of active atoms and available sites. Thus temperature is a dominant parameter in defining a sintering cycle. Other important factors include the particle size, applied pressure, sintering time, formation of liquid phase, heating rate, and process atmosphere. Some of the key processing changes and their effects are listed in Table 2.3.

Table 2.3 Processing effects in sintering.[38]

Changes to Aid Sintering	Effects
Decrease in particle size	Faster sintering
	Greater expense
	Higher impurity level
	Increased hazard
Increase in time	Greater expense
	Grain growth and coarsening
	Reduced productivity
Increase in temperature	Greater shrinkage
	Grain growth
	Greater expense
	Less precision
	Higher properties
	Furnace limitations
	Pore coarsening
Increase in green density	Less shrinkage
	Smaller pores
	Higher final density
	Uniform dimensions
	Density gradients
Increase in alloying/additives	Higher strength
	Homogeneity problems
	Higher sintering temperatures
Use of sintering aids	Faster sintering
	Lower sintering temperatures
	Embrittlement
	Distortion
	Grain growth control

2.5.3 Solid State Sintering

In this dissertation, solid state sintering is the first densification method investigated. For reference, a classic solid state sintering process is described where idealized conditions of mono-sized spherical particles in point contact that consolidate under isothermal conditions are assumed. In reality, most sintering is carried out using powder compacts containing non-spherical particles that have a wide particle size distribution and packing density. Sintering occurs over a range in temperature rather than isothermally. Also, gradients introduced by thermal stress and atmosphere interactions have a significant influence to the process. Nevertheless, the classic model gives a basic view of sintering process upon which more sophisticated models and computer simulation may be built.

2.5.3.1 Mass Transport

Driven by reduction of free energy, various mass transport phenomena occur during the sintering process, including: surface diffusion, bulk diffusion, grain boundary diffusion, evaporation-condensation, viscous flow, and plastic flow.[38] The actual mass transport process is a mixture of these individual mechanisms and incorporates three major stages as shown in Figure 2.17 and Table 2.4.

Figure 2.17 Illustration of the densification of three adjacent particles.[37]

Table 2.4 Three major sintering stages and their characteristics.[37]

Sintering Stages	Characteristics
Initial stage	Particle surface smoothing and rounding of pores
	Grain boundaries form
	Neck formation and growth
	Homogenization of segregated material by diffusion
	Open pores
	Small porosity decreases <12%
Intermediate stage	Intersection of grain boundaries
	Shrinkage of open pores
	Porosity deceases substantially
	Slow grain growth
	Differential pore shrinkage and grain growth in heterogeneous compact
Final stage	Closed pores
	density > 92%
	Closed pores intersection grain boundaries
	Pores shrink to a limiting size or disappear
	Pores larger than the grain shrink very slowly

2.5.3.2 Initial Stage

The growth of the sinter bond from an initial loose powder contact is characterized as the initial stage of sintering. In this stage the neck size is sufficiently small that neighboring necks grow independent of one another. The initial stage ends when the necks begin to impinge at approximately a neck size ratio X/D of 0.3, Figure 2.18. There is only a minor level of densification.

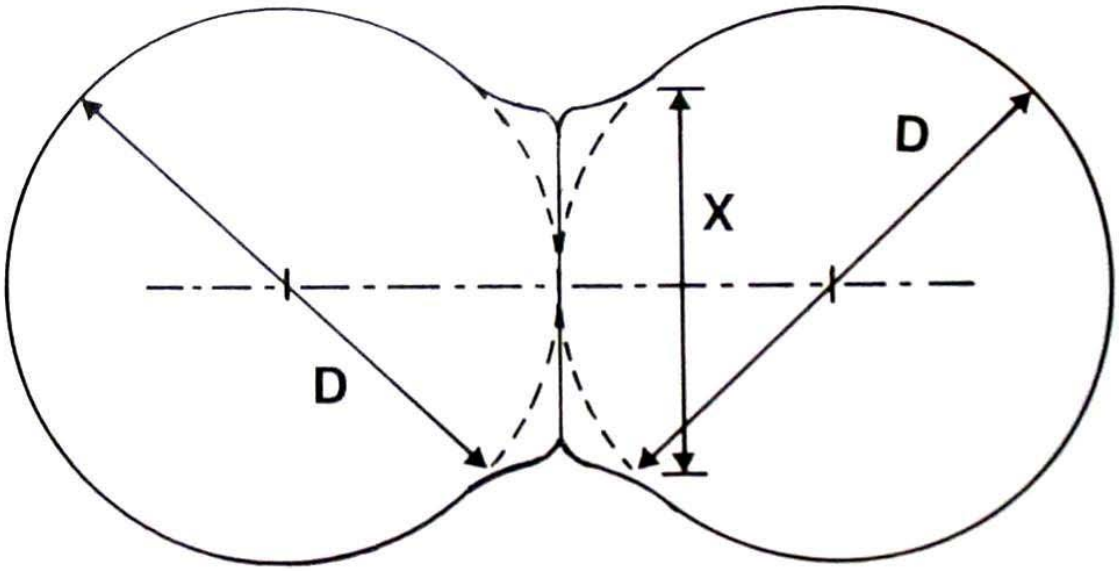

Figure 2.18 Illustration of neck growth between two spherical particles of diameter D.[37]

2.5.3.3 Intermediate Stage

Characterized by simultaneous pore rounding, densification, and grain growth, the intermediate stage is of most importance to densification, determining the properties of the sintered compact. It begins after the formation of a pore and grain-boundary matrix at the end of the initial stage. The pore shape approximates a continuous cylindrical channel throughout the matrix as shown in Figure 2.19. During this stage, the cylindrical pore simply shrinks, driven by elimination of the surface energy of the pore structure. When the length to radius ratio exceeds a critical value, the cylindrical pore will break up into a string of spherical pores, as shown in Figure 2.20.

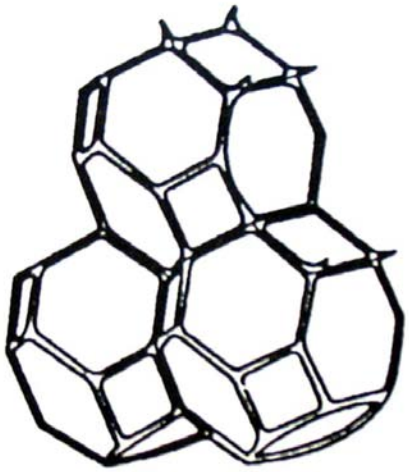

Figure 2.19 Illustration of a portion of the pore and pore and grain-boundary matrix.[37]

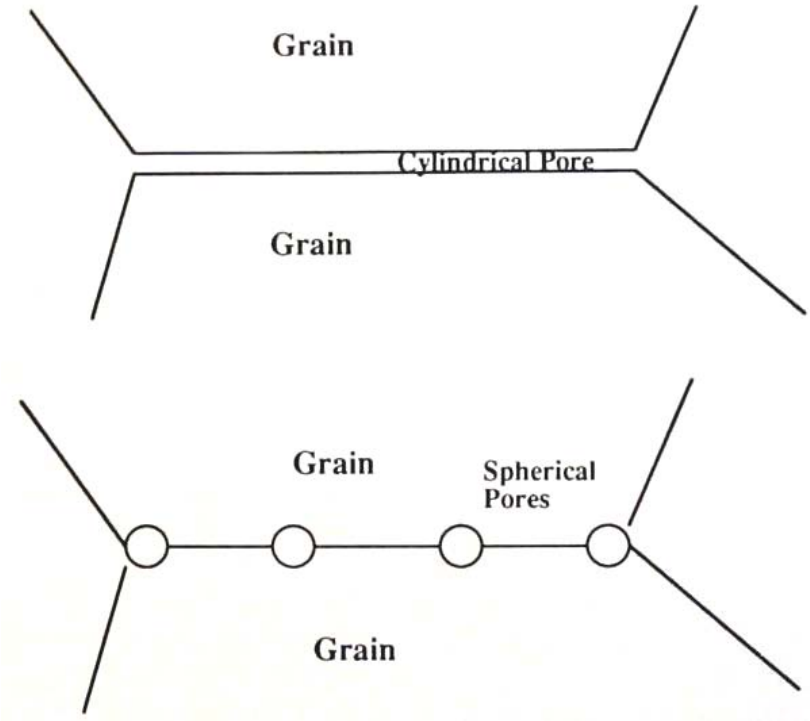

Figure 2.20 Illustration of breaking up of a cylindrical pore into a string of spherical pores.[37]

2.5.3.4 Final Stage

During this stage, the removal of these closed pores takes place. The string of pores at the grain boundary will migrate to the point of lowest energy: the intersection of four grains in three dimensions, as shown in Figure 2.21. And the pore at the intersection then shrinks continuously to zero size in a stable fashion. However, this trend may be hindered by abnormal grain growth that consumes neighboring grains and trap the pores inside, as illustrated in Figure 2.22. The final density is then limited to less than the theoretical density.

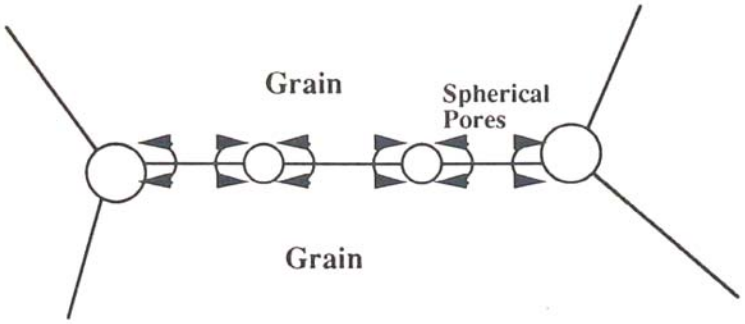

Figure 2.21 Migration of spherical pores from grain boundary to the four grain intersections.[37]

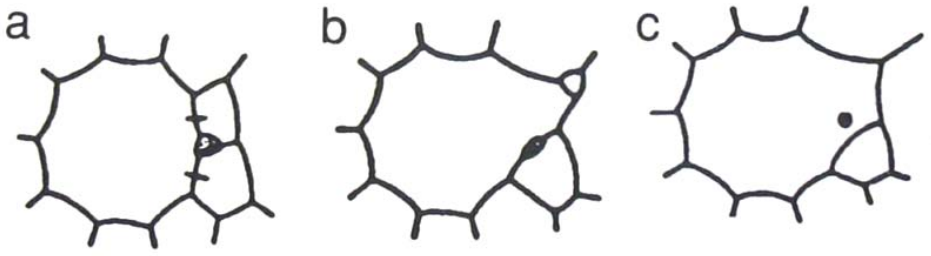

Figure 2.22 Pore detachment from grain boundary.[37]

2.5.4 Liquid Phase Sintering

Liquid phase sintering is the second densification method used in this research to allow high volume fraction of metal phase in the composites fabricated. It utilizes the formation of a liquid phase to increases the sintering rate of the powder compact. Currently, it is used for fabrication of many products, including dental porcelains, cemented carbide cutting tools, automotive connecting rods, and refractory ceramics. The major advantages of liquid phase sintering are lower cost at reduced processing temperature, and fabrication of composite materials.

Liquid phase sintering densification occurs in stages as sketched in Figure 2.23. Initially, mixed powders are heated to a temperature where non-reactive liquid forms. Three stages of densification are encountered after the liquid formation: 1) particle rearrangement stage where the solid particles are drawn together by the capillary action of the liquid; 2) dissolution-reprecipitation stage where part of the refractory solid particles is dissolved in the liquid phase and then precipitate; and 3) final densification where solid state grain growth takes place to achieve final sintered density. Approximate time scale for liquid phase sintering is summarized in Figure 2.24.

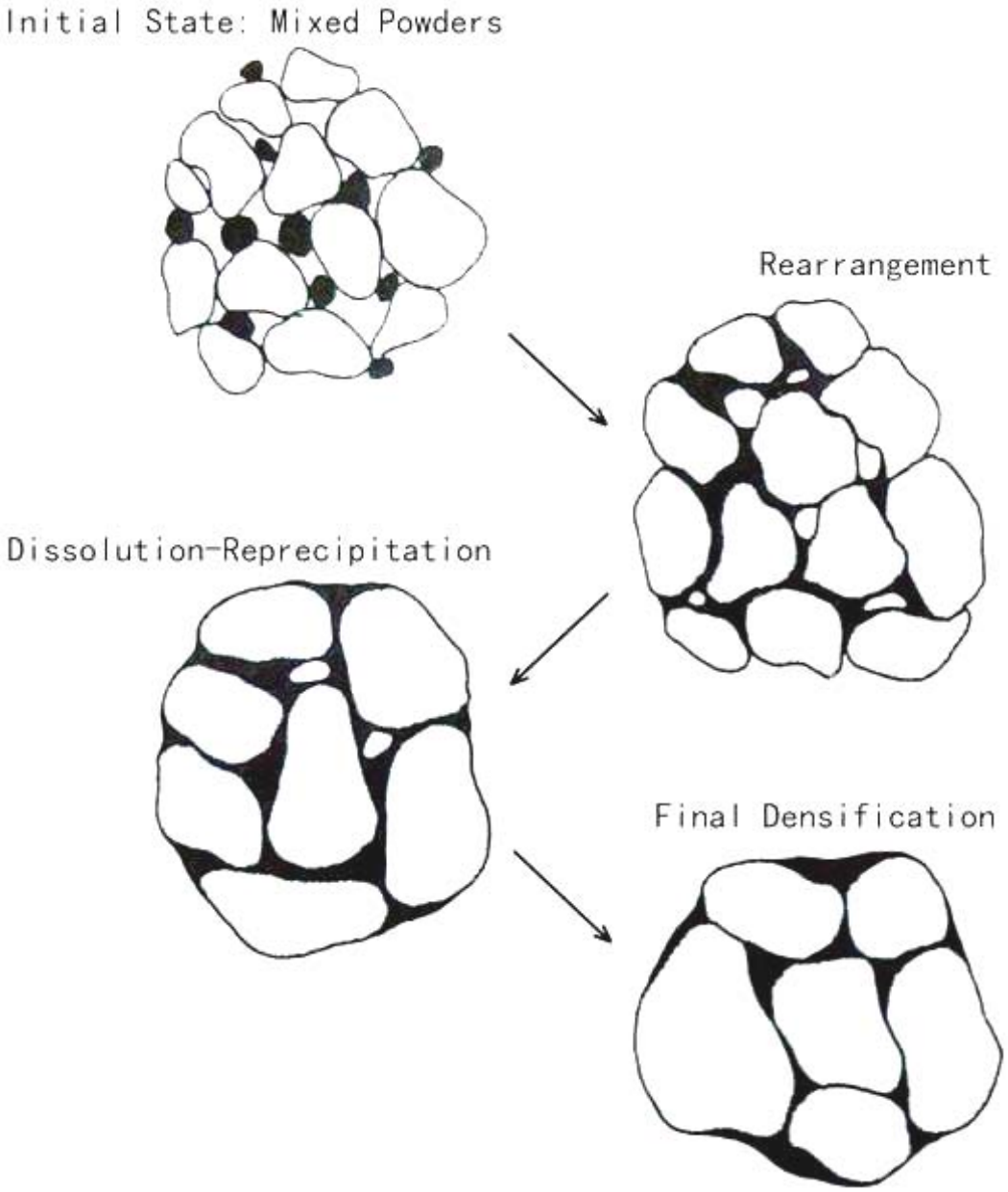

Figure 2.23 Schematic diagram of the classic liquid phase sintering stages.[38]

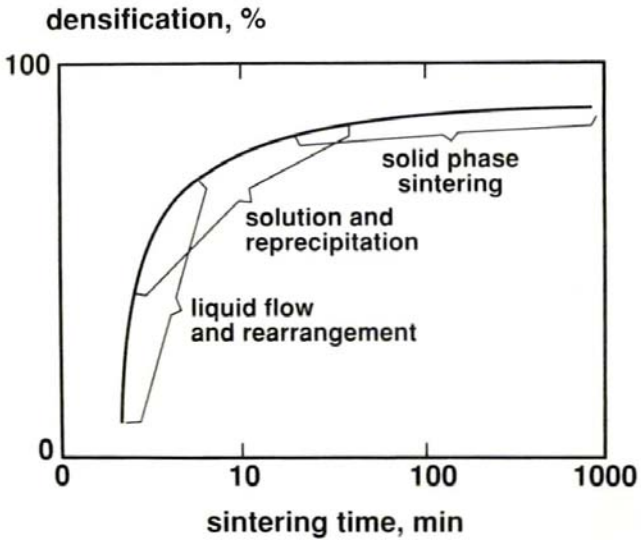

Figure 2.24 Approximate time scale for liquid phase sintering, where densification occurs by a progression of overlapping stages after the liquid forms.[38]

2.5.4.1 Solubility Interactions

After the formation of liquid phase, there are four possible solubility interactions, as shown in Table 2.5. For classic liquid-phase sintering, the solid is soluble in the liquid, but the reverse solubility of the liquid in the solid is low. This ensures that the liquid is not transient.

Table 2.5 Solubility interactions during liquid phase sintering.[38]

		Solid solubility in liquid	
		Low	High
Liquid solubility in solid	Low	Limited densification & rearrangement	Extensive densification
	High	Swelling & transient liquid phase	Mixed swelling & densification

2.5.4.2 Rearrangement

With the formation of a wetting liquid, particles may pack to a higher density rapidly, releasing liquid to fill pores between grains. The solid-liquid surface energy is lower than the solid-vapor surface energy, resulting in reduced system energy. During rearrangement the compact exhibits viscous response to the capillary action. The apparent viscosity of the compact increases due to elimination of porosity; as a consequence, the densification rate decreases continuously. Full density by rearrangement is possible if enough liquid is formed. Rearrangement may be inhibited, if rigid particle contacts formed through compaction or solid-state diffusion are present.

2.5.4.3 Dissolution-Precipitation

As densification by rearrangement slows, solubility and diffusivity effects become dominant. The solubility of a grain in its surrounding liquid varies inversely with the grain size: small grains have a higher solubility than large ones. The difference in solubility establishes a concentration gradient in the liquid. Material is transported from the small grains to the large grains by diffusion through the liquid. The net result is a progressive growth of the larger grains at the expense of the smaller grains, giving fewer grains with a larger average size. This allows the growing grains to better fill in space.

2.5.4.4 Final densification

In the final stage, liquid-phase sintering is controlled by the slow densification of the rigid solid structure. Processes dominant in this stage have been active earlier, but only become significant late in the cycle. Microstructural coarsening continues and the residual pores enlarge if they contain trapped gas, giving compact swelling. In general,

properties of most liquid-phase sintered materials are degraded by prolonged final-stage sintering. Hence, a short sintering time is preferred in practice.

2.5.4.5 Phase Diagram

A binary phase diagram corresponding to the composition and temperature for classic liquid-phase sintering is shown in Figure 2.25. A typical sintering temperature would be slightly above the eutectic temperature with a composition in the L+ S_2 region. Examination of phase diagram makes it possible to determine the temperature of liquid-phase formation and the composition of the liquid.

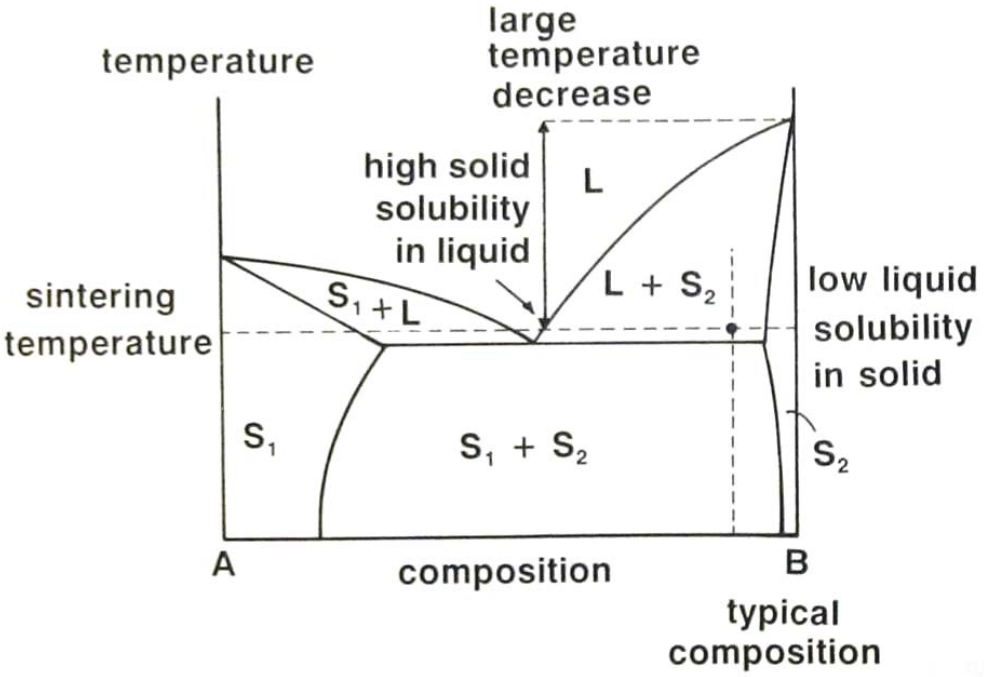

Figure 2.25 Model binary phase diagram showing the showing the composition and temperature associated with liquid phase sintering in the L+S_2 phase field.[38]

2.5.4.6 Spreading of Sintering Aid

In the early portion of liquid-phase sintering using mixed powders, the melted sintering aid often forms at local regions in the green compact. Subsequent wetting of the sintering aid on solid particles spreads the liquid within the particle network. This process reduces free energy, accompanied with an increase in the liquid-vapor and solid-liquid surface areas and a decrease in the solid-vapor surface area. This requires that

$$\gamma_{SV} > \gamma_{SL} + \gamma_{LV}$$

where γ is the surface energy and the subscripts denote the interface: *SL* = solid-liquid, *LV* = liquid-vapor, and *SV* = solid-vapor. As shown in Figure 2.26, the degree of wetting is characterized by the contact angle θ; and the balance of three surface energies determines its magnitude:

$$\gamma_{SV} = \gamma_{SL} + \gamma_{LV} \cos\theta$$

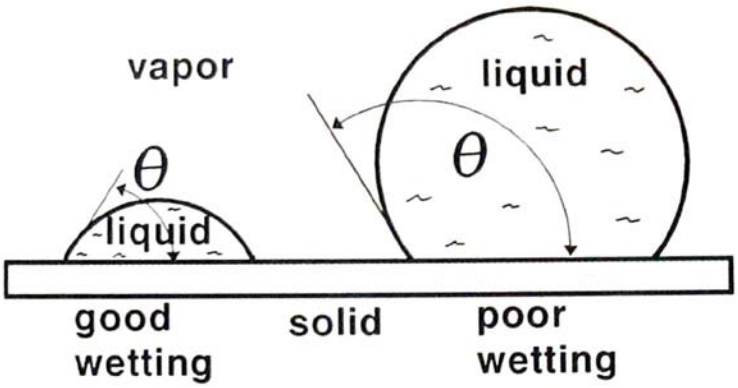

Figure 2.26 Geometric representations of the solid-liquid-vapor equilibrium conditions for good wetting and poor wetting conditions.[38]

Driven by reduction of free energy, a wetting liquid preferentially flows to smaller capillaries. When there is insufficient liquid to fill all the pores, the wetting liquid pulls the particles together to minimize the energy. This gives rise to the rearrangement. In contrast, a poor wetting liquid causes swelling of the compact, and may possibly exude liquid from surface pores. In sintering practice, the spreading of the liquid phase should be confined within the particle compact to prevent loss of liquid phase; preferably, noble metal crucible or substrate should be used.

2.5.4.7 Solubility of Small Particles

The effect of size on the solubility of small particles may be described as:

$$ln\frac{C}{C_0} = \frac{4\gamma_{SL}\Omega}{DkT}$$

where Ω is the atomic volume, γ_{SL} is the solid-liquid surface energy, D is the particle diameter, C is the solubility of the particle, and C_0 is the equilibrium solubility corresponding to a flat surface. Apparently, small particles have a higher solubility than large particles.

2.5.4.8 Capillarity

When the liquid phase is trapped between particles, capillarity gives a strong pressure difference between the liquid meniscus and the vapor. This pressure difference causes rearrangement, densification, and contact flattening[39] and is depending on the liquid curvature, which in turn is affected by the amount of liquid, contact angle, particle separation, and particle sizes. The force between the two spheres depends on the meniscus diameter X as follows:

$$F = \frac{\pi}{4} X^2 \Delta P + \pi X \gamma_{LV} \cos \psi$$

where ΔP is the pressure difference, and ψ is the angle as shown in Figure 2.27a. At equilibrium, the energy of the configuration must be at a minimum. For a wetting liquid (θ = 0), the capillary force is attractive and tries to achieve zero separation between the particles. Alternatively, for a non-wetting liquid, the liquid causes separation of the particles. These two conditions are contrasted in Figure 2.27b. For liquids that do not completely wet a solid, there is an equilibrium separation between particles connected by a liquid bridge.

a)

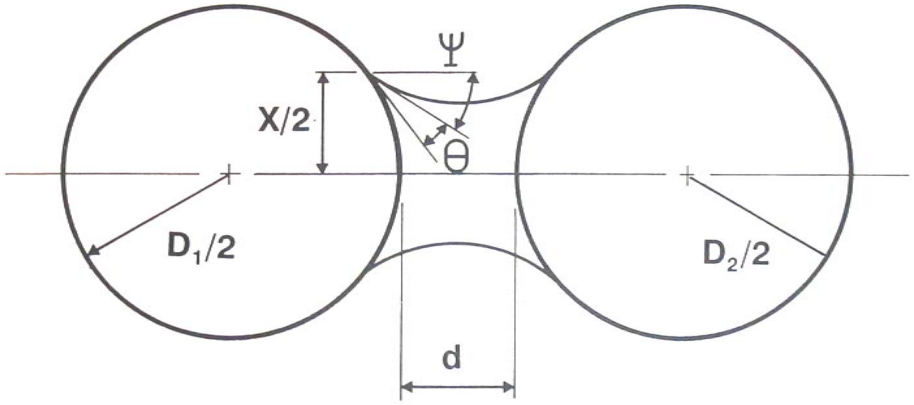

b)

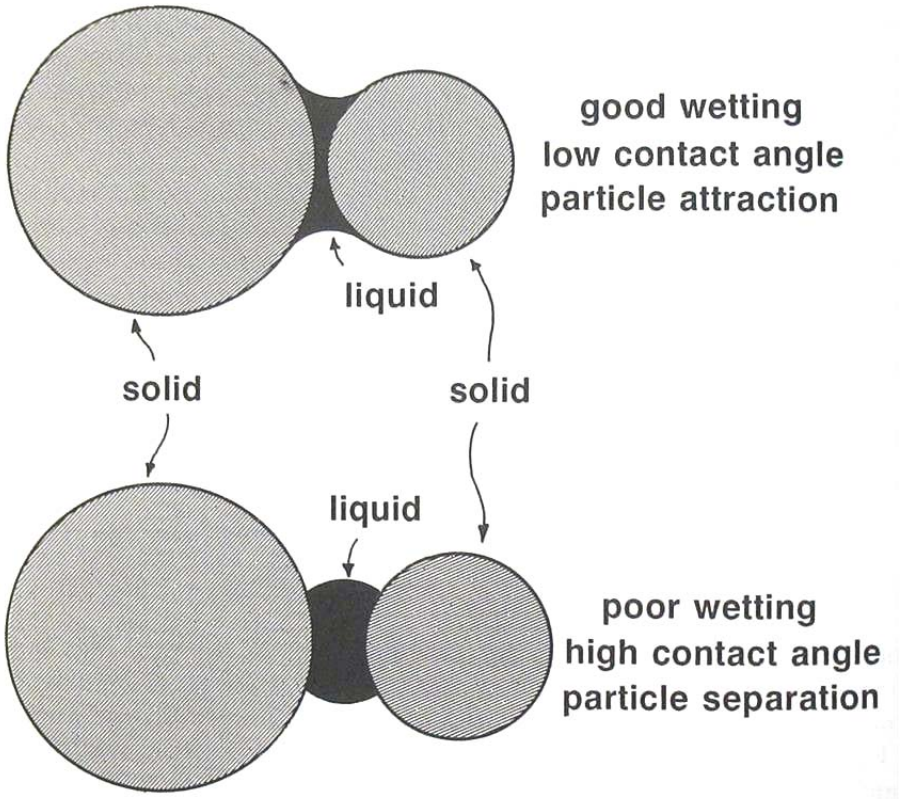

Figure 2.27 Capillary force between particles: a) model for calculating the capillary force: two spherical particles with a liquid bridge and the geometric factors, and b) effects of good wetting and poor wetting on particles.[38]

2.5.5 Sintering Atmosphere

Sintering atmosphere is one of the key factors that influences sinter bonding and compact composition. This first function of sintering atmosphere is to assist removal of surface contaminants and organic binders. There are seven major types of atmosphere in use: air, inert gas, hydrogen, dissociated ammonia, nitrogen based, natural gas based, and vacuum. In all these atmospheres, a main concern is the partial pressure of the reactants and the reaction equilibrium at sintering temperature.

An important aspect of successful sintering is the thermochemical reactions between the sintering powder and the atmosphere.[38] Volatile species may either direct form or by reactions with the atmosphere. The most common reactions involve oxygen and carbon. One of the best understood examples is the oxidation and reduction of metals; and another one is the carburization-decarburization reactions.

The oxidation reaction of a metal in equilibrium may be represented as:

$$xM_{(s)} + O_{2(g)} \leftrightarrow M_x O_{2(s)}$$

For this reaction, the equilibrium constant K is:

$$K = \frac{a_{M_x O_2}}{(a_M)^x P_{O_2}} = \frac{1}{P_{O_2}}$$

where a designates the activity of the of solid phase and P_{O_2} is the oxygen partial pressure. And the equilibrium condition may be determined by the standard free energy for the reaction:

$$\Delta G = -RTlnK = RTlnP_{o_2}$$

Similar concerns exist with atmosphere-controlled carbon reactions. Carbides can be formed or decomposed during sintering, based on the equilibrium between the materials involved. Two major reactions involve carbon monoxide and methane respectively:

$$xM_{(s)} + 2CO_{(g)} \leftrightarrow M_xC_{(s)} + CO_{2(g)}$$

$$xM_{(s)} + CH_{4(g)} \leftrightarrow M_xC_{(s)} + 2H_{2(g)}$$

Control of the carbides is very important to many sintered products, including cermets, cemented carbides, tool steels, and silicon carbide.

Control of the sintering atmosphere provides an opportunity to control material chemistry and degree of sintering; however, the atmosphere is not constant during sintering. The composition of the evolved gas depends on temperature, in turn affecting the thermochemical reactions.[40] Not only is the type of atmosphere important, but also the flow rate, sintering temperature, type of materials and contaminants, collectively determine the instantaneous composition.[38] To analyze the atmosphere *in situ*, it usually requires dew point analyzer, mass spectrometer, specific probes for oxygen and carbon, infrared analyzers, and gas chromatographs. The analysis information is then used during sintering to make corrections to the operation parameters.

2.7. Composite Materials

In this research, the particle reinforced composites are fabricated, and may be regarded as either ceramic or metal matrix composites based on BT/Ni ratio. These composites serve as functional structural components; together with complementing pure ceramic counterparts, they form integral complex composite structures in a form with disparate material distribution. The following content in this section provides a brief description to composite materials.

2.6.1 Definition

Composite materials (or composites) are engineered materials made from two or more constituents that have significantly different physical or chemical properties and remain distinct on a macroscopic level within the finished structure.[41-43] As illustrated in Figure 2.28, these constituents either serves as a reinforcement material in the form of discontinuous phases (such as particles or fibers), or as a matrix material in one continuous phase. Not only different are these constituents at the molecular level, but also macroscopically identifiable with distinctive properties and generally mechanically separable. Many materials, such as metal alloys, solvent-swelled polymers, and glasses, are excluded by this definition.

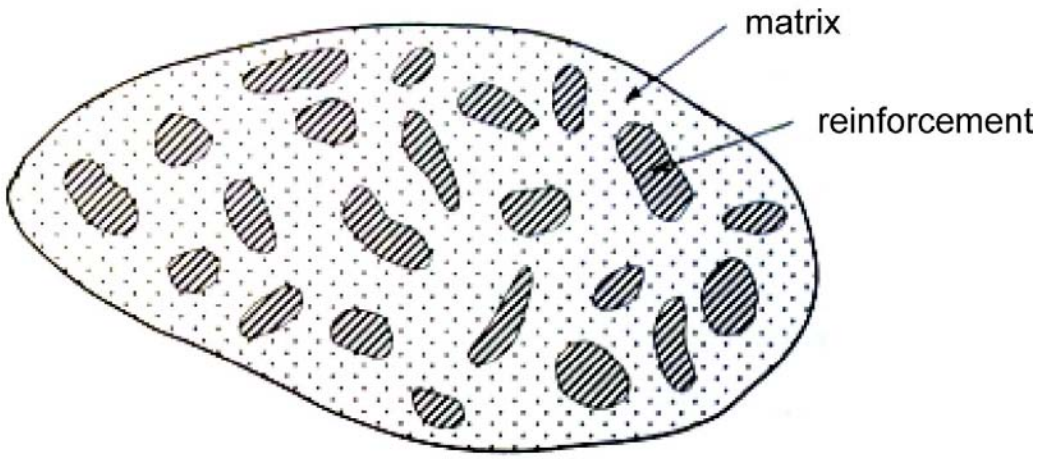

Figure 2.28 A schematic illustration of a composite material.[41]

2.6.2 Classification of Composite Materials

Composite materials are usually classified either by the form of the reinforcement, or by the nature of the matrix.[41-43] By the form of the reinforcements, composites fall into three large categories: fiber-reinforced composites, particles-reinforced composites, and laminar composites, as shown in Figure 2.29. According to the material nature of the matrix, composite materials are categorized as ceramic, metal, and polymer matrix composites.

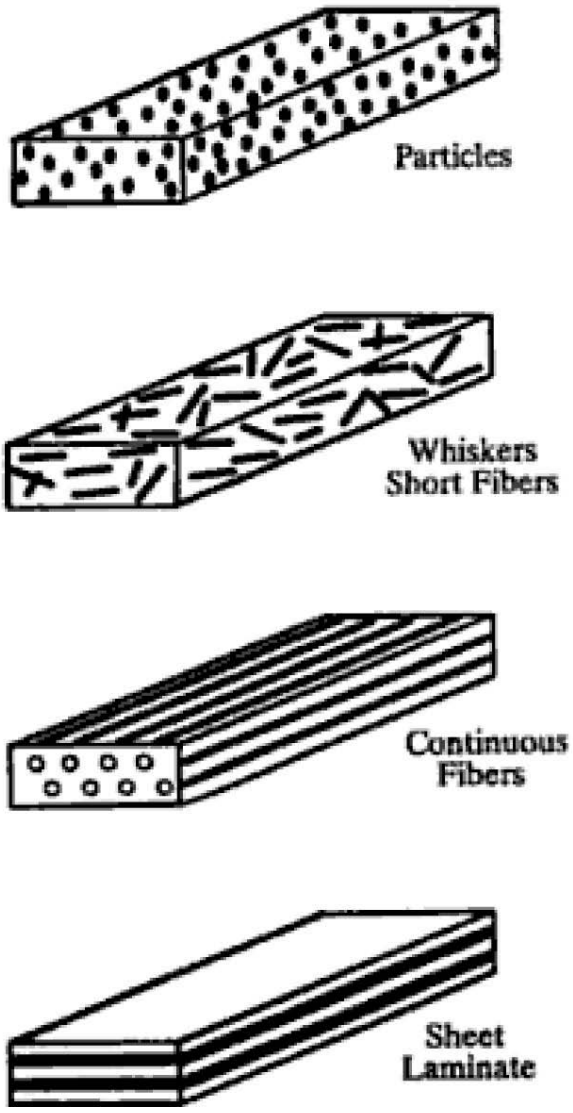

Figure 2.29 Types of composite material based on the form of the reinforcement.[42]

2.6.3 Properties of Composite Materials

The properties of composite materials result from many factors including properties of the constituent materials, their geometrical distribution, and their interactions. Therefore, for describing a composite material it is necessary to specify: the nature of the constituents and their properties, the geometry of the reinforcement and its distribution, and the nature of the matrix-reinforcement interface.

The advantages of composite materials fall under three headings: first, composites enable a unique combination of properties to be achieved; second, the resulting properties can be made to vary continuously over a range; third, composites can sometimes attain a value of a given physical property not attainable by either of the two components alone.[43] Examples of composite materials and their applications are given in Table 2.6.

Table 2.6 Examples of composite materials and their applications.[41]

	Constituents	Areas of Application
Polymer Matrix Composites		
Paper, cardboard	Resin/fillers/cellulose fibers	Printing, packaging
Particle panels	Resin/wood shavings	Woodwork
Fiber panels	Resin/wood fibers	Building
Coated canvas	Pliant resins/cloth	Sports/building
Impervious materials	Elastomers/bitumen/textiles	Roofing, earthworks
Tires	Rubber/canvas/steel	Automobiles
Laminates	Resin/fillers/glass fibers/carbon fibers	Multiple areas
Reinforced plastics	Resins/microspheres	
Ceramic Matrix Composites		
Concrete	Cement/sand/gravel	Civil engineering
Ceramic-carbon composites	Ceramic/carbon fibers	Automobiles
Ceramic composites	Ceramic/ceramic fibers	Thermomechanical items
Metal Matrix Composites		
	Aluminum/boron fibers Aluminum/carbon fibers	Space
Sandwiches		
Skins	Metals, laminates, etc.	
Cores	Foam, honeycombs, balsa reinforced plastics	Multiple areas

2.8. Functionally Graded Materials

2.7.1 Definition

Functionally graded materials (FGMs) refer to the category of engineered materials characterized by the gradual transition in composition, microstructure, and material properties.[44] Motivated by the functional performance requirements that vary with locations, the FGMs may be designed for specific functions in a manner that optimizes the overall performances.[44, 45]

2.7.2 Applications

Kawasaki and Watanabe first proposed the concept of FGM in 1984 using compositionally graded ceramic-metal interlayer in a thermal barrier for aerospace application.[46] Such a FGM thermal barrier possesses superior heat resistance and sufficient toughness to stop crack propagation while effectively eliminating thermal stress concentration. Since then, a variety of processing techniques have been developed for fabrication of FGM materials. Examples of successful applications of the FGM concept are shown in Table 2.7.

Table 2.7 Examples of FGM applications.[45]

Application	Materials	Processing Techniques
Thermal barrier; anti-oxidation coatings	ZrO2 on Ni-Cr; SiC on C/C composite	Plasma spraying; CVD
Cutting tools: cemented carbides/diamond/SiC	TiC-TiCN-WC-Co; diamond and SiC	Sintering
Thermaoelectric materials	BiTe/PbTe/SiGe	SHS*/Dynamic Pseudo Isostatic Compaction
Optical film: bandpass filter	SiO2-TiO	Helicon sputtering

* SHS stands for self-propagating high-temperature synthesis

Figure 2.30 illustrates an example of Ti/hydroxyapatite FGM[47] for use as a biocompatible dental implant: the FGM implant in Figure 2.30a has its composition gradually changing from 100% Ti metal at the left end to 100% HA at the right end. The left end, as the upper part of dental implant where occlusal force is directly applied, is designed to achieve high mechanical strength; and the right end is to be implanted inside the jaw bone and requires high biocompatibility. Presumably Ti has higher mechanical strength, but inferior biocompatibility than hydroxyapatite. The use of FGM allows for combination of necessary mechanical properties and biocompatibility at different locations of the implant without formation of a discrete boundary. Figure 2.30b shows the illustration for the gradual transition in related properties of the FGM implant, and Figure 2.30c illustrates a conventional full ceramic implant for which properties such as strength and biocompatibility are constant throughout.

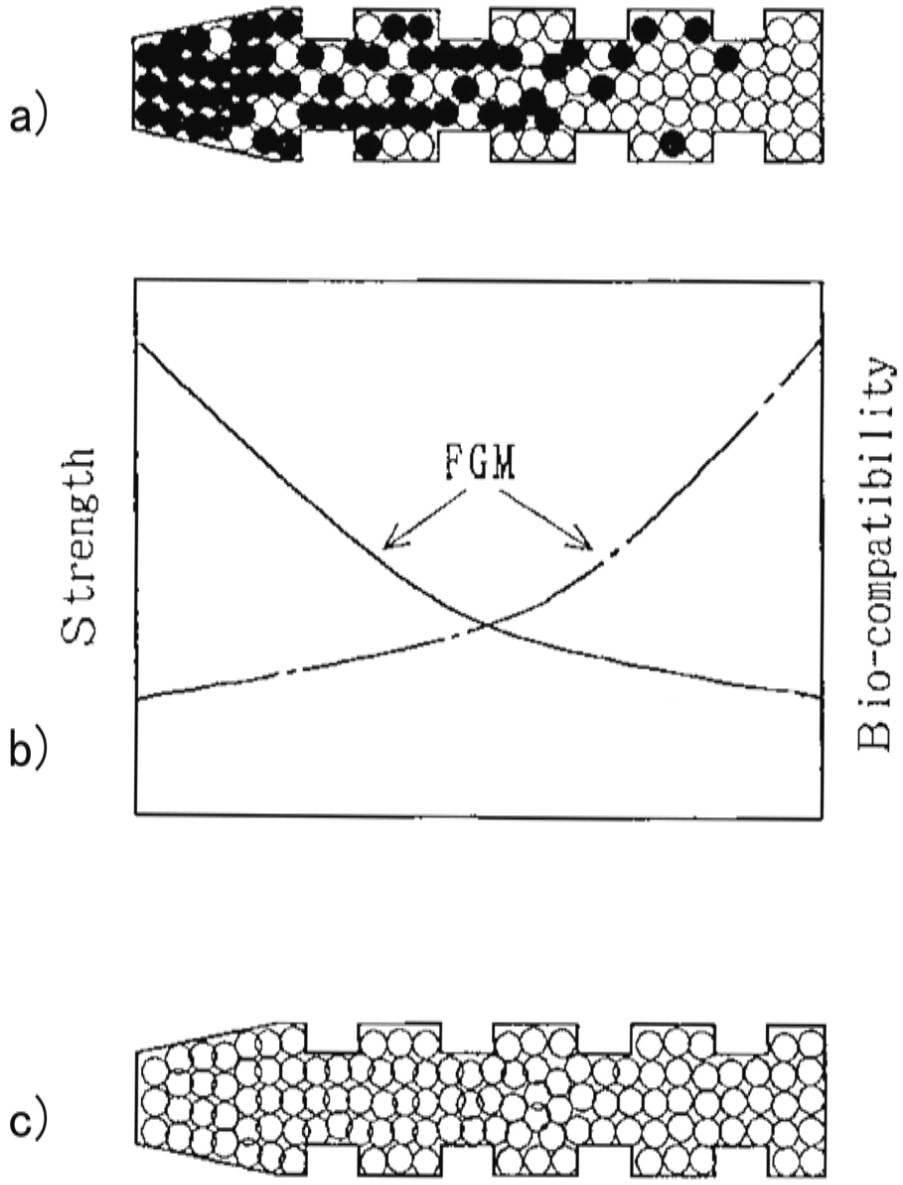

Figure 2.30 Schematic illustration of functionally graded dental implant vs. full ceramic dental implant: a) functionally graded dental implant made of Ti(●) and hydroxyapatite (○), b) expected properties of the functionally graded dental implant, and c) full ceramic implant.[47]

2.7.3 Processing

For the fabrication of functionally graded materials containing a metallic phase, there are two major categories of techniques: constructive processes and transport based processes, as outlined in Figure 2.31. In the constructive processes, the FGM is constructed layer by layer, a strategy similar to the SFF concept. The second class of processes creates gradients within a component relying on natural transport phenomena such as fluid flow, diffusion of atomic species or the conduction of heat to create gradients in local microstructures and/or compositions, albeit within a narrower window of possible structures. While emphasizing on the distribution of compositional gradient, these constructive processes usually lack the ability of SFF to fabricate near net shape parts. However, in many other ways, these processes face problems very much like those encountered in this research. Understanding the fundamentals and mechanisms in these processes are helpful to appreciate the many challenges in the fabrication of BT-Ni composite structures through Robocasting. For this purpose, major constructive processes are described in detail in the following section, followed by a brief summary to the transport based processes.

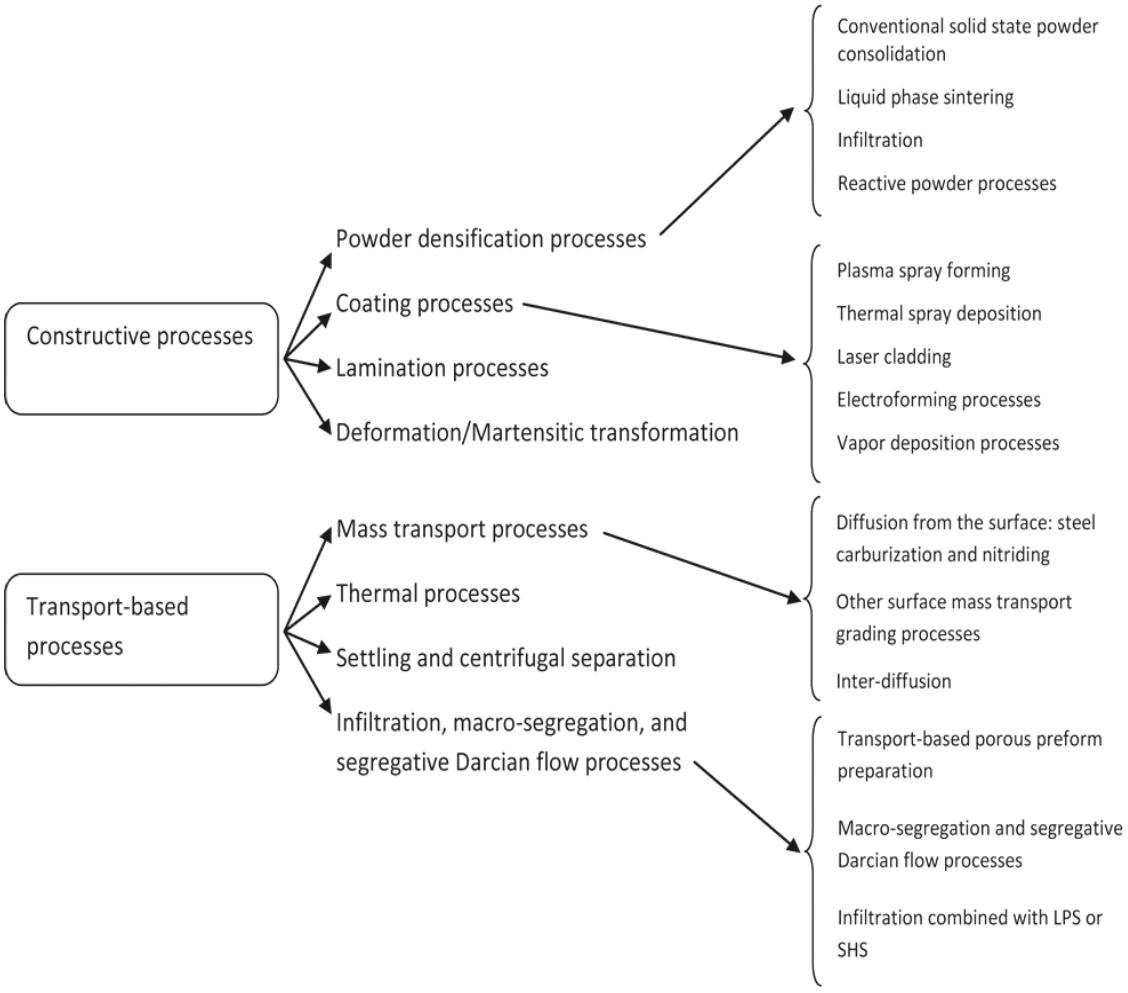

Figure 2.31 Classification of FGM processing methods involving a metallic phase.[44]

2.7.4 Major Constructive Processes

2.7.4.1 Powder Processing Techniques

One major task in the powder production of an FGM is to create a compositional gradient of the powder during preform packing. Various methods are available, ranging from manual packing of discrete powder layers to highly automated computer controlled systems. FGM preforms with unidirectional compositional gradients have been fabricated using various powder layering techniques. One common method involves stacking

prepared discrete layers of uniform composition,[48, 49] as illustrated in Fig. 2.32. Other methods include filtration,[50] dipping approach,[51] and slip casting.[52] Automated techniques have been developed. For the continuous production of FGM strips, a computer-controlled system is illustrated in Figure 2.33a. For cylindrical FGM parts, a centrifugal powder packing system is illustrated in Figure 2.33b.

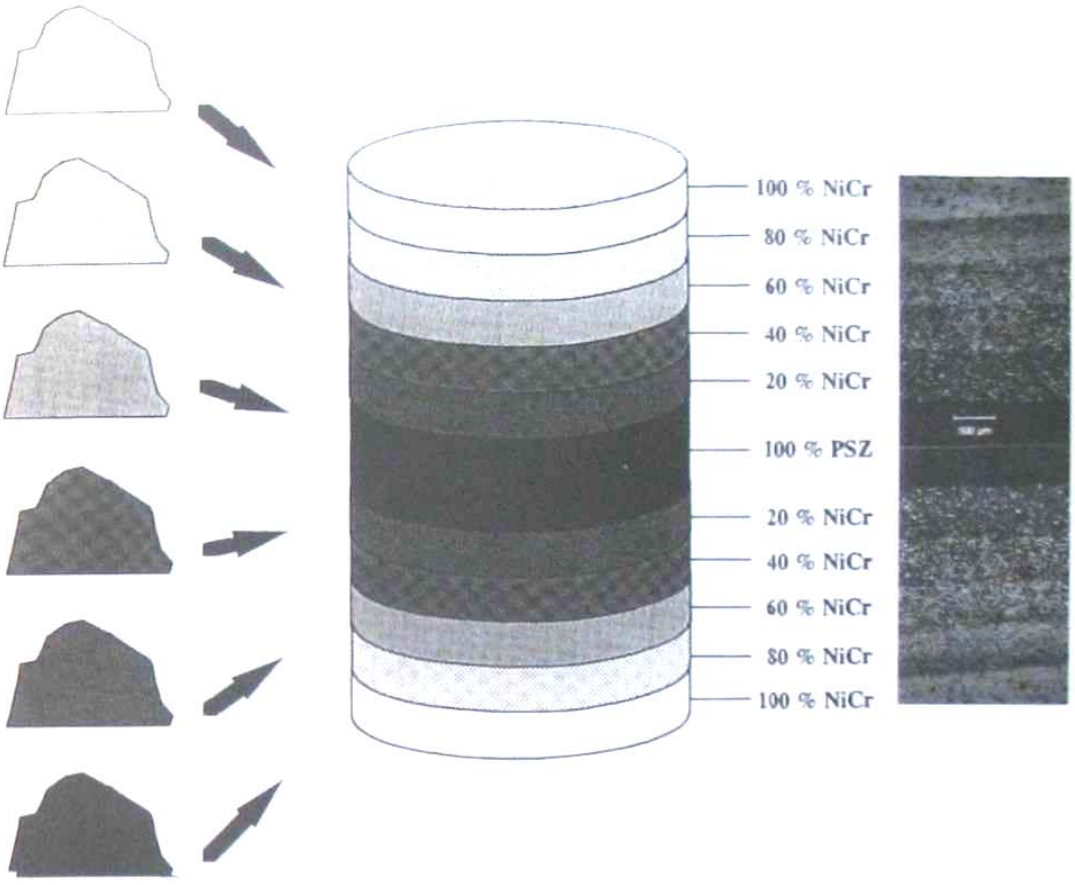

Figure 2.32 Schematic illustration of a FGM structure formed by powder blending, powder stacking and sintering. The micrograph on the right is for the corresponding structure after densification.[44]

a)

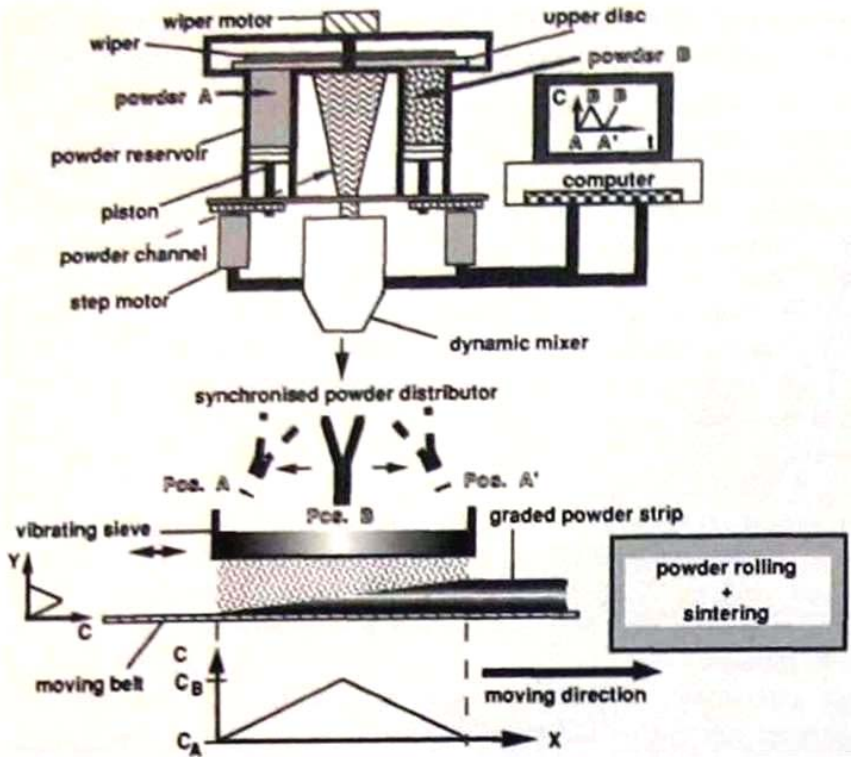

b)

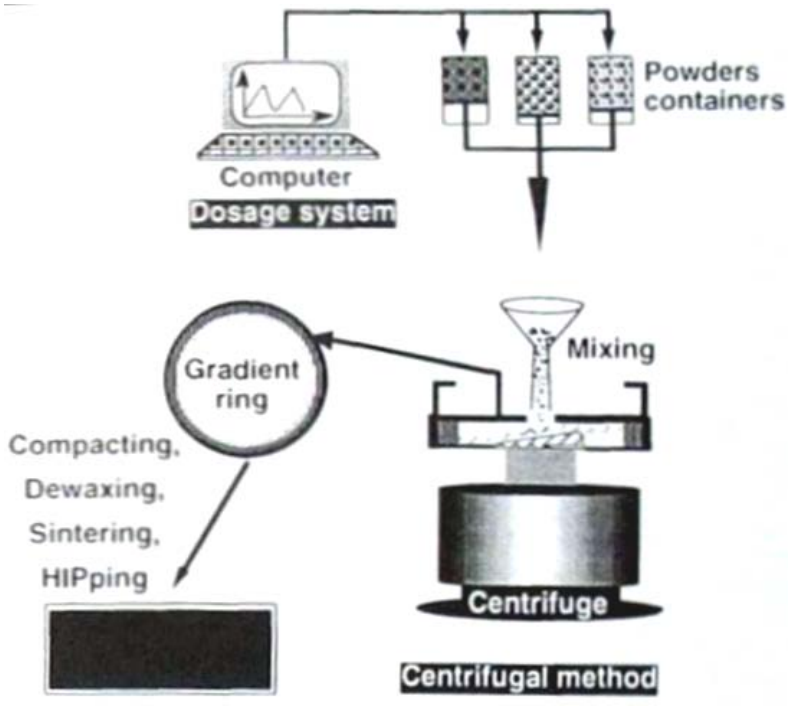

Figure 2.33 Schematic of automatic powder stacking systems: a) for FGM strip production[53]; b) for graded cylindrical structures.[54]

Powder densification processes generally include four techniques: 1) conventional solid state powder consolidation, 2) liquid phase sintering, 3) infiltration, and 4) reactive powder processes. As the solid state powder consolidation and liquid phase sintering are major processing methods in the current study, they are described in more details than the rest FGM fabrication techniques.

Conventional solid state powder processing techniques fabricate ceramic-metal FGM by first making a powder preform containing materials with desired gradient. The preform is then consolidated by conventional techniques, such as cold pressing, pressureless sintering, and hot isostatic pressing. The initial distribution of materials is considered unchanged after the consolidation process, provided that the mutual diffusion of constituent phases is negligible during the processing time frame.

Discrepancy in densification rate between compositionally graded layers is undesirable, as they cause warping and possibly cracking in the FGM during densification. Therefore, these effects must be considered. Particularly, these effects require that a relatively uniform initial powder density within the green compact has to be established; if powder blends are packed initially to different volume fractions for compositionally graded layers, subsequent full densification will cause uneven shrinkage in the component, resulting in warpage or cracking in the dense FGM.

Prediction of the densification kinetics of an FGM structure requires understanding of the densification rate of each composition in the structure; various theories have been proposed to address the question, however their suitability is depending on the volume and size ratios of the phases present.[44]

For a composite with two constituents, there are various scenarios to consider: 1) at a sufficiently low volume fraction of one phase in the other, densification of the composite is primarily controlled by the single percolating matrix phase; and the second isolated phase, however, still influences local densification kinetics; 2) when the inclusion volume fraction becomes sufficiently high for significant percolation to occur, discrepancies in densification rate are much more drastic between compositional graded layers: above the specific volume fraction, the secondary inclusion phase may carry load; for densification of the composite, both percolating phases must densify. If it does not also densify, it resists contraction of the composite powder mixture.[55 56]

In the case of single phase densification with a non-percolating and non-densifying refractory phase, the reduction of densification rate for the powder matrix[57-60] can be rationalized and modeled: when the matrix and inclusion particles have commensurate radii ($R = R_{p,matrix}/R_{p,inclusion} \approx 1$), the inclusions alter both the initial powder packing density and the evolution of inter-particle neck geometries. Therefore greater deformation of the matrix particles is required before reaching a given compact density.[60, 61] When the radius of the inclusion particles is significantly larger than that of the matrix particles, i.e. R « 1, the modeling should instead focus on local stresses in the densifying matrix, resembling a continuum having a stress-dependent density evolution function.[62-64] In the non-percolating regime, although the retarding effect of isolated inclusion phase on the densification of local matrix phase could be significant, the difference in global densification rates between compositions with varying inclusion volume fractions is generally insignificant.

The specific volume fraction beyond which inclusion percolation starts resisting global shrinkage of the powder compact is not known with certainty. It is for sure somewhere above the percolation threshold, since more than one inclusion-inclusion contact is required to resist bending of adjoining inclusion particle chains.[56, 65, 66]

For equiaxed powder blends, Bouvard and Lange proposed that touching inclusions begin resisting global shrinkage when each inclusion on average makes contact with three neighboring inclusions. In their simulated computer program,[67] this critical inclusion volume fraction relative to the total solid volume as a function of $R = R_{p,matrix}/R_{p,inclusion}$ is plotted in Fig. 2.34a.[65] Since further densification will increase the number of inclusion-inclusion contacts, the fraction of ceramic given by Fig. 2.34a is an upper bound for the allowable non-densifying refractory phase in a graded structure. The critical inclusion fraction is also influenced by inclusion aspect ratio: for example, short fibers may start percolating at volume fractions as low as five percent.[68]

The upper limit to the unsintered refractory phase volume fraction incorporated in a fully densified composite was found to be restricted to values lower than 30-40% volume fraction. Above this limit, porosity was observed.[48, 69, 70] Experimental data[71] are superimposed on Bouvard and Lange's theoretical curve in Figure 2.34b and an overall reasonable agreement with the theory is obtained. In particular, the theoretical prediction and experimental observation both suggest that the refractory phase densification becomes necessary for composite densification above the critical inclusion volume fraction; and this critical value increases as R decreases.[44] Therefore, it is possible to sinter an FGM containing reasonably wide variations in the volume fraction of the

refractory phase companied with a much smaller matrix particle size, if the more refractory phase in the densified FGM may be discontinuous.[72]

Pushing this idea further, the matrix material may be uniformly coated on the refractory particles, thus preventing the formation of contacts between refractory particles. This strategy has been used to speed the densification of ceramic composites[73] to retard densification of BT-Ni composites,[74] to produce a functionally graded transition from 0 to 80 % TiN in Ni.[72] Also, the sintering rates in coated inclusion-based composites did not vary significantly with the inclusion volume fraction.[73] Using this approach, densification kinetics of the FGM can be relatively uniform. Therefore, it is possible to create significant refractory volume fraction variations via matrix densification only.

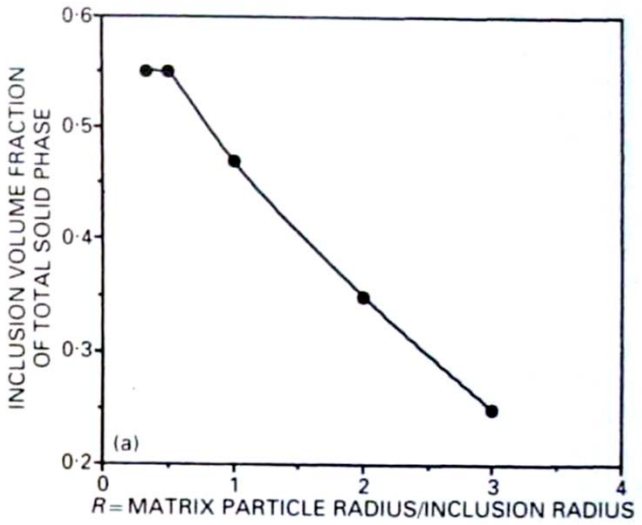

a)

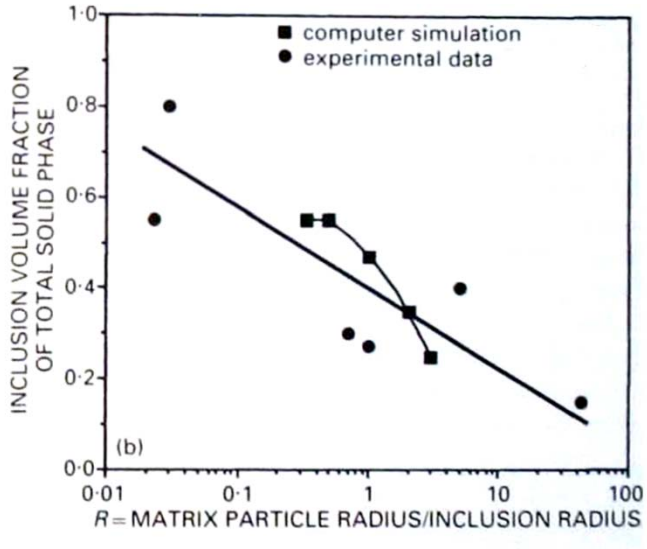

b)

Figure 2.34 a) Volume fraction of equisized spherical inclusion phase above which there is sufficient percolation for this phase to prevent sintering of the matrix in the as-packed green powder compact: from computer simulation of Bouvard and Lange,[65] and b) Experimental data for the volume fraction of second phase at the onset of percolation measured in densified FGM composites produced by powder metallurgy, superimposed on the above theoretical curve.[71] Within experimental error, measured values generally agree with the theoretical predictions.[73]

Two-phase densification is required when a continuous refractory phase is desired**.** The inclusion particle network must consolidate during the densification process along with the metal matrix phase. To avoid warping or cracking, especially in unconstrained sintering, it is imperative that the two phases densify at the same rate. Even slight discrepancies in local sintering rates will have deleterious effect on component morphology.[49]

It is a considerable challenge to achieve identical sintering rates uniformly across a wide span of volume fractions of the two phases, because sintering rates vary significantly with the nature and properties of ceramic and metal materials; particularly, metals generally densify at a much faster rate than ceramics.[44] Matsuzaki[75] surveyed candidate metal/ceramic combinations for high-temperature applications. Non-oxide covalent ceramics that have too high a sintering temperature, such as SiC, were removed from consideration. Oxides with higher level of ionic bonding and lower sintering temperatures were retained as more suitable candidates. On the other hand, metals at the higher end of possible sintering temperature range have to be considered.

Within the comparable sintering temperature ranges, sintering kinetics must be tuned so that the two powders will have the same densification rate under identical processing conditions. A variety of methods have been demonstrated, including particle size control,[76] sintering aids,[77] a combination of particle size control and sintering aids,[78] densification of the powder compact within an appropriate temperature gradient by means of (i) laser beam surface heating,[79] (ii) microwave sintering,[80] and (iii) using electric discharge heating.[71]

When the powders are densified in simple configurations by hot-pressing within a die, the criticality of the identical sintering rate under similar conditions is somewhat reduced. The die may resist the deformation and potential failure of the powder compact; and the applied high pressure may induce macroscopic material flow to compensate for the shrinkage differences while maintaining the shape of the component. This technique was found advantageous over hot isostatic pressing for one-dimensional FGM disk fabrication,[44] however not much better than hot isostatic pressing for more complex FGM geometries.

Liquid phase sintering is an attractive process for FGM preform densification, with major advantages including: 1) low sintering temperature, 2) much faster densification rate than in solid-phase sintering, 3) high volume fraction of a refractory phase may be accommodated in some systems, and 4) stresses during sintering are low, since sintering rate differentials can be compensated by macroscopic compact flow.[38, 44] However, the presence of a liquid phase permits motion of liquid and solid phases relative to one another, which could under circumstances reduce or even eliminate gradients initially placed in the structure during powder packing.[38, 44]

Infiltration method involves first producing a preform of a refractory phase with graded porosity, and then infiltrating it with a melted phase. The refractory phase must be insoluble in the liquid, be sufficiently percolating to stand on its own weight before infiltration, and be strong enough to resist compression by the melt during pressure-assisted infiltration. Depending on the processing route used, infiltration processing can both be constructive or transport-based. Compared to liquid phase sintering, the infiltration method has the advantage of no homogenization of the refractory phase by

diffusion or motion of the liquid. However, the refractory phase can only vary between two limits: i) the minimum volume fraction where the porous preform has sufficient percolation to achieve enough mechanical strength, and ii) the maximum volume fraction where enough porosity is maintained for infiltration of melt.

Reactive powder processes are similar to a combustion process, where exothermic reaction between two or more phases is self-sustaining with the heat released. FGMs may be produced by spatial variation of the initial reactant distribution in the powder preforms. The reaction may be ignited uniformly throughout the powder compact, or started in one location of the powder compact and then propagates along the length of the sample, known as self-propagating high-temperature synthesis (SHS), as illustrated in Figure 35.

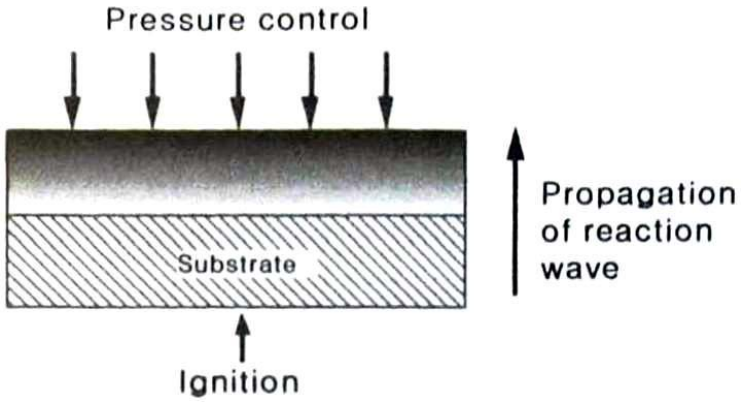

Figure 2.35 Schematic of the SHS process.[45]

2.7.4.2 Coating Processes

In coating processes, graded outer layers are deposited onto a prefabricated bulk component. The coated functionally graded layers usually serve as a gradual transition from a bulk component to its protective outer coating that resists harsh conditions.

Various FGM coating processes are available, including plasma spraying, electroforming and vapor deposition.

Plasma Spray Forming uses a plasma gun to rapidly heat and accelerate particles below 100 μm in diameter.[81] The particles are melted and flattened upon impact with a solid substrate, as illustrated in Figure 2.36. This feature, especially carried in low-pressure or vacuum environments, enables the deposition of relatively dense coatings, and reduces the need for post-treatment. The major requirement to this process is that the powder material not be decomposed. For fabrication of ceramic-metal FGMs, plasma spraying is an attractive method because it can simultaneously melt ceramic and metal phases, blending them in ratios controlled through relative powder feeding rates.

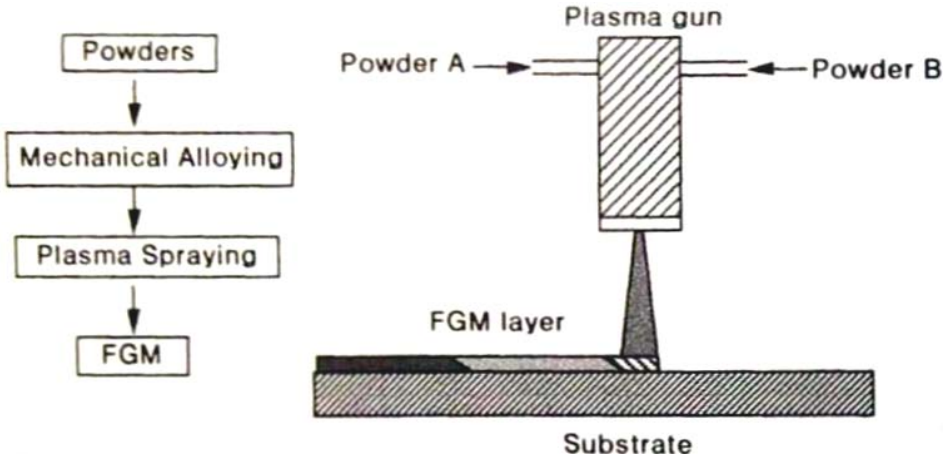

Figure 2.36 Schematic of plasma spraying of FGM coating.[45]

Thermal Spray Deposition sprays a jet of atomized molten metal onto a substrate and builds up a metal layer upon solidification. This process may fabricate composites, by injecting reinforcing particles into the metal spray.[82] The reinforcing particles, typically ceramics, generally remain solid and are coated by metal droplets to form a

near-dense composite material. Compared with plasma spraying, the principal limitation of this process for composite fabrication is that only the metal phase is melted. Consequently, the volume fraction of the more refractory phase is limited by its packing density and the volume of the metal phase sprayed between particles. Thus, phase volume fraction of the refractory phase incorporated has a maximum in the vicinity of 30-40 %.

Electroforming Process has been used for fabrication of metal/metal and metal/ceramic graded materials. An electrolytic cell featuring dual anodes of Cu and Ni, as shown in Figure 2.37, is used to deposition graded metal foils. Ceramic reinforcement may be incorporated by adding ceramic particles to the electrolytic solution, and incorporating these particles into the growing metal layer during electro-deposition.

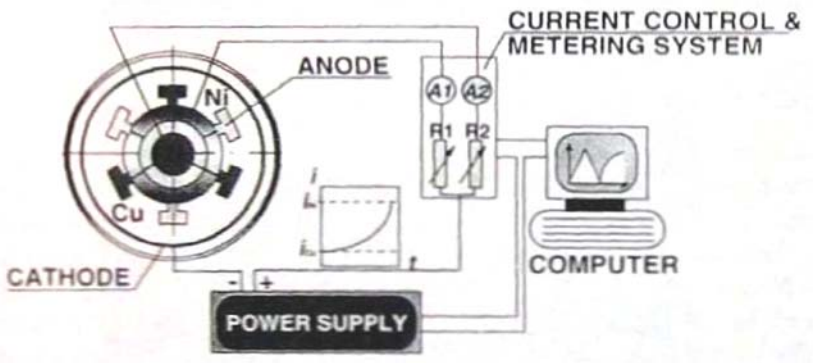

Figure 2.37 Schematic illustration of the apparatus for the electro-deposition of graded bimetallic layers.[44]

Vapor Deposition Process has the advantage that very thin layers may be produced. With steep composition gradients, however, a reduced stability of the FGM at elevated temperature may result.[83] Various deposition techniques are used for fabrication

of FGMs, such as partially reactive physical vapor deposition,[84] metal evaporation and ion irradiation,[85] and plasma assisted CVD.[86]

2.7.4.3 Lamination Processes

In lamination processes, dense layers are stacked and bonded to form a graded structure. By varying the relative thicknesses of each layer across the structure, FGMs with varying volume fractions, layer widths, and hence local properties may be produced.[87]

2.7.4.4 Deformation/Martensitic Transformation

By imposing a strain gradient in selected materials, gradients of Martensitic volume fraction may be produced with a proper temperature range.[88] Although limited in selection of materials, this process provides a simple method for production of materials containing continuous variations in saturation magnetism, which has potential application for position measuring devices.[44]

2.7.5 Transport Based Processes Characteristic Time Scales

The characteristic time for a material to be affected by the conduction of heat is

$$\tau_h \approx \frac{L_c^2}{\alpha_T}$$

and by the diffusion of matter is

$$\tau_d \approx \frac{L_c^2}{D}$$

where α_T is the thermal diffusivity, D is the diffusion coefficient, and L_c is the depth.

In metallic solids, the thermal diffusivity α_T is roughly on the order of 10^{-4}–10^{-6} $m^2 \cdot s^{-1}$, i.e. the material depth can be affected at a rate on the order of a millimeter per second by heat conduction.[89] Within a time frame of usual processes, this depth means that controlled heat conduction near surface may alter local microstructures. The example is the surface hardening of steels.

In liquid metals, D is roughly on the order of 10^{-9}–10^{-8} $m^2 \cdot s^{-1}$. This means that the depth is affected at a rate of 100 μm per second.[90] Due to the stronger effect of co-occurring convection in most cases, diffusion in liquid metals is generally impractical as a processing method.

In solid phases, D is roughly within one or two orders of magnitude of 10^{-13} $m^2 \cdot s^{-1}$, except for faster diffusing interstitial systems such as C or N in Fe.[44] Thus, it is mostly with interstitial systems that solid state diffusion creates compositional gradients over macroscopic lengths within a reasonable processing time. The examples are carburization and nitridation of steel.

The characteristic time for transport within mixed solid and liquid phases can be estimated by considering two situations: 1) the system contains primarily the liquid phase and solid particles migrate within the liquid phase; and 2) the system contains primarily the solid phase which occupies a volume fraction above the percolation threshold, and the liquid phase moves through a porous solid.

In the first case, the velocity v of solid particles in the liquid may be estimated using Stokes' law[91]:

$$v = \frac{2R_p^2(\rho_s - \rho_l)\gamma}{9\mu_f}$$

leading to a characteristic time τ_f equal to:

$$\tau_f = \frac{9\mu_f L_c}{2R_p^2(\rho_s - \rho_l)\gamma}$$

where μ_f is the liquid viscosity, R_p is the solid particle radius, ρ_s and ρ_l the solid and liquid densities respectively, γ the acceleration. Liquid metal viscosities[90] are generally between 10^{-3}–10^{-2} Pa·s. Hence the motion of solids in liquids may be used to create graded materials, and alternatively become a major concern in constructive processes when liquid and solid phases coexist unless the time frame is very short.

In the second case, the liquid velocity v is governed by Darcy's law:

$$v = -\frac{K_P}{\mu_f}(\nabla P - F_b)$$

where K_P is the permeability of the porous medium divided by the pore volume fraction, P is pressure in the liquid, andF_b is the body force acting on the liquid. Typically, liquid metal surface tension[90] is on the order of 1 J·m^{-2}, and a curvature difference will cause pressure difference to reach 0.1 MPa. In one second, the liquid will migrate a distance of 1 mm to 1 cm. Hence, the liquid movement may create FGMs, and erase compositional gradients in constructive processes, if the processing time frame is not very short.

2.9. Residual Stress

Temperature changes can generate high internal stresses to composites as a result of unequal thermal expansion or contraction between the constituent phases. Likewise,

different local deformation fields generated by different elastic and plastic properties under mechanical loading can cause internal stresses and strains. A graded structure can mitigate abrupt transitions in composition or microstructure at both the microscopic and macroscopic scales, and optimally control the distribution of residual stress.

2.8.1 Rule of Mixture Approximations

To quantitatively analyze the thermomechanical properties of the metal-ceramic composite, methods for estimating the effective properties of the underlying dual phase or multiphase structures are required. The overall mechanical properties of a binary phase composite depends on parameters such as concentration, shape and contiguity, and spatial distribution of each phase.[48, 65, 66, 69] Two example models are parallel (e.g., aligned fibers in a continuous matrix) or series (e.g., laminated sheets) as given in the following equations:

$$X_c = X_1 \cdot f_1 + X_2 \cdot f_2$$

$$X_c = \left\{ \frac{f_1}{X_1} + \frac{f_2}{X_2} \right\}^{-1}$$

and

$$f_1 + f_2 = 1$$

In this rule of mixtures, X is the isotropic material property of the composite, f the volume fraction of the phase, and the subscripts c, 1, and 2 denote composite, phase 1 and 2 respectively. Most composites are a combination of these two models.

CHAPTER 3 AQUEOUS COLLOIDAL FUGITIVE INK

3.1 Introduction

Robocasting uses highly concentrated aqueous colloidal inks to fabricate near net shape complex objects layer-by-layer. In its original concept, highly concentrated aqueous suspensions were used as inks for fabrication of space-filling components. These inks solidified either by a drying-induced pseudo-plastic to dilatant transition[5, 92-95] or temperature-induced phase change.[96] Initial fluidity of the inks allowed creation of continuous layers. For creation of designs with spanning features, colloidal inks with Herschel-Bulkley rheology were formulated to allow self-supporting filaments with spans on the order of several filament diameters.[30, 34] More intricate designs with longer spans or cantilevered features require a fugitive support material during the printing process.

For compatible processing with other inks, a fugitive ink must satisfied the following requirements: 1) be able to consistently flow though extrusion nozzle in the size range of Ø0.1-1mm; 2) be aqueous-based so that it will adhere to the ceramic substrate and build materials, but not diffuse into the oil bath; 3) maintain enough mechanical strength after extrusion through the nozzle for shape retention and supporting

subsequently added build materials; 4) be able to resist drying stress; and 5) allow easy removal prior to sintering step. Here, carbon black is selected as the particulate phase in the fugitive ink based on the following considerations: 1) it is stable under normal conditions with its chemistry extensively studied, 2) it is dispersible in water in the form of sub-micron sized particles, and 3) it is commercially available at a low cost. Alternative candidate materials include carbon-based synthetic and naturally-occurring polymer particles, e.g. starch powder. However, usually inferior chemical and physical stability limited their usefulness in the Robocasting process. Thus, for this part of the study, carbon black became the candidate of choice.

Carbon black (CB) is manufactured by controlled vapor phase pyrolysis of heavy hydrocarbons. It is readily available and commonly used as a reinforcing agent in tires and other rubber products, as a black pigment in printing inks and paints, and as a UV stabilizing and conductive agent. Primary aggregates, composed of permanently fused, near-spherical primary particles, are the smallest dispersible units of carbon black. Dispersions of carbon black and related rheological behaviors have been extensively studied in organic solvents and polymer melts. Rheological properties of aqueous carbon black dispersions have been investigated to a lesser extent, with surfactants composed of hydrophobic anchoring groups and stabilizing polymeric chains.[97-99] However, the specific Herschel-Bulkley gel behaviors along with high concentration, low drying shrinkage required by Robocasting has not been addressed in aqueous carbon black systems.

Here, an aqueous carbon black colloidal gel is developed and characterized for use as a fugitive support material in Robocasting. Preparation of this carbon black gel

occurs in a multi-step process: firstly, the optimal concentration for selected surfactant is determined through rheological measurements; secondly, dispersing the carbon black particles in water; thirdly, concentrating the sol by centrifugation; and finally, gelation of the particles. This gel demonstrates good processing compatibility in terms of printing, drying, and burnout. Optimal surfactant concentration is determined by shear viscometry. Oscillatory measurements reveal Herschel-Bulkley flow behavior and a storage modulus comparable to ceramic inks. Scanning electron microscopy indicates minimum drying shrinkage. Thermogravimetric characterization (TGA and DTA) is used to study its oxidation. This carbon black is readily oxidized in air at 650 °C, but requires a higher temperature in CO_2. Finally, the success is demonstrated by example ceramic structures of hydroxyapatite (HA) and barium titanate (BT) containing large spanning structural features.

3.2 Experimental Section

3.2.1 Materials

Carbon black (Monarch 120A58, Cabot Corporation, Billerica, MA) with primary particle size of 75 nm,[100, 101] aggregate size distribution 100-600 nm,[102] manufacturer suggested particle density in the range of 1.8 g/cm^3 and specific surface area of 31.25 m^2/g,[102] is selected for the particulate phase. Scanning electron micrograph (JEOL JSM-6360) of as-received powder is shown in Figure 3.1a. High resolution transmission electron micrograph (HRTEM) for its aggregates is given in Figure 3.1b.[102] Nonylphenol ethoxylate (AGNIQUE NP4070, Cognis, Cincinnati, OH), a 70% by weight aqueous solution of a surfactant composed of a nonylphenol head group and a polyethylene oxide

(PEO) tail with 40 units of ethylene oxide (EO), is used to stabilize carbon black in aqueous medium. Two similarly structured PEO surfactants (Makon 10 and Makon 12, Stepan, Northfield, Illinois) with 10 and 12 units of EO respectively on their hydrophilic tails, are used for comparison. Defoamer (Surfynol DF-210, Air Products and Chemicals, Inc., Allentown, PA) is used as received. ABA block copolymer (Pluronic F-127, P2443-250G, SigmaAldrich, St. Louis, MO) is dissolved in de-ionized (DI) water as 40% by weight stock solution. Hydroxypropyl methylcellulose (HPMC) (Methocel F4M, Dow Chemical Company, Midland, MI) is dissolved in DI water as 5% by weight stock solution. DI water wherever mentioned has a nominal conductivity 5×10^{-4} $(ohm\cdot cm)^{-1}$. Paraffin oil (Ultra-Pure, Lamplight Farms, Menomonee Falls, WI) is used for the oil bath.

3.2.2 Surfactant Concentration Determination

To determine optimal surfactant concentration, varying amounts of carbon black and surfactant NP 4070 are separately added to pre-determined DI water to yield aqueous suspensions with varying carbon black and surfactant concentration. The detailed suspension composition is shown in Table 3.1. A sonic dismembrator (model 500, Fisher Scientific, Pittsburgh, PA) is used, at 50% of maximum power for 10 minutes, to assist breaking apart carbon black agglomerates. Subsequently, rheometry (C-VOR 200, Bohlin Instruments, Cirencester, Gloucestershire, UK) is used to characterize the apparent viscosity profile for each carbon black suspension in a sweep of shear rate from 0.2-3 s^{-1}.

a)

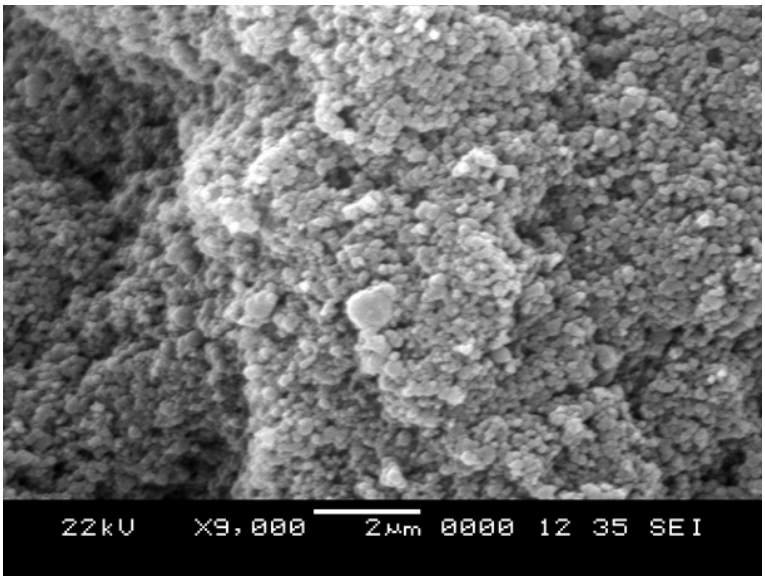

b)

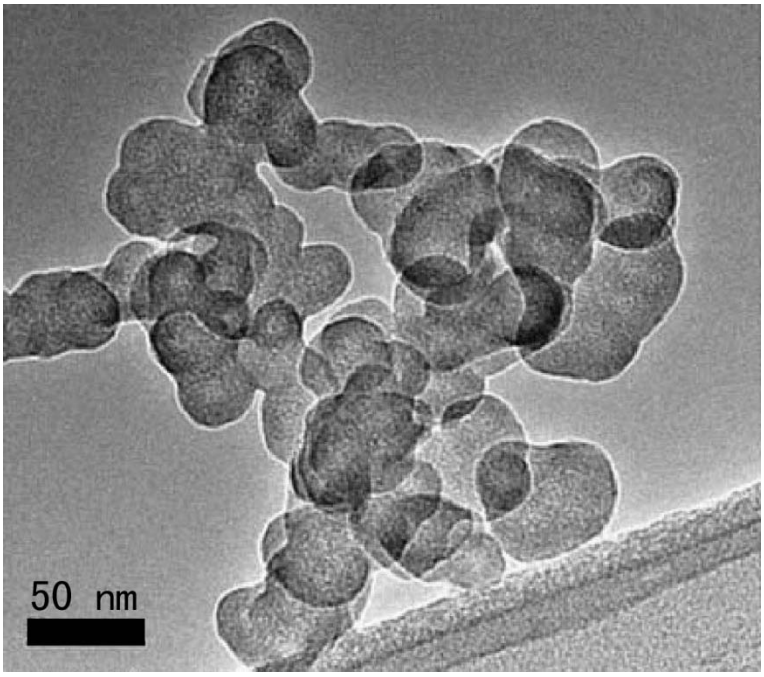

Figure 3.1 a) SEM image of as-received carbon black powder, and b) HRTEM of Monarch 120 aggregates[102] to illustrate the hierarchy structures in carbon black aggregates.

Table 3.1 Suspension compositions for viscometry sweeps.

Suspension #	1	2	3	4	
DI water (g)	16.224	16.179	15.993	15.906	
NP4070 (g)	0.155	0.199	0.393	0.496	
CB (g)	3.593	3.600	3.601	3.612	
Cal. Surf. Conc. (mg/m^2)	0.966	1.238	2.445	3.076	
ϕ_{solids}	0.11				
Suspension #	5	6	7		
DI water (g)	14.390	14.280	13.962		
NP4070 (g)	0.263	0.317	0.598		
CB (g)	5.409	5.409	5.406		
Cal. Surf. Conc. (mg/m^2)	1.089	1.313	2.478		
ϕ_{solids}	0.17				
Suspension #	8	9	10	11	
DI water (g)	10.082	10.233	10.008	9.631	
NP4070 (g)	0.538	0.701	1.001	1.302	
CB (g)	9.007	9.015	9.012	8.998	
Cal. Surf. Conc. (mg/m^2)	1.338	1.742	2.488	3.241	
ϕ_{solids}	0.32				
Suspension #	12	13	14	15	16
DI water (g)	10.213	10.741	10.133	9.462	8.405
NP4070 (g)	1.081	1.148	1.799	2.514	3.771
CB (g)	16.207	16.204	16.207	16.194	16.201
Cal. Surf. Conc. (mg/m^2)	1.494	1.587	2.486	3.477	5.214
ϕ_{solids}	0.44				

3.2.3 Preparation of Carbon Black Colloidal Gel

Carbon black gel is prepared in three steps: 1) a carbon black suspension is prepared at a lower concentration; 2) the carbon black suspension is concentrated by centrifugation; and 3) appropriate amount of polymer additives is added to achieve desired ink behavior. First, a surfactant concentration of 1.5 mg/m^2 determined by viscosity measurements is used for dispersing carbon black in water. In a 500 mL glass beaker, 13.0 g of nonylphenol ethoxylate solution is added to 370.0 g of DI water, and then 190.0 g of carbon black powder is gradually added. The sonic dismembrator is used, at 50% of maximum power for 15 minutes, to assist breaking apart carbon black agglomerates while the suspension is magnetically stirred. A total of 0.14 g defoamer is added to suppress foaming. Water evaporation is compensated. At this point, the solid volume fraction (ϕ_{solids}) of carbon black is approximately 21.6%.

Subsequently, aliquots of the carbon black dispersion are then transferred to 50 mL TEFLON centrifuge tubes and spun at 11000 rpm for 10 minutes (Model 5804 with a fixed-angle rotor F-34-6-38, Eppendorf AG, Hamburg, Germany). After decanting the supernatant, carbon black sediment is collected at ϕ_{solids}=0.50 by calculation.

Finally, an amount of 34.16 g of such sediment is loaded into a 125 mL mixing cup, into which are also added 2.73 g of Pluronic F-127 stock solution and 0.36 g of Methocel F4M stock solution. Before mixing, the temperature of these materials is lowered to around 1 °C.[103, 104] Subsequently, a rigorous mixing, using a non-contact planetary mixer (AR-250, THINKY, Tokyo, Japan), is applied to homogenize the carbon

black gel at ϕ_{solids}=0.44 by calculation. In this way, carbon black ink with ϕ_{solids} in the range from 0.40 to 0.44 and appropriate rheological behavior may be prepared.

3.2.4 Rheological Characterization of Carbon Black Gel

The rheological properties of above carbon black gel is compared to a hydroxyapatite (HA) colloidal gel[33] prepared by polyelectrolyte induced bridging-flocculation.[105] The HA gel is a representation of typical ceramic gels used in Robocasting. Also, to examine the effect of HPMC addition, a carbon black gel with no HPMC addition is also studied. Finally, the effect of EO chain length on gel behaviors is investigated in the following way: while keeping other constituents unchanged, same amount of either Makon 10 or Makon 12 surfactant is used in place of Pluronic F-127 surfactant. All carbon black gels investigated have ϕ_{solids}=0.44 and the HA gels has a ϕ_{solids}=0.47. For each measurement, a sample at 3.6 mL is loaded into the cup and bob geometry of a rheometer (C-VOR 200, Bohlin Instruments, Cirencester, Gloucestershire, UK) using a 10 mL syringe (BD, Franklin Lakes, NJ) and subjected to 30 minutes oscillatory pre-shear at 1Hz with a controlled shear stress at 0.02 Pa, then undisturbed for 30 minutes. Next, an oscillatory stress sweep measurement is carried out from stress amplitude τ_{min}=10 Pa to τ_{max}=1000 Pa at a frequency of 1Hz. The complex shear modulus (G*) is measured as a function of τ; however, only the storage (or shear elastic) modulus (G') is reported here. Next, shear stress τ as a function of shear rate $\dot{\gamma}$ is measured across the range from $\dot{\gamma}_{min} = 10^{-3}$ s^{-1} to $\dot{\gamma}_{max} = 10^{3}$ s^{-1}.

3.2.5 Drying Shrinkage Characterization

To investigate the drying shrinkage of carbon black gel, a carbon black lattice structure is assembled by extruding ϕ_{solids}=0.44 carbon black ink through Ø0.01" nozzle (5125-0.25-B, EFD, East Providence, RI) with 0.20 mm layer thickness and 7 mm/s printing speed, at a calculated volumetric flow rate 344 nL/s. After printing, this lattice is dried overnight at 80 °C. Scanning electron microscopy is used to examine the as-dried lattice structure.

3.2.6 TG/DTA Analysis of Carbon Black Burnout

Thermogravimetric analysis (TG/DTA 6200, SII Nano Technology, Tokyo, Japan) is used to characterize oxidation of carbon black gel structures. Separate samples weighted around 20mg or less are used for the heating profiles from 25 °C to 1000 °C at a ramp rate of 5 °C/min in stagnant air, and from 25 °C to 1100 °C at a rate of 5 °C/min and a constant feed of CO_2 at 400 mL/min.

3.3 Results and Discussion

3.3.1 Surfactant Concentration Determination

This viscosity measurement for carbon black suspensions suggests an optimal 1.5 mg/m^2 surfactant concentration for ink preparation. The dependence of η_{app} on surfactant concentration for carbon black suspensions is shown in Figure 3.2. The trend lines have no significance beyond a guide to connect the measured data points. Suspensions with ϕ_{solids} = 0.11 and ϕ_{solids} = 0.17 exhibit a relatively high η_{app} at surfactant concentrations below 0.9 mg/m^2 and 1.1 mg/m^2 respectively; in the same surfactant concentration range,

ϕ_{solids}=0.32 and ϕ_{solids}=0.44 suspensions are too agglomerated to allow a meaningful viscosity measurement. An increasing η_{app} is observed for ϕ_{solids}=0.32 and ϕ_{solids}=0.44 at surfactant concentrations greater than 1.3 mg/m^2 and 1.5 mg/m^2, respectively. In the same surfactant concentration range η_{app} of ϕ_{solids}=0.11 and ϕ_{solids}=0.17 suspensions exhibits no significant change. An explanation for the observed η_{app} behavior is likely to include these considerations: i) at a low ϕ_{solids}, less collision and friction between carbon black particles result in a very low η_{app}, provided that the agglomeration in suspension is statistically insignificant. It is likely the case for the suspensions with ϕ_{solids} = 0.11 and ϕ_{solids} = 0.17 at the surfactant concentration $\geq$1.25 mg/m^2. When the surfactant concentration is too low, as 0.9 mg/m^2 for the ϕ_{solids} = 0.11 suspension and 1.1 mg/m^2 for the ϕ_{solids} = 0.17 suspension, the amount of agglomerated particles increases. These particles collide with one another upon shearing and lead to higher η_{app}. ii) As ϕ_{solids} increases, the η_{app} of the suspension is expected to increase and the effect of agglomerated particles on the magnitude of η_{app} becomes significant. Suspensions with less than 1.3 mg/m^2 surfactant concentration become dilatant. A higher surfactant concentration is needed to achieve a low η_{app}. This trend is shown by the minimal η_{app} of fully dispersed ϕ_{solids}=0.44 suspension at surfactant concentration of 1.5 mg/m^2, and of ϕ_{solids}=0.32 suspension at surfactant concentration of 1.3 mg/m^2 where insignificant agglomeration could still exist. iii) An excessive surfactant addition (>1.5 mg/m^2) shows a positive correlation with the η_{app} of high ϕ_{solids} suspensions due to the increase of surfactant concentration in the aqueous medium; however, such increase in low ϕ_{solids} suspension is much less and insignificant to cause a rise in η_{app}. Based on these analyses,

the optimized surfactant concentration is chosen at 1.5 mg/m^2. This value is consistent with the concentration value in the range of 1.5-2.0 mg/m^2, given in adsorption isotherms and viscosity profiles for 10% (w/w) carbon black (Elftex 125, Cabot Chemical Corporation, Ellesmere Port, UK) dispersions reported by Miano et al.[98], using nonylphenol polypropylene oxide-polyethylene oxide surfactants with different ethylene oxide chain lengths. The higher values in his study could likely be ascribed to the extra section of polyethylene oxide chain in the surfactant molecule structure and possibly different carbon black surface physicochemical properties.

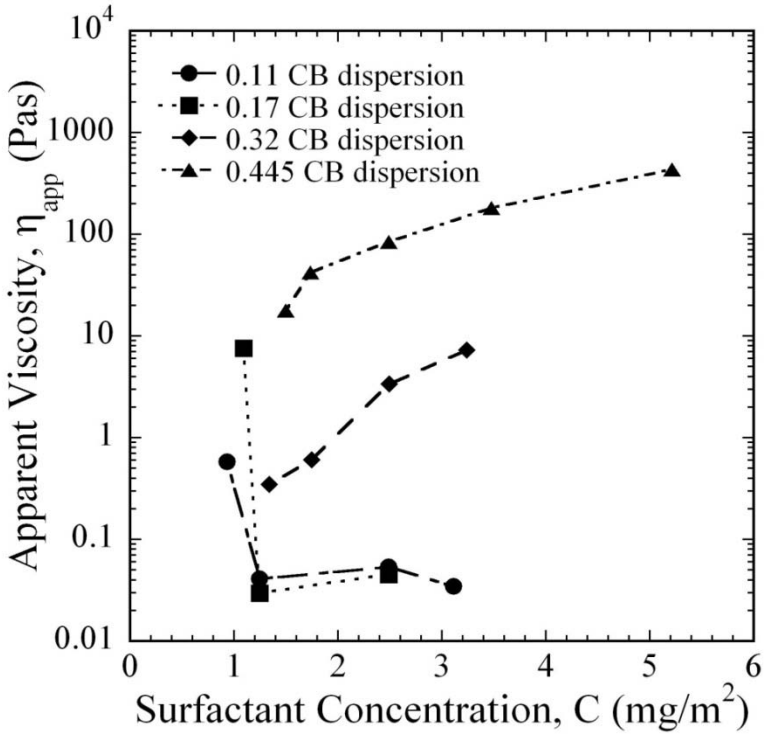

Figure 3.2 Apparent viscosity η_{app} of carbon black dispersions at ϕ_{solids} from 0.11 to 0.445. The surfactant concentration is calculated per unit particle surface area. Apparent viscosity η_{app} of each carbon black suspension is compared at shear rate $\dot{\gamma}$ = 1 s^{-1} only. Error bars are too narrow to show on this plot.

3.3.2 Gel Preparation

The dispersion, centrifugation, and mixing steps are necessary for achieving a high ϕ_{solids} carbon black ink. Sonication and stirring speed up the breaking and stabilization of carbon black agglomerates in a low ϕ_{solids} suspension. The subsequent centrifugation step concentrates carbon black particles prior to further mixing and dilution. By comparison, direct mixing of the carbon black powder with those polymeric additives can only reach a maximum ϕ_{solids}=0.42. At ϕ_{solids}>0.42, the mixture appears dilatant.

3.3.3 Rheological Characterization of Carbon Black Ink

Oscillatory measurement indicates the carbon black gel has commensurate Herschel-Bulkley gel responses to a ceramic ink used in Robocasting. Compared to the HA ink, the carbon black gel has a lower storage modulus but a higher yield stress. Polymer additive HPMC, although at a low concentration, strengthens the elastic response of the carbon black gel. Figure 3.3 shows the oscillatory and steady flow behavior of carbon black and HA gels. In Figure 3.3a, the HA gel has a storage modulus of G'=300 kPa, while for carbon black gel G'=17 kPa (with HPMC) and G'=7.2 kPa (without HPMC). The yield stress for a polymeric system is usually taken as the stress magnitude where G' drops to 90% of the plateau value during a stress sweep experiment starting from low stress.[106] For HA ink, $\tau_y \approx 55.4$ Pa with strain $\gamma \approx 0.2\times10^{-3}$. For carbon black gel with HPMC, $\tau_y = 153$ Pa with an order of magnitude higher strain $\gamma \approx 1.0\times10^{-2}$ and for carbon black gel without HPMC, $\tau_y = 31.3$ Pa with strain $\gamma \approx 4.75\times10^{-3}$.

The storage modulus of a colloidal gel depends on several factors, including solid volume fraction, shear modulus of particles, and the strength, stiffness and density of inter-particle bonds. A detailed characterization of differences in colloidal structures of HA and carbon black gels is beyond the scope of this work. However, it is obvious that HA particles have a higher modulus than carbon black primary aggregates at room temperature. To attain a high green density through efficient packing, the size of ceramic particles is usually in the range of several microns, and the thickness of polyelectrolyte adsorbate by comparison is insignificant; but the thickness of adsorbed polymer molecules on much smaller carbon black aggregate surface has to be taken into account. It is evident based on the strain data that the adsorbed non-ionic surfactant molecules build up a layer of soft cushion on carbon black surface that interact over a larger separation[107, 108] than the thin layer of polyelectrolyte molecules[109, 110] adsorbed on HA particles.

Figure 3.3b shows shear stress τ as a function of shear rate $\dot{\gamma}$ for these gels. Curve-fitting with Herschel-Bulkley model $\tau = \tau_y + k\dot{\gamma}^n$ yields coefficients with 95% confidence bounds, as listed in Table 3.2:

Table 3.2 Herschel-Bulkley model parameters for CB and HA gels.

	CB gel with HPMC	CB gel without HPMC	HA ink
n	0.379 (0.348, 0.411)	0.346 (0.325, 0.367)	0.433 (0.414, 0.451)
k	393.6 (328.4, 458.8)	201.7 (180.4, 223)	368.1 (339.6, 396.6)
τ_y	573 (515.1, 630.9)	97.42 (80.12, 114.7)	54.35 (31.6, 77.09)

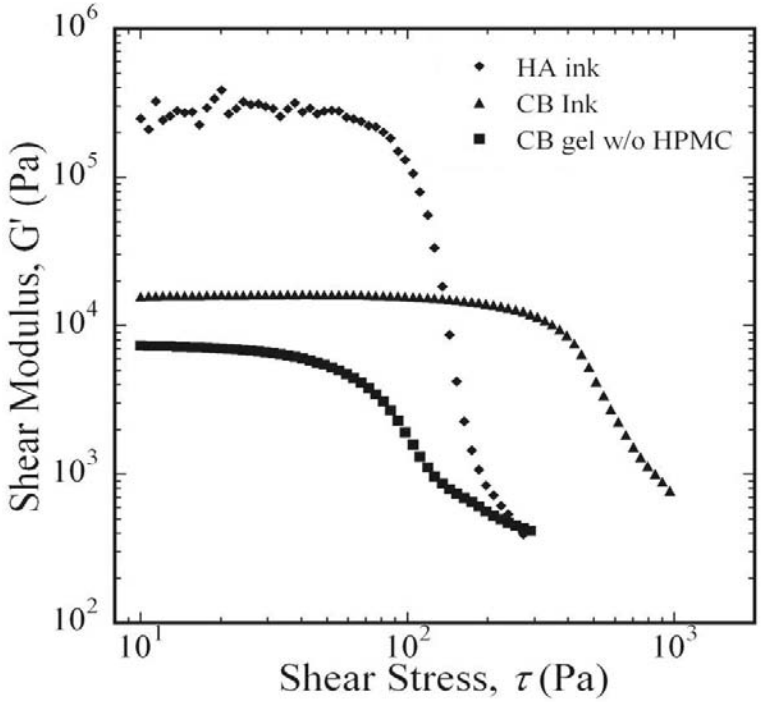

a)

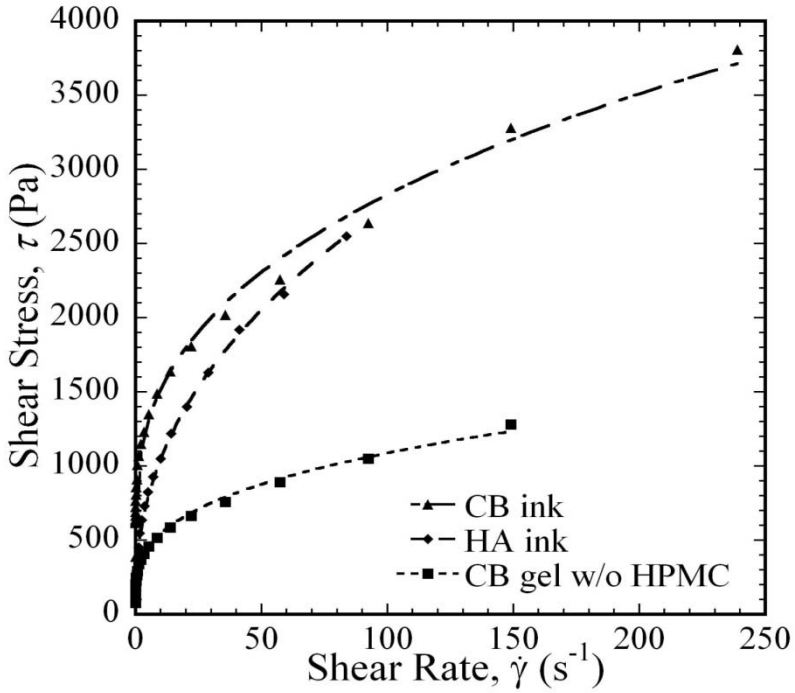

b)

Figure 3.3 Comparison of rheological properties of carbon black ink, carbon black gel without HPMC, and HA: a) G' as a function of τ; b) τ as a function of $\dot{\gamma}$.

For HA ink, yield stress τ_y measured here is consistent with the value of 55.4 Pa estimated from oscillatory measurement; but for both carbon black gels τ_y is larger than its counterpart from oscillatory shear measurement. Nevertheless, the difference in yield stress are considered insignificant here in so much as a positive displacement syringe pump is used to extrude the colloidal inks in subsequent processing rather than a pressure driven system. The effect on shape retention after printing may be more significant, but the slightly higher value of yield stress in the carbon black ink is desirable since it is to act as a more rigid support material.

The EO chain length has a large influence on the carbon black ink behavior. Oscillatory measurement under the same condition indicates a 70% decrease to around 5kPa for the elastic modulus of the corresponding carbon black ink (ϕ_{solids} = 0.44), and a 78% decrease to 33.9Pa for its yield stress, as shown in Figure 3.4. As the Makon 10 and Makon 12 have comparable EO chain lengths, the carbon black inks formulated with them have near identical rheological responses.

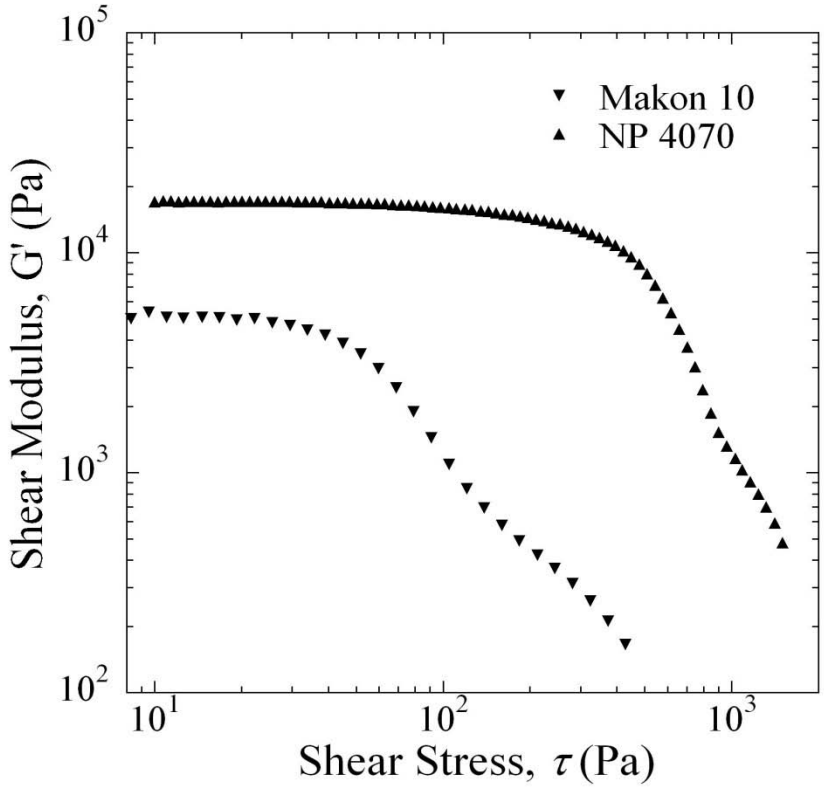

Figure 3.4 Comparison of oscillatory behavior between ϕ_{solids} = 0.44 carbon black gels stabilized by Makon 10 and NP 4070 respectively.

3.3.4 Gelation Mechanism

The gel behavior of this carbon black gel is the result of a synergy between carbon black particles and all non-ionic polymer molecules. The gelation mechanism of many ceramic inks used in robocasting is assumed to use reversible electrostatic cross-linking between adsorbed polyelectrolyte molecules and oppositely charged polyelectrolyte in solution, e.g. ammonium polyacrylate and poly(ethylenimine). In a sense, these gels may be regarded as particle filled, polymeric hydrogels that have properties between those of high concentration polymeric hydrogels and high concentration colloidal gels of pure ceramic particles based on electrostatic double layers.

In the case of the aqueous carbon black gels studied here, no bridging flocculation by polyelectrolyte is possible; and gelation is dependent on hydrogen bonding of the non-ionic polymers, with the reinforcing effect of the carbon black particles. The polymer concentration is significantly higher than in ceramic colloidal gels, partly because of the higher specific surface area of smaller particles. The dissolved polymer Pluronic F-127 has a concentration enough to form a hydrogel without carbon black particles, but it would be a much weaker one.

Enough hydrogen bonding sites must be present to allow gel behavior. In the absence of extra polymer free in solution, the solid volume fraction of carbon black dispersion has to be greater than a threshold value Φ_{gel} so that the inter-particle separation may fall below twice of the surfactant layer thickness, resulting in compression and inter-penetration of PEO chains of adsorbed NP4070 molecules.[98] After that, gel behaviors replace viscous flow; elasticity increases as the particles network compacts further. It has been shown that terminally anchored PEO tails (MW = 4800) may extend more than 30 nm in good solvent condition[111]. For the NP4070 surfactant with MW = 1600 PEO tails, a value of around 10 nm is reasonable in water. Layer thicknesses for similarly-structured nonylphenol polypropylene oxide-polyethylene oxide surfactants adsorbed on carbon black in highly concentrated dispersions were calculated.[98] which also supports the estimate of 10 nm thickness for the NP4070 surfactant. The average separation distance between carbon black particles is estimated for different ϕ_{solids} and packing types in Table 3.3. Considering the hierarchy structure of carbon black aggregates,[102] the maximum packing density by weight for the carbon black gel is unlikely to be very high, much volume must be occupied by the internal voids in those aggregates. This calculation

confirms the overlapping and interpenetration of adsorbed PEO chains. A schematic illustration of this carbon black hydrogel is shown in Figure 3.5.

Table 3.3 Calculated separation distance between carbon black particles.

Packing type	Packing density	Separation distance (nm)		
		ϕ_{solids}=0.40	ϕ_{solids}=0.42	ϕ_{solids}=0.44
Face-centered cubic	0.7405	17.07	15.59	14.20
Random close	0.634	12.43	11.02	9.70
Simple cubic	0.5236	7.04	5.71	4.47

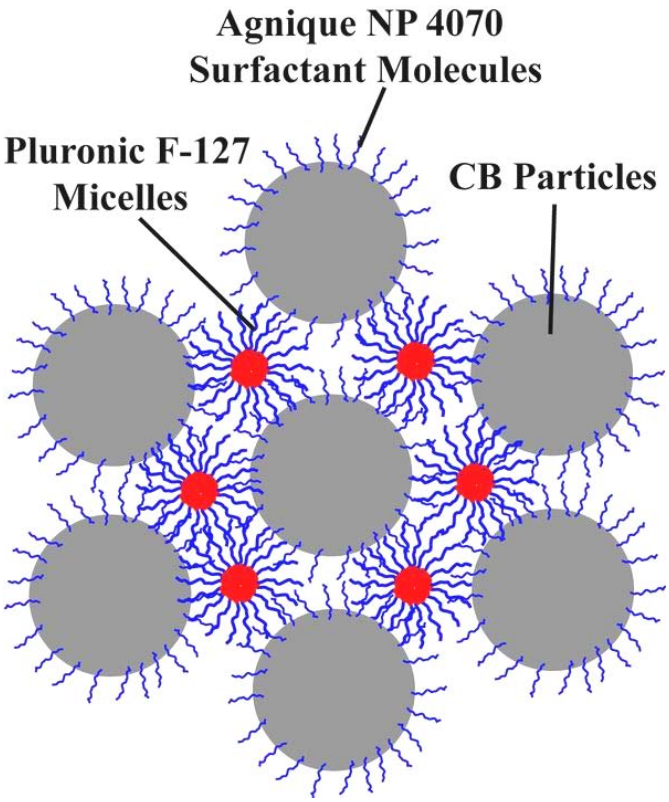

Figure 3.5 Schematic illustration of carbon black hydro-gel network. The effect of HPMC is not depicted here. Presumably HPMC strengthens inter-linking between NP4070 surfactant molecules and Pluronic F-127.

PPO units of Pluronic F-127 may adsorb to less hydrophobic sites on the surface of carbon black particles;[97] and the PEO tails with 100 EO units may interact at a larger distance. The carbon black gel has a Pluronic F-127 concentration at 7.0 wt% of the aqueous medium, much higher than its critical micelle concentration.[112] Entropy/hydrophobic effect leads to gelation of these spherical micelles,[103, 104] which are able to further compress and interpenetrate with the PEO tails of NP4070 molecules through hydrogen bonding[113, 114] to form an gel network.

Primarily used as a viscosifier for ceramic inks, HPMC molecules are also able to interact with PEO tails through hydrogen bonding.[115-118] Interestingly, its presence at around 0.11% by weight in the aqueous medium leads to a significant increase of storage modulus and yield stress, and a much larger strain to attain yield stress, i.e., 0.01 vs. 0.00475, for the carbon black gel.

Hence, to achieve a Herschel-Bulkley behavior with a reasonably high storage modulus, it is desirable that the carbon black ink has a high solid volume fraction, a surfactant molecular structure with long PEO tails complemented with enough concentration of Pluronic F-127 and HPMC.

3.3.5 Printing Carbon Black Ink

The ϕ_{solids}=0.44 carbon black ink may be extruded through 100 μm nozzle size consistently, which is a challenge for many ceramic gels. A plausible explanation includes factors such as smaller particle size, more compliant and homogeneous interactions between each surfactant covered particles, and lubricating effect of layered graphene substructures of carbon black particles. Figure 3.6 shows a carbon black lattice

structure before and after drying, with a filament size of 200 μm. Figure 3.6a illustrates the lattice structure immediately after removal from the oil bath. An aluminum oxide plate is used as the substrate during printing. The structure consists of 20 layers with each layer having a perimeter box with a thickness of 3 filaments (c.a., 0.6 mm) and an array of *x* or *y* oriented rods spaced at 0.5mm to leave a 0.3 mm gap. Upon removal from the oil bath, the structure retains some oil in the interstitial space of the lattice.

In figure 3.6b, the water and oil have evaporated under ambient conditions. Shape retention of the lattice structure is reasonably well without visually discernible cracking of local structures. It implies good interlocking of particles to resist the capillary force exerted by liquid meniscus during drying. The structure in this state can be handled easily with forceps or fingers and is comparable in strength to a ceramic green body that has low binder content.

3.3.6 Shape Retention and Drying Shrinkage

The carbon black ink, though with a lower shear elastic modulus (G') magnitude in the plateau region compared to the HA ink, displays good shape retention during printing and subsequent drying processes; but for each ceramic ink, a carbon black ink has to be tailored to confer compatible drying shrinkage.

For assembling a fugitive support structure with spanning feature, the ink elasticity is directly related to the shape of spanning features along with the buoyant force compensated weight of the span.[30] The self weight of the span is partially offset by the difference in specific gravity of the ink filament and the fluid bath into which it is printed (i.e., the oil bath in Robocasting). Since the carbon black ink has a lower specific gravity

a)

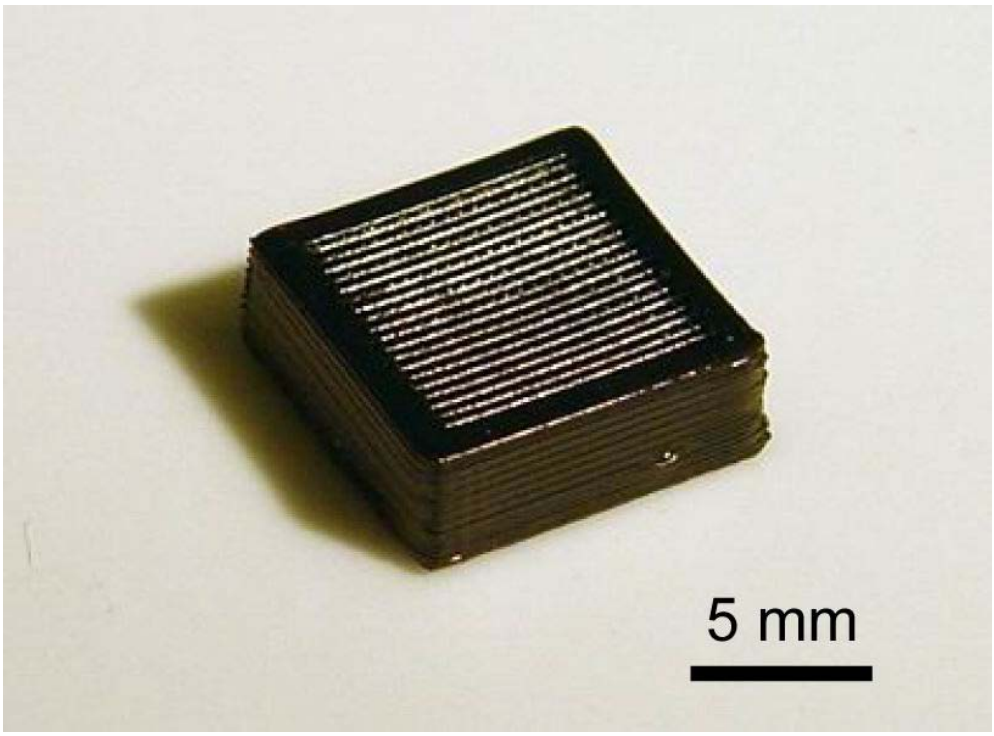

b)

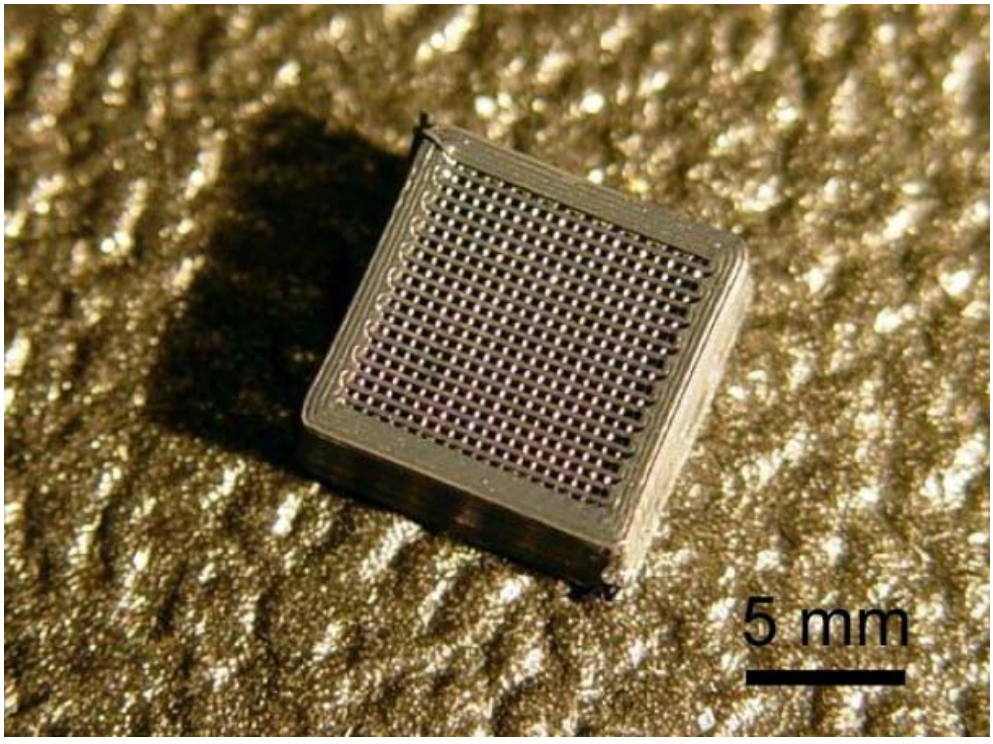

Figure 3.6 A carbon black lattice structure after: a) printing and b) drying.

than ceramic based inks of comparable concentration, the lower modulus in the carbon black ink may still lead to comparable spanning behavior. However, the modulus should be as high as possible in the support material to facilitate low distortion of the support material as new layers of ceramic ink are deposited atop it. In the context of the current Robocasting process, potential approaches to attain higher storage moduli would require electrostatic attraction in place of hydrogen bonds between carbon black particles, for example with the use of hydrophobic-ionic surfactant[99] or surface functionalization.[119] Due to the lack of a commercial source of hydrophobic-ionic surfactant and the complexity in the latter, neither of the two approaches is explored here.

Drying shrinkage of a colloidal ink depends on various factors including particle size distribution, solid volume fraction, quantities of polymeric additives, interaction strength between particles, and surface tension at liquid/air interface. For attaining precise structural features, matching drying behaviors of carbon black and ceramic inks are required. The higher polymer content in the carbon black ink could yield a greater degree of shrinkage, but experimental observation indicates only 1% linear drying shrinkage. Figure 3.7 shows the as-dried filaments of ϕ_{solids}=0.44 carbon black ink. These filaments are aligned in a lattice structure, with diameter measured at around 0.251-0.252 mm using image analysis software. Similar shrinkage for ceramic printing inks has been observed in previous studies and the carbon black ink is deemed successful on this basis, and yields desired result when used as a support material.

a)

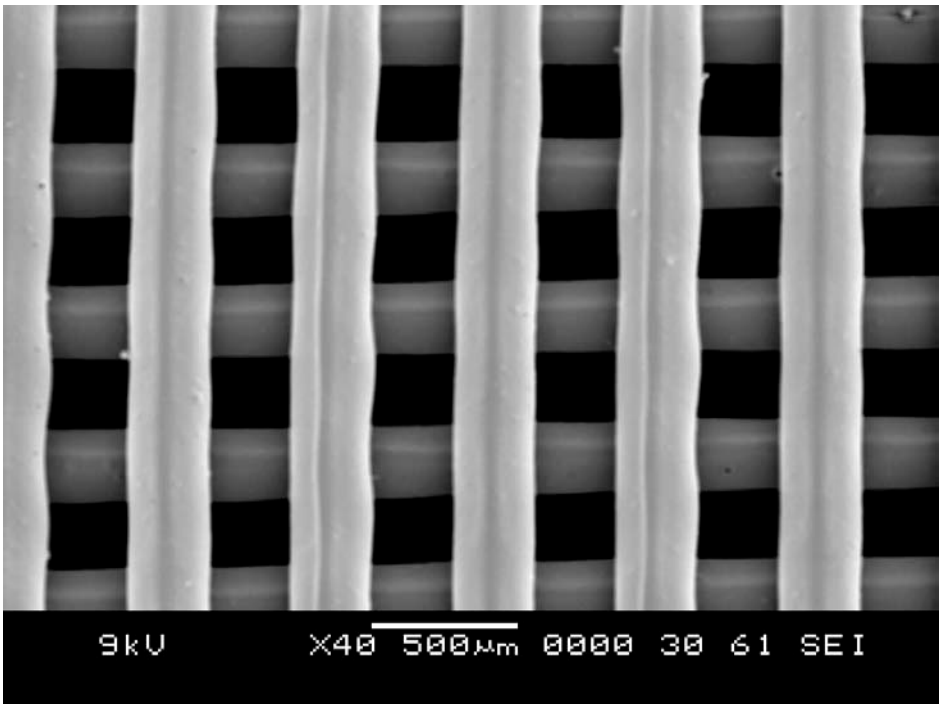

b)

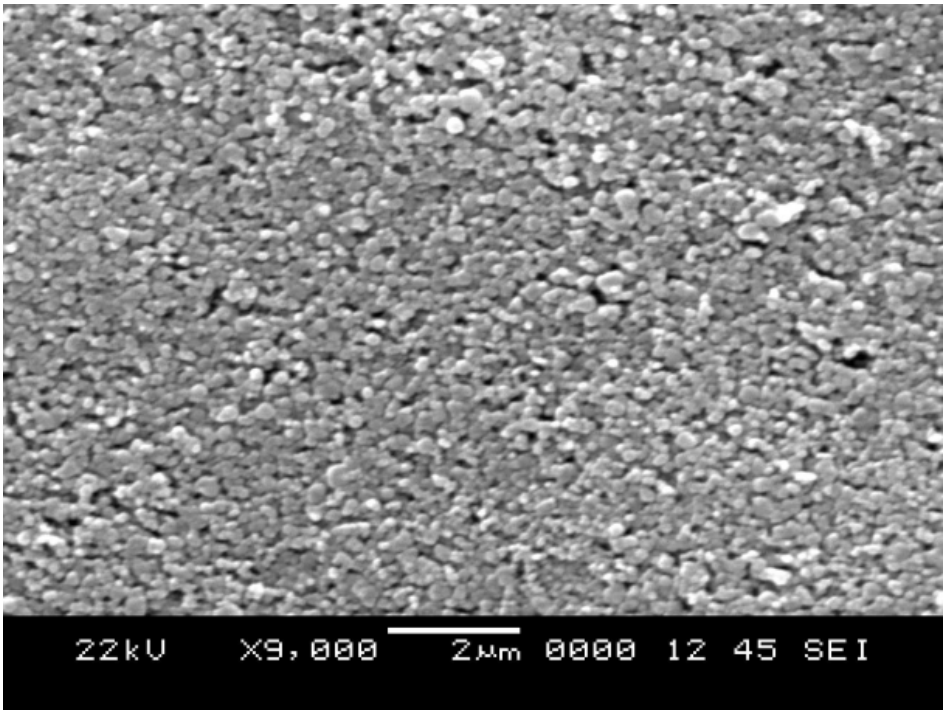

Figure 3.7 SEM images of a) carbon black lattices structure b) as-dried carbon black ink.

3.3.7 TG/DTA Analysis of Carbon Black Oxidation

This carbon black ink may readily be oxidized in air at temperature around 650 °C; but requires a temperature higher than 900 °C to complete at a reasonable rate in CO_2, with a calculated activation energy E_a of 165.80 $kJmol^{-1}$ in the temperature range from 895 °C to 1038 °C. Hence, this carbon black ink may easily be removed through oxidation in air when used as support structure for ordinary ceramic inks. However, to use this carbon black fugitive ink for a metal ink requires a refractory metal material with moderate oxidation resistance. For metal inks that sinter at lower temperatures, other fugitive materials should be investigated.

TG/DTA results of oil-containing and as-dried (80 °C in oven, overnight) carbon black inks are shown in Figure 3.8 and 3.9. Both oil-containing and as-dried inks have similar oxidation behaviors in air, as indicated in Figure 3.8a and Figure 3.8b, except for the initial 38.5% weight loss in Figure 3.8a due to evaporation of oil that has retained in the interstitial voids. The hydrocarbon oil used for oil bath has a boiling point in the range of 254-283 °C. The gradual weight loss in the range from 263.7 °C to 344.2 °C in Figure 3.8b probably corresponds to decomposition of polymeric additives. As the temperature increases from 344.2 °C to 459.6 °C, only slight weight change is observed. That might be attributed to releasing of volatiles from cleavage of covalent bonds in some functional groups.[120] Above 459.6 °C, oxidation of carbon black accelerates and comes to completion by 643.4 °C. Within this temperature range, it is commonly agreed that oxidation of carbon black in air is a first order reaction for CO_2 release,[121] with activation energy E_a in the range of 100-200 $kJmol^{-1}$ influenced by factors including nature of carbon black[121], metal ion inclusion (as a catalyst), and aromatic or aliphatic origin. This

TGA plot is in agreement with previous observation.[122] Hence, it is determined that at 650 °C burnout of carbon black support may be carried out to completion at a reasonable speed in air. For ceramics, burnout in an oxidizing atmosphere is acceptable and one may expect that the carbon black will be removed by about 650 °C before the onset of sintering process of common ceramic materials.

For metal materials, removal of the carbon black support material has to be achieved using an atmosphere non-oxidizing to metals. Candidate gases are those commonly used to react with carbon at elevated temperatures, such as steam and CO_2. Initial trial with steam at elevated temperature leads to corrosion to steel parts such as flange and valves used on the tube furnace, so it is not considered and only CO_2 is studied. Figure 3.9 shows TGA and DTA curves for the oxidation of 9.632 mg as-dried carbon black in CO_2. With these data, the Arrhenius equation is used to calculate the activation energy E_a for the oxidation of carbon black in CO_2, as shown in Figure 3.10. The relevant calculation is listed in Table 3.4. Activate energy E_a is estimated to be 165.80 $kJmol^{-1}$ in the temperature range from 895 °C to 1038 °C. The data points outside this temperature range suggest different oxidation kinetics. In the TGA plot, the first peak at 323.2 °C is likely due to decomposition of polymeric additives. It coincides with the weight loss for oxidation of carbon black ink in air as shown in Figure 3.8. Starting from 524.0 °C, weight loss at an increasing rate is observed and reach maximal rate at 1082.5 °C; but significant weight loss is only observed at temperatures higher than 900 °C. Hence, when used with this carbon black ink, the metal ink must have a much higher sintering temperature than 900 °C. And the actual oxidation process will depend on material chemistries and process variables involved.

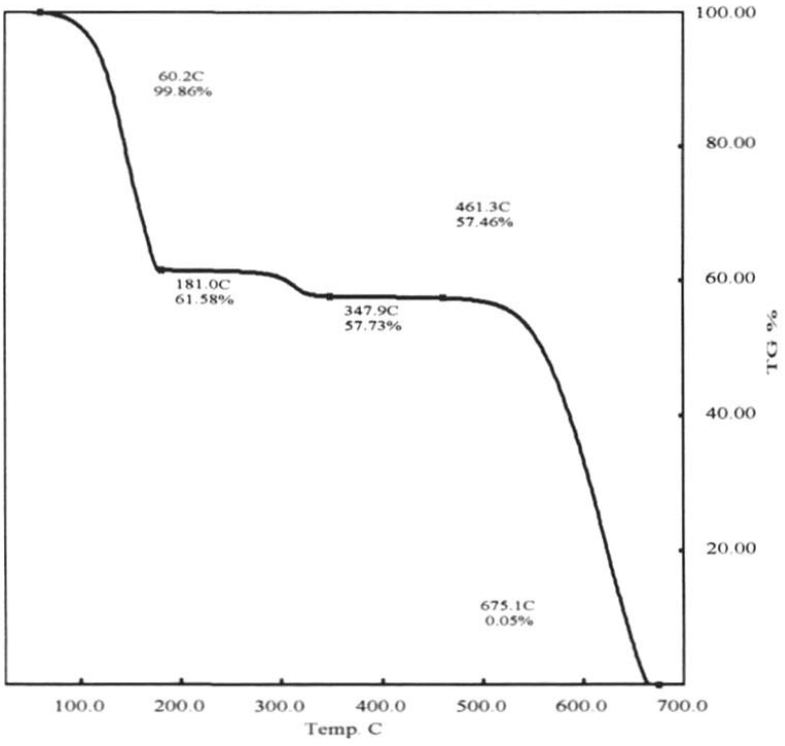

a)

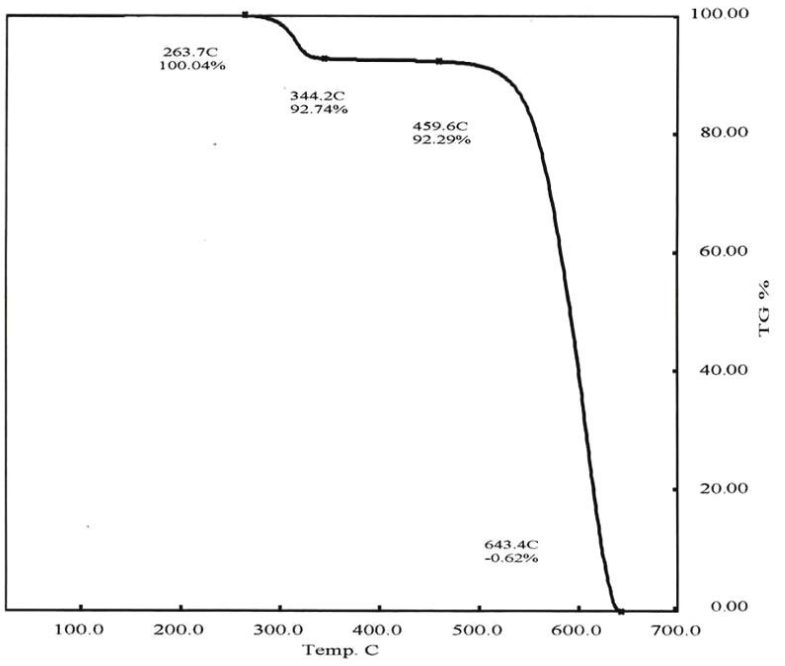

b)

Figure 3.8 TGA plot for CB oxidation in air a) oil-containing CB ink, b) as-dried CB ink.

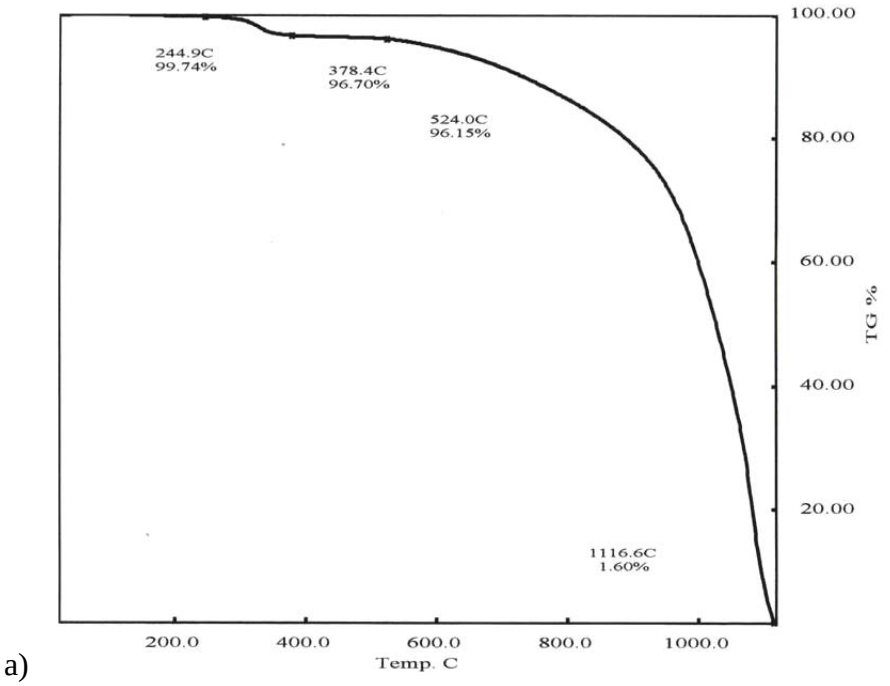

a)

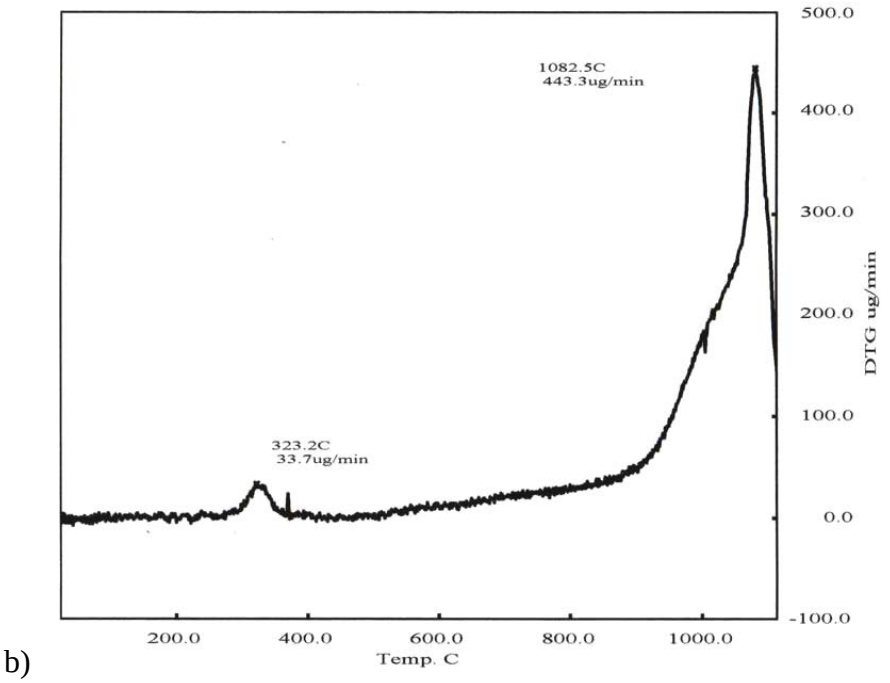

b)

Figure 3.9 Thermogravimetric analysis of oxidation of as-dried carbon black gel in CO_2: (a) TGA plot (b) DTA plot.

Table 3.4 Calculated values for determining E_a.

Data #	1	2	3	4	5	6
Temp. (K)	873.15	949.15	1048.20	1168.20	1219.20	1263.20
1000/T (K^{-1})	1.15	1.05	0.95	0.86	0.82	0.79
ln(k) ($kg \cdot m^{-2} \cdot s^{-1}$)	-21.00	-20.54	-20.23	-19.37	-18.66	-18.15
Data #	7	8	9	10	11	
Temp. (K)	1287.70	1311.20	1335.20	1343.20	1355.70	
1000/T (K^{-1})	0.78	0.76	0.75	0.74	0.74	
ln(k) ($kg \cdot m^{-2} \cdot s^{-1}$)	-17.66	-17.29	-16.98	-16.42	-15.74	

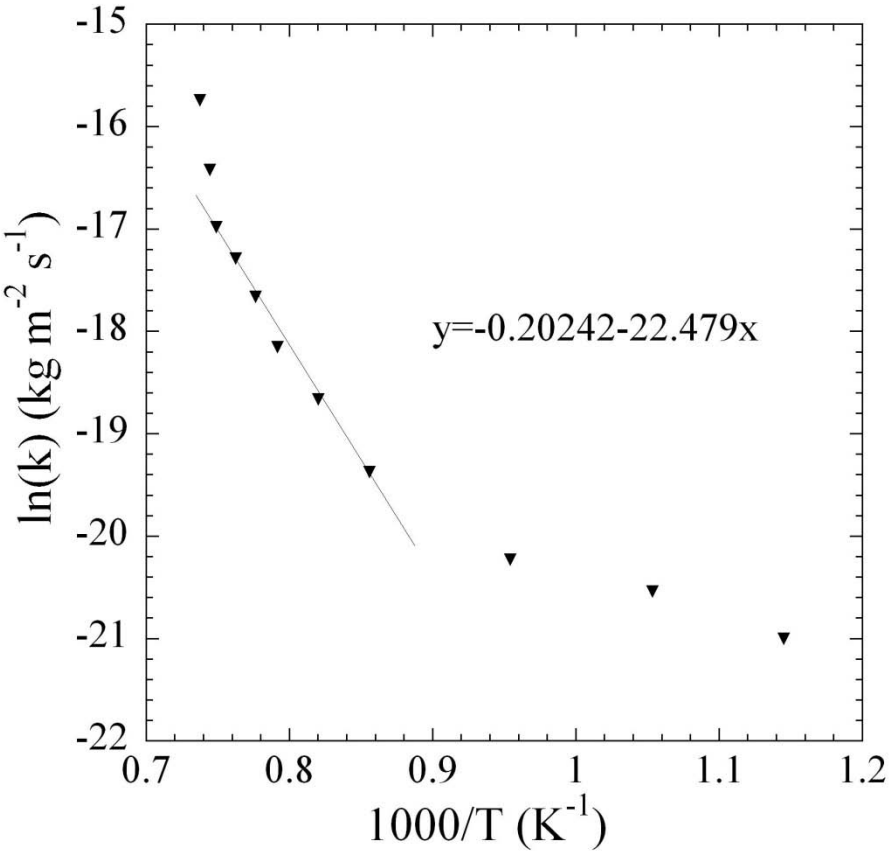

Figure 3.10 Arrhenius plot for the oxidation of carbon black ink in CO_2.

3.3.8 Fabrication of Complex Ceramic Objects

Complex ceramic objects of BT and HA have been fabricated with the carbon black ink as fugitive support material. This success confirms the usefulness and complementing properties of carbon black gel as a fugitive ink for ceramic inks in Robocasting. Figure 3.11 illustrates the use of carbon black gel as fugitive support material, and complex ceramic objects enabled by this fugitive material. In Figure 3.11a, a BT ink was deposited in a non-space filling lattice configuration such that it held a three dimensional periodicity and had the shape of a cube with empty interior and square holes in each face of the cube. The carbon black ink is seen to fill the square holes in the side of the cube. In Figure 3.11b, the green structures had been dried and removed from substrate, subsequently placed in an alumina crucible and heat-treated at 750 °C in air. A negligible amount of ash content < 0.1 wt% was observed, which was from non-volatile impurity introduced into carbon black and polymeric additives during manufacturing. Figure 3.11c illustrates two pieces of such BT lattice, sintered at 1350 °C in air with a tube furnace (GSL 1600X, MTI Corporation, Richmond, CA). Figure 3.11d shows a similarly structured HA lattice sintered at 1150 °C in air with a tube furnace (Thermolyne F21100, Barnstead International, Dubuque, Iowa). Figure 3.11e shows a periodic BT structure after burnout of carbon black support material. The rheological properties and sintering behaviors of BT and HA inks are representative for ceramic inks used in the robocasting process.

a)

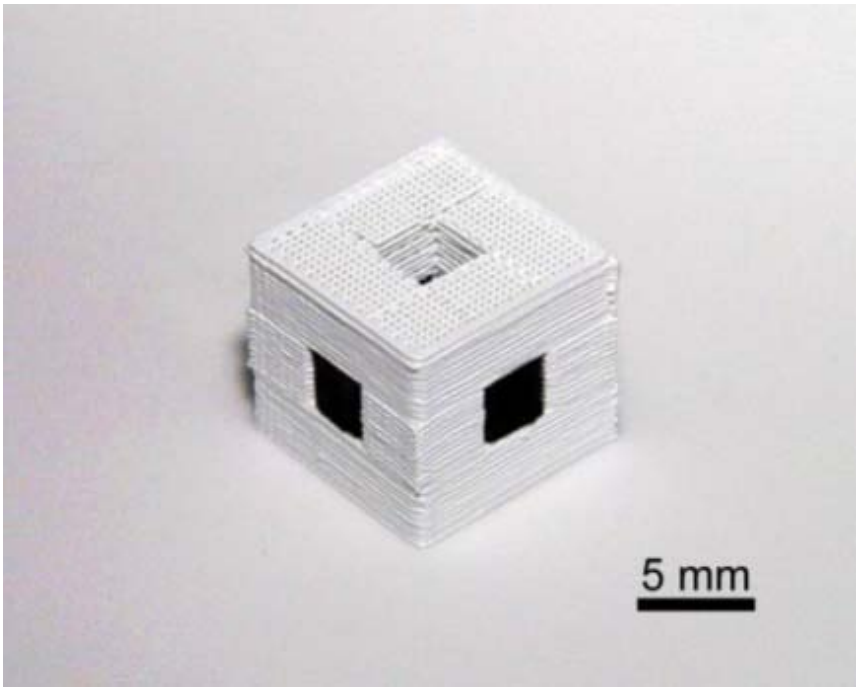

b)

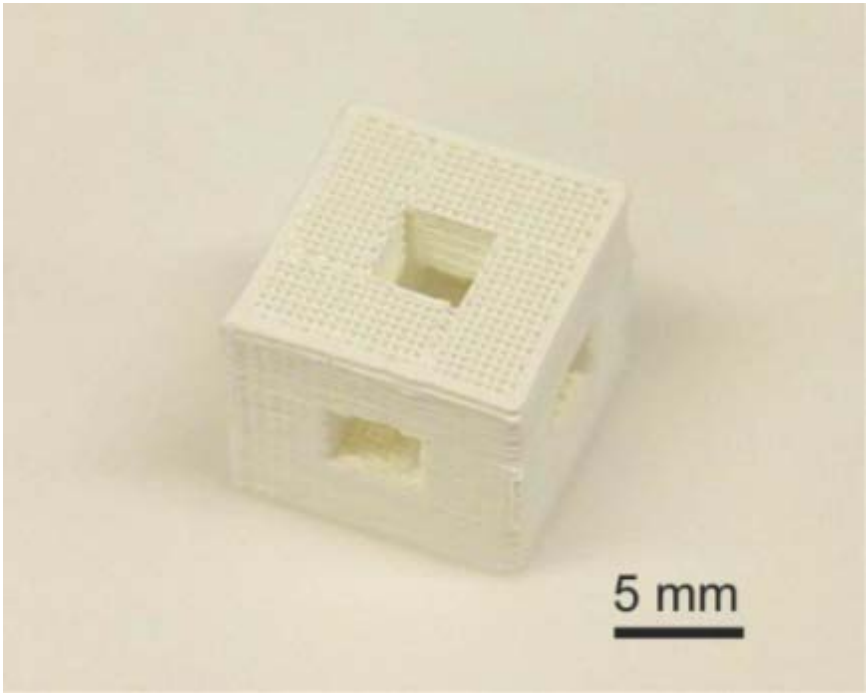

c) 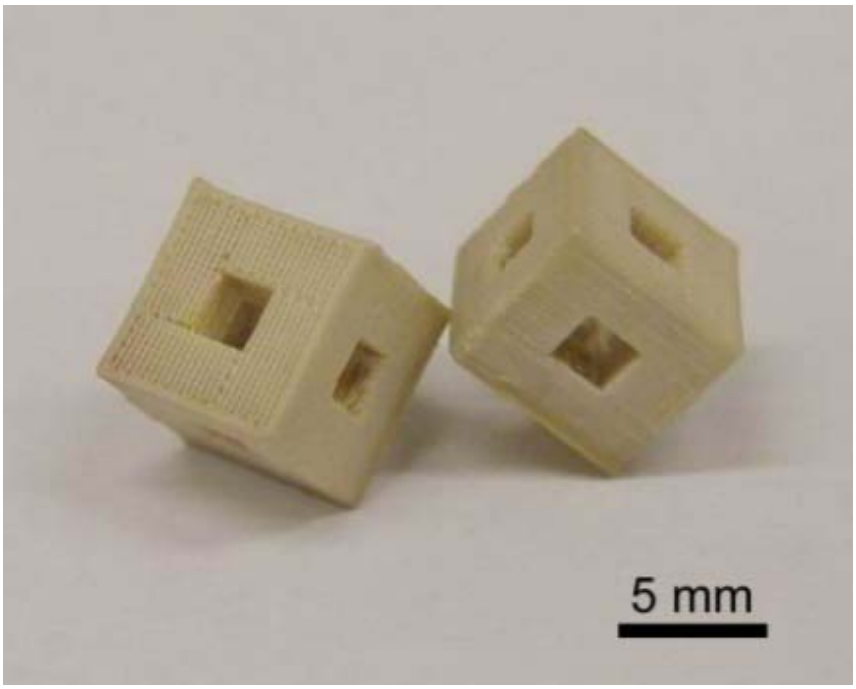

d) 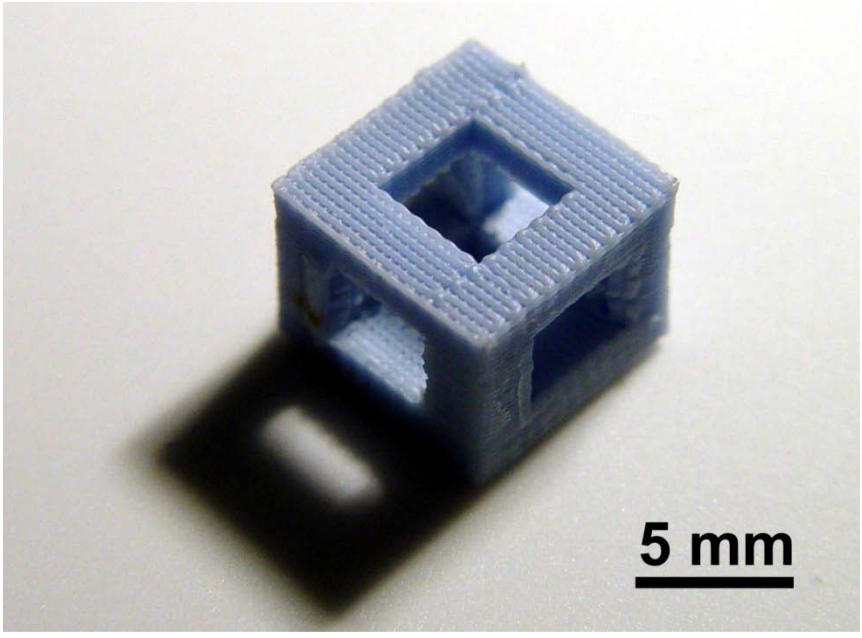

e) 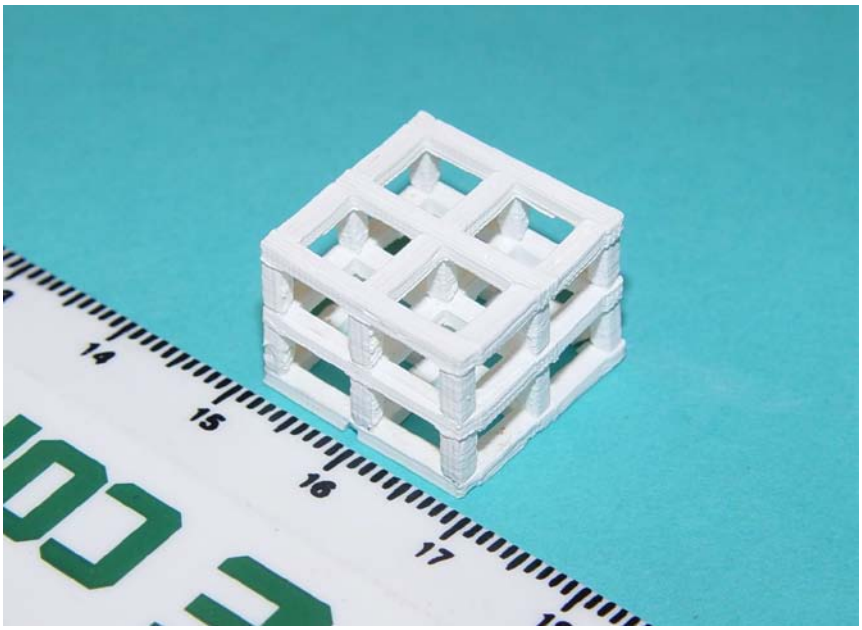

Figure 3.11 a) Non-space filling frame lattice printed with BT and carbon black inks; b) BT structure after burnout of carbonaceous content; c) sintered BT structures positioned against each other; d) a sintered non-space filling frame HA lattice, and e) a periodic BT structure after burnout of carbonaceous content.

Three important features of the carbon black ink can be stated from observation of these results. First, the carbon black ink prints easily alongside the ceramic inks and acts as a sufficient support material in the wet printing state. Second, co-drying of the ceramic and carbon black inks did not cause cracking of the main structure; an indication that drying shrinkage is comparable in each. Third, the burnout stage did not cause cracking or destruction of the ceramic structure and resulted in good shape retention of the ceramic structure. This compatibility of carbon black ink with these ceramic inks suggests that it may also be used as fugitive support material for other ceramic compositions.

3.4 Conclusion

A fugitive support material for Robocasting process was successfully developed using carbon black and polymer additives to form a non-ionic gel network in an aqueous medium. A type of carbon black powder Monarch 120A58 is first dispersed in water with the use of nonylphenol ethoxylate surfactant, and then gelled through interactions with non-ionic polymer additives Pluronic F-127 and Methocel F4M. The dispersion step requires a lower concentration of carbon black dispersion followed by concentration through a centrifugation process. Careful study of surfactant and polymeric additive effects on the rheology of carbon black suspensions resulted in colloidal gels with elastic and flow properties comparable to those observed in ceramic-based printing inks. The carbon black gel maintains its shape upon extrusion through the deposition nozzle, has negligible shrinkage after drying, and leaves only negligible ash content after burnout in air. The compatibility with BT and HA inks suggests that the carbon black ink may be compatible with other ceramic compositions. For ceramics, burnout in an oxidizing atmosphere is acceptable and one may expect that the carbon black will be removed by about 650^{o}C. For materials such as metals that require a non-oxidizing atmosphere, removal of the carbon black support material could be achieved; however, its feasibility depends on material chemistries and process variables involved. The development of this support material is expected to benefit the practitioners of aqueous colloidal gel solid freeform fabrication processes by allowing for a wider range of shapes to be printed, including those with large spans and cantilevered elements.

CHAPTER 4 AQUEOUS NICKEL INK

4.1. Introduction

Colloidal inks used in solid freeform fabrication have limited material selections with respect to metals due to two major reasons: 1) many metals oxidize readily on exposure to air and may be pyrophoric if finely divided, and 2) the size of particles that are often used in processes such as powder metallurgy, laser engineered net shaping (LENS), Selective Laser Sintering, and electron beam melting (EBM) are relatively large and pose a significant challenge to use in an extrusion system for colloidal inks. Nonetheless, the ability to use metals in a solid freeform fabrication process is highly attractive because of mechanical and electrical properties. Additionally, the use of metal and ceramic inks in combination suggests ceramic-metal composite devices and metal-ceramic joints with graded composition. Examples of the use of metal inks includes various metal particle filled aqueous and organic inks used in micropen,[123, 124] fused deposition modeling,[125, 126] and other similar direct-write processes.[127-130]

Robocasting has used aqueous colloidal ceramic inks, such as alumina for photonic band gap,[30] calcium phosphates for biomedical,[33] and PZT[6] and barium titanate[105] for ferroelectric purposes. A tungsten based ink has been used in Robocasting for functional graded materials[131] and biocompatible scaffolds.[132] However, no other

metal inks have been reported for Robocasting and this is likely due to lack of a readily available powder source and difficulty in sintering. This thesis project seeks to assemble $BaTiO_3$-Ni composite structures using an aqueous $BaTiO_3$ ink and requires development of an aqueous colloidal ink of Ni to serve as the metal phase. Of critical importance is matching the flow behavior of the inks, the amount of shrinkage during drying, the rate and amount of shrinkage during sintering, and the chemical stability of both species during the sintering operation.

Ni has outstanding corrosion resistance and relatively low cost. Commercial production of Ni powder usually involves hydrothermal reduction of Ni salt[140] or decomposition of nickel carbonyl (Mond Process),[141] through which particles as small as 100 nm with controlled shape and morphology may be synthesized. In electronics industry, Ni powder has generally been used with organic solvents or polymeric binders for screen printing, tape casting, or conductive trace printing. At room temperature in air, Ni spontaneously develops a NiO surface layer of several atoms thick in air[133, 134] and this layer is electrically conductive. After equilibrium in water, Ni particles present a stable surface chemistry of NiO and is relatively stable in basic condition.[135] This suggests that Ni powder may be processed via aqueous colloidal route and should possess an amphoteric surface chemistry typical of most metal oxides. Aqueous Ni suspensions have been studied with the use of various polymeric dispersants[136-139] for fabrication of Ni objects through injection molding or slip casting to achieve up to 97% of theoretical density after sintering.[136]

Here, an aqueous colloidal Ni gel is developed for use in the Robocasting process. Complex nickel structures are printed and pressureless sintered to achieve >99.0%

theoretical density with well-controlled microstructure. Rheological measurements are used to determine optimal dispersant concentration for ink preparation. After creating a stable Ni suspension at a solid volume fraction $\phi_{solids} = 0.57$, the suspension is flocculated to achieve a colloidal gel at $\phi_{solids} = 0.472$. Again, rheological measurements are used to assess flow behavior after flocculation. Thermogravimetric analysis (TGA) is used to estimate residual carbon content in sintered Ni. Hardness measurement and metallography of sintered nickel structures are presented as measures of the final product properties. Finally, fabricated objects of various shapes using nickel ink are demonstrated.

4.2. Experimental Section

4.2.1. Materials

A near-spherical shaped nickel powder (ENP 800, Umicore, Fort Saskatchewan, Alberta, Canada), with a mean particle size 0.8 μm and theoretical density of 8.908 g/cm^3, is used as the colloidal phase. The manufacturer assay reports a tap density of 4.0 g/cm^3, 0.15% carbon (proprietary polymer used by manufacturer for powder synthesis) and 0.6% oxygen by weight, and specific surface area 0.9 m^2/g. A 50% by weight aqueous solution of polyethylenimine (PEI) with MW 2k (PEI-2K) (Cat # 408700, SigmaAldrich, Milwaukee, WI), a branched PEI with MW 25k (PEI-25K) (Cat # 408727, SigmaAldrich, Milwaukee, WI), and a 50% by weight aqueous solution of branched PEI with MW 50k-100k (PEI-50K) (ICN Biomedical, Aurora, OH) are compared for use as dispersant. An 40% by weight aqueous solution of the ammonium salt of poly(acrylic acid) (PAA) (Darvan 821A, R.T. Vanderbilt Co., Norwalk, CT) is used as the flocculant. Hydroxypropyl methylcellulose (HPMC) (Methocel F4M, Dow Chemical Company,

Midland, MI) 5% by weight stock solution in de-ionized (DI) water is used as viscosifier. DI water wherever mentioned has a nominal conductivity 5×10^{-4} $(ohm\cdot cm)^{-1}$. Paraffin oil (Ultra-Pure, Lamplight Farms, Menomonee Falls, WI) is used for oil bath during the printing operation.

4.2.2. Dispersion of Nickel

The dispersant and its optimal concentration are determined by viscosity measurement for aqueous nickel suspension. Apparent viscosity (η_{app}) is measured as a function of shear rate ($\dot{\gamma}$) at a fixed solid volume fraction (ϕ_{solids}) of 0.50. Polyelectrolyte PEI-2K, PEI-25K, and PEI-50K are used individually as dispersant at different concentrations. A rheometer, (model C-VOR 200, Bohlin Instruments, Cirencester, Gloucestershire, UK) with a cup and bob geometry (C14 serrated), is used for η_{app} characterization. The bob has a nominal 14 mm diameter and the gap between the cup and bob is 0.7 mm. Temperature is fixed at 23 °C and evaporation of water during measurement is minimized by a solvent trap. For each measurement, a nickel suspension sample of 3.6 mL is loaded into the cup and bob geometry using a 10 mL syringe (BD, Franklin Lakes, NJ) and subjected to 60 seconds rotational pre-shear at 0.2 s^{-1}, then undisturbed for 30 seconds followed by a sweep from 0.2 s^{-1} to 6 s^{-1}. A scanning electron microscope (JSM-6360, JEOL, Peabody, MA) is used to characterize particle shape and size of Ni powder.

4.2.3. Flocculation of Nickel

The nickel ink is prepared in a series of addition and mixing steps. In a 125 mL poly(propylene) mixing cup, 0.140 g of PEI-25K is added to 5.80 g of DI water, and then

70.0 g of ENP 800 nickel powder is added. A rigorous mixing, using the non-contact planetary mixer (AR-250, THINKY, Tokyo, Japan), is applied for 2 minutes to homogenize the aqueous nickel suspension at ϕ_{solids} = 0.57. Subsequently, 1.40 g of HPMC stock solution and 0.35 g of Darvan 821A are added to the suspension, followed by thorough mixing. Finally, 1.10 g of DI water is mixed with the nickel gel to lower the solid volume fraction to ϕ_{solids} = 0.472. Following this preparation, the Ni colloidal gel may be consistently extruded though a 200 diameter μm printing tip (5127-0.25-B, EFD, East Providence, RI).

4.2.4. Rheological Characterization of Nickel Gels

The viscoelastic behavior of the Ni ink is characterized by oscillatory shear measurement for Darvan 821A:PEI-25K ratios of 5:2, 3:2 and 2:2. The Bohlin C-VOR 200 rheometer with the C14 serrated cup and bob geometry is used to measure rheological properties. Temperature is fixed at 23 °C and a solvent trap is used to minimize water evaporation. For oscillatory measurement of shear modulus, the nickel ink is subject to a 60 minute oscillatory pre-shear at 1Hz with a controlled shear stress at 0.02 Pa, then undisturbed for 30 minutes. Afterwards, an increasing shear stress (τ) from 10 Pa to 1000 Pa is applied. Complex shear modulus (G^*) is measured as a function of stress amplitude, but elastic shear modulus (G') is the only data reported. The yield stress (τ_y) of the gel is taken as the stress magnitude where G' dropped to 90% of the maximum value during a stress sweep experiment starting from low stress.

4.2.5. Thermal Degradation of Binders

Binder removal for green Ni structures is carried out in air in a tube furnace (Thermolyne F21100, Barnstead International, Dubuque, Iowa) for 8 hours with a temperature set point at 260 °C and a heating ramp rate of 5 °C/min. A thermogravimetric analyzer (TG/DTA 6200, SII Nano Technology, Tokyo, Japan) is used to characterize thermal degradation of polymer additives under the same conditions.

4.2.6. Sintering and Metallography

Densification of Ni powder compacts is carried out at 900 °C for 2 hours in a reducing atmosphere. A tube furnace (GSL 1600X, MTI Corporation, Richmond, CA) is used for this sintering process. A high purity gas mixture of 2% H_2 and 98% N_2 is used in the furnace at a flow rate of 50 standard cubic centimeters per minute at 23°C (controlled by a mass flow controller: Tylan FC-260, Entegris, Chaska, Minnesota). Two cycles of vacuuming and flushing are first used to purge air out of the alumina tube prior to the thermal cycle. The temperature profile for sintering is shown in Figure 4.1. A ramp to 700 °C at 5 °C/min is followed by an isothermal hold of 2 hours. This is followed by a ramp to 900 ^{o}C at 2 °C/min and an isothermal hold of 2 hours. Finally the sintered nickel is cooled to room temperature at 5 °C/min and the flowing gas is terminated. Following sintering, the density of Ni structures is measured using the Archimedes immersion method.

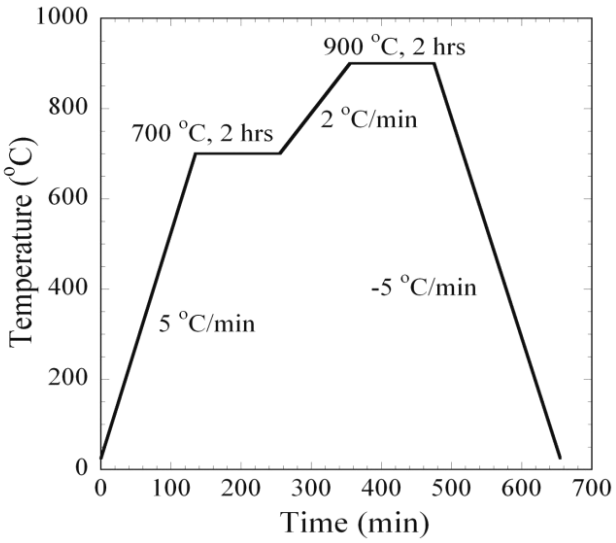

Figure 4.1 Temperature profile for sintering of nickel.

The grain size and microstructure of sintered Ni specimens are examined by metallography. The samples are first cross-sectioned using a diamond saw (Labcut 1010, Extec, Enfield, CT) and then polished (Labpol 8-12, Extec, Enfield, CT) with diamond pastes at 3 to 0.25 μm particle size (DiaDuo, Struers, Denmark). A 10% solution of Marble's reagent (4 g CuSO4 + 20 mL HCl + 20 mL H_2O) is used for etching. Optical and scanning electron micrographs are collected.

4.2.7. Hardness Test

Microindentation Vickers test (0.5 kgf load for 5 seconds) is used to measure sintered Ni hardness. Green nickel specimens are printed using a space-filling pattern of 12×12×4 mm dimension, and molded using 3 mL syringe barrels (EFD, East Providence, RI) as control. After binder removal and sintering under described conditions, these Ni specimens are cross-sectioned, embedded in epoxy resin, and polished by 3-0.5 mm diamond paste.

4.3. Results and Discussion

4.3.1. Dispersant Selection and Concentration Determination

PEI-25K at a concentration of 2mg/(g Ni powder) yields a lowest apparent η_{app}, and is selected for nickel ink preparation. The η_{app} of each sample at shear rate $\dot{\gamma} = 1\ s^{-1}$ is shown in Figure 4.2. The lines have no significance beyond a guide to connect the measured data points. PEI-25K and PEI-50K demonstrate similar η_{app} dependence on PEI concentration, whereas the PEI-2K has a significantly higher η_{app} below concentrations of about 4mg/g. This behavior is likely due to an inability of the small PEI-2K to form a sufficiently thick steric layer to overcome attractive van der Waals forces between particles until more than monolayer coverage is achieved. The minimum of $\eta_{app} = 10.3$ Pa·s at 2mg/g for PEI-25K is taken to be the appropriate concentration. It should be noted, that without any PEI additions, the viscosity of Ni suspensions is too high for practical handling in the Robocasting process. Figure 4.3 shows the morphology and size distribution of the Ni particles used. The 5μm scale bar shows that there are no particles above 2.5μm in this powder and the range of particle size extends well below 1μm. The manufacturer reported average particle size of 0.8μm appears valid.

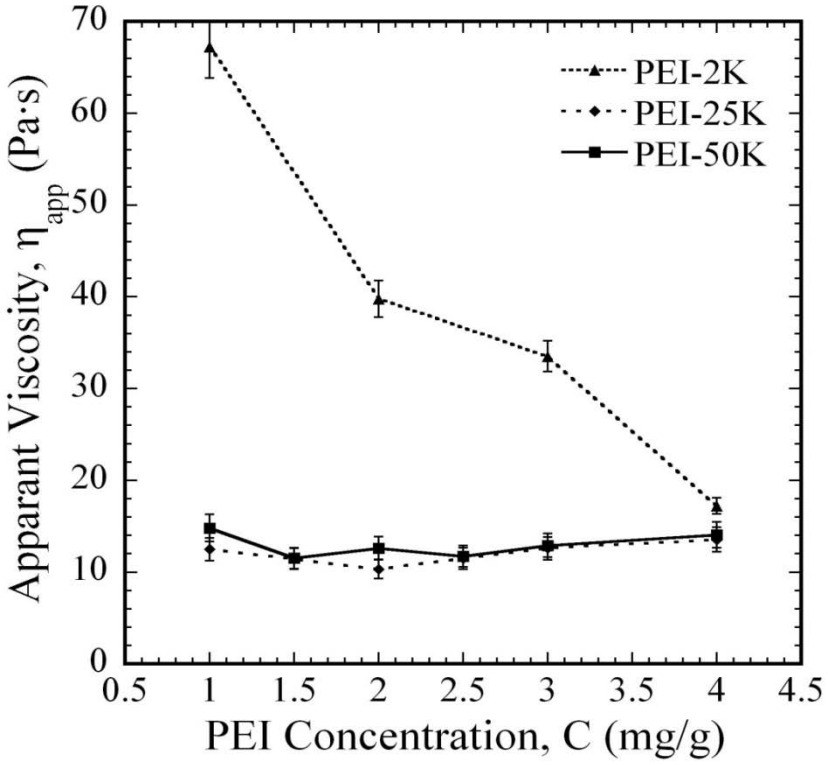

Figure 4.2 Apparent viscosity of ϕ_{solids} = 0.50 nickel suspension at shear rate $\dot{\gamma}$ = 1 s^{-1}.

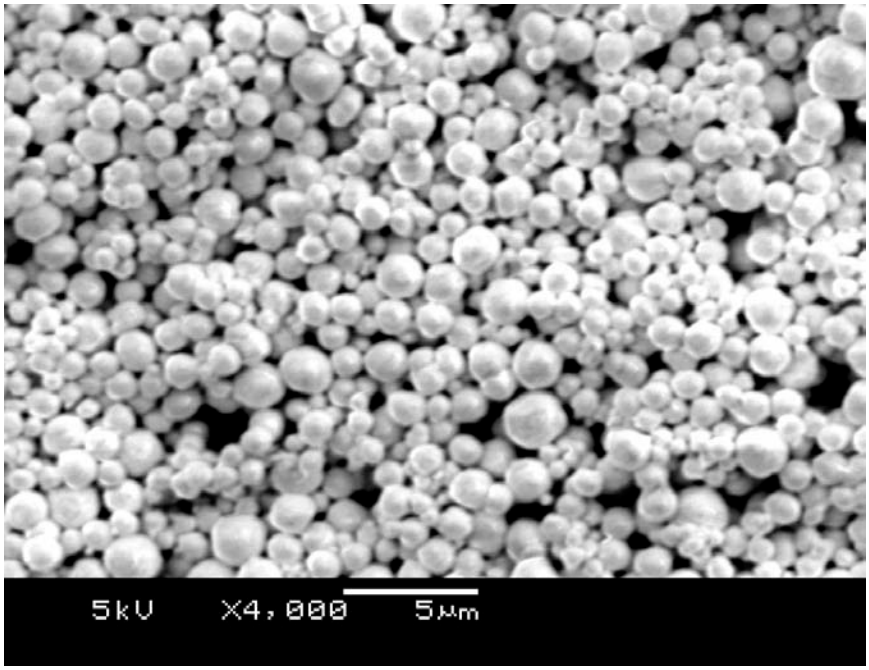

Figure 4.3 SEM image of ENP 800 nickel powder.

4.3.2. Preparation of Nickel Ink

Surface chemistry of ENP800 Ni powder in water favors PEI-25K as dispersant. The isoelectric point (IEP) of nickel particles in water is debatable due to the evolution of nickel hydroxylates on the particle surface.[135, 137, 142-144] Despite these discrepancies, nickel ink preparation is performed at a basic pH $\geq$ 8.0. ENP 800 nickel powder and water are observed reach an equilibrium pH $\approx$ 8.0 at ambient temperature (~23 °C). A rise in pH above neutral conditions with the addition of an insoluble metal oxide indicates the adsorption of H^+ ion from solution due to a negatively charged surface. That is, the change in pH moves in the direction to neutralize the surface. In the presence of PEI-25K addition, ENP 800 nickel suspension has an equilibrium pH $\approx$ 8.2. This pH range favors adsorption of positively charged PEI (IEP = 10.8) on nickel, and then bridging flocculation by negatively charged PAA (IEP = 3.5 - 4).[105]

4.3.3. Rheological measurement

The rheological behavior of Ni gels is shown to depend strongly on the ratio of Darvan 821A:PEI-25K (or A:C to signify anionic to cationic polyelectrolyte ratio). As shown in Figure 4.4, the as-prepared Ni colloidal ink with A:C=5:2 displays rheological behaviors similar to ceramic colloidal gels[32, 105] for Robocasting, while less Darvan addition leads to weaker elastic response. A plateau region of shear elastic modulus around 300 kPa with yield stress $\tau_y \approx$ 154.4 Pa is observed in this Ni ink with ϕ_{solids}=0.472. The yield stress is taken to be the stress at which the elastic shear modulus drops to 90% of its plateau value. Both shear elastic modulus and yield stress decreases as Darvan concentration deceases, indicating less inter-particle linking in the concentrated particle

network. The Ni gel with A:C=3:2 has an elastic modulus of *G'*=65 kPa and a yield stress τ_y=33.9 Pa. The Ni gel with A:C=2:2 has an elastic modulus around 16.5 kPa and a yield stress 25.2 Pa. These large ratios of anionic to cationic polyelectrolyte are indicative of the more effective ionization of the PEI molecule compared to Darvan 821A. In many ceramic suspensions, the opposite motif of dispersion and flocculation is used (i.e., Darvan 821A is the dispersant and PEI is the flocculant). In these cases, the A:C ratio is often in the range of 3:1 to 4:1.

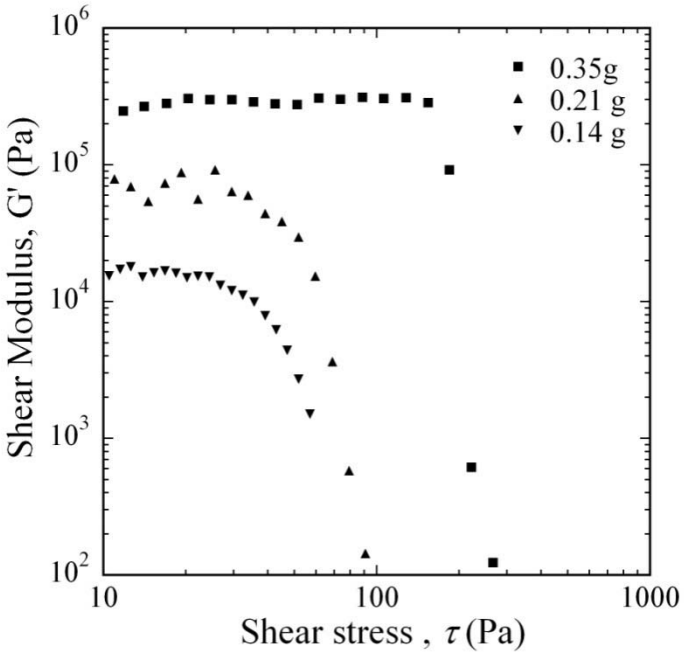

Figure 4.4 Shear modulus G' vs. shear stress τ of Nickel gels (ϕ_{solids} = 0.472) with varying flocculant (PAA) concentration.

4.3.4. Thermal Degradation of Binders

As Ni is prone to oxidation at elevated temperature in air, binder removal for Ni green structure has to be carried out at limited temperature. After thermal degradation at

260 °C for 8 hours, the residual carbon content is estimated to be lower than 0.4% by total weight. TGA analysis indicates partial weight loss for all polymer additives. Residual carbonaceous content is expected to further degrade in the subsequent sintering process and result in carbon content in the sintered Ni.

The chemical kinetics of nickel oxidation has been investigated[133, 134, 145-147] and may be described as chemisorption followed by oxide nucleation and subsequent growth. Below 400°C, the oxidation reaction is limited by diffusion of oxygen through the oxide film.[145, 148, 149] At higher temperatures, the oxidation of Ni is dominated by diffusion of Ni vacancies along grain boundaries in NiO,[145, 150-156] and associated with grain growth within the NiO film.[145] The weight gain as the result of oxidation may be summarized as follows: 1) below 270 °C, the surface oxide layer remains stable, 2) between 270 °C and 300 °C, the surface oxide has a less than 1% mass increase over prolonged exposure to oxygen, 3) above 300 °C Ni oxidizes at an increasing rate proportional to temperature. Hence, the binder removal temperature for green nickel parts is chosen at 260 °C and a prolonged isothermal hold of 8 hours is used. Excessive Ni oxidation is to be avoided since it will either require removal in a subsequent reduction step or hamper sintering and compromise mechanical properties in the sintering operation.

Measured weight loss profiles by TGA indicate only partial weight loss for the polymer additives, as shown in Figure 4.5. After heat treatment at 260 °C for 8 hours, the weight loss is 51.8%, 52.3%, and 77.5% for Darvan 821A, PEI-25K, and HMPC, respectively. Assuming the thermal degradation kinetics for these polymers is the same in the presence of Ni, an estimated 0.214% by weight carbonaceous material will remain after thermal degradation, as shown in Table 4.1. Assuming the initial 0.15% carbon

content in Ni powder is unchanged in this process, which is unlikely, the total carbon content after thermal degradation will be 0.364% by weight or less.

The different thermal degradation kinetics of three polymers may be ascribed to the differences in their molecular structures and covalent bonds: PEI is highly branched containing C-C and C-N bonds; PAA has a carbon chain backbone with -COOH functional group, and HPMC is a cellulose derivative, i.e., modified polymerized glucose rings, containing C-O and C-C bonds. The C=O and C-O bonds requires lower thermal energy to break than C-C and C-N.[157] Also, these polymer additives are coated on nickel particle surface during actual binder removal, NiO may have a catalytic effect to the thermal degradation of these polymers. But these two aspects are not investigated further due to the negligible amount of residual carbon content. In the course of subsequent reducing atmosphere sintering process, thermal degradation of residual carbonaceous content will likely occur, and eventually lead to lower carbon content.

Table 4.1 Calculated residual carbonaceous content with a polymer additive origin.

Polymer Origin	DARVAN 821A	PEI-25K	HPMC
Weight (g)	0.35×0.4=0.14	0.14	1.4×0.05=0.07
Weight loss%	51.8	52.3	77.5
Residual Weight (g)	0.067	0.067	0.016
Total residual Weight (g)	0.150		
Weight% (based on 70g Ni)	0.214		

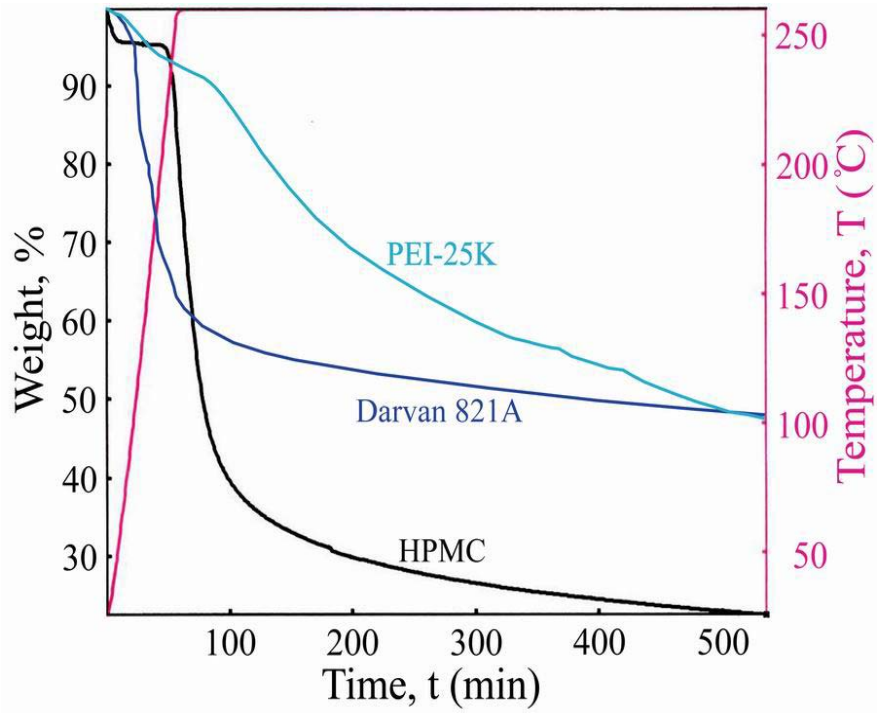

Figure 4.5 Thermogravimetric analysis of thermal degradation Darvan 821A, PEI-25K, and HMPC.

4.3.5. Sintering and Metallography

After sintering in reducing atmosphere at 900 °C, Ni parts fabricated using the ϕ_{solids}=0.472 ink have sintered density >99.0% of theoretical, as measured by Archimedes method. Example sintered nickel rods (from a cylindrical mold) and lattices (fabricated by Robocasting) are shown in Figure 4.6. Metallography reveals good microstructure with small grain sizes and little porosity. Several factors contribute to the high sintered density and good microstructure, including an appropriate sintering profile, a high green density, and homogeneity in particle packing; all these factors act concertedly to yield a high sintered density.

Archimedes method indicates 99.1±0.1% of theoretical density for solid specimens, and a calculated 100±0.1% density for latticed specimens. Short diffusion distance for pore exclusion in the radial direction of filaments likely contributes to the higher density of the lattice specimens. Metallography of the solid specimens reveals small grain sizes with little porosity, as shown in Figure 4.7a. This microstructure shown has grain sizes no larger than 20 μm with an ASTM grain size number of n = 12.6 (Planimetric Procedure, ASTM E112 Section 9) and nominal grain diameter of 4.6 μm. For comparison, the best result reported in literature for powder metallurgy formation of Ni Components has a microstructure with grain size range from 3-30 μm, an average grain size of 5 μm, but at slightly lower density of 97%.[136]

a)

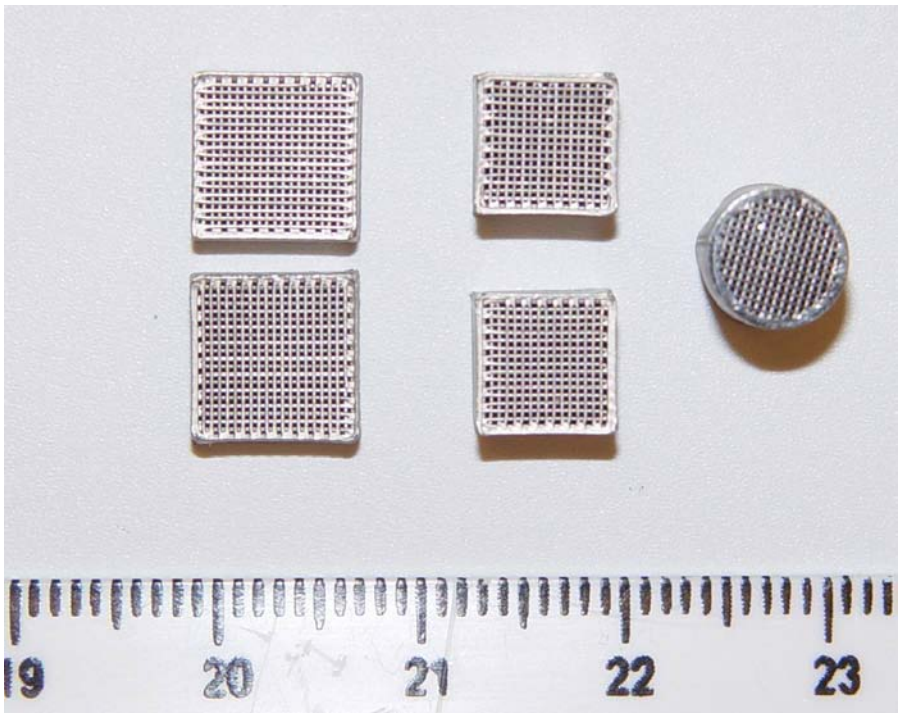

b)

Figure 4.6 Sintered Ni structures: a) top view of box-shaped and cylindrical lattices, and b) solid cylindrical rods; the one on the right has a matte cross-section after etching with 10% Marble's reagent. (Scale unit: mm)

The sintering temperature used here allows densification without excessive grain growth to the microstructure. The chosen temperature profile is based on several considerations. First, a sintering temperature higher than 900 °C promotes fast grain growth and excessive entrapment of pores, resulting in lower sintered density. This has been observed in trials by other researchers.[136, 139] Second, dilatometry study[136, 139] indicates increased densification rate for similarly sized nickel powder at temperature around 900 °C, shortly before reaching terminal density. Third, the 2 hours plateau at 700 °C isothermal hold is intended to ensure that the NiO surface layer is completely reduced by the controlled atmosphere while the thermal degradation of residual carbonaceous matter completes before significant densification occurs. Finally, isothermal hold at 900 °C allows time for densification.

It should be noted that the general rule of thumb for powder sintering is that a higher green density leads to a higher sintered density.[37, 38] After drying the colloidal inks described here, the ϕ_{solids}=0.472 ink will reach a slightly higher particle packing density due to the compressive stress by receding liquid meniscus. This contributes to the low porosity in sintered Ni. Also, the homogeneous particle-packing/porosity-distribution is an important factor in densification. The dispersion-flocculation strategy ensures homogeneous distribution particles and porosity in the green structure within the time frame of ink processing. For comparison, a nickel ink with ϕ_{solids} = 0.43 and sintered at 1000 °C for 2 hours yields 92% of theoretical density and ASTM grain size number of G = 14.6, as shown in Figure 4.7b. Its high porosity and abnormal grain growth may be ascribed to lower green density and too high a sintering temperature. Similar unsatisfying results are reported in the literature, where lower green density and higher sintering

temperature[138, 139] lead to 92-95% sintered density and average grain sizes ranging from 30 to 60 μm.

a) 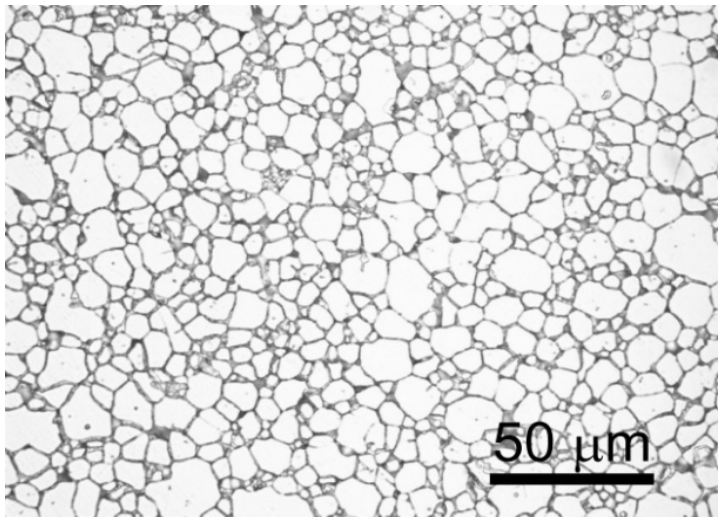

b) 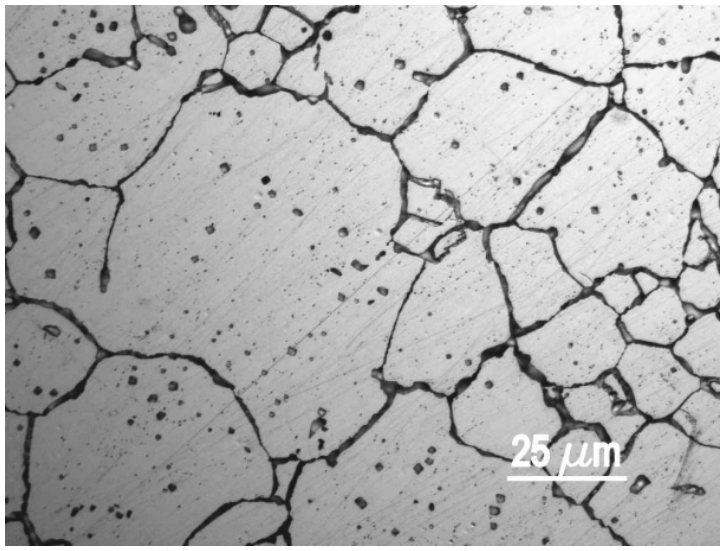

Figure 4.7 Grain structures of sintered nickel samples: a) 99.2% dense sample from ϕ_{solids} = 0.472 nickel ink sintered at 900 °C for 2 hours; and b) 92.0% dense sampl from ϕ_{solids} = 0.43 nickel ink sintered at 1000 °C, 2 hours; many pores are trapped in the Ni grains.

4.3.6. Hardness Test

Microindentation Vickers test on the 99.2% dense specimen yields an average hardness of VPN120, with measured diagonal length d_1 and d_2 of the pyramid between 85μm and 90 μm, as shown in Table 4.2. This value suggests good mechanical behavior similar to that achieved by casting or other powder metallurgy routes. An example of the pyramid indent for hardness test is shown in Figure 4.8. Depending on processing history and impurity content, Ni may exhibit different hardness values: a VPN71 has been reported for annealed Ni tape[158] without mentioning carbon concentration; Ni 201 with a carbon content at 0.02% by weight has a hardness equivalent to VPN79 and Ni 200 with a carbon content at 0.15% by weight has a hardness equivalent to VPN104.[159] A hardness value of VPN120 is reasonable for a Ni specimen with a 99.2% density and carbon content less than 0.364% by weight. The exact form of carbon in Ni specimen is not investigated, but nickel carbide (Ni_3C) is only thermodynamically stable at temperature greater than 500 °C.[160, 161] Thus, at ambient temperature, the Ni_3C might exist in a metastable state in the sintered nickel parts.

Table 4.2 Microindentation Vickers test measurement for Ni specimens.

Indent #	1	2	3	4	5	6	7	8	9
d_1 (μm)	87.8	89.4	87.2	88.5	86.7	87.6	89.2	87.7	86.3
d_2 (μm)	88.3	89.2	86.9	89.1	86.5	87.3	89.8	87.9	86.6
Hardness VPN	120	116	122	118	124	121	116	120	124

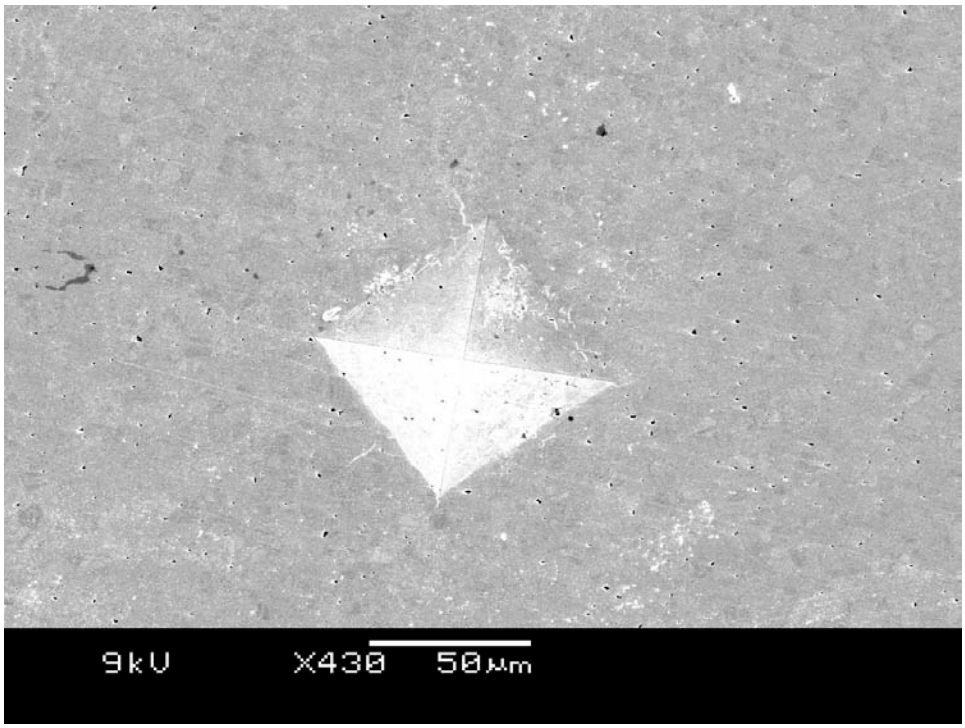

Figure 4.8 Scanning electron micrograph of the pyramid indent on 99.2% dense nickel specimens.

4.3.7. Fabrication of Nickel Objects

Various shaped nickel lattices are fabricated, as shown in Figure 4.9. The bowtie structure (i) in Figure 4.9a is printed with Ø=200 μm nozzle and has a negative Poisson's ratio through buckling of struts during compression. The cubic (ii) and ring (iii) lattices are printed with Ø=250 μm nozzle to demonstrate the versatile designs achievable in Robocasting. Figure 4.9b shows two nickel lattices with large spanning features. To achieve this complex design, a fugitive rice starch ink (described in Appendix B) is used as support material for the nickel ink and an atmosphere of carbon dioxide and hydrogen is used during sintering. Figure 4.9c shows a scanning electron micrograph of the filaments in a sintered nickel lattice structure.

a) 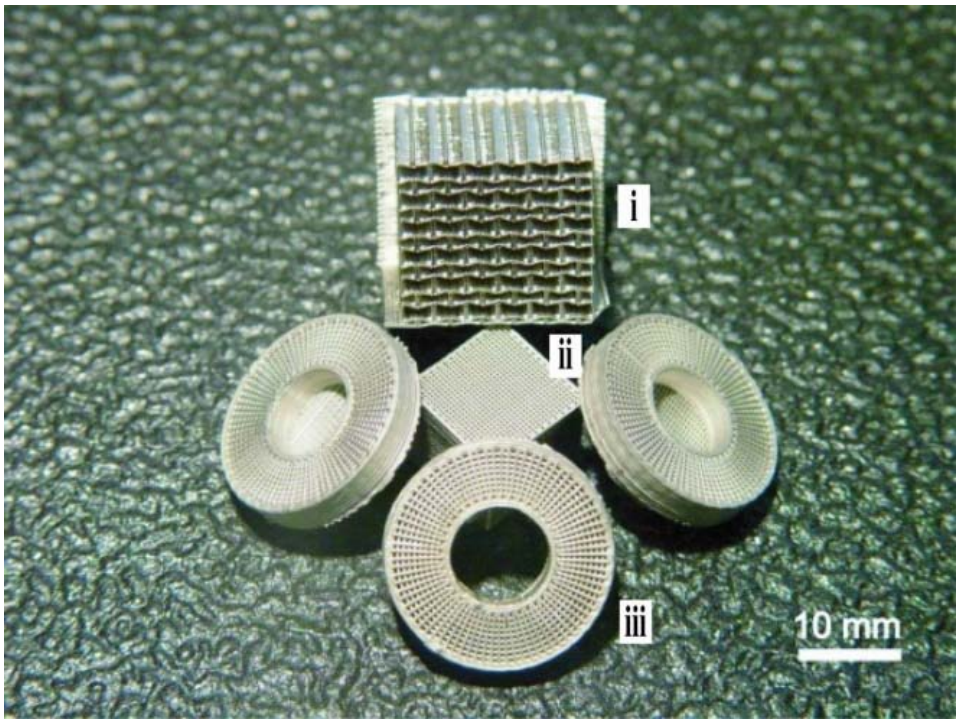

b) 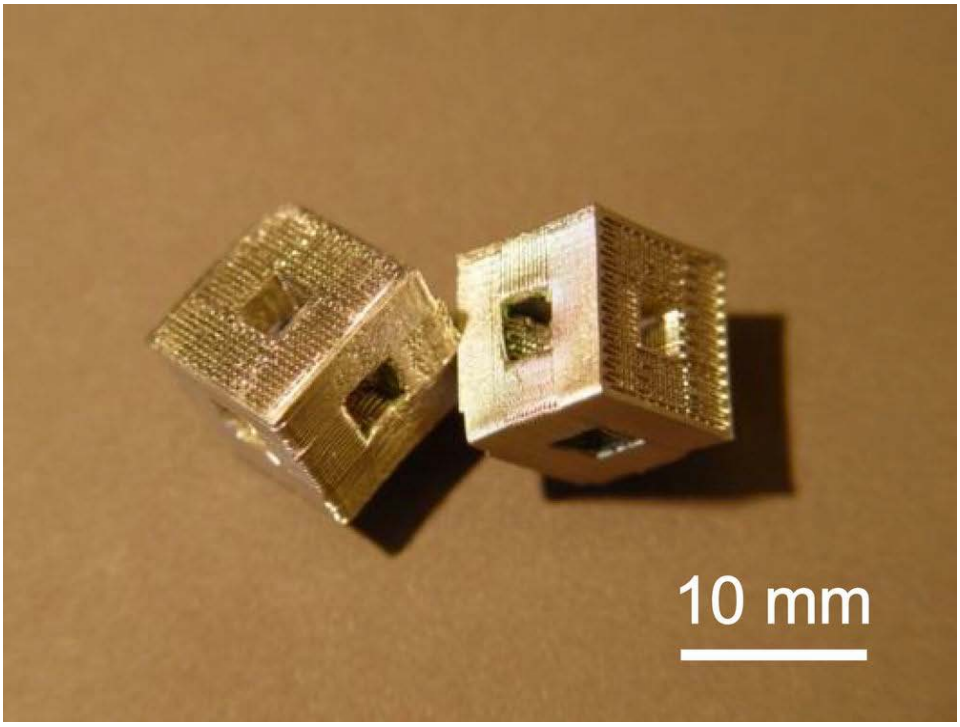

c) 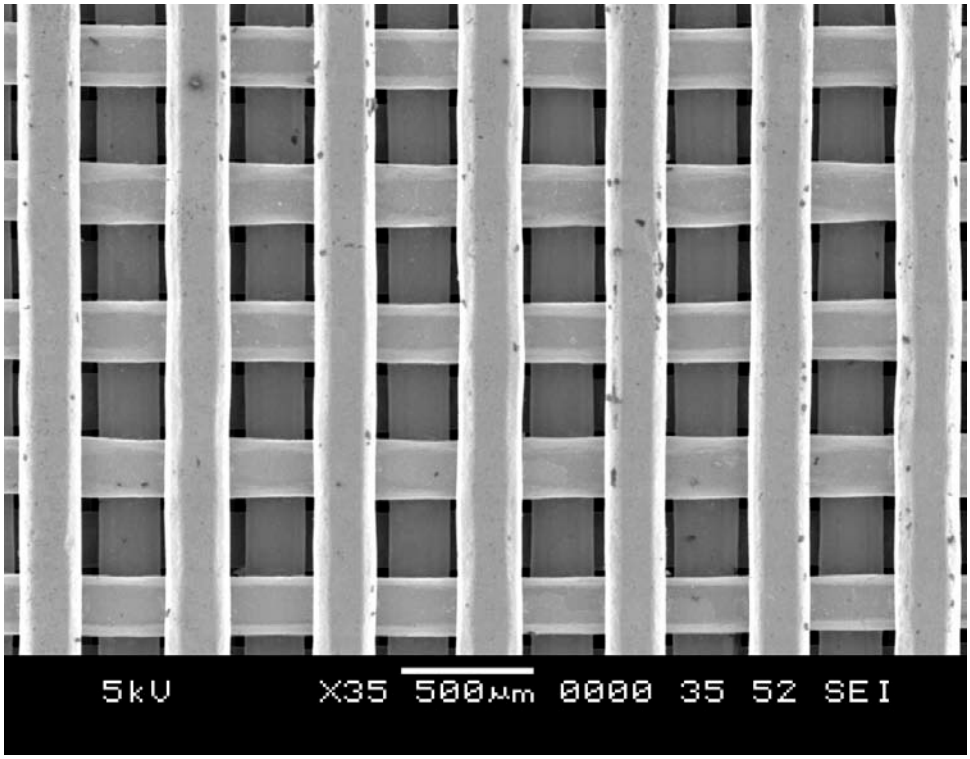

Figure 4.9 Sintered nickel lattices: a) bowtie, cubic, and ring lattices; b) lattices containing large spanning features; c) SEM image of nickel filaments in a nickel lattice.

4.4. CONCLUSIONS

The preparation and characterization of a concentrated aqueous colloidal nickel ink for Robocasting is described. Viscosity measurement is used to determine optimal dispersant concentration for ink preparation. A nickel suspension at 57.0% solid concentration is prepared, using PEI-25k as dispersant. Bridging flocculation using PAA leads to a nickel gel. The addition of HPMC and DI water yields appropriate colloidal gel behaviors at 47.2% solid volume fraction. For this Ni ink composition, thermogravimetric analysis suggests less than 0.364% by weight carbon content after binder removal at 260 °C. Green Ni structures are sintered in reducing atmosphere at 900 °C to achieve >99.0% theoretical density. Metallography and hardness test reveal controlled microstructure and mechanical properties of sintered Ni specimens comparable to low carbon content Ni prepared by other methods. Finally, fabrication of complex Ni structures is demonstrated. The knowledge gained here serves as the basis for the fabrication of BT-Ni composite structures, and may also be useful to researchers and practitioners in the fields of powder metallurgy, multilayer ceramic capacitors, batteries, fuel cells, composition gradient materials, and ceramic-metal composites.

CHAPTER 5 BARIUM TITANATE NICKEL COMPOSITES BY SOLID STATE SINTERING

5.1. Introduction

Robocasting has been used to assemble complex ceramic,[6, 30, 33, 34] polymer,[36] and metal[132] structures ranging in application from bone scaffolds[33] to piezoelectric sensors.[6] In most designs, filament size, geometry, material properties, and structural characteristics are the exploited parameters and composition is uniform throughout the structures. In concept, Robocasting can vary composition in two ways. First, a mixing nozzle setup can blend ink streams in various ratios for a smooth in composition gradient. Second, serial deposition of component inks can create distinct material interfaces and abrupt composition change. The latter case represents the limiting situation where an abrupt interface could cause co-sintering and thermal expansion problems. Nevertheless, this method is easier to accomplish from a printing standpoint and allows for exploring the engineering properties of pure ink compositions to achieve functional heterogeneous structures.

Composites of BT and Ni have been extensively studied and serve various functions in the electronics industry, such as multilayer ceramic capacitors. Depending on particle size, solid state sintering of BT green compacts usually takes place at temperature of 1250-1350 °C, while sintering of nickel compacts requires a non-

oxidizing atmosphere and a much lower temperature around 900 °C. For co-sintering of BT and Ni, two strategies are commonly used in industry: 1) solid state sintering with the use of pure BT and blended BT-Ni compositions, and 2) liquid phase sintering using a flux (also named fluxing agent or sintering aids) to lower the sintering temperature of BT. In the first strategy, blending refractory BT into Ni serves to retard sintering kinetics of the metal. This strategy leaves the electrical properties of BT unaltered and maintains sufficient electrical conductivity for Ni, but causes embrittlement of the Ni by the substantial ceramic inclusion. These materials compatibility issue are common to any forming operation that requires co-sintering of metal and ceramic.

Four major challenges faces Robocasting of BT-Ni composite structures: *i*) formulating colloidal inks with compatible printing and drying characteristics, *ii*) co-sintering of metal and ceramic at compatible densification rates to reach identical final shrinkages, iii) avoiding unwanted changes in material composition and properties, and *iv*) mismatch in thermal expansion coefficient that may cause interfacial stresses in co-sintered composite structures. Whereas *i*) is a matter of colloidal processing, *ii*) is determined by various factors including mass diffusion at an elevated temperature, particle size distribution, and volume ratio and spatial distribution of constituent powder materials, iii) relates to interactions of powder materials and sintering atmosphere, and *iv*) are strongly dependent on the interface between the two materials and the geometric design of the composite structure.

In this chapter, the solid state sintering route is investigated with the ultimate goal to fabricate BT-Ni composite structures with discrete material interfaces. Two levels of composites are dealt with, i.e., the material being extruded and the arrangement of

materials within the overall structure. The following nomenclature is adopted for referring to each material composition: BT refers to pure $BaTiO_3$ material, Ni refers to pure Ni material, and Ni(m) refers to a mixture of Ni and BT with BT considered as an inclusion phase. A strategy for preparation of binary composite inks from BT and Ni powders is described. The formulation of Ni(m) colloid inks is described in detail. Relevant rheological properties of Ni(m) colloid inks are characterized. To assess the parameter space where successful co-sintering may be achieved, sintering behaviors of the Ni(m) inks and pure BT ink are investigated independently by measuring sintered shrinkage after firing. Various temperatures profiles with peak temperature from 1200 °C to 1350 °C are employed. Viable compositions for the Ni(m) composite ink that co-sinter with pure BT while maintaining the ferroelectric properties of the BT and the electric conductivity of the Ni are identified. Micro-indentation Vickers hardness tests are used to reveal the mechanical properties of the sintered composites. Finally, example structures in the form of a multilayer lattice and parallel bowtie stripes are printed, co-sintered, and re-oxidized (for BT) under proper conditions.

5.2. Experimental Section

5.2.1. Materials

A Ni powder (UNP 600, Umicore, Fort Saskatchewan, Alberta, Canada) is used as the metal phase, with manufacturer provided assay indicating a specific surface area of 1.5 m^2/g, a particle size distribution with D_{10}=0.862 μm, D_{50}=1.589 μm, D_{90}=2.85 μm, a tap density 3.2 g/cm^3, and 0.1% carbon, 0.005% sulfur, 0.7% oxygen by weight as impurities. The impurities are presumed to come from surface oxide, and from

proprietary stabilizer molecules used for particle synthesis. A BT powder (Ticon HPB, Ferro Electronics Corporation, Penn Yang, NY) with a reported particle size distribution of D_{10}=0.55 μm, D_{50}=1.21 μm, D_{90}=2.96 μm, a specific surface area of 2.7 m^2/g, a particle density 5.95 g/cm^3 and a tap density 1.68 g/cm^3 is used as the ceramic phase. For preparation of composite ink, a 50% by weight aqueous solution of branched polyethylenimine (PEI-50K) with MW 50k-100k (ICN Biomedical, Aurora, OH) is used as dispersant for aqueous Ni suspension; and an 40% by weight aqueous solution of the ammonium salt of poly(acrylic acid) (Darvan 821A, R.T. Vanderbilt Co., Norwalk, CT, MW=5000-6000) (PAA) is used as received for preparation of aqueous BT suspension. For preparation of BT ink, Darvan 821A and a high molecular weight poly(acrylic acid) (MW=90k) (Polysciences, Warrington, PA) (PAA-90K) solution (adjusted to 20% by weight at pH=8.2 using concentrated ammonia and de-ionized (DI) water) are used as dispersant, and a 25% by weight aqueous solution of PEI-50K is used as flocculation agent. Hydroxypropyl methylcellulose (HPMC) (Methocel F4M, Dow Chemical Company, Midland, MI) 5% by weight stock solution in de-ionized (DI) water is used as viscosifier. DI water wherever mentioned had a nominal conductivity 5×10^{-4} $(ohm\cdot cm)^{-1}$. Paraffin oil (Ultra-Pure, Lamplight Farms, Menomonee Falls, WI) is used for oil bath during the printing operation. A mixture of 5% hydrogen with balance nitrogen is used as processing gas for sintering, and a high purity nitrogen gas is used for re-oxidation of BT.

5.2.2. Preparation of Colloidal Inks

Batches of aqueous colloidal Ni(m) inks having a BT:Ni solid volume ratio=20:80,

40:60, 60:40, 80:20 are separately prepared; also prepared is an aqueous colloidal BT ink. A final solid volume fraction ϕ_{solids}=43% is targeted for all inks described here. Preparation of a Ni(m) ink involves four steps. First, aqueous suspensions of BT and Ni powders are prepared separately with corresponding solid volume fraction calculated. Second, calculated amounts of BT and Ni suspensions are added together to achieve a predetermined BT/Ni ratio. Third, an appropriate amount of Darvan 821A is added to flocculate the suspension. Finally, appropriate amount of HPMC stock solution and DI are added to achieve a HPMC concentration of 7 mg/mL in the aqueous medium and proper ink rheology for robocasting. A non-contact planetary mixer (AR-250, THINKY, Tokyo, Japan) is used after each material addition in the whole procedure. In the Ni suspension, 8.0 mg of 50% by weight PEI-50K solution per gram of Ni powder is used as dispersant; and in the BT suspension, 7.5 mg of Darvan 821A per gram of BT powder is used. The range of Ni(m) ink formulations are listed in Table 5.1.

For preparation of pure BT ink, 4.8 mg of Darvan 821A and 7.2 mg of 20% by weight high molecular weight PAA-90K solution per gram of BT are added in DI water as dispersant. Next, appropriate amount of HPMC stock solution is added to achieve a HPMC concentration at 7 mg/mL for the ink. Finally, 25% by weight PEI solution at 4.5 mg for every gram of barium titanate is used to flocculate the suspension; and appropriate amount of DI water is added to adjust to ϕ_{solids}=0.43. Rigorous mixing is applied after each material addition.

Table 5.1 Formulations for pure BT and BTNi composite inks

1 Ni(m) Ink Preparation

i) Pure component suspensions

a. BT suspension			b. Ni suspension		
DI Water	8.500	g	DI Water	9.000	g
Darvan 821A	0.450	g	PEI-50K (50% wt.)	0.800	g
BT powder	60.000	g	Ni powder	100.000	g
BT particle density	5.950	g/cm^3	Ni particle density	8.904	g/cm^3
Solid volume fraction	0.530		Solid volume fraction	0.534	
total weight	68.950	g	total weight	109.800	g
total volume	19.034	mL	total volume	21.031	mL
BT volume	10.084	cm^3	Ni volume	11.231	cm^3

ii) Ni(m) inks

a. 20BT80Ni (solid volume=1 cm^3:4 cm^3)			b. 40BT60Ni (solid volume=2 cm^3:3 cm^3)		
BT suspension	6.838	g	BT suspension	13.675	g
Ni suspension	39.106	g	Ni suspension	29.330	g
HPMC (5% wt.)	0.928	g	HPMC (5% wt.)	0.928	g
DI Water	1.109	g	DI Water	1.307	g
Darvan 821A	0.168	g	Darvan 821A	0.112	g

c. 60BT40Ni (solid volume=3 cm^3:2 cm^3)			d. 80BT20Ni (solid volume=4 cm^3:1 cm^3)		
BT suspension	20.513	g	BT suspension	27.350	g
Ni suspension	19.553	g	Ni suspension	9.777	g
HPMC (5% wt.)	0.928	g	HPMC (5% wt.)	0.928	g
DI Water	1.236	g	DI Water	1.322	g
Darvan 821A	0.056	g			

2. BT Ink Preparation

DI Water	8.500	g
Darvan 821A	0.288	g
PAA-90K (20% wt.)	0.432	g
BT powder	60.000	g
HPMC (5% wt.)	1.871	g
PEI-50K (25% wt.)	0.270	g
DI Water	2.006	g

5.2.3. Rheological Characterization

For Ni(m) and BT inks, oscillatory rheological measurement is used to characterize and compare their gel behaviors. A Bohlin C-VOR 200 rheometer with the C14 serrated cup and bob geometry is used. Temperature is fixed at 23 °C and a solvent trap is used to minimize water evaporation. The ink is first subject to a 30 minute oscillatory pre-shear at 1Hz with a controlled shear stress at 0.02 Pa, then undisturbed for 30 minutes. Afterwards, an increasing shear stress (τ) ranging from 10 Pa to 1000 Pa is applied. Complex shear modulus (G^*) is measured as a function of stress amplitude, but elastic shear modulus (G') is the only data reported. The yield stress (τ_y) of the gel is taken as the stress magnitude where G' dropped to 90% of the maximum value during a stress sweep experiment starting from low stress.

5.2.4. Sintering Shrinkage

Sintering shrinkage is assessed by measuring pre and post sintering dimensions of cylindrical shaped samples of each ink composition. Green cylindrical rods of length in the range of 15-20 mm for each ink composition are molded with 3 mL syringe barrels (Ø=9.6 mm) (EFD, EFD, East Providence, RI) for use as samples. After drying, binder removal in air is performed at 260 °C in a tube furnace (Thermolyne F21100, Barnstead International, Dubuque, Iowa) for 8 hours. Subsequently, a series of sample rods of each composition are fired in a tube furnace (GSL 1600X, MTI Corporation, Richmond, CA) to peak temperatures of 1100 °C, 1200 °C, 1250 °C, 1300 °C, and 1350 °C without an isothermal hold, and then let cool to room temperature. The heating ramp rate is 5 °C/min. All these heating cycles are demonstrated in Figure 5.1.

At the beginning of each firing procedure, two cycles of vacuuming and flushing are used to purge air out of the tube furnace. A mass flow controller (Tylan FC-260, Entegris, Chaska, Minnesota) with a maximum flow rate of 200 standard cubic centimeters per minute (sccm) at room temperature is used for controlling the processing gas flow rate. A 5% H_2, 95% N_2 mixture is bubbled through water contained in a flask and then fed through the tube furnace. By adjusting flow rate, oxygen partial pressure in the tube furnace may be adjusted to prevent Ni oxidation with negligible reduction of BT. A typical flow rate is in the range from 50-100 sccm. An oxygen probe (DS, Australian Oxytrol Systems, Eaglehawk, Victoria, Australia) is used to monitor oxygen partial pressure above the sample. After that, the post firing diameter is measured at mid-length point of each rod using a micrometer.

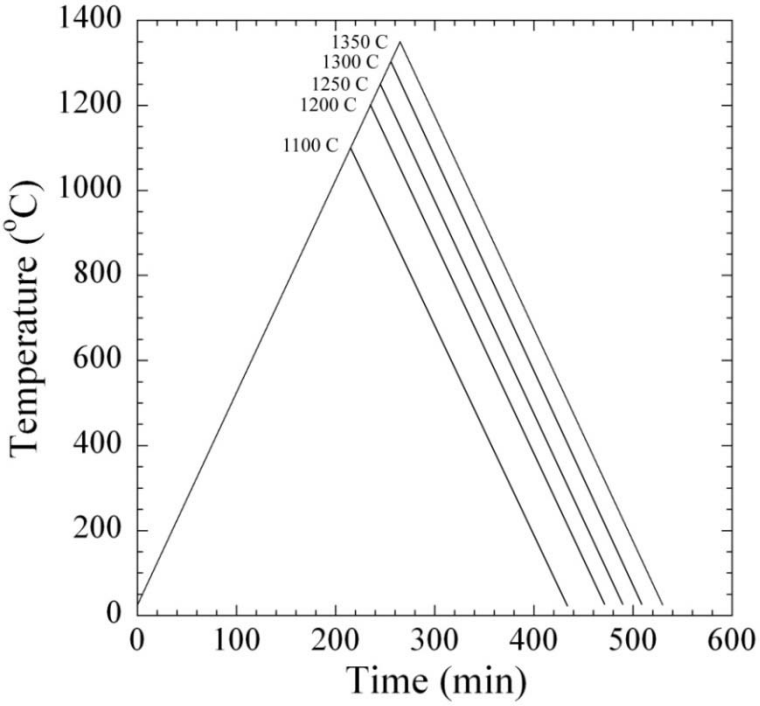

Figure 5.1 Temperature profiles for firing rod-shaped specimens, with the same heating ramp rate for all specimens at 5 °C/min, and no isothermal hold.

5.2.5. Co-sintering and Re-oxidation

Specimens with abrupt transitions in composition are created by serial printing using the pure BT ink alongside Ni(m) inks. Binder removal for the composites is carried out in air (Thermolyne F21100, Barnstead International, Dubuque, Iowa) for 8 hours at 260 °C. Co-sintering of BT-Ni(m) green structures is conducted in the tube furnace (GSL 1600X, MTI Corporation, Richmond, CA) with the pre-described atmosphere control using moist H_2/N_2 gas mixture. A 5 °C/min temperature ramp rate and 1 hour isothermal hold at 1350 °C are used for all sintering cycles, as shown in Figure 5.2. Annealing (re-oxidation) of sintered BT-Ni(m) composites is carried out at 800 °C for 24 hours in a dry nitrogen atmosphere to re-oxidize the BT component.

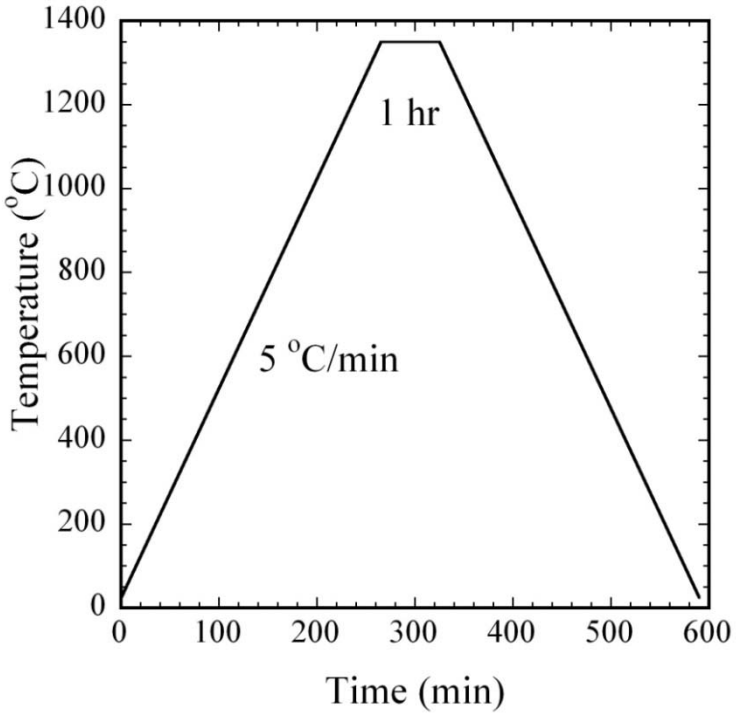

Figure 5.2 Temperature profile for co-sintering of composites

5.2.6. Hardness of Composites

Microindentation Vickers test (0.5 kgf load, 5 seconds) is used to measure hardness of Ni(m) composites. For each Ni(m) composition, cylindrical rod specimens are sintered in moist H_2/N_2 gas at 1350 °C for 1 hour. In preparation for hardness testing, these specimens are cross-sectioned using a diamond saw (Labcut 1010, Extec, Enfield, CT), embedded in epoxy resin, and then polished using a polisher (Labpol 8-12, Extec, Enfield, CT) with diamond pastes at 3 to 0.25 μm particle size (DiaDuo, Struers, Denmark). For comparison purposes, density of each sample is determined by Archimedes method.

5.3. Results and Discussion

5.3.1. Preparation of Colloidal Inks

Despite the dissimilar surface chemistries of BT and Ni particles, Ni(m) gel may be prepared by directly blending polyelectrolyte stabilized BT and Ni suspensions. The initial gel strength depends on the mixing ratio of BT to Ni, and may require adjustment by appropriate polyelectrolyte addition to achieve proper gel strength for use in Robocasting. Pure BT ink is prepared using a dispersant containing the predetermined amount of PAA and PAA-90K followed by flocculation using PEI, so that its solid volume fraction and drying behavior become compatible to Ni(m) inks.

The surface chemistry of nickel and barium titanate as colloidal particles are complex and disagreement exists in the literature about their isoelectric point,[135, 137, 142-144, 162, 163] Nevertheless anionic PAA stabilized BT and cationic PEI stabilized Ni suspensions may be directly blended to form the Ni(m) colloidal gel ink. After rigorous

mixing, BT and Ni phases appear uniformly blended and remain stable without observable phase separation. This is expected behavior since the affinity of PAA for the surface of BT and PEI for Ni are not likely to cause dispersant displacement; rather, it is expected that hetero-flocculation will occur. This process is illustrated in Figure 5.3. Hetero-flocculation of BT and Ni particles occurs through reversible electrostatic "bridging" between adsorbed oppositely charged polymer molecules. At this point, the gel strength (i.e., magnitude of yield stress and shear elastic modulus) depends on the interaction strength between adsorbed PEI and PAA, and the density of those bridging points (i.e. volume ration of BT and Ni particles). The mixing process is thus of utmost importance to homogenize the blended ink and set the initial structure of the colloidal gel.

For a thoroughly-blended composite gel with a BT:Ni volume ratio around 80:20, the ink rheology at ϕ_{solids}=0.43 after HPMC and DI water addition is satisfactory for printing and no further addition of PEI or PAA is needed. However, for a blend with a higher BT volume fraction, an addition amount of PEI is needed to achieve acceptable rheology at ϕ_{solids}=0.43. Conversely, for an ink with higher Ni volume fraction, an additional amount of PAA is needed. In either direction, it seems the appropriate ratio of total PAA to PEI is of the order 3:2. The extreme cases represent pure component ink formulations: a PAA stabilized aqueous BT suspension is flocculated by PEI; and a PEI stabilized aqueous Ni suspension is flocculated by PAA.

a)

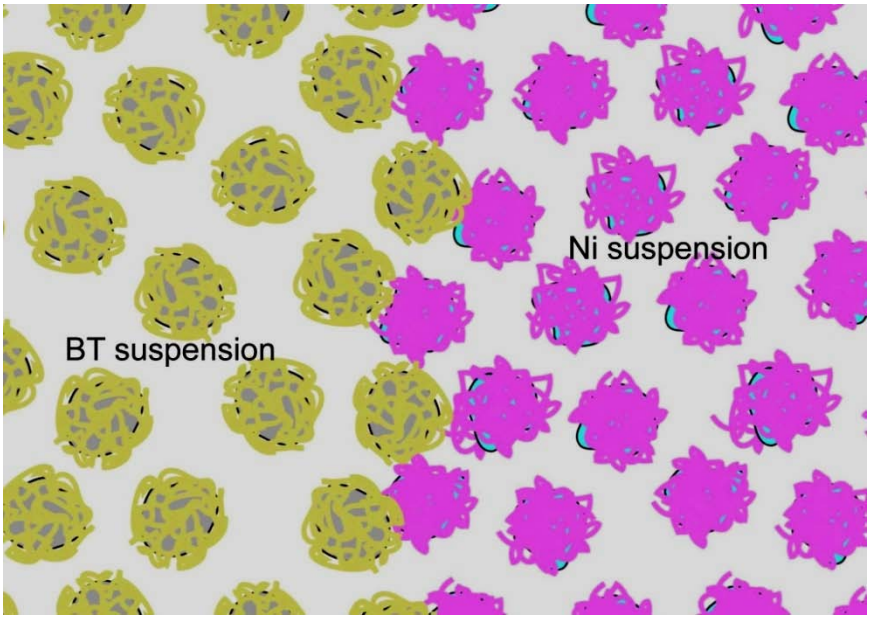

b)

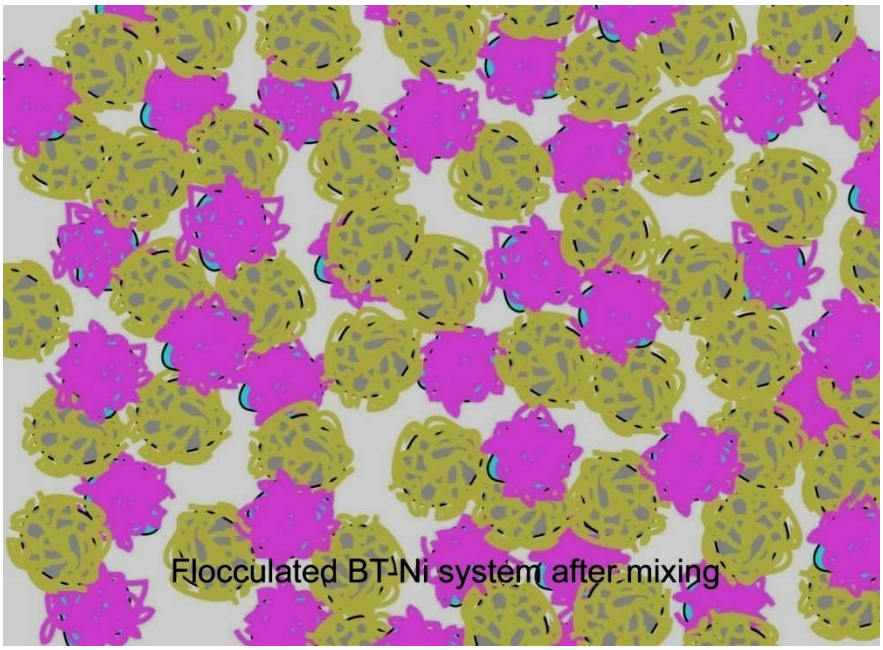

Figure 5.3 Schematic illustrations of direct blending anionic PAA-stabilized BT and cationic PEI-stabilized Ni suspensions: a) before mixing, electrostatic-bridging only occurs at interface between two suspensions; b) after rigorous mixing, two phases are homogenized by shear stress, and flocculation occurs between BT and Ni particles.

The combined use of PAA and PAA-90K for BT ink preparation serves two purposes. First, at ϕ_{solids}=0.43, the BT gel prepared with only lower molecular weight PAA lacks sufficient elasticity to form self supporting structures. By supplementing higher molecular weight PAA-90K as a fraction of the total dispersant, the barium titanate ink has sufficient elasticity at ϕ_{solids}=0.43 without unduly increasing viscosity.[109, 110] The short chain dispersant (Darvan 821A) is thought to adsorb tightly to the BT surface, whereas the PAA-90K may form a more extended polymer brush that enhances interaction with the PEI flocculant molecules. Second, PAA-90K seems to reduce the drying shrinkage difference between the BT ink and the Ni(m) composite ink. All these inks may be extruded through 200 μm diameter nozzle consistently without clogging.

5.3.2. Rheological Characterization

The Ni(m) inks with various BT:Ni ratios demonstrate similar aqueous colloidal gel behaviors at ϕ_{solids}=0.43 (see Figure 5.4) and are comparable to ceramic colloidal gels used in Robocasting. Shear elastic modulus and yield stress of a colloidal gel depends on several factors, including solid volume fraction, shear modulus of particles, and the strength, stiffness and density of inter-particle bonds. For Ni(m) inks, the measured shear elastic moduli range from G'=160kPa for BT:Ni=4:1 to G'=280 kPa for BT:Ni=1:4. Fro comparison, the BT ink has a measured shear elastic modulus of 99kPa. The difference in G' can likely be attributed to the relatively stiffer interparticle bonds formed during heteroflocculation compared to simple bridging flocculation of BT gels with PEI addition.

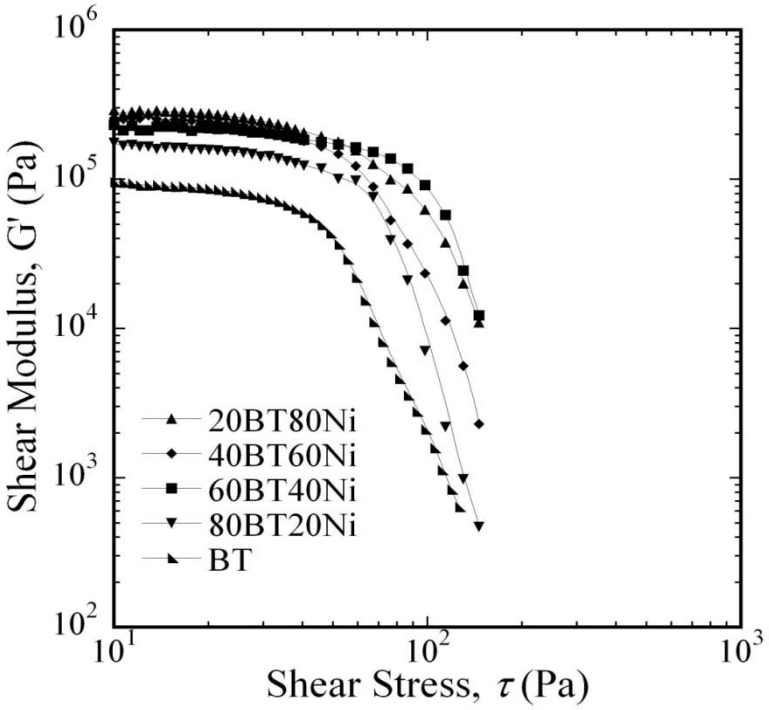

Figure 5.4 Oscillatory behavior for the ϕ_{solids}=0.43 composite inks and BT ink: G' as a function of τ.

5.3.3. Sintering Shrinkage

Sintering shrinkage differences between pure BT and Ni(m) composites is highly composition dependant. A high BT:Ni ratio for Ni(m) favors co-sintering of heterogeneous BT–Ni(m) composite structures due to compatible sintering temperature and shrinkage rate. Also, thermal expansion coefficient of the Ni(m) is more closely matched to pure BT resulting in lower residual stress at interfaces. Less compatible co-sintering is observed as BT:Ni decreases.

To quantify this difference in sintering behavior of Ni(m) compositions is assumed isotropic in the molded cylinder samples and the sintering strain ε is calculated as:

$$\varepsilon = 1 - \frac{D_f}{D_o}$$

where D_o and D_f are the green and sintered cylinder diameters, respectively. The lower bound for ε is 0 and indicates no sintering shrinkage. In this case the volume faction of porosity is approximately equal to $1\text{-}\phi_{solids}$ for the Ni(m) ink. The upper bound for ε occurs for full densification and is theoretically $\varepsilon_{max}=1-(\phi_{solids})^{1/3}$. In this accounting, the drying shrinkage is ignored; however, drying shrinkage is usually small and can justifiably be ignored so long as cracks don't occur in the drying stage. Examples of as-dried (green) and fired Ni(m) cylinders are shown in Figure 5.5.

By comparison, BT is refractory relative to Ni with an onset temperature for sintering around 1200 °C, and nickel has a sintering temperature around 900 °C and a lower onset temperature. In the Ni(m) materials, Ni particles in contact with each other in the green body may sinter well before sintering of BT initiates. On the other hand, as sintering of the Ni particles proceeds beyond the necking state and lead to elimination of porosity, the refractory BT particles will slow the rate of sintering. The collective effect is an expectation that sintering of Ni(m) material will be intermediate to pure Ni or pure BT with a strong dependence on the composition, mixedness of phases and nature of the particles themselves (e.g., particle size).

Figure 5.5 Optical images of Ni(m) cylinders before and after firing: a) BT:Ni=1:4 green bodies, and b) fired Ni(m), from left to right: BT:Ni=4:1, 3:2, 2:3, and 1:4.

As the BT and Ni particles used in the study have comparable sizes, i.e. $\frac{d_{BT}}{d_{Ni}} \approx 1$, the extreme situation that a few substantially larger Ni particles are embedded in a particle network of much smaller BT does not apply. It may be deduced that the effective mechanism for sintering of the Ni(m) composites is for the Ni to form a continuous matrix with embedded BT particles that are dragged along during the sintering process. Figure 5.6 shows the variation of ε for each ink composition after fired to temperatures 1100-1350 °C. The BT:Ni=1:4 Ni(m) ink has the highest Ni volume fraction and largest differences in sintering strain compared to the pure BT composition throughout the temperature range studied. The BT:Ni=4:1 Ni(m) ink has the lowest Ni volume fraction and smallest differences in sintering strain compared to the pure BT composition. The sintering stains of BT:Ni=2:3 and 3:2 Ni(m) inks are also in corresponding order.

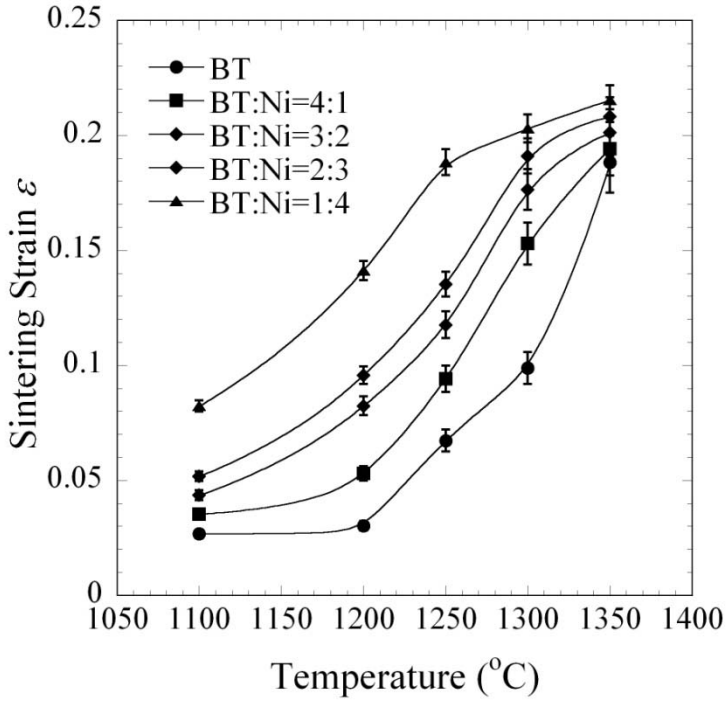

Figure 5.6 Sintering strain of pure BT and Ni(m) inks.

None of the compositions reached full density. As all the cylindrical rods started with ϕ_{solids}=0.43, complete elimination of porosity would result in a sintering strain ε of 0.245. The largest ε observed is in the range from 0.18 to 0.22 at 1350 °C for these samples, which corresponds to residual porosity in the range of 9%-22% by volume. The explanation to these observations includes the following: *i*) subjected to the same temperature profile, composition that has a high solid volume fraction of Ni will have larger shrinkage as a collective effect of more local Ni-Ni densification. *ii*) BT particles acts as a refractory phase in the BT-Ni composite at temperatures lower than 1350 °C, preventing the sintering of the Ni matrix, especially for composition with high BT volume fractions. This makes complete exclusion of porosity difficult for these composites without the assist of an external pressure. *iii*) Pure BT is usually sintered at 1350 °C for 1 hour to reach a high degree of densification; a lack of isothermal hold at 1350 °C leads to its high porosity.

5.3.4. Co-Sintering and Re-oxidation

After binder burnout at 260 °C, only the Ni(m) ink with BT:Ni=4:1 composition successfully co-sinters with pure BT at 1350 °C without cracking. Unfortunately, such high ceramic content leads to brittle mechanical behavior and the Ni(m) has low conductivity due to the minimal metallic phase. This lack of metallic properties in the BT-Ni composite phase must be remedied for uses where metallic properties provide crucial functions. Nevertheless, mechanical brittleness may not be problematic for many electronic applications and the dielectric and ferroelectric behavior of the BT phase may be more important.

The reducing atmosphere used in the sintering operation leads to formation of oxygen vacancies in the BT phase, which is known to cause significant dielectric loss due to in this material. For dielectric applications of BT, these oxygen vacancies must be reduced substantially. Re-oxidation serves this purpose. Carried out at 800 °C, re-oxidation of BT usually takes an isothermal hold of 24 hours or longer to achieve a reasonable result. The mechanism of this re-oxidation step is to let oxygen in the protective atmosphere (high purity N_2) diffuse into BT crystal lattice and neutralize oxygen vacancies. Due to the low oxygen partial pressure in the high purity N_2 atmosphere, this diffusion process requires a significant amount of time to proceed. Ni is only slightly oxidized on the surface and remains electrically conductive, due to its slower oxidation rate than BT and likely the passivation effect of surface oxide layer. The dimension of the BT component is also a factor that effects the re-oxidation time.

5.3.5. Hardness of Composites

Hardness measurement indicates a linear relationship between the hardness of a Ni(m) component and its BT volume fraction, and large variations in hardness of sintered composite specimens containing a high volume fraction of BT. Density measurement indicates 5-10% porosity for these composites. The results of hardness test and density measurement are listed in Table 5.2. The relative density is the ratio of measured density to the theoretical density, i.e. the calculated density of a 100% dense material with the same binary composition.

The large variations of hardness in BT:Ni = 3:2 and 4:1 are likely due to inhomogeneous distribution of porosity. Hence, it is postulated that a high ceramic

volume fraction may cause variations in sintered microstructure. Porosity is common in pressureless sintered composites of this kind, as the temperature profile can hardly optimize sintering kinetics for both phases to allow complete pore exclusion; the result is that many pores are trapped within the composite.

A plot of hardness as a function of composition is given in Figure 5.7. Extrapolation of the linear-fit for the hardness data suggests that pure nickel and barium titanate have a Vickers hardness number of 99 and 387 respectively. These two hardness values are slightly lower than the Ni hardness VPN 120 measured in Chapter 4 and external reported hardness value for BT[164] VPN 400 in a BT-Ag composite. The lower value here may be ascribed to the porosity in these composites that contributes to the total plastic deformation of the test specimens. Figure 5.8 shows optical micrographs of the polished cross sections of sintered composite cylindrical rods for hardness test.

Table 5.2 Measured Hardness and density of BT/Ni composites.

	20BT80Ni	40BT60Ni	60BT40Ni	80BT20Ni
Vickers Hardness (VPN)	164	221	235	351
Standard Deviation (VPN)	2	3	12	26
Theoretical Density (g/cm3)	8.316	7.725	7.133	6.542
Archimedes Density (g/cm3)	7.868	7.431	6.475	6.067
Relative Density	0.946	0.962	0.908	0.928

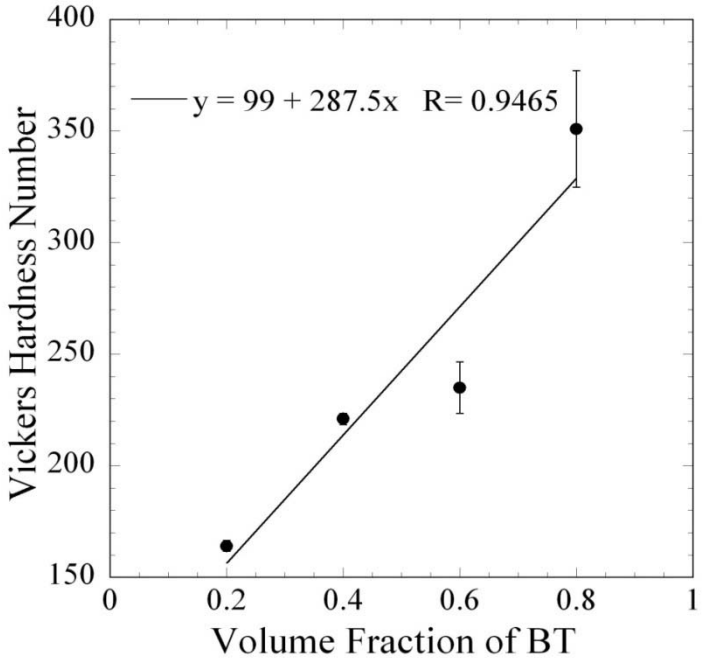

Figure 5.7 Vickers hardness number as a function of BT ratio in BT-Ni composites (error bars for 0.2 and 0.4 BT compositions are too short to show on this plot).

a)

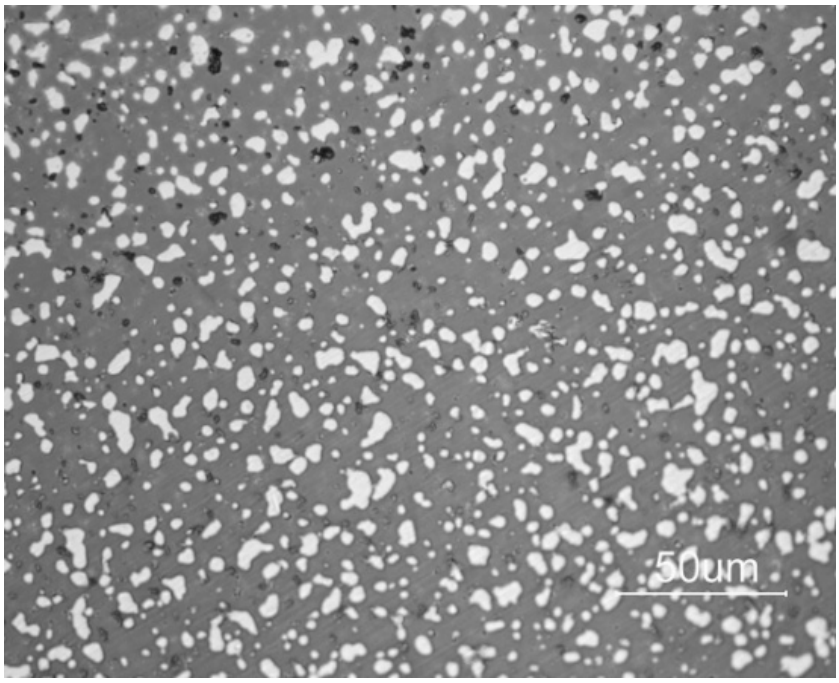

b)

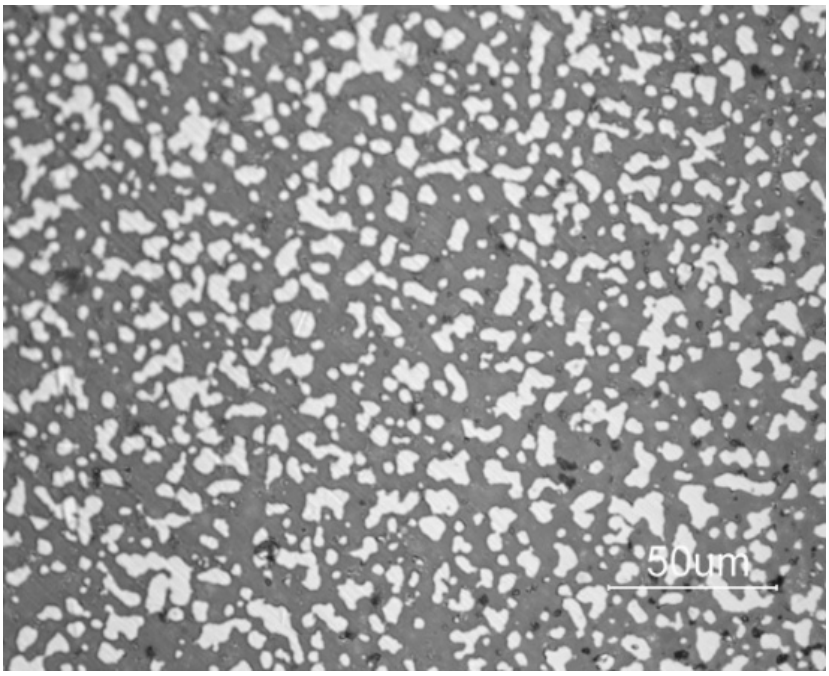

Figure 5.8 Optical micrographs of sintered Ni(m): a) BT:Ni=4:1 and b) BT:Ni=3:2. The bright islands are Ni, grey matrix is are BT, and the dark spots are pores.

5.3.6. Fabrication of BT-Ni composite Structures

Two types of BT-Ni composite structures are fabricated by serial printing of BT and Ni(m) inks: 1) 2D NPR bowtie network and 2) MLCC lattices. Figure 5.9 shows a sintered complex graded NPR structure resembling interconnected alternating layers of bowtie shaped stripes. This NPR structure is a 2D simplification of the proposed 3D NPR composite structure. The white colored stripes are BT before re-oxidation, and the dark colored stripes are Ni(m) with a BT:Ni ratio of 4:1. The interface between the two compositions is at the mid-point of a thin wall of stacked filaments at around 160 μm in thickness. These filaments are printed with Ø200 μm nozzles. Each unit of the bowtie stripes is slightly distorted as the result of the printing process and supposedly the internal stress generated during sintering process. Both ends of the bowtie stripes are deformed during drying process because these free-standing thin walls are then not structurally stable; gravitation and unbalanced surface tension from the lamp oil cause these thin walls to skew sideways. However, the BT:Ni=4:1 Ni(m) bowtie stripes are brittle due to the high BT inclusion. To achieve the proposed non-linear load deformation characteristics of a NPR composite structure, a much higher Ni solid volume fraction is preferred to use in the Ni(m) component to allow sufficient ductility. But this is in conflict with the requirement of successful co-sintering in the solid state sintering paradigm.

A composite lattice not shown here is a structure resembling a multilayer ceramic capacitor, assembled with pure BT and Ni(m) (BT:Ni=4:1) inks. As the sintered Ni(m) (BT:Ni=4:1) has a low electrical conductivity due to high ceramic inclusion. To achieve this specific structure and function with a lower BT inclusion in the Ni(m) electrodes (for

a higher electric conductivity), a manipulation of material processing for composite structures assembled with BT:Ni=2:3 Ni(m) ink and pure BT ink is performed. A 300 °C temperature is used in the binder removal step. After 6 hours of thermal treatment in air, the Ni phase grows a thin layer of oxide on surface so that this oxide surface layer modifies the sintering kinetics of Ni(m) ink and enables co-sintering with pure BT.

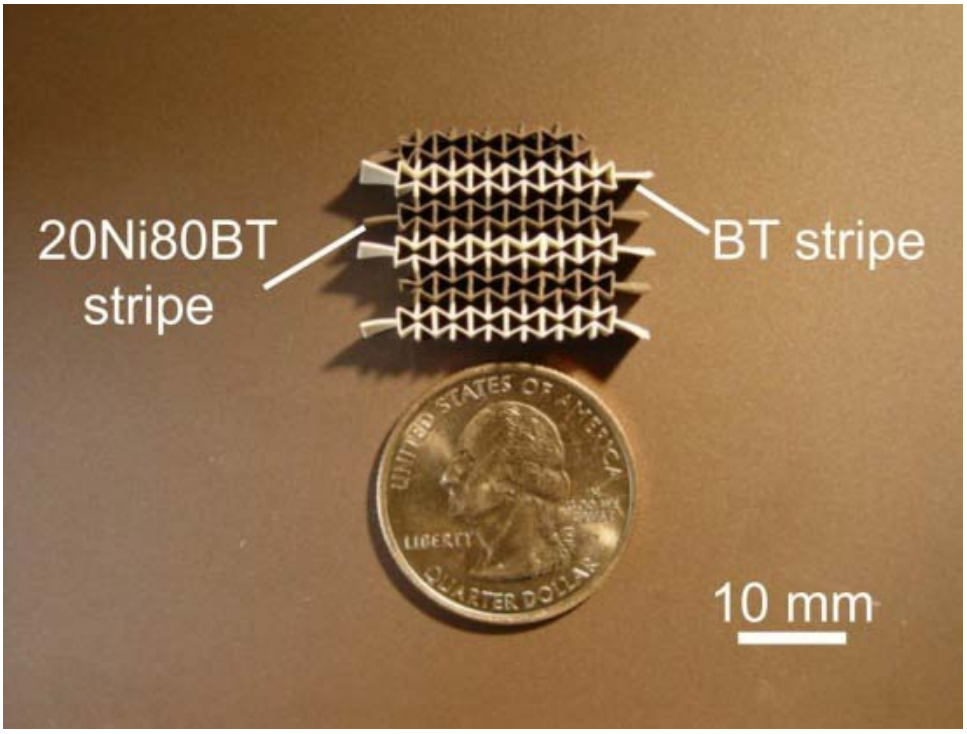

Figure 5.9 Co-sintered compositional graded bow-tie stripe network of BT:Ni=4:1 Ni(m) (20Ni80BT) and pure BT before annealing.

A weight increase of 0.133 g (1.456% by weight) is observed due to oxidation when 9.135 g of Ni powder has been heated at 300 °C for 6 hours in air; by calculation, 5.3% of Ni has been oxidized to NiO on the Ni particle surface with negligible linear expansion. NiO has a melting temperature of 1955 °C. When sintering atmosphere is appropriate, the NiO may increase the onset temperature for sintering of Ni particles and

modify the sintering kinetics of the Ni(m) ink, so that co-sintering of BT and Ni(m) may be accomplished at a higher Ni volume fraction than the BT:Ni=4:1 composition. The evolution of the NiO during sintering process is not studied in detail, but it is likely that the NiO will be reduced to metal state eventually. However, this method is not considered a repeatable standard procedure, and frequently hard to control due to process variables involved. Thus, it is not described in the experimental section.

Figure 5.10a shows composite lattices assembled with pure BT ink and BT:Ni=2:3 Ni(m) ink using Ø250 μm nozzle and annealed at 800 °C for 24 hours in N_2. The layered pattern is designed such that interleaved layers of BT and Ni(m) form a structure similar to a multilayer capacitor. That is, the Ni(m) layers are alternately terminated to form electrodes. The BT:Ni=2:3 Ni(m) rods appear gray in color, whereas the BT rods are cream colored. The center sample has been demarcated with a numerical scheme along the bottom edge. Here, regions 1 represent the termination ends of the multilayer structure. Region 2 denotes the extension of one set of electrodes to the terminations. And, region 3 represents the active area of the multilayer structure where layers of dielectric are sandwiched between oppositely charged electrodes. The electrode scheme is more clearly demonstrated with the cross-section of Figure 5.10b. In this figure, the open, 3D lattice nature of the structure is apparent. The top numbers correspond with the regions demarcated in Figure 5.10a, whereas the left-hand side labels denote the various anode (a1, a2, etc.), dielectric (d1, d2, etc.), and cathode (c1, c2, etc.) layers. In this picture, the terminal end is connected to the anode layers.

The intersections created by overlapping rods from adjacent anode, dielectric, and cathode layers form an array of parallel connected capacitors for each dielectric layer.

Hence, the sample shown in Figure 5.10b contains nine active dielectric layers. The cross-sectional diameter of the rods in these structures is ~150 μm. Accordingly, the area of contact between the electrode and dielectric layers is a fraction of the circular cross-section of the lattice rods. The area for each intersection is estimated to be a_i=0.015 mm^2. Hence, the total active area per layer is found by the formula: $A_i = NMa_i$, where NM represents the number of intersections per layer. The capacitance can be calculated by

$$C = \frac{\varepsilon_0 \varepsilon_r NM a_i L}{l}$$

where ε_0 and ε_r are the permittivity of free space and the relative permittivity for BT, respectively, L is the number of dielectric layers, and l is the layer thickness.

A crude resistivity measurement indicated that the metallic layers had an electrical conductivity of $\sigma = 10^7$ S·m^{-1}. A capacitance of 1.7 nF was measured for a sample with A_i = 15 × 18 × 0.015 = 3.51 mm per layer, L = 5, and l = 0.125 mm. The solution for ε_r revealed a relative permittivity of 1247. This value is in good agreement with a previously measured dielectric constant for this $BaTiO_3$ of 1100.

a)

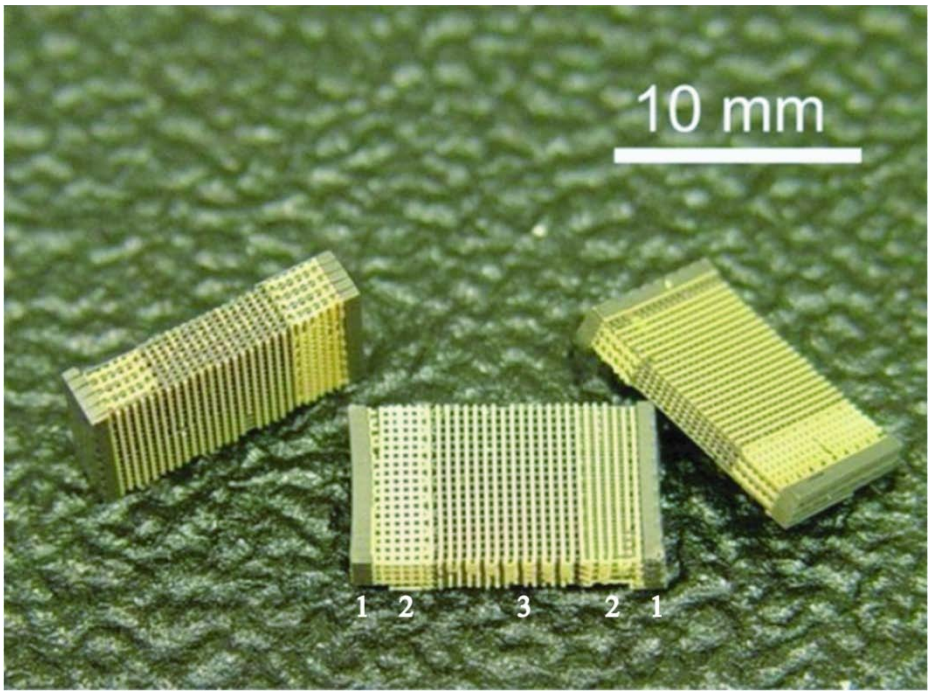

b)

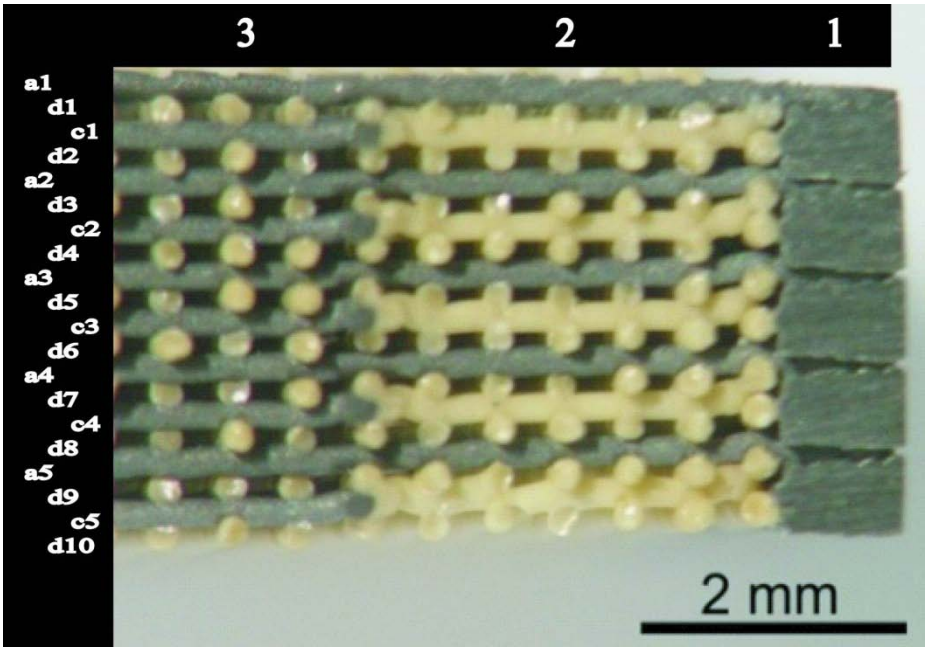

Figure 5.10 Co-sintered compositional graded structures: a) MLCC composite lattices of BT:Ni=2:3 Ni(m) (dark color) and pure BT (cream color), annealed; b) cross-section of the MLCC composite lattice denoting the electrodes and dielectric filaments.

Figure 5.11 show a scanning electron micrograph of the material interface between sintered BT:Ni=2:3 Ni(m) and pure BT filaments. The specimen is remained unpolished for observation. The up-left portion of the SEM image shows the BT:Ni=2:3 Ni(m) and the lower-right portion is the BT phase.

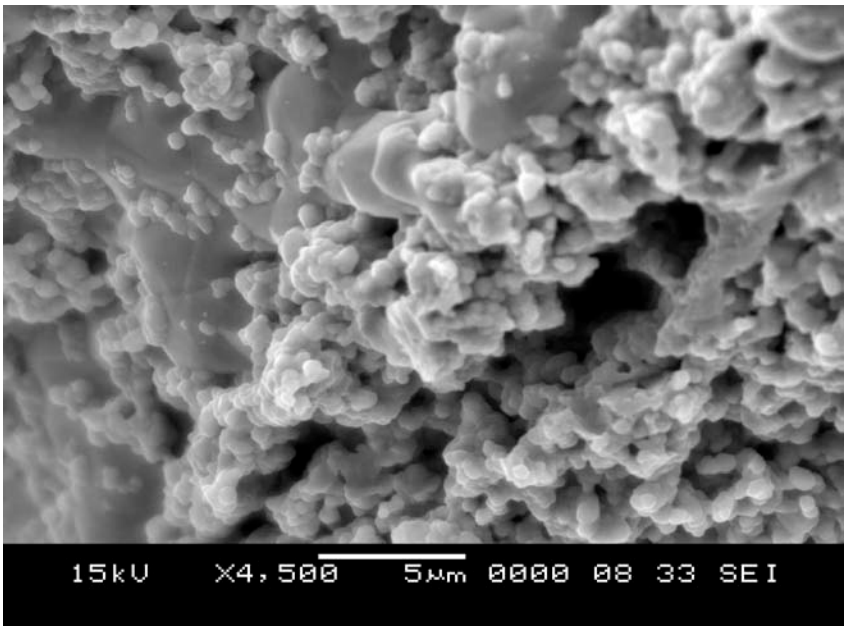

Figure 5.11 scanning electron micrograph of the BT:Ni=2:3 Ni(m) and pure BT interface for the composite lattice.

5.4. Conclusions

Freeform fabrication of complex ceramic-metal composite structures has been achieved through Robocasting. Solid state sintering is used for densification of the composite structures with Ni(m) that contains a Ni solid volume fraction of 20%. To achieve a higher solid volume fraction of Ni in the composite will require a different strategy to overcome sintering problems. Aqueous colloidal composite inks at ϕ_{solids}=0.43 with BT:Ni solid volume ratios 1:4, 2:3, 3:2, and 4:1 are formulated by direct-blending polyelectrolyte stabilized aqueous suspensions assisted by rheology adjustment. A ceramic barium titanate ink at ϕ_{solids}=0.43 is formulated to have the same solid volume fraction and compatible drying behavior. Sintering shrinkage study indicates that sintering shrinkage mismatch to BT ink increases as Ni solid volume fraction increase in the Ni(m) ink. Assembly of BT-Ni composite structures have been achieved by serial printing of BT ink and a compatible Ni(m) ink followed by densification through reducing atmosphere sintering at 1350 °C. Oxygen vacancies in the BT phase is diminished by re-oxidation in nitrogen gas at 800 °C for a prolonged period of time to achieve an estimated dielectric constant of 1247. Hardness test indicates a linear relationship between the hardness of a Ni(m) component and its BT volume fraction. The findings in this chapter may be useful to researchers and practitioners in the field of ceramics, composites, functionally graded materials, solid state fuel cells, biomaterials, and solid freeform fabrication.

CHAPTER 6 BARIUM TITANATE NICKEL COMPOSITES BY LIQUID PHASE SINTERING

6.1. Introduction

As shown in chapter 5, Robocasting promises fabrication of ceramic-metal composites for novel applications. Co-printing strategies include real-time mixing of colloidal inks for graded structures and serial printing for abrupt material transitions. However, major challenges in the ensuing densification process result from mismatches in sintering kinetics and thermal expansion coefficient between the ceramic and metal components. These difficulties often lead to distorted or cracked structures and failure of the printed structure as a functional device. The efforts described in chapter 5 seek to achieve co-sintering by significant inclusion of refractory BT particles in the Ni phase. This approach met with limited success at a volume fraction of BT around 80%. While this solution preserves the pure BT properties in the ceramic phase and the Ni and BT mixture is conductive for electrical applications, this solution is wholly inadequate if one desires mechanical ductility from the metallic phase. Clearly an alternative approach is in order.

Liquid phase sintering involves using minor additions of sintering aids to lower sintering temperature and increase sintering rate. Additionally, liquid phase sintered parts often have low stress during sintering because the liquid allows for rapid particle rearrangement.[38, 44] Liquid phase sintering is extensively used in the field of multilayer ceramic capacitors (MLCCs), where thin laminates of BT-based ceramic and base metals, such as Ni or Cu, are co-sintered into alternating layers of electrodes and dielectrics in a monolithic form. Sintering aids (or flux) such as Li_2O, B_2O_3, MgO, Al_2O_3, SiO_2, CaO, ZnO, CaF_2, La_2O_3[165-167] have been explored for this process. Most compositions allow sintering only above 1100 °C. Recently, sintering aids based on a eutectic composition of ZnO-B_2O_3 with Li_2O additive for sintering around 1000 °C has been reported by Randall et al[167] to fabricate X5R/X7R dielectrics. However, all these sintering aids are used in non-aqueous systems where ceramic and metal particles are dispersed in organic binder for screen printing or tape casting of MLCCs. To use these materials in the Robocasting process, they must be homogenously incorporated in aqueous colloidal inks, either as a solute in the aqueous medium or as dispersed colloidal particles, without deteriorating the printability of colloidal inks. Likewise, these additives should not degrade mechanical or electrical properties of sintered composites.

Here, aqueous colloidal inks containing ZnO-B_2O_3-Li_2O sintering aids are developed for Robocasting of BT-Ni composite structures. The low firing temperature composition for the ceramic phase is referred to as LFBT for brevity. Successful densification of LFBT-Ni composite structures with as low as 20% by volume $BaTiO_3$ inclusion in the metallic phase is successfully achieved at 1000 °C in an inert or reducing atmosphere. The LFBT ink is formulated by adding zinc oxide, zinc borate and lithium

acetate dihydrate in an aqueous BT suspension. The Ni based ink includes some BT, as described in Chapter 5 for Ni(m), and an addition of lithium acetate dihydrate. This ink type will be referred to as Ni'(m). Polyelectrolyte is used to adjust ink rheology. Solid volume fractions for both inks are maintained around ϕ_{solids}=0.43. Sintering behavior for both inks is characterized. The appropriate flux concentration is determined to achieve successful co-sintering. Electron dispersive spectroscopy (EDS) is used to examine sintered composites and the interface between materials. Hardness testing is used to evaluate the mechanical properties of sintered LFBT specimens. Finally, electric properties of the LFBT are characterized.

6.2. Experimental Section

6.2.1. Materials

A BT powder (Ticon HPB, Ferro Electronics Corporation, Penn Yang, NY) with a particle size distribution of D_{10}=0.55 μm, D_{50}=1.21 μm, D_{90}=2.96 μm, a specific surface area of 2.7 m^2/g, a particle density of 5.95 g/cm^3, and a tap density 1.68 g/cm^3 is used as the ceramic phase. A Ni powder (ENP 800, Umicore, Fort Saskatchewan, Alberta, Canada) with a mean particle size 0.8 μm, a tap density of 4.0 g/cm^3, 0.15% carbon and 0.6% oxygen by weight, and specific surface area 0.9 m^2/g is used as the metal phase. Lithium acetate dihydrate ($LiAC{\cdot}2H_2O$) with a density 1.3 g/cm^3 (Li2O density 2.013 g/cm^3) (100 g, 62393, Sigma-Aldrich, St. Louis, MO), zinc borate ($2ZnO{\cdot}3B_2O_3{\cdot}3.5H_2O$) with a density 2.69 g/cm^3 (1 kg, 14470, Sigma-Aldrich, St. Louis, MO), zinc oxide (ZnO) (500g, 4358-01, Mallinckrodt Baker, Phillipsburg, NJ) with a density 5.606 g/cm^3 are used as fluxing agents. An aqueous solution of PAA-PEO comb-brush copolymer

(pH=4.4, 31.5% by weight) (Adva Flow Superplasticizer, W.R.Grace, Cambridge, MA) is adjusted to pH=8.2 and a concentration of 30% by weight using concentrated ammonia at a 1:27.8 weight ratio and then used as dispersant for aqueous ZnO and zinc borate suspensions. A 25% by weight aqueous solution of cationic nonlinear polyethylenimine (PEI-50K) with MW 50k-100k (ICN Biomedical, Aurora, OH) is used as flocculation agent for low-fire BT ink, and a 50% by weight aqueous solution of the same polymer is used as dispersant for Ni suspension. An 40% by weight aqueous solution of ammonium salt of anionic poly(acrylic acid) (MW=5000-6000, PAA-6K) (Darvan 821A, R.T. Vanderbilt Co., Norwalk, CT) is used as dispersant for BT; and an aqueous solution of anionic poly(acrylic acid) (MW=240k, 25% by weight of polymer) (PAA-240K) (Polysciences, Warrington, PA) is diluted to 20% and pH=8.2 using concentarted ammonia and DI water and then used as flocculation agent for BT/Ni composite ink. Hydroxypropyl methylcellulose (HPMC) (Methocel F4M, Dow Chemical Company, Midland, MI) 5% by weight stock solution in de-ionized (DI) water is used as viscosifier. DI water has a nominal conductivity 5×10^{-4} $(\text{ohm}\cdot\text{cm})^{-1}$. Paraffin oil (Ultra-Pure, Lamplight Farms, Menomonee Falls, WI) is used for oil bath. A mixture of 5% hydrogen with balance nitrogen is used as processing gas for sintering, and a high purity nitrogen gas is used for re-oxidation of BT.

6.2.2. Preparation of Colloidal Inks

An aqueous colloidal LFBT ink is prepared based on the $ZnO\text{-}B_2O_3\text{-}Li_2O$ sintering aids. The Ni'(m) phase is prepared in several BT:Ni ratios: 1:19, 3:37, 1:9, 1:4, and 3:7. The Ni'(m) inks are similar to those discussed in Chapter 5, but with $LiAC\cdot2H_2O$ dissolved in the aqueous medium. A fixed total solid volume fraction $\phi_{solids}=0.43$ is used

for all these inks. A non-contact planetary mixer (AR-250, THINKY, Tokyo, Japan) is used after each material addition in all the procedures involved. Due to the lengthiness of processing steps and various compositions involved, brief descriptions are provided in the following paragraphs, and detailed ink formulation is listed in Table 6.1.

Preparation of aqueous LFBT ink involves four steps. First, aqueous suspensions of BT, ZnO, and zinc borate powders are prepared separately with solid volume fraction calculated for each. Second, calculated amounts of BT, ZnO, and zinc borate suspensions are added together and mixed thoroughly. Third, appropriate amount of as-received crystalline lithium acetate dihydrate is added to the mixture and is expected to completely dissolve in the aqueous medium during process. Finally, an appropriate amount of 25% by weight PEI-50K stock solution, HPMC stock solution, and DI water are added to control rheological behavior. The PEI-50K is the flocculating agent for the suspension to counteract the dispersing behavior of Darvan 821A and the HPMC stock solution and DI water are controlled to achieve a HPMC concentration of 7 mg/mL in the aqueous medium and reach solid volume fraction ϕ_{solids}=0.43.

Preparation of Ni'(m) inks involves four steps. First, aqueous suspensions of BT and Ni are prepared separately with solid volume fraction calculated for each. Second, calculated amounts of BT and Ni are added together to achieve the desired BT:Ni ratio. Third, an appropriate amount of as-received lithium acetate dihydrate is added to the mixture and is expected to completely dissolve in the aqueous medium during processing. Finally, an appropriate amount of 25% by weight PEI-50K stock solution, HPMC stock solution, and DI water are added to control rheology. The PEI-50K is to flocculate the suspension while the HPMC stock solution and DI water are to achieve a HPMC

concentration of 7 mg/mL in the aqueous medium and reach solid volume fraction ϕ_{solids}=0.43. In this way, the aqueous colloidal Ni'(m) ink with proper rheology for Robocasting is prepared.

In the BT suspension, 7.5 mg of Darvan 821A per gram of BT powder is used as a dispersant. In the Ni suspension, 4.0 mg of 50% by weight PEI-50K solution per gram of Ni powder is used as dispersant. For ZnO suspensions, 13.5 mg Adva Flow solution is used per gram of powder; and for zinc borate suspensions, 22.4 mg Adva Flow solution is used per gram of powder.

Table 6.1 Formulations of aqueous colloidal inks for liquid phase sintering

1.	**Suspension preparation**					
a.	**BT suspension**			**b.**	**Ni suspension**	
	DI Water	8.500	g		DI Water	9.000	g
	Darvan 821A	0.450	g		PEI-50K (50% wt.)	0.400	g
	BT powder	60.000	g		Ni powder	100.000	g
	BT particle density	5.950	g/cm^3		Ni particle density	8.904	g/cm^3
	Solid volume fraction	0.530			Solid volume fraction	0.544	
	total weight	68.950	g		total weight	109.800	g
	total volume	19.034	mL		total volume	21.031	mL
	BT volume	10.084	cm^3		Ni volume	11.231	cm^3
c.	**ZnO suspension**			**d.**	**Z.B. suspension**	
	DI Water	5.000	g		DI Water	5.000	g
	Adva Flow (20% wt.)	0.393	g		Adva Flow (20% wt.)	0.317	g
	ZnO powder	29.089	g		Z.B. powder	14.128	g
	ZnO particle density	5.606	g/cm^3		Z.B. particle density	2.690	g/cm^3
	Solid volume fraction	0.490			Solid volume fraction	0.497	
	total weight	34.482	g		total weight	19.445	g
	total volume	10.582	mL		total volume	10.569	mL
	ZnO volume	5.189	cm^3		Z.B. volume (Z.B.=zinc borate)	5.252	cm^3
2.	**LFBT ink preparation**					
	BT suspension	68.950	g			
	ZnO suspension	0.37	g			
	Zinc borate suspension	1.82	g		Flux concentration:	
	LiAC·2H2O	1.64	g		ZnO	1.43%	wt.
	HPMC (5% wt.)	1.96	g		B2O3	0.75%	wt.
	PEI-50K (25% wt.)	0.34	g		Li2O	0.38%	wt.
	DI water	2.093	g			

This table continues to the next page.

Table 6.1 Formulations of aqueous colloidal inks for liquid phase sintering (continued)

3.	**Ni'(m) inks**					
a.	**BT:Ni=1:19**			**b.**	**BT:Ni=3:37**	
	BT suspension	6.838	g		BT suspension	6.838 g
	Ni suspension	39.106	g		Ni suspension	39.106 g
	LiAC·2H2O	0.67	g		LiAC·2H2O	0.67 g
	HPMC (5% wt.)	0.947	g		HPMC (5% wt.)	0.947 g
	Darvan 821A	0.174	g		Darvan 821A	0.162 g
	PAA-240K (25% wt)	0.13	g		PAA-240K (25% wt)	0.13 g
	DI water	0.96	g		DI water	0.97 g
c.	**BT:Ni=1:9**			**d.**	**BT:Ni=1:4**	
	BT suspension	3.419	g		BT suspension	6.838 g
	Ni suspension	43.994	g		Ni suspension	39.106 g
	LiAC·2H2O	0.67	g		LiAC·2H2O	0.67 g
	HPMC (5% wt.)	0.947	g		HPMC (5% wt.)	0.947 g
	Darvan 821A	0.15	g		Darvan 821A	0.1 g
	PAA-240K (25% wt)	0.13	g		PAA-240K (25% wt)	0.13 g
	DI water	0.98	g		DI water	1.039 g
e.	**BT:Ni=3:7**					
	BT suspension	6.838	g			
	Ni suspension	39.106	g			
	LiAC·2H2O	0.67	g			
	HPMC (5% wt.)	0.947	g			
	Darvan 821A	0.048	g			
	PAA-240K (25% wt)	0.13	g			
	DI water	1.113	g			

6.2.3. Rheological Characterization

For the LFBT and Ni'(m) inks, oscillatory measurement is used to characterize rheological behaviors. A Bohlin C-VOR 200 rheometer with the C14 serrated cup and bob geometry is used. Temperature is fixed at 23 °C and a solvent trap is used to minimize water evaporation. The ink is first subject to a 15 minute oscillatory pre-shear at 1Hz with a controlled shear stress at 0.02 Pa, then undisturbed for 15 minutes. Afterwards, an increasing shear stress (τ) ranging from 1 Pa to 1000 Pa is applied. Complex shear modulus (G^*) is measured as a function of stress amplitude, but elastic shear modulus (G') is the only data reported. The yield stress (τ_y) of the gel is taken as the stress magnitude where G' dropped to 90% of the maximum value during a stress sweep experiment starting from low stress.

6.2.4. Sintering Study

After printing square shaped lattice specimens for each ink composition, these specimens are fired in a reducing atmosphere. After cooling, the sintering strain ε of each specimen is measured for sintering shrinkage study

$$\varepsilon = 1 - \frac{L_f}{L_o}$$

where L_o and L_f are the length of green and sintered lattices respectively (L_o = 10.6 mm). This treatment has already been used in Chapter 5 to study sintering shrinkage of BT and Ni(m) inks by solid state sintering. Specimens with a dimension of 10.6×10.6×4 mm for each ink composition listed in Table 6.1 are printed with a lattice pattern, using Ø=0.25mm nozzle (5125-0.25-B, EFD, East Providence, RI) with 0.20 mm layer

thickness. Each layer of the structure consists of a parallel array of filaments printed in a serpentine pattern and aligned with the *x* or *y* axis in alternating layers. For comparison purpose, also used are Ni(m) inks that have the same BT:Ni ratios and solid volume fraction but no LiAC2H $_2$O addition. These BT-Ni inks are similar to those described in Chapter 5, so the details of composition and processing are not repeated here.

After drying, binder burnout is performed at 260 °C in a tube furnace (Thermolyne F21100, Barnstead International, Dubuque, Iowa) for 8 hours. Subsequently, specimens of each composition are fired in a tube furnace (GSL 1600X, MTI Corporation, Richmond, CA) to peak temperature at 700 °C, 800 °C, 900 °C, and 1000 °C with an isothermal hold of 2 hour, and then cooled down to room temperature. Heating ramp rate is 5 °C/min. At the beginning of each firing procedure, two cycles of vacuuming and flushing are used to purge air out of the tube furnace. A mass flow controller (Tylan FC-260, Entegris, Chaska, Minnesota) with a maximum flow rate of 200 standard cubic centimeters per minute (sccm) at room temperature is used for controlling the processing gas flow rate. The $5H_2/95N_2$ mixture is bubbled through water and then fed through the tube furnace. By adjusting its flow rate, oxygen partial pressure in the tube furnace may be adjusted to prevent Ni from oxidation with negligible reduction to BT. A typical flow rate is in the range from 50-100 sccm.

6.2.5. Fabrication of BT-Ni Composites

Specimens with abrupt transitions in composition are created by serial printing using the LFBT alongside Ni'(m) inks. Binder removal for the composites is carried out in air (Thermolyne F21100, Barnstead International, Dubuque, Iowa) for 8 hours at

260 °C. Co-sintering of BT-Ni'(m) green structures is performed with a 2 hour isothermal hold at 1000 °C in the tube furnace (GSL 1600X, MTI Corporation, Richmond, CA), as shown in Figure 6.1. The 2 hour isothermal hold at 600 °C is intended to ensure complete decomposition of $LiAC{\cdot}2H_2O$ to form Li_2O.[167] A 5 °C/min temperature ramp rate is used to heat the furnace to 600 °C and a 2.5 °C/min temperature ramp rate is used from 600 °C to 1000 °C. The slower ramp rate is intended to mitigate possible temperature gradient in the sample structure. Controlled sintering atmosphere involves the use of either dry N_2 gas or moist $5\%H_2/95\%N_2$ gas mixture. The latter will require a subsequent re-oxidation step in dry N_2 atmosphere at 800 °C for 24 hours or longer.

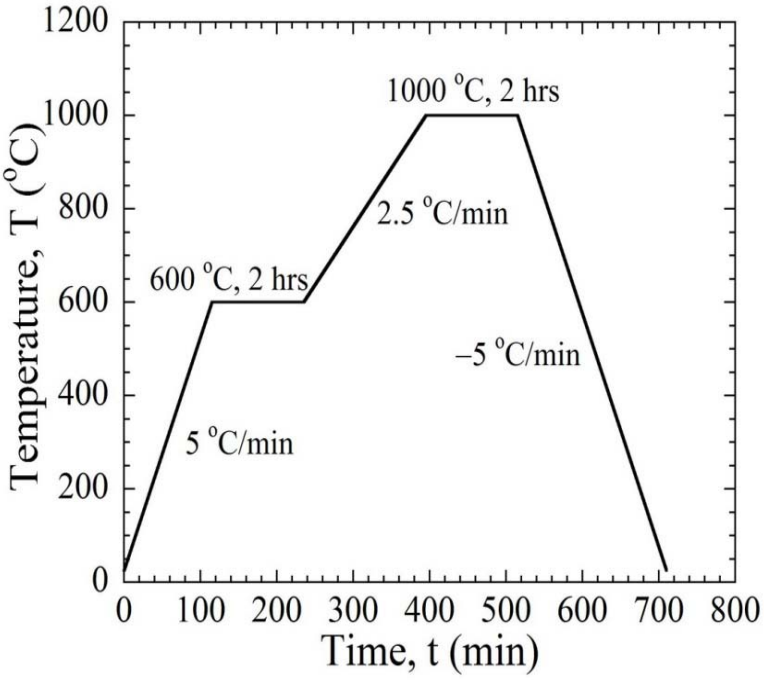

Figure 6.1 Temperature profile used for liquid phase sintering of BT-Ni composites.

6.2.6. Hardness Test

Microindentation Vickers test (0.5 kgf load for 5 seconds) is used to measure hardness of LFBT composites. Cylindrical rod specimens are sintered in moist H_2/N_2 gas at 1000 °C for 2 hours according to Figure 6.1. In preparation for hardness test, these specimens are cross-sectioned using a diamond saw (Labcut 1010, Extec, Enfield, CT), embedded in epoxy resin, and then polished (Labpol 8-12, Extec, Enfield, CT) with diamond pastes at 3 to 0.25 μm particle size (DiaDuo, Struers, Denmark).

6.2.7. Energy Dispersive Spectroscopy (EDS) Characterization

EDS is used to examine the element distribution in sintered composite structures. Composite lattice structures resembling MLCCs, similar to those shown in Figure 5.9, are assembled by co-printing the LFBT and low-fire 20BT80Ni/LiAC composite inks. The sintered specimen is embedded in epoxy resin and diced using a diamond saw (Labcut 1010, Extec, Enfield, CT). Afterward, the cross-section of the specimen is polished (Labpol 8-12, Extec, Enfield, CT) with particle size=9, 3, and 0.25 mm diamond pastes (DiaDuo, Struers, Denmark). Energy dispersive spectrometry (FEI Quanta 600 field emission gun ESEM with Evex EDS, Hillsboro, Oregon) is used for the examination.

6.2.8. Piezoelectricity and Dielectric Constant

Square LFBT specimens (16×16×4 mm) are printed using a space-filling pattern and sintered (LHT 02/17, Nabertherm GmbH, Lilienthal, Germany) in air at 1000 °C for 2 hours for electric characterization. Top and bottom surfaces of these specimens are polished with particle size=9, 3, and 0.25 mm diamond pastes. Electrodes layers are gold sputter-coated for poling at 7 kV, and piezoelectric coefficient is measured afterwards.

Measurement of dielectric constant is carried out in the frequency range of 1 Hz to 1 MHz and temperature range of −60 °C to 160 °C.

6.3. Results and Discussion

6.3.1. *Preparation of Colloidal Inks*

The sintering aids are added in ways best suited to handling properties. The colloidal LFBT ink is prepared by blending sintering aids into aqueous suspension of BT, followed by rheological adjustment with the use of high molecular weight polyelectrolyte PEI-50K. In the LFBT ink, the sintering aids composition is chosen to be $ZnO:B_2O_3:Li_2O=1.425:0.75:0.375$ by weight, i.e., a total of 2.55% by weight sintering aids with 97.45% by weight BT in a sintered ceramic. This specific composition is achieved by adding calculated amounts of zinc oxide, zinc borate and LiAC·2H $_2$O. Each Ni'(m) ink is a hetero-gel of blended aqueous suspensions of BT and Ni, with a predetermined BT:Ni ratio and a concentration of LiAC in the aqueous medium. The key in this preparation stage is to homogenously blend calculated amounts of sintering aids into the BT and Ni'(m) inks without deteriorating the usability of these inks for Robocasting process. The following discussions in this regard are focused on four aspects: 1) addition of sintering aids to colloidal BT suspension, 2) addition of $LiAC·2H_2O$ to Ni(m) suspension, 3) the effect of high LiAC concentration on ink preparation, and 4) the use of high molecular weight PEI-50K and PAA-240K for rheological adjustment.

First, ZnO and zinc borate powders have limited solubility in water, and may be dispersed in aqueous BT suspension. In this regard, these components simply act as a minor colloidal phase alongside the BT particles. Figure 6.2 shows the scanning electron

micrographs for these two powders. The ZnO and zinc borate powders have particle sizes in the range of 2μm to ≈0.1μm in diameter. The zinc borate appears to have a wider particle size range. The use of PAA-PEO comb-brush copolymer Adva Flow is able to create solid volume fraction >49% with low viscosity for both ZnO and zinc borate suspensions. Adva flow is a comb co-polymer with anionic polelectrolyte backbone and non-ionic polyethylene oxide side chains. The dispersion mechanism is by strong adsorption of the backbone to the particle surface and steric hinderance to flocculation.[168-171] Subsequent rigorous mixing presumably allows homogenous distribution of these two sintering aids in the BT suspension. The non-ionic nature of the side chains means the ZnO and zinc borate colloids will be passive inclusions in the BT colloidal gel. Other the other hand, $LiAC{\cdot}2H_2O$ has mm-scale crystal size and a solubility of 40.8 g/100 mL in water at 20 °C. Hence, $LiAC{\cdot}2H_2O$ is directly added and dissolved in the aqueous medium of colloidal suspension. By calculation, the $LiAC{\cdot}2H_2O$ dissolved in a BT ink at room temperature allows a maximum concentration equivalent to around 0.375% by weight of Li_2O in the final sintered low fire BT ceramic. As a Li_2O concentration higher than 0.375% by weight is difficult to achieve, the original eutectic concentration of $ZnO:B_2O_3:Li_2O=1.91:1.01:0.5$ by Randle et al[167] is multiplied by a factor of 0.75 so that the sintering aids concentration becomes $ZnO:B_2O_3:Li_2O=1.425:0.75:0.375$ by weight. Mathematical calculations based on simple chemistry and known information will lead to proper quantities for each materials involved.

1) 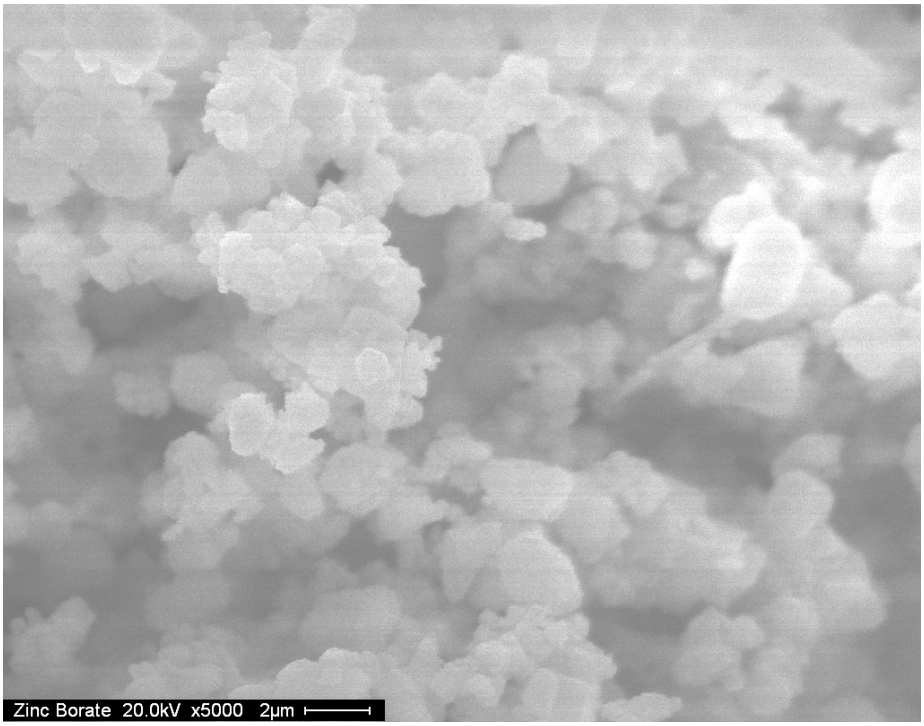

2) 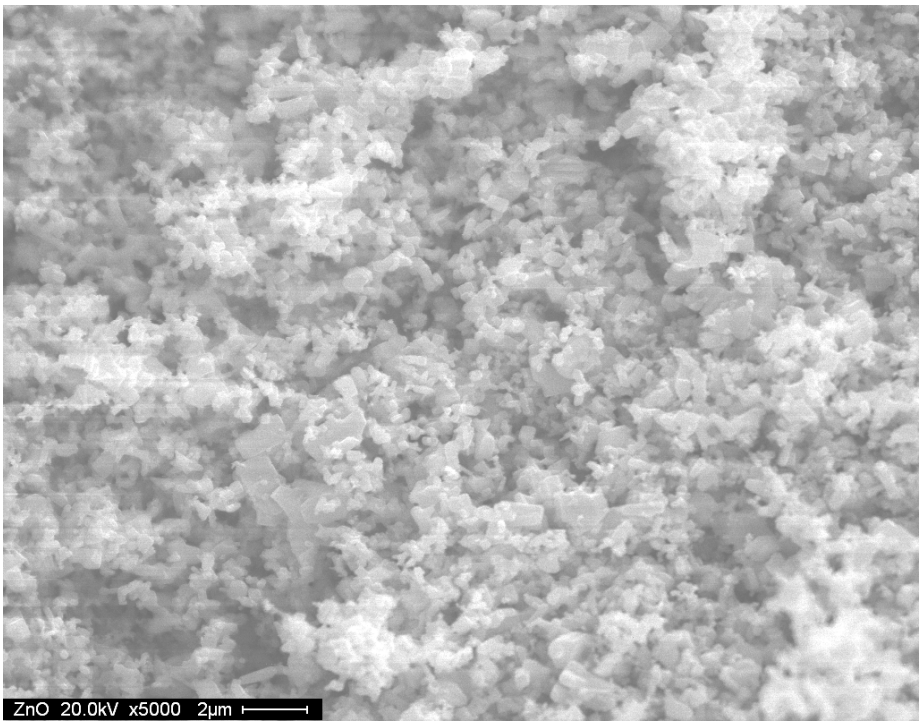

Figure 6.2 Scanning electron micrographs of ZnO and zinc borate powders: a) zinc borate powder, and b) ZnO powder. (Gratitude goes to Yu, Di)

Second, the added $LiAC{\cdot}2H_2O$ is amenable to the ink preparation concept used in Robocasting. Salt addition has been a strategy to formulate aqueous colloidal ceramic gels. Usually, the added salt is either a fugitive composition during heating process, or a constituent element of the ceramic system, or both. An example is $BaCl_2$ addition for BT inks,[105] where $BaCl_2$ is used to flocculate the aqueous BT suspension. In this study, the primary function of added Li^+ is to serve as a low melting temperature flux that stimulates mass transfer during the sintering process for the ceramic phase. And the acetate group is a fugitive content during sintering process. Nevertheless, their effect of flocculating BT and Ni(m) suspensions is obvious. An increase in viscosity occurs after $LiAC{\cdot}2H_2O$ addition, indicating flocculated particle networks. As LiAC is a monovalent salt and a less effective flocculation agent,[105] the resulting colloidal gels has a low elastic behavior and requires rheological adjustment. This is achieved by subsequent addition of polyelectrolyte, i.e. PEI-50K in the LFBT ink, and PAA-240K and Darvan 821A in the Ni'(m) inks.

Third, the only purpose of LiAC in the Ni'(m) ink is to balance Li^+ concentration for the LFBT and Ni'(m) inks. Consider the scenarios when LFBT ink is co-printed with a Ni(m) ink that contains no LiAC concentration in the form of a composite ensemble, there would be a concentration gradient of Li^+ between the LFBT ink and Ni(m). $Li^+(aq)$ will diffuse from the LFBT to the Ni(m) component. The outcome is that the initial concentration in the LFBT decreases and the final Li concentration in a composite structure depends on volume ratio of both inks, provided that a homogeneous concentration of $Li^+(aq)$ may be achieved within the as-printed composite ensemble. To maintain Li_2O concentration in the ceramic phase required for liquid phase sintering, this

diffusion process is inhibited by providing an equal $Li^+(aq)$ concentration in the Ni'(m) colloidal ink.

Finally, the addition of high molecular weight PEI-50K and PAA-240K leads to stronger flocculation and proper ink rheological behaviors with addition of DI water and HPMC stock solution. The PEI-50K is a highly branched aliphatic polyamine that contains primary, secondary, and tertiary amine groups in a B1:2:1 ratio and possesses a spherical morphology[172] with a calculated size of 12 nm in an infinite dilute aqueous solution.[105] The high ionic concentration may reduce its hydraulic radius, but likely to a limited extend due to its branched spherical morphology. It is also known that PEI in the size range of 7-12 nm may effectively flocculate ceramic suspensions and the resulting gels exhibit minimal difference in shear stress-dependent G' behavior.[105] It is postulated that the PEI-50K molecules may patch between Darvan 821a (PAA-6K) coated ceramic particles and lead to stronger flocculation for this LFBT gel in presence of a high salt concentration. Similarly, the use of high molecular weight PAA-240K allows effective adjustment of rheology for the Ni'(m) inks containing high LiAC concentration. Due to its high molecular weight, the PAA-240K has a size enough to cause strong flocculation, but significantly increases the viscosity of the ink as well. Thus, Darvan 821A (PAA-6K) and PAA-240K solutions at appropriate ratios are used to adjust the composite ink to proper ink rheology.

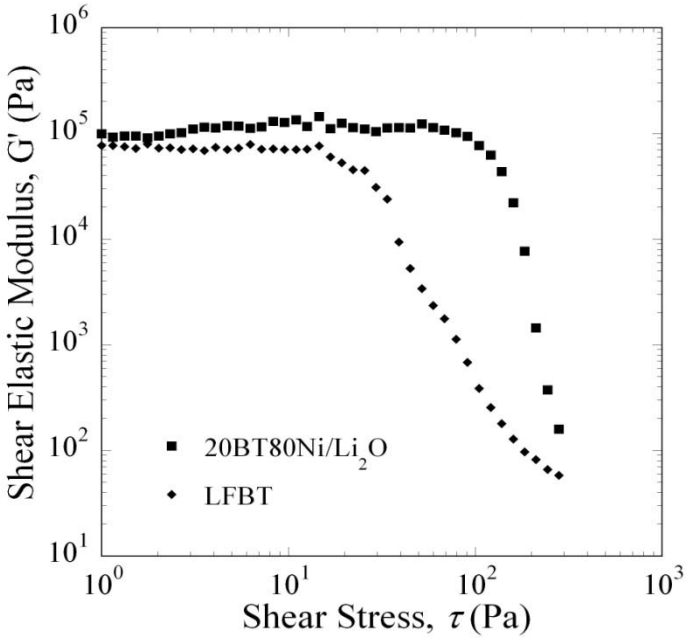

Figure 6.3 Oscillatory behavior for the ϕ_{solids}=0.43 LFBT ink and 20BT80Ni composite ink: G' as a function of τ.

6.3.2. *Rheological Characterization*

The LFBT and a Ni'(m) ink with BT:Ni=1:4 have similar rheological behaviors to the pure BT and Ni(m) gels described in Chapter 5 (seen Figure 5.4) respectively. Figure 6.3 shows the shear elastic modulus G' as a function of shear stress τ for these two inks. The LFBT ink has a storage modulus around 70kPa, and a yield stress around 20Pa; the 20BT80Ni/Li_2O has a storage modulus of around 120kPa, and a yield stress around 100 Pa.

6.3.3. *Sintering Study*

In assessing the suitability of LFBT and Ni'(m) formulations for successful co-sintering of composite structures, two approaches are taken. First, the sintering strain ε

for independent structures of LFBT and various Ni(m) and Ni'(m) compositions are evaluated after a constant heating and cooling rate experiment. Here, the temperature is raised to a maximum value and then cooled and the dimensions of the sample are measured. Quantitative comparison is made between the composition dependent ε at various temperatures for Ni(m), Ni'(m) and LFBT. The second method is direct observation of the structural integrity of composite lattice structures after sintering and cooling. The criterion for success or failure is somewhat subjective here, but warping and cracking are taken as signs that the composition is not suitable for producing quality components.

When sintered separately, all Ni(m) and Ni'(m) specimens demonstrate noticeable differences in ε from LFBT specimens. Figure 6.4a shows the ε of fired LFBT and several Ni(m) compositions as a function of temperature and Figure 6.4b shows the ε of fired LFBT and several Ni'(m) compositions as a function of temperature. For these ϕ_{solids}=43% inks, $0 < \varepsilon < 0.245$, where the value 0.245 corresponds to complete densification, and the value 0 corresponds to as-printed length. Figure 6.5 shows the samples of fired LFBT and Ni'(m) lattices used to generate Figure 6.4b. However, co-sintering of composite structures assembled using those inks demonstrate different results. Disrupted structures and local cracks are observed in composite structures assembled with LFBT and Ni(m) inks, while those assembled with LFBT and Ni'(m) inks containing 20%-30% solid volume fraction BT are largely free from structural distortions or local cracks. An explanation to this difference includes 1) diffusion of Li^+ in as-printed composite ensembles, and 2) phenomena occurring in liquid phase sintering.

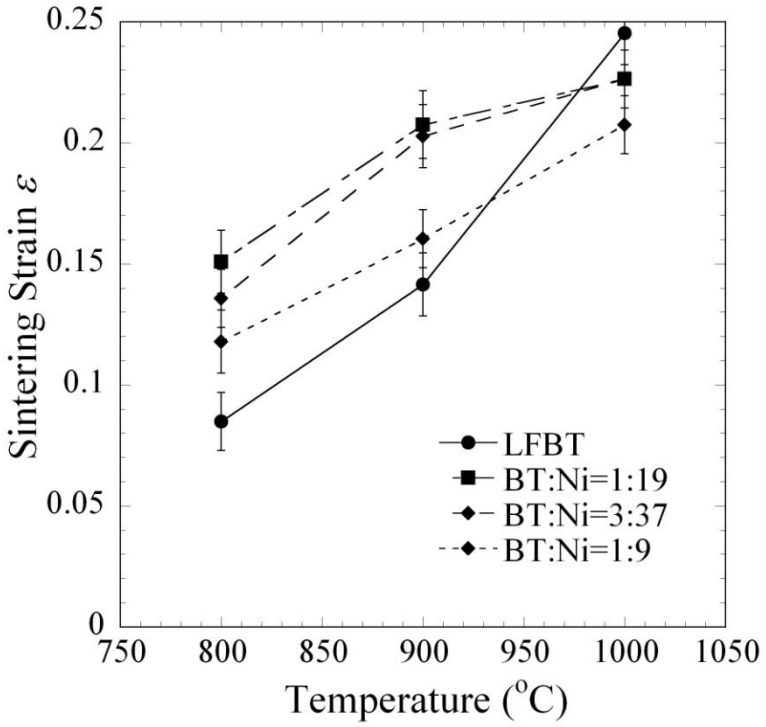

a)

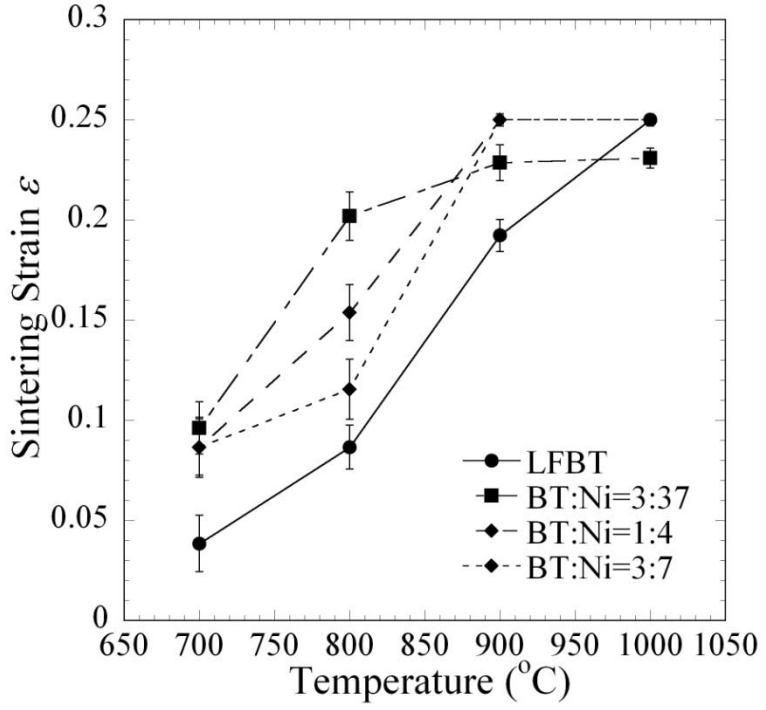

b)

Figure 6.4 Sintering strain comparison: ε as a function of temperature for fired square lattices printed with a) LFBT and Ni(m) inks, and b) LFBT and Ni'(m) inks.

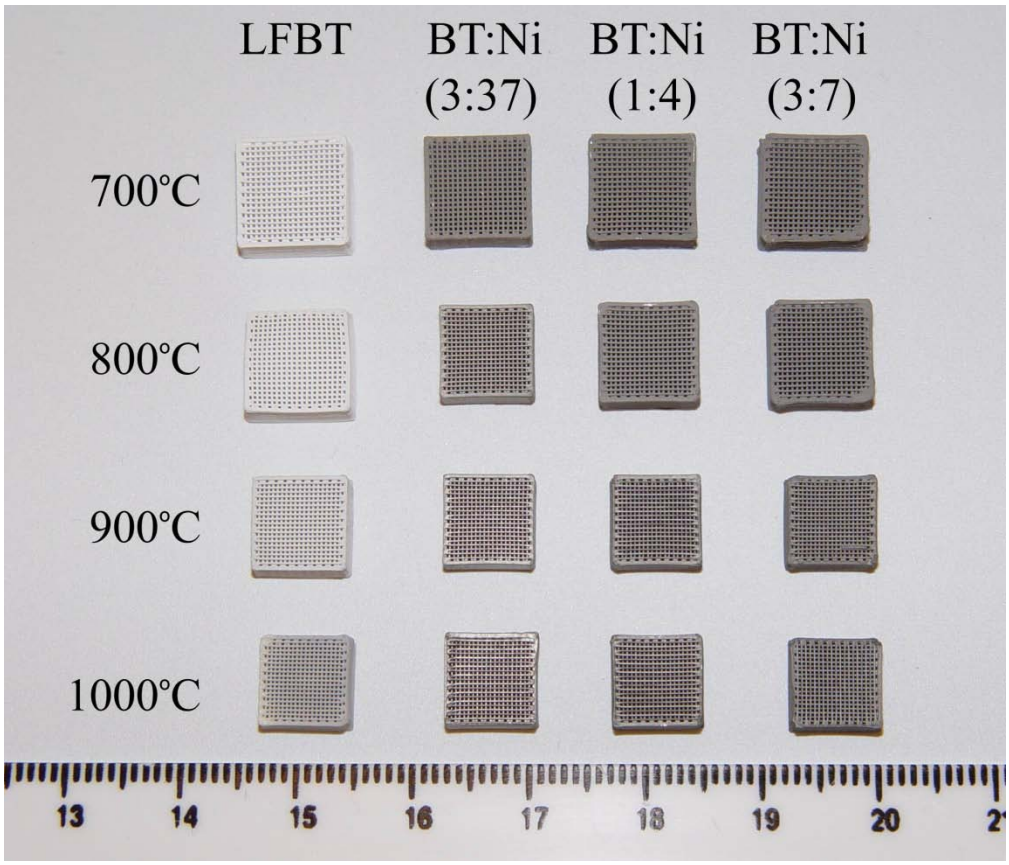

Figure 6.5 Optical image of the separately fired LFBT and Ni'(m) lattices. These lattices are singled out from a larger population. The averaged length is used to calculate sintering strain ε in Figure 6.4b. The lattices in each column are of the same composition, but fired at different temperatures with a 100 °C interval.

As already mentioned in the discussion section for ink preparation, a concentration gradient of Li^+ between LFBT and Ni(m) within a composite structure will lead to migration of Li^+ to the Ni(m) region. After firing, the expected result is a smaller ε of an LFBT component than what is indicated in Figure 6.4a. ZnO and B_2O_3 binary mixture has a eutectic region >961 °C (phase diagram is shown in the Appendix E). Without enough Li_2O, their function as a sintering aid is hampered, especially at lower temperatures. In another words, there is no enough liquid phase formation to promote fast

mass transport in LFBT network.[167] Sintering stress may not be adequately alleviated by particle rearrangement due to lack of enough liquid phase. Eventually, sintering strain mismatch will lead to local distortions and cracks in the composite structures. Figure 6.6 shows a deformed and cracked MLCC lattice structure due to use of Ni(m) ink.

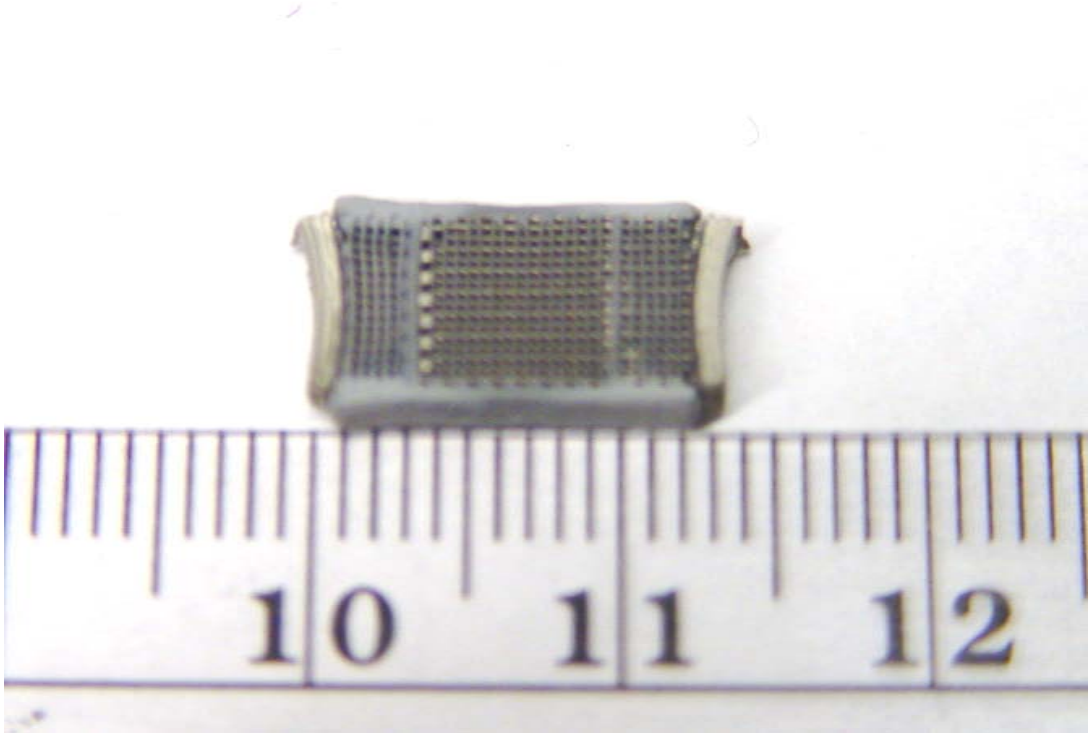

Figure 6.6 A cracked and distorted MLCC lattice assembled with the LFBT ink and BT-Ni ink containing no Li^+ concentration.

The Li^+ content in the LFBT is balanced by the Li^+ concentration in the Ni'(m) ink, allowing for successful co-sintering of composite structures with BT:Ni ratios ranging from 1:4 to 3:7 despite the noticeably different sintering shrinkage observed for these compositions, as indicated in Figure 6.5. The likely explanation for this success is that during the sintering process, a sufficient quantity of Li_2O in the LFBT component forms

the ZnO-B_2O_3-Li_2O eutectic system and leads to increased sintering rate of LFBT to match that of Ni'(m). Although this is not obvious from the observations of Figure 6.5, the liquid phase between particles in the LFBT may allow for stress relaxation during the isothermal holds. At the sintering temperature, the BT particle network demonstrates plasticity,[38] and stresses are alleviated by plastic deformation of the particle network.

A direct proof of this point is the LFBT lattice fired at 800 °C, as shown in Figure 6.5. This LFBT lattice has rounded edges at a macroscopic level; and at a microscopic level, relative positions between relevant particles must have shifted or rearranged. The likely cause of this deformation is the temperature gradient within the particle network. As melting absorbs heat, the outer portion must have liquid formation prior to melting of sintering aids located at inner portion of the lattice. It also suggests that melting of sintering aids starts around this temperature. Nevertheless, after fired at higher temperatures, i.e. 900 °C, and 1000 °C, the rounded edge disappears and the lattice returns to square shape. This indicates that even plastic deformation occurs during liquid phase sintering process, the initially defined geometric characteristics may be restored after sintering process completes. These lattices are pressureless sintered in a tube furnace at atmospheric pressure, so the restoring effect is by the sintering process itself. This validates the use of liquid phase sintering for near net shaping through Robocasting, provided that the volume of liquid phase formed during sintering is much less than solid phase so as not to generate free liquid volume and cause unwanted viscous flow of the particles. In this work, the volume of ZnO-B_2O_3-Li_2O sintering aids is estimated to be ~5% of total ceramic volume in sintered LFBT.

The above discussion is mainly focused on the sintering behavior of LFBT. On the other hand, sintering of Ni particles in the composite structure proceeds differently. As Ni particles are insoluble in the ZnO-B_2O_3-Li_2O liquid phase, and have a sintering temperature of 900 °C, densification of Ni matrix should follow the solid state sintering model. Neck formation of the percolating Ni particle network is likely to occur at the early stage of the sintering process. This is obvious by comparing the specimens fired at 800 °C. The BT:Ni=3:37 Ni'(m) lattice demonstrates a significant sintering strain, indicating that neck formation of Ni particle network had already occurred at a lower temperature. Neck formation of Ni particles in lattices of BT:Ni=1:4 and 3:7 Ni'(m) must have occurred, but their sintering strain is resisted by a higher refractory BT inclusion. Nevertheless, the expected result is the formation of interlocked Ni particle network in these lattice specimens. Hence, the structure of Ni'(m) components with a high Ni content in a composite structure is relatively fixed as compared to the LFBT components, and stress relaxation during densification must largely be accomplished by particle rearrangement in the LFBT components.

6.3.4. *Fabrication of BT-Ni Composites*

Heterogeneous BT-Ni composite structures have been successfully fabricated with the use of the LFBT ink for ceramic components, and either the BT:Ni=1:4 or 3:7 Ni'(m) ink for metal components. A thorough screen of all possible compositions is not done, but presumably any composition between BT:Ni=1:4 and 3:7 is compatible to the LFBT ink. All these composite structures have slight deformation compared to the original CAD designs, due to the pulling effect by the moving nozzle tips during ink-printing process and the internal stresses involved throughout the sintering process. The

successes in fabricating these composite structures suggest that liquid phase sintering is a useful technique for freeform fabrication of heterogeneous ceramic metal composite structures. Figure 6.7 demonstrates a MLCC lattice assembled with the LFBT ink and BT:Ni=1:4 Ni'(m) ink, where the metallic electrode filaments are in silver color, and the LFBT is in light gray color due to loss of oxygen atoms during reducing atmosphere sintering. The low BT inclusion in the electrodes and terminations allows for good electric conductivity and a reasonable mechanical ductility.

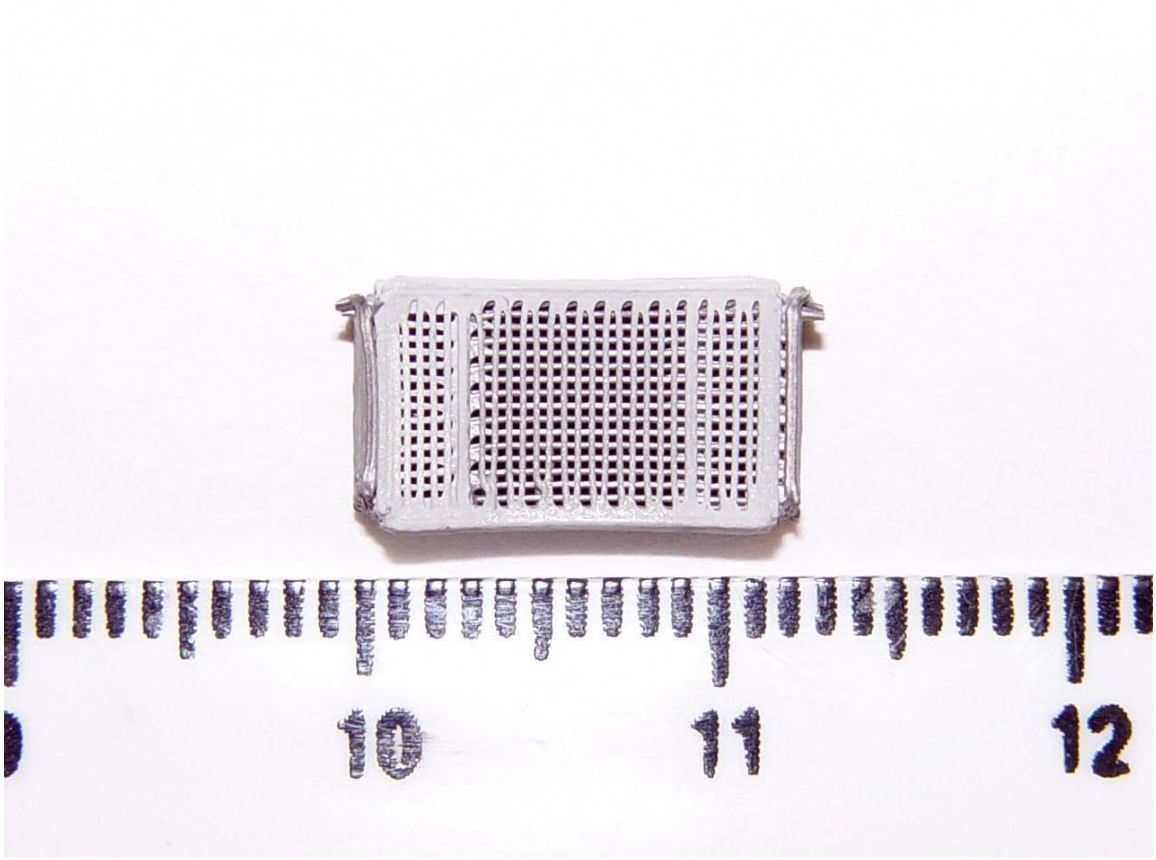

Figure 6.7 A sintered MLCC lattice assembled with the LFBT ink and BT:Ni=1:4 Ni'(m) ink.

Figure 6.8 shows the bowtie-shaped negative Poisson's ratio (NPR) capacitor arrays. Again, these bowtie structures are 2-D simplification of the proposed 3D NPR network containing metallic struts for non-linear load deformation mechanical behavior and BT nods for piezoelectric response. The one on the left has dark LFBT components in partially reduced state, due to loss of oxygen atoms during reducing atmosphere sintering. The sliver-colored elements are the metallic component of BT:Ni=1:4 Ni'(m). The one on the right is a similar structure, but after re-oxidation (annealing) to reduce oxygen vacancies in the LFBT phase. The LFBT turns into its normal yellowish color, and the electrodes turn into dark color due to formation of NiO. But the NiO formed is only a thin surface layer; and the electrodes remain conductive. This re-oxidation step is a common practice in MLCCs industry to prolong device life. The annealing time depends on many factors, including oxygen partial pressure during annealing, dimension of the LFBT ceramic, and geometric confinement such as electrodes that constrain the boundary condition for oxygen diffusion. In Figure 6.9, a similar NPR capacitor array is sintered in N_2. It has the LFBT components in yellowish color and the NPR electrodes electrically conductive, similar to the one in Figure 6.8 after re-oxidation. Figure 6.10 shows another arrangement of a 2-D NPR composite structure where parallel arrays of NPR bowtie LFBT and BT:Ni=3:7 Ni'(m) stripes are joined at the very ends of extending thin walls of stacked filaments from both sides. This NPR composite structure has another form of the proposed nonlinear load deformation electromechanical behaviors.

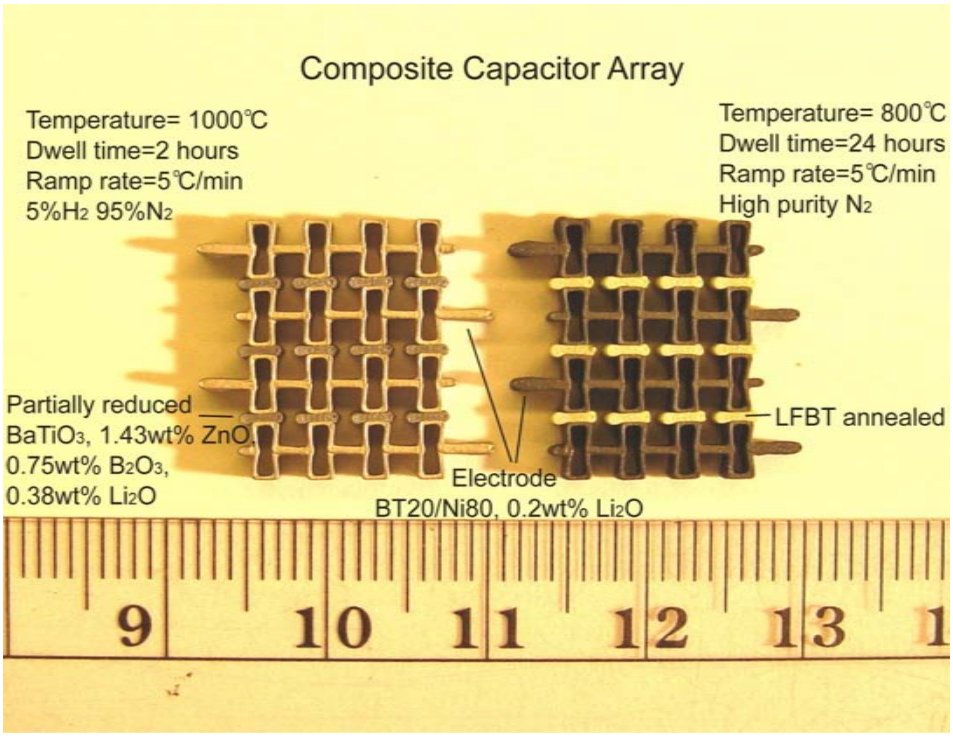

Figure 6.8 Composite capacitor arrays before (left) and after (right) re-oxidation of sandwiched LFBT dielectric. (scale in centimeter)

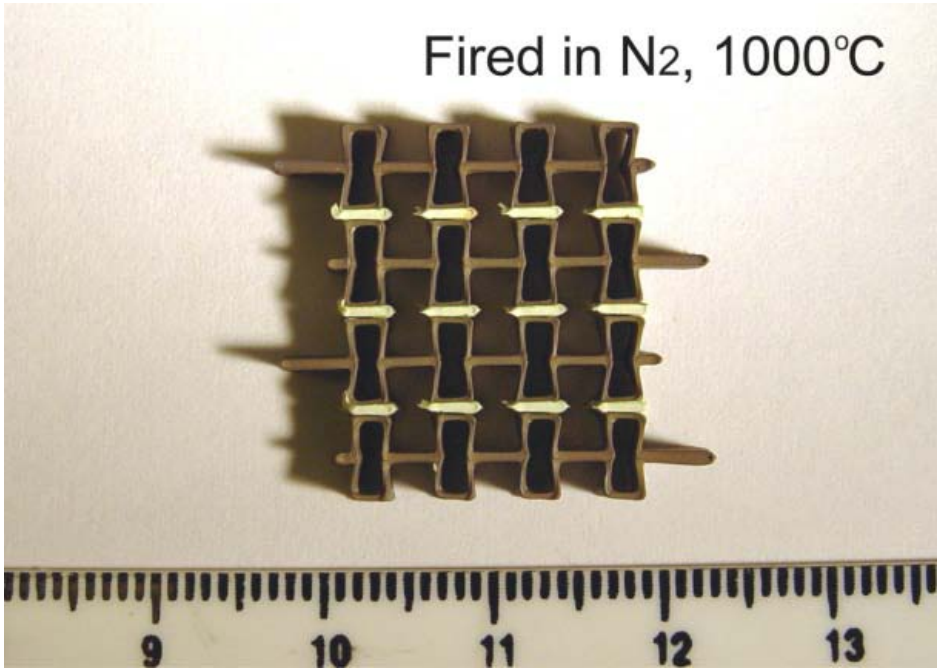

Figure 6.9 An NPR composite array sintered in dry N_2 at 1000 °C. (scale in centimeter)

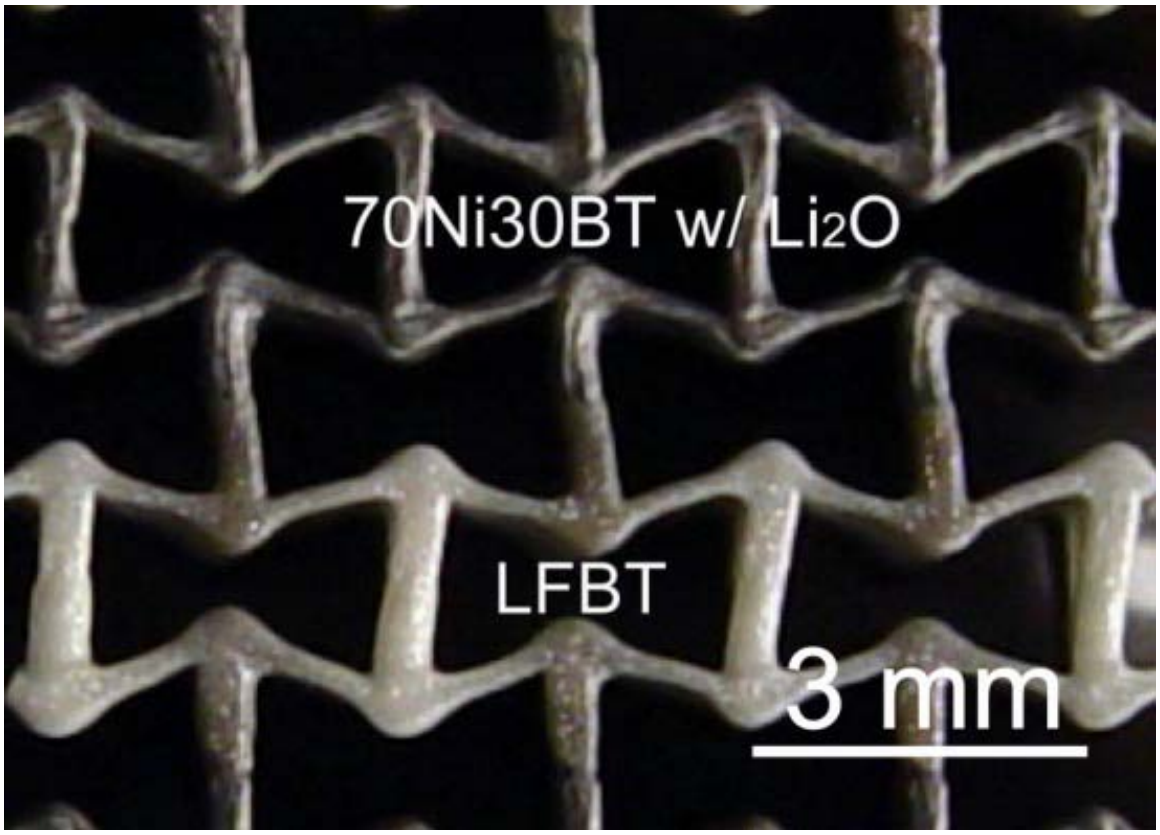

Figure 6.10 A NPR composite of parallel LFBT and 30BT70Ni/Li_2O bowtie stripes that are joined at the ends of extending thin walls of stacked filament from both sides.

The LFBT and Ni'(m) inks described here have demonstrated good compatibility in terms of printing, drying, and sintering behaviors, and would likely allow for successful fabrication of the proposed 3-D NPR composite networks described in Chapter 2. However, a specifically designed ink-printing algorithm for this purpose has yet to be developed.

6.3.5. *Hardness Test*

A Vickers hardness number VPN479 is observed for the LFBT specimen, higher than the predicted value of VPN387 for pure (but porous) BT. Figure 6.11 shows a

scanning electron micrograph of a pyramidal indent on a sintered LFBT specimen. The average diagonal distance used for the hardness calculation is 44 μm, which yields a Vickers hardness number VPN479. This hardness is 23.8% greater than the value (VPN387) from extrapolation of the BT-Ni composite hardness data in Chapter 5. The higher hardness value here is probably due to the higher sintered density of the LFBT specimen, in comparison to the 91%-96% theoretical density for the BT/Ni specimens where the porosity allows more plastic deformation.

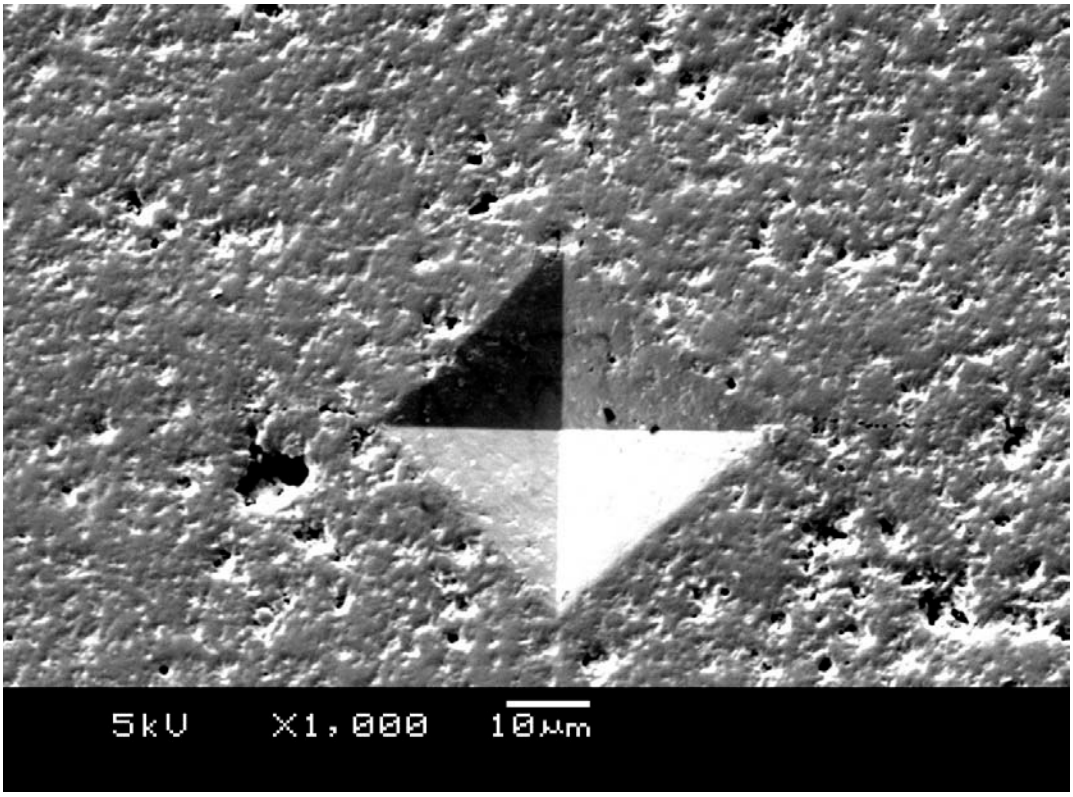

Figure 6.11 SEM of a pyramidal indent on a sintered LFBT specimen

6.3.6. *Energy Dispersive Spectroscopy (EDS) Characterization*

Examination by EDS reveals that LFBT and BT:Ni=1:4 Ni'(m) components have good cohesion and form an integral device. There is no noticeable inter-diffusion

between BT and Ni phases. But Zn element is detected in the BT:Ni=1:4 Ni'(m) component, indicating mass transport of the liquid phase from the LFBT to the BT:Ni=1:4 Ni'(m) component during sintering process. This migration of liquid phase is likely due to the BT inclusions in the Ni'(m) component that allow spreading of liquid phase through the percolating BT network in Ni'(m). Figure 6.12 shows an optical image of cross-section of the specimen examined by EDS.

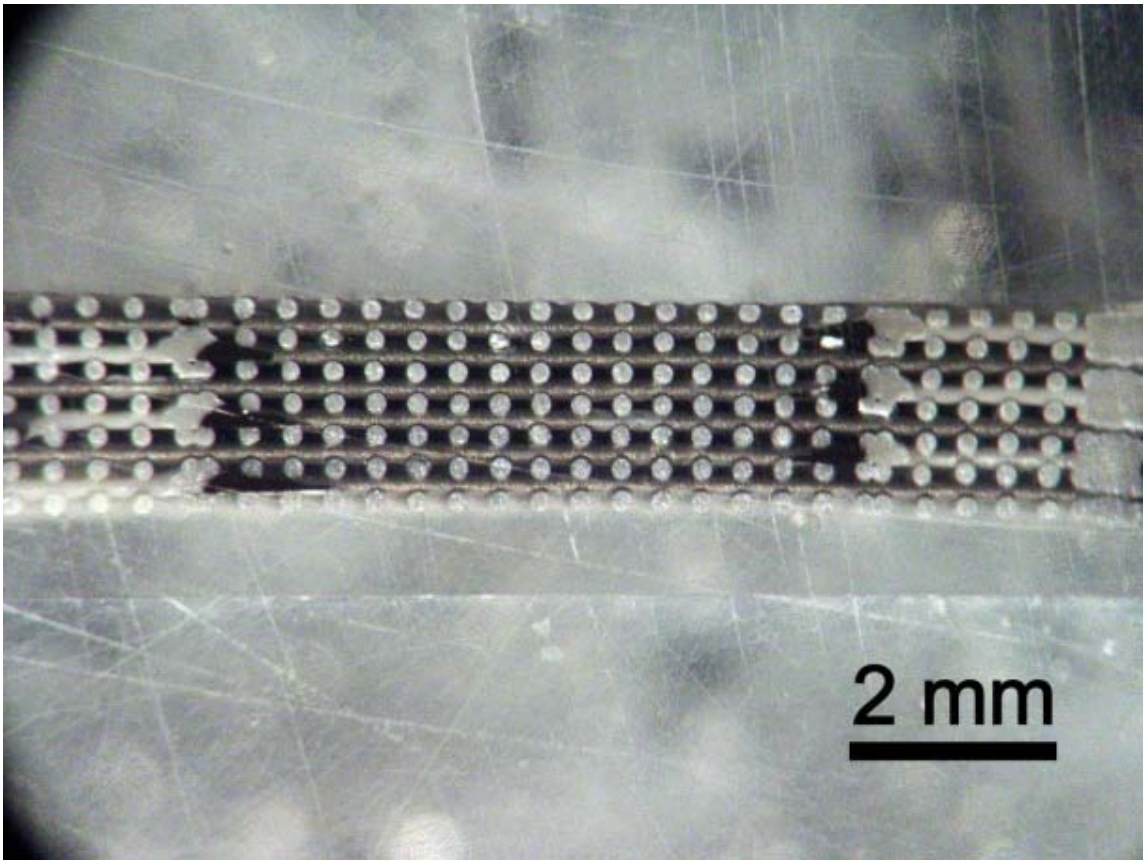

Figure 6.12 Optical image of the cross section of a MLCC lattice for EDS examination. The specimen is embedded in epoxy for handling. The dark grey colored filaments are BT:Ni=1:4 Ni'(m) and the ivory colored filaments are LFBT.

Figure 6.13 to Figure 6.20 shows the EDS analysis result for the specimen illustrated in Figure 6.12 at a random region. Figure 6.13 is a scanning electron micrograph for the examined cross-section, where horizontal parallel stripes are cross-sections of BT:Ni=1:4 Ni'(m) filaments in axial direction, and round areas are cross-sections of LFBT filaments perpendicular to the BT:Ni=1:4 Ni'(m) filaments. Dark areas are interstitial void space filled by epoxy resin. Dents on the LFBT cross-section are likely due to miss BT grains scraped off during cutting and polishing processes. Other than that, little porosity is observed on sintered LFBT and BT:Ni=1:4 Ni'(m). This indicates that both compositions have reached high density after sintering. Across the region examined, no micro crack is observed at interfaces between both compositions. Figure 6.14 shows the EDS energy spectrum for the mapping elements in the composite structure.

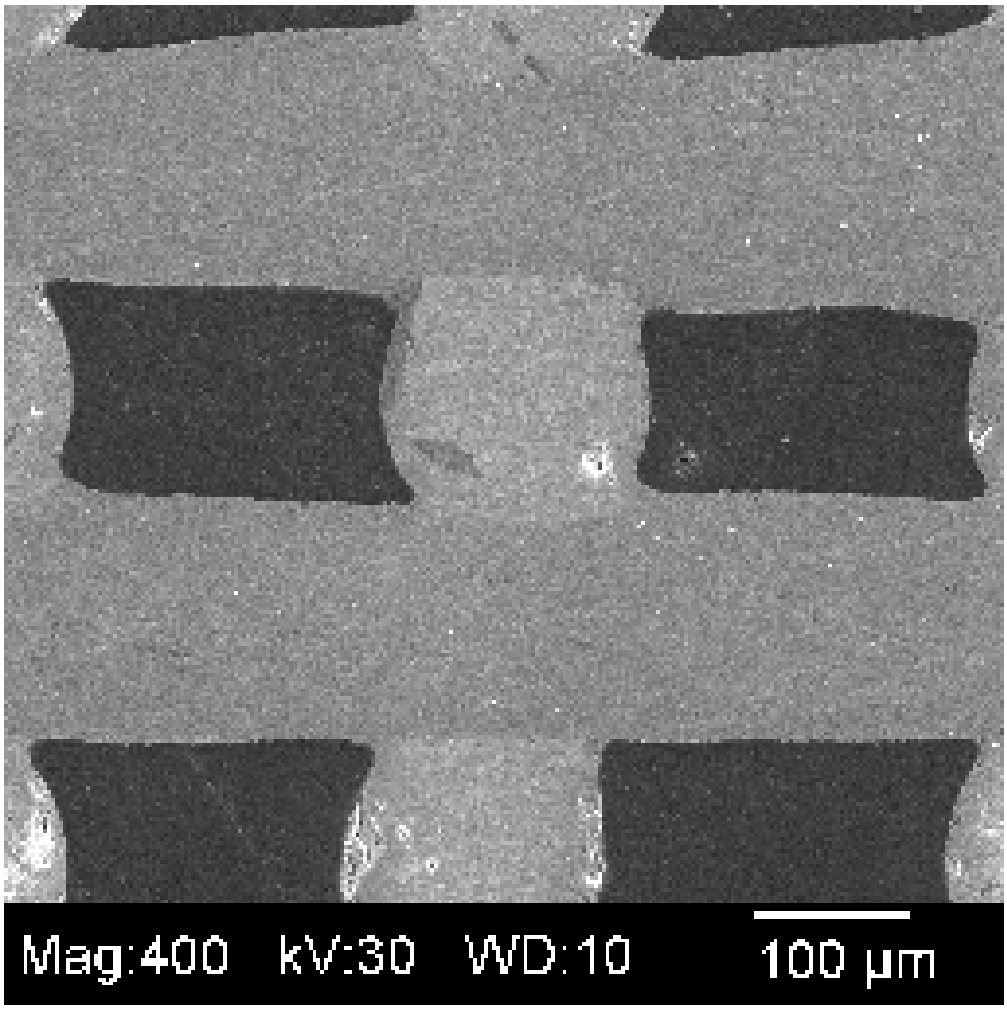

Figure 6.13 Scanning electron micrograph for a random cross-section of the specimen examined by EDS.

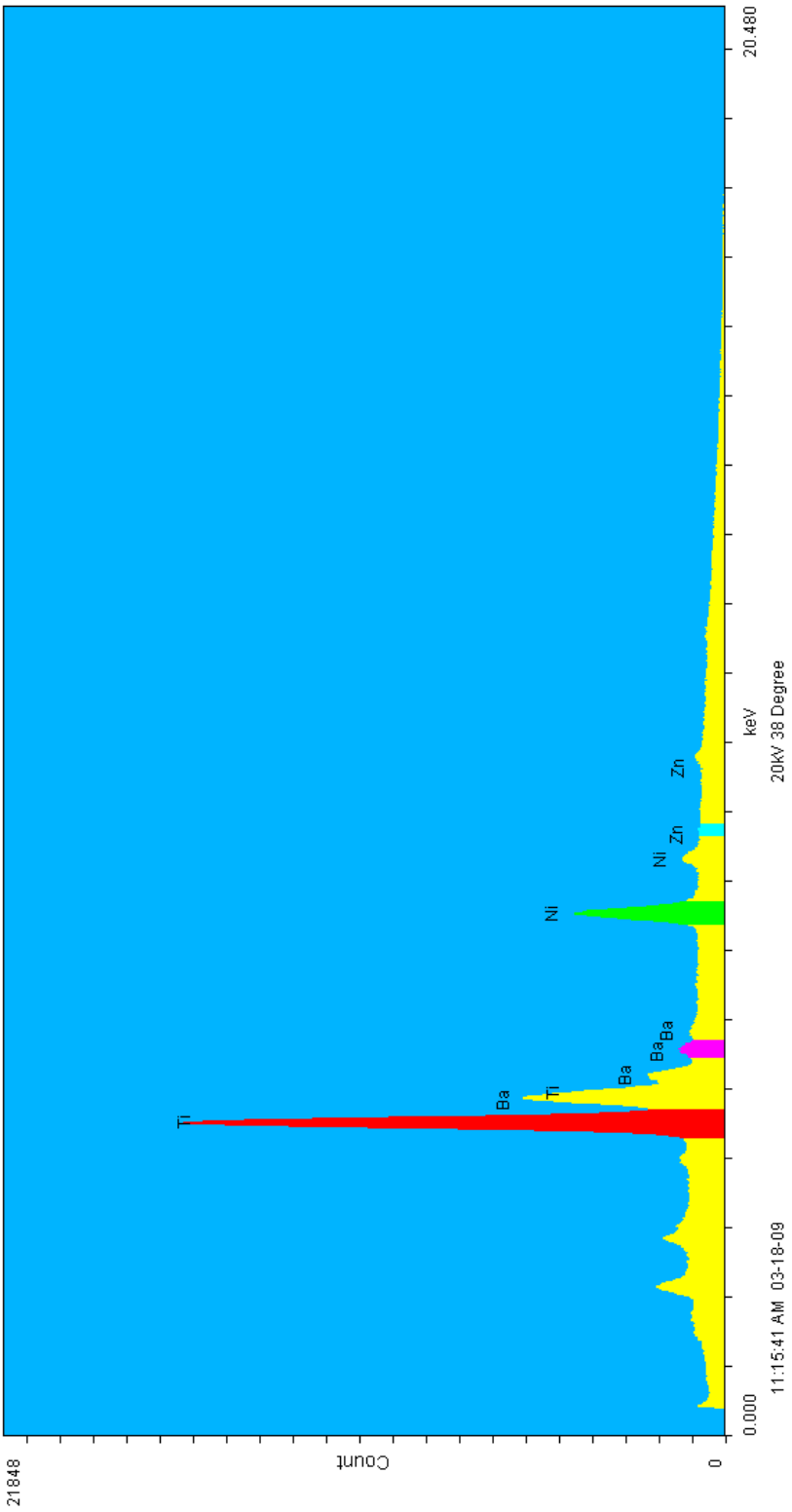

Figure 6.14 EDS energy spectrum for elements in the composite structure.

Figure 6.15 shows the mapping of Ti element on the cross section of composite specimen. Resolution is 512×512 pixels across the region examined. Intensity of relevant color indicates element concentration. Here, each red dot corresponds to positive detection of Ti element within a pixel. Discrete transition of Ti concentration is observed. It indicates that there is no significant mass transfer of Ti element from LFBT into BT:Ni=1:4 Ni'(m).

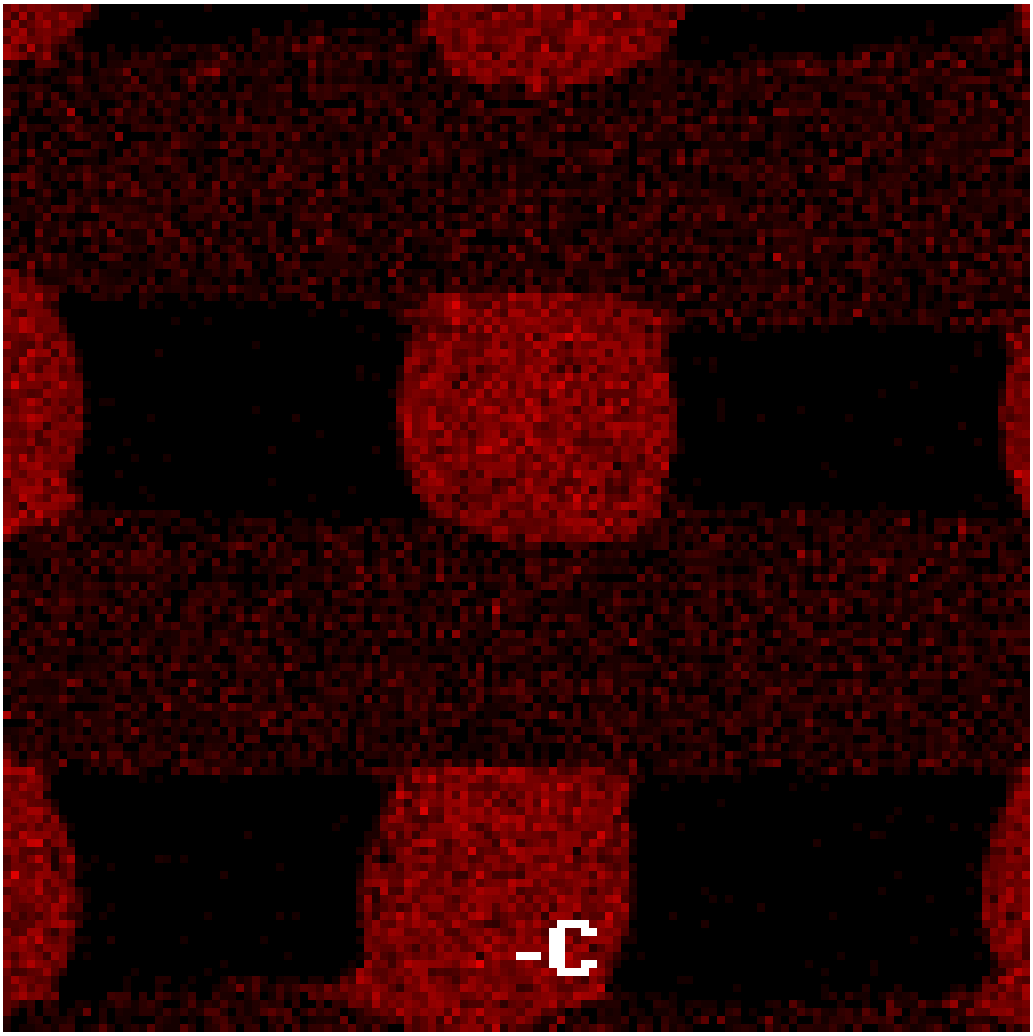

Figure 6.15 Mapping of Ti element across the region shown in Figure 6.13. Each red dot indicates one positive detection of Ti element.

Figure 6.16 shows element mapping for Ni across the same region at a 512×512 pixel resolution. Each green dot corresponds to positive detection of Ni element within a pixel. It suggests that Ni particles are locked in position during liquid phase sintering, and there is no noticeable diffusion of Ni into the LFBT component.

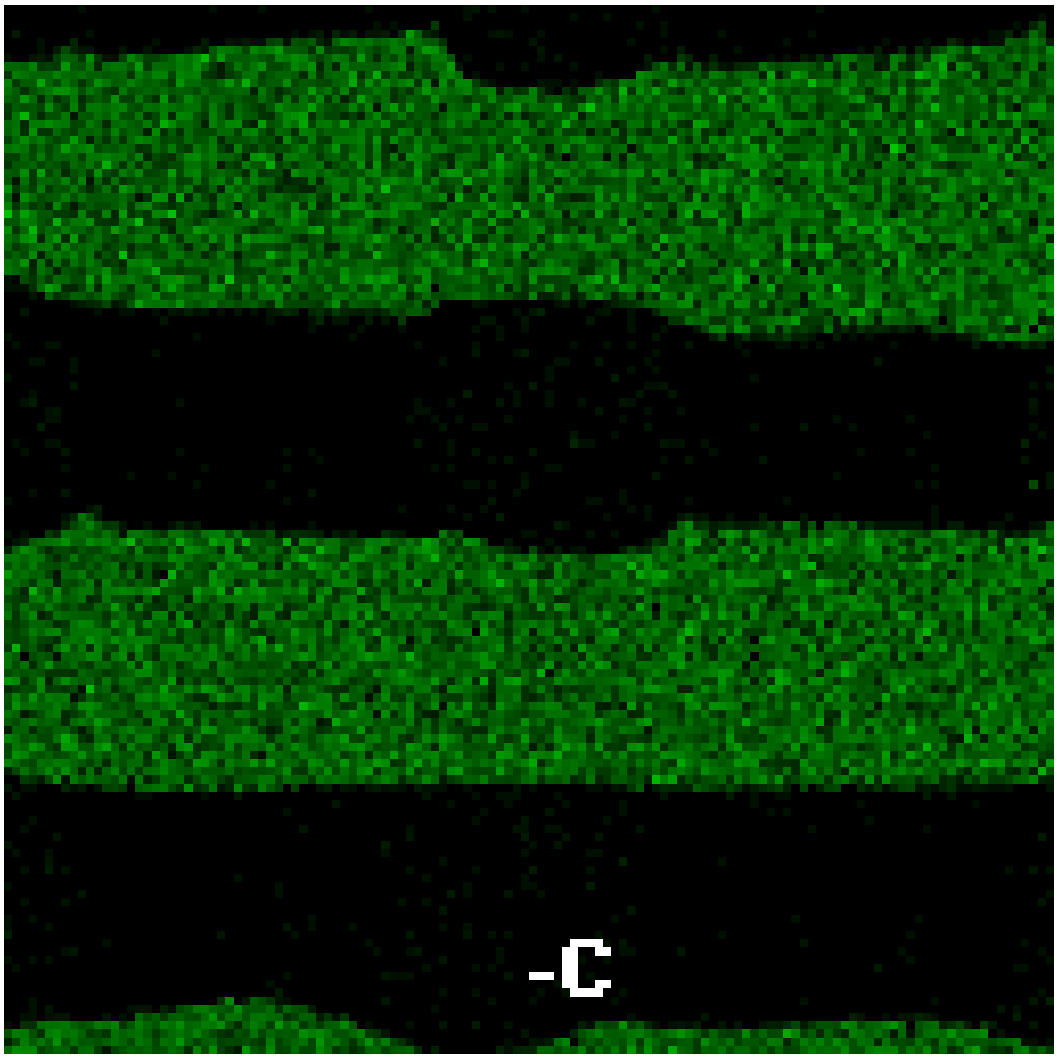

Figure 6.16 Mapping of Ti element across the region shown in Figure 6.13. Each green dot indicates one positive detection of Ni element.

Figure 6.17 and Figure 6.18 show element mappings for Ba across the same region at a 512×512 pixel resolution. Each yellow dot in Figure 6.17 and magenta dot in Figure 6.18 corresponds to positive detection of Ba element within a pixel. Discrete transition of Ba concentration is observed. It suggests that there is no significant mass transfer of Ba element from LFBT into BT:Ni=1:4 Ni'(m).

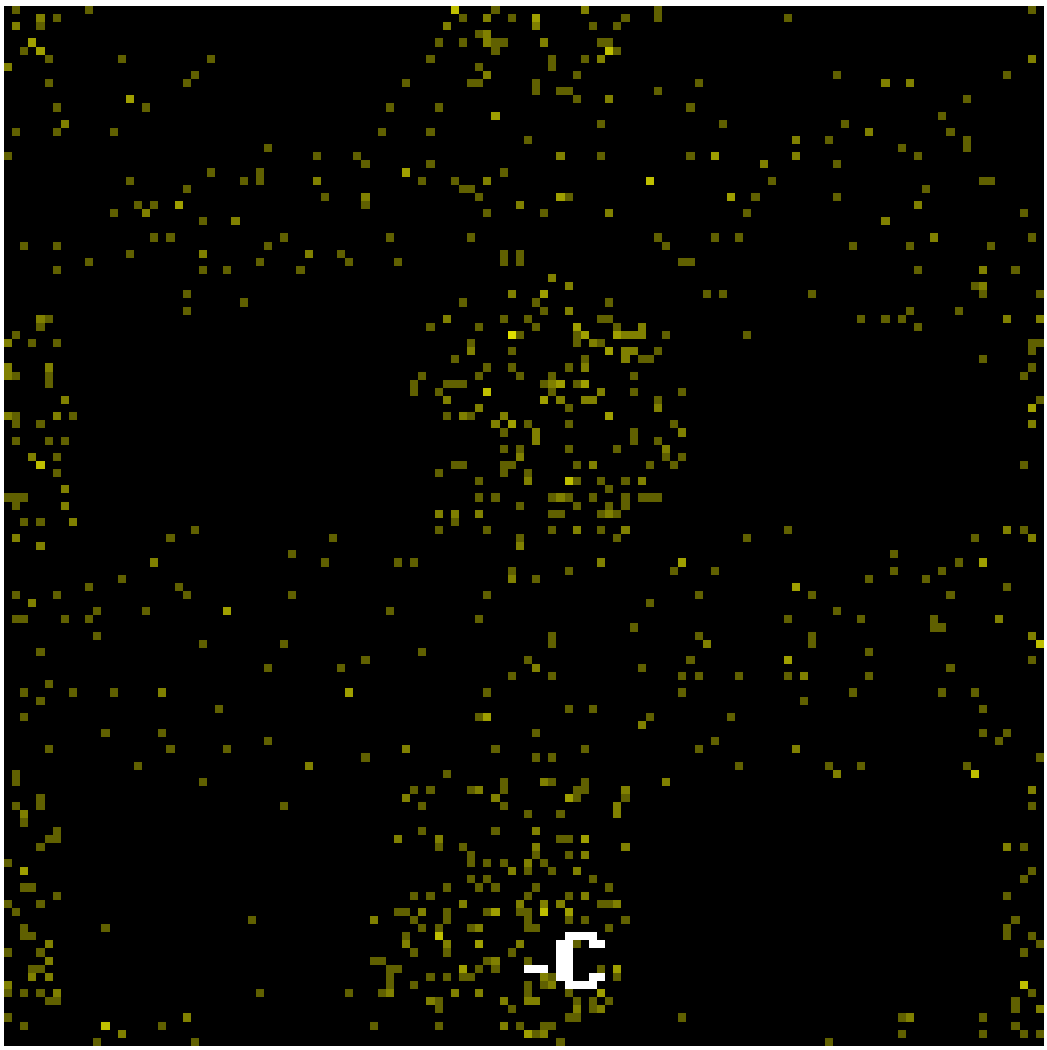

Figure 6.17 Mapping of Ba element across the region shown in Figure 6.13. Each yellow dot indicates one positive detection of Ba element.

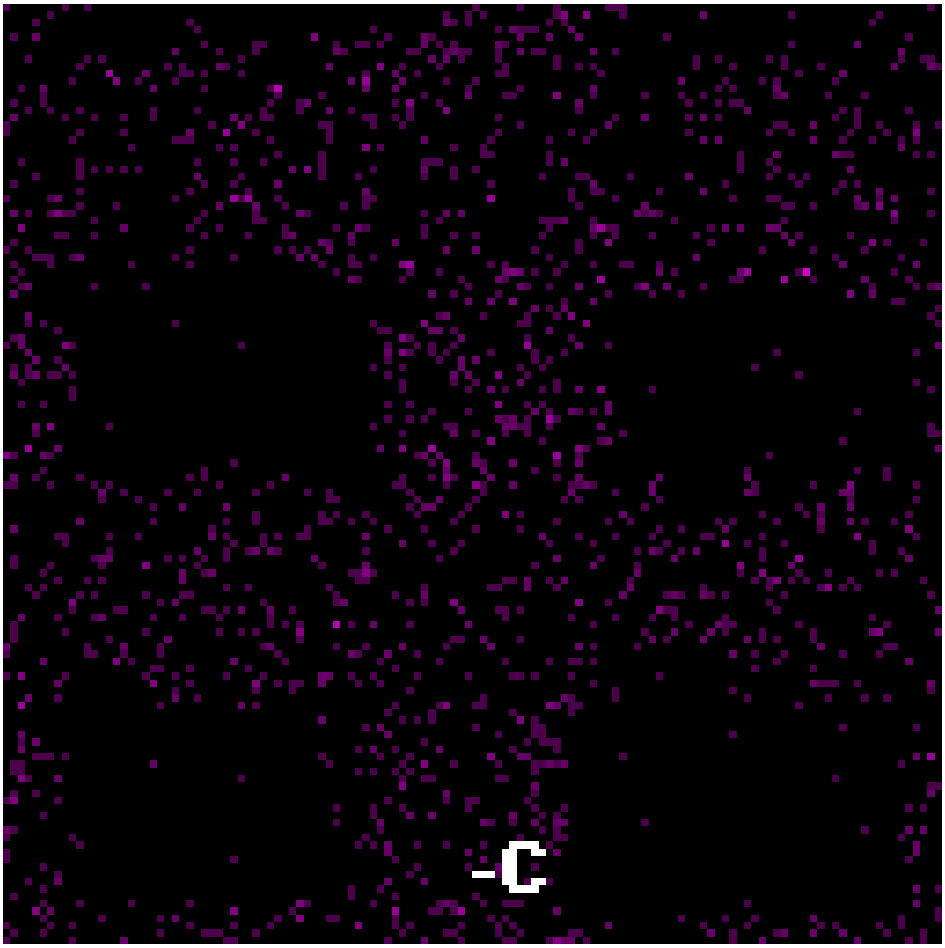

Figure 6.18 Mapping of Ba element across the region shown in Figure 6.13. Each magenta dot indicates one positive detection of Ba element.

Figure 6.19 shows element mapping for Zn across the same region at a 512×512 pixel resolution. Each blue dot corresponds to positive detection of Zn element within a pixel. Zn element is detected throughout the cross section of the composite specimen, although at a low intensity. As a constituent in the sintering aids, spreading of ZnO along with B_2O_3 and Li_2O is expected during liquid phase sintering. Due to the low atomic number of Li and B, EDS mapping for them is impossible.

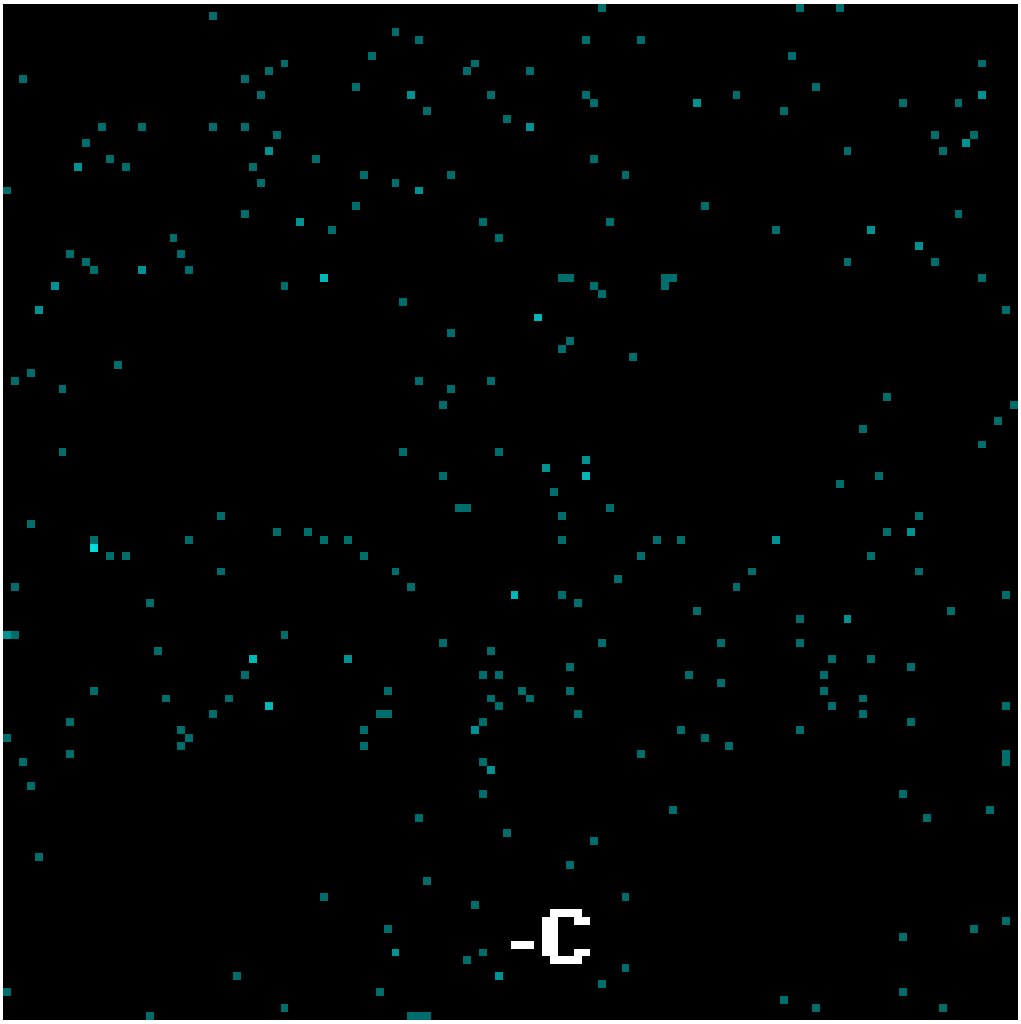

Figure 6.19 Mapping of Zn element across the region shown in Figure 6.13. Each blue dot indicates one positive detection of Zn element.

Figure 6.20 shows combined element mapping across the same region at a 512×512 pixel resolution. All the colored dots in Figure 6.14-Figure 6.19 are shown here.

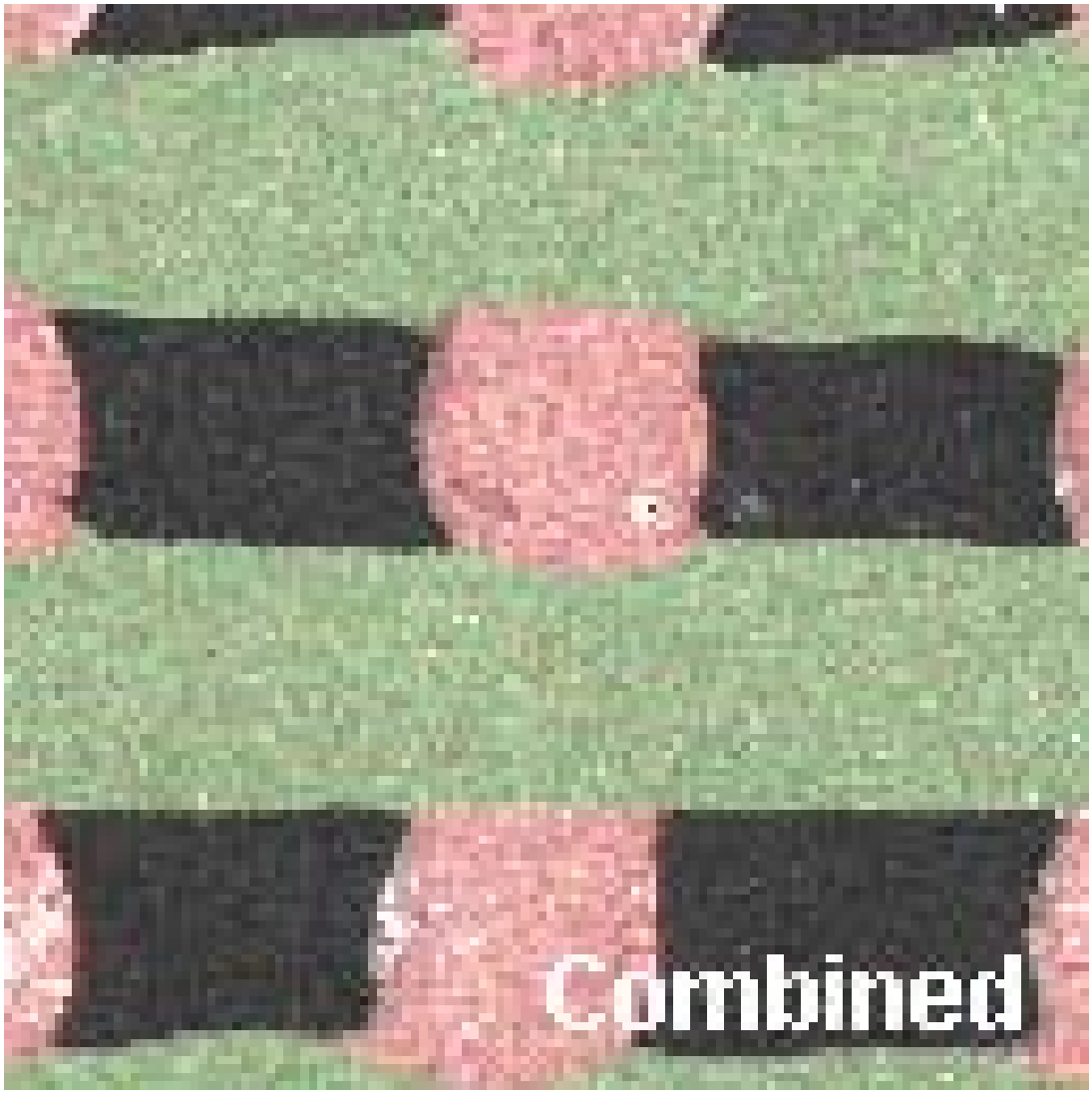

Figure 6.20 EDS analysis for the cross-section of composite lattice: a combined pattern for Ba, Ti, Ni, and Zn elements.

6.3.7. *Piezoelectricity and Dielectric Constant*

The piezoelectricity of the LFBT has been confirmed. After poling, the LFBT specimens sintered in air has a rather low piezoelectric coefficient of 6 pm/V. It is probable that the LFBT specimen is not fully poled yet. The hysteresis loop for the LFBT specimen is shown in Figure 6.21. Figure 6.22 gives the dielectric constant and dissipation factor curves at 1-100 kHz for the LFBT specimen. Probably due to the lower Li_2O concentration and the lack of core shell grain boundary, the K has around ±25% deviation. The dissipation factor at low frequency 1 kHz is relatively large. But the dielectric properties are more relevant to the ceramic capacitor application than to the biomedical purpose.

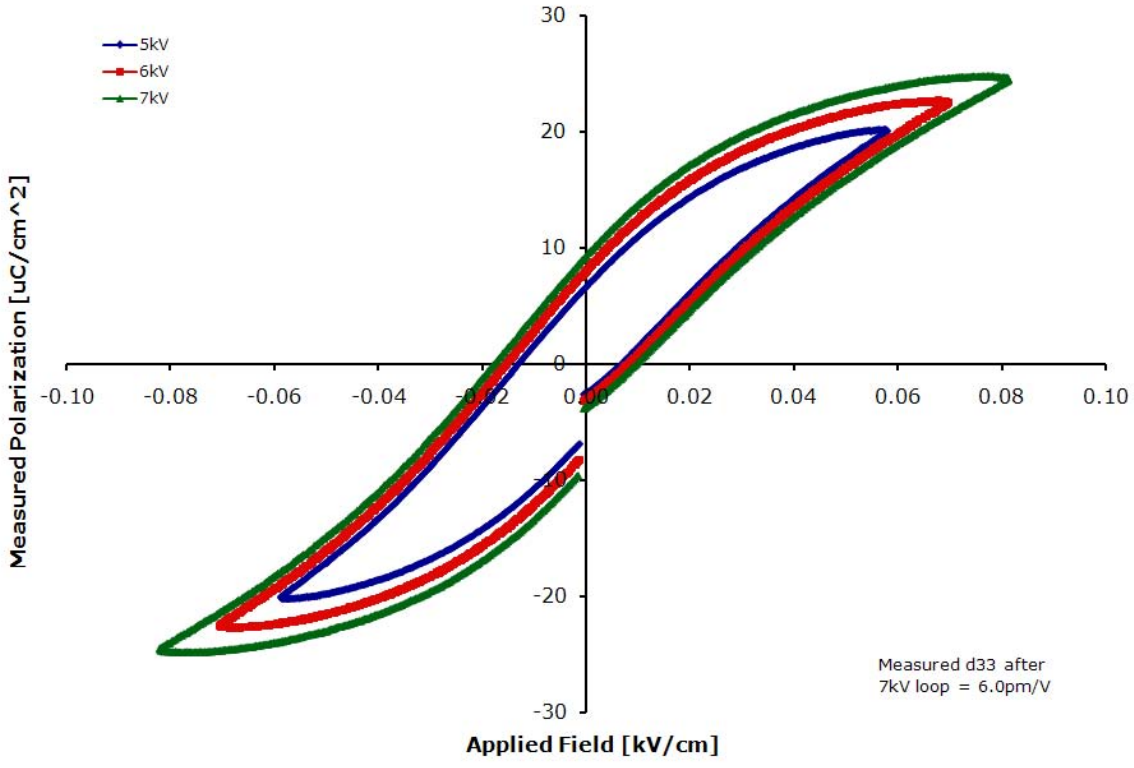

Figure 6.21 The hysteresis loop for the LFBT specimen sintered at 1000 °C in air.

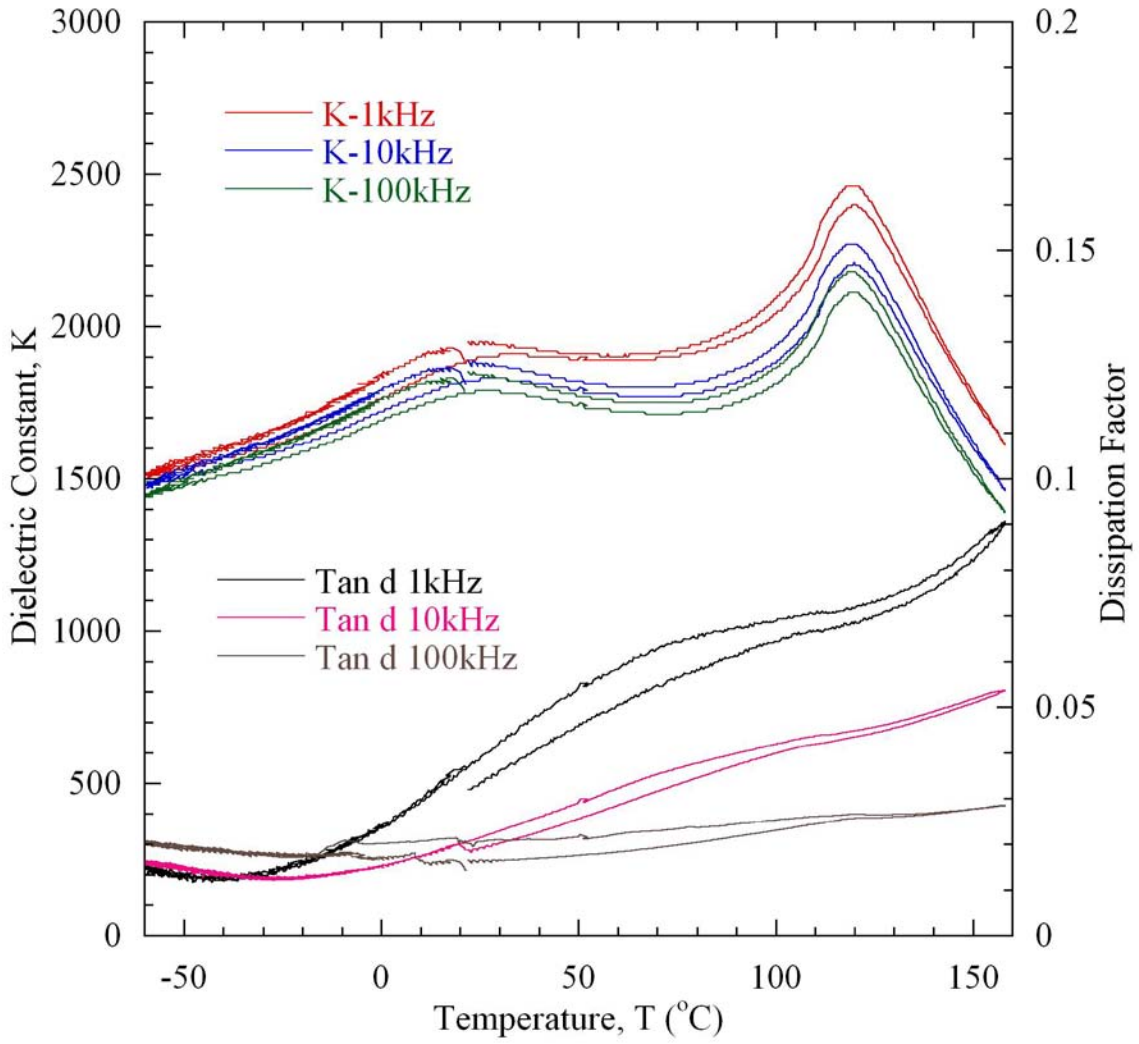

Figure 6.22 Dielectric constant and dissipation factor at 1-100 kHz for the LFBT specimen.

6.4. Conclusions

Aqueous colloidal LFBT ink has been formulated based on a ZnO-B_2O_3-Li_2O sintering aids. Ni(m) ink of Chapter 5 is modified by adding appropriate amounts of BT and Li^+ content. These colloidal inks have compatible sintering behavior and allow densification of composite structures to near full density. Sintering study validates the use of liquid phase sintering for near net shaping through Robocasting. Complex ceramic-metal composite structures have been fabricated through serial printing of these inks, followed by densification at 1000 °C. Vickers hardness test indicates a 23.8% increase compared to the extrapolated BT hardness value based on porous Ni(m) composite specimens. EDS reveals that LFBT and BT:Ni=1:4 Ni'(m) components have good cohesion and form an integral device without noticeable inter-diffusion between BT and Ni. Transport of Zn element from LFBT to BT:Ni=1:4 Ni'(m) is observed. Characterization of sintered specimens confirms the piezoelectricity for the LFBT composition and reveals its dielectric properties. The success in fabrication of ceramic metal composites suggests that liquid phase sintering is an effective densification method for Robocasting. Complex heterogeneous ceramic metal structures may be assembled to allow for various advanced applications. The findings in this chapter may be useful to researcher and practitioners in the field of solid freeform fabrication, MLCCs, ceramics, composites, functionally graded materials, and biomaterials.

CHAPTER 7 CONCLUSIONS AND RECOMMENDATIONS

7.1. Conclusions

Four major tasks are successfully accomplished in the context of freeform fabrication of heterogeneous geometrically-complex ceramic-metal composite structures by Robocasting technique. First, an aqueous colloidal carbon (CB) black fugitive ink has been developed for assembly complex geometric structures that contain long spanning and cantilevered features. Second, an aqueous colloidal nickel (Ni) ink has been developed for assembly of metallic objects and for understanding of relevant physicochemical properties. Third, aqueous colloidal composite inks for solid state sintering of heterogeneous geometrically-complex ceramic-metal composite structures have been developed. Finally, compatible aqueous colloidal ceramic and metal inks for liquid phase sintering of heterogeneous geometrically-complex ceramic-metal composite structures have been developed.

These accomplishments expand the capabilities of the Robocasting process and offer better understanding of the challenges and potential solutions for successful co-sintering of metal-ceramic composite structures. This new capability was demonstrated with the assembly of: 1) complex ceramic objects that contain long spanning features, fabricated with barium titanate (BT) and hydroxyapatite (HA), 2) Ni objects of various

geometric features, including non-space-filling lattices of various shapes and negative Poisson's ratio (NPR) bowtie structures, 3) ceramic capacitor lattices that contain a Ni volume fraction of 20% in the composite component through solid state sintering, and 4) heterogeneous negative Poisson's ratio low-fire BT-Ni composite bowtie structures and multilayer ceramic capacitor lattices that contain a Ni volume fraction of 80% in the Ni'(m) component through liquid phase sintering. The relevant studies for each task are summarized as follows:

1. Development of the aqueous colloidal CB fugitive ink:

   i. The optimal surfactant concentration for a specific CB powder Monarch 120A58 is determined. Viscometry indicates that a 1.5 mg/m^2 surface concentration of nonylphenol ethoxylate surfactant yields lowest viscosity for high concentration aqueous CB suspension.

   ii. A solid volume fraction ϕ_{solids}=0.44 aqueous CB gel is developed.

   iii. Rheological properties of aqueous colloidal CB gels are characterized. The results indicate that the carbon black gel has a higher yield stress than typical ceramic inks using by Robocasting, by a lower shear elastic modulus; and gelation is by hydrogen bond between non-ionic polymeric additives.

   iv. Drying shrinkage of the aqueous colloidal CB gel is determined. Scanning electron micrograph indicates 1-2% linear drying shrinkage of as dried gel.

   v. Oxidation behavior of carbon black ink is characterized by thermogravimetric analysis. It is determined that CB Monarch 120A58 may readily be oxidized in air at temperature 650 °C, but requires a temperature higher than 900 °C to complete

at a reasonable rate in CO_2, with a calculated activation energy E_a of 165.80 $kJmol^{-1}$ in the temperature range from 895 °C to 1038 °C.

2. Development of the aqueous colloidal Ni ink:

   i. The optimal dispersant concentration for the specific Ni powder ENP 800 is determined. Viscometry indicates that a 2 mg/(g Ni powder) concentration for a cationic polyelectrolyte polyethylenimine (MW=25k) yields lowest viscosity for high solid volume fraction aqueous suspensions of Ni at pH=8.2.

   ii. A solid volume fraction ϕ_{solids}=0.472 aqueous Ni gel is developed.

   iii. Rheological properties of aqueous colloidal Ni gels are characterized. Oscillatory measurement indicates a 300 kPa shear elastic modulus for the Ni gel used for Robocasting; and the Ni gel has a decreasing shear elastic modulus when flocculant (Darvan 821A) addition decreases.

   iv. Thermal degradation of polymer additives for Ni ink preparation is characterized by thermogravimetric analysis. Residual carbonaceous content in a Ni green structure is estimated to be less than 0.364% by weight after binder removal in air.

   v. Temperature profile for reducing atmosphere sintering of Ni in $5\%H_2 95\%N_2$ is determined. A 700 °C, 2 hours isothermal hold is used to ensure complete reduction of surface NiO; and a subsequent isothermal hold for 2 hours at 900 °C sinter Ni structure to >99.0% of theoretical density.

   vi. Microstructure and hardness of Ni sinter are examined. The microstructure has an ASTM grain size number of G = 12.6 (Planimetric Procedure, ASTM E112 Section 9) and nominal grain diameter of 4.6 μm, and a Vickers hardness VPN120.

3. Development of aqueous colloidal composite inks for solid state sintering:

i. Various aqueous colloidal Ni(m) composite inks with different BT:Ni ratios (i.e. 1:4, 2:3, 3:2, and 4:1 by solid volume ratio) have been developed, as well as a pure BT ink. A solid volume fraction of ϕ_{solids}=0.43 is used for all inks.

ii. Rheological properties of aqueous colloidal Ni(m) gels and BT gel are characterized. The Ni(m) gels have shear elastic moduli in the range from 163 kPa to 280 kPa; and the BT gel has a shear elastic modulus of 99 kPa.

iii. Sintering strain data of each composite ink in the temperature range from 1100 °C to 1350 °C are determined. Sintering strain increases as Ni volume fraction increases in the Ni(m) ink; and the BT:Ni=4:1 Ni(m) ink has least sintering shrinkage difference from pure BT.

iv. Processing conditions are determined for co-sintering. Co-sintering is achieved only with the BT:Ni=4:1 Ni(m) ink for the pure BT ink in a reducing atmosphere at 1350 °C. Re-oxidation is carried out in nitrogen at 800 °C for 24 hours to diminish oxygen vacancies in the reducing-atmosphere sintered BT phase.

v. Hardness and density of sintered Ni(m) specimens are examined. A linear relationship exists between the hardness of a Ni(m) specimen and its BT volume fraction. Extrapolated BT and Ni hardness are VPN99 and VPN 387 respectively. And the density of sintered Ni(m) specimens is between 91% and 96% of theoretical.

4. Development of aqueous colloidal composite inks for liquid phase sintering:

   i. Various aqueous colloidal Ni'(m) inks with different BT:Ni ratios, i.e. BT:Ni=1:19, 1:4, and 3:7 by solid volume ratio, have been developed. A solid volume fraction of ϕ_{solids}=0.43 is used for all inks. An aqueous colloidal LFBT ink has been developed. This ink is based on the ZnO-B_2O_3-Li_2O sintering aids and contains 1.43% ZnO, 0.75% B_2O_3 and 0.375% Li_2O by sintered weight.

   ii. Rheological behaviors of the LFBT ink and the BT:Ni=1:4 Ni'(m) ink have been characterized. The LFBT ink has a shear elastic modulus around 70kPa, and a yield stress around 20Pa; the BT:Ni=1:4 Ni'(m) ink has a shear elastic modulus of around 120kPa, and a yield stress around 100 Pa.

   iii. Sintering strain data of each ink composition fired separately in the temperature range from 700 °C to 1000 °C are determined.

   iv. Composite structures of BT-Ni have been fabricated through liquid phase sintering. The BT inclusion in the metallic Ni'(m) component is between 20%-30% by volume with negligible Li_2O and balance Ni.

   v. Hardness of LFBT sinter has been determined. Vickers hardness test indicates a VPN479, 23.8% increase compared to the extrapolated BT hardness based on porous Ni(m) composite specimens.

   vi. While there is no inter-diffusion between BT and Ni phases, mass transport of liquid phase is confirmed by energy dispersive spectroscopy (EDS).

   vii. A piezoelectric coefficient of 6 pm/V and a ±25% deviation of dielectric constant have been measured for sintered LFBT specimen.

7.2. Recommendations

In the context of fabrication of ceramic metal composite structures by Robocasting, future investigations are encouraged to continue in the following aspects:

1. *Fugitive ink*. A search for a better powder material than carbon black Monarch 120A58 should include the following considerations: i) ash free after thermal degradation and oxidation, 2) lower temperature for complete removal by thermal degradation and oxidation; 3) flocculation by electrostatic interaction. Possible candidates are synthesized thermosetting polymer particles, thermoplastic polymer powder cross-linked by high energy radiation, e.g. γ-ray, and water-insoluble starch or cellulose derivatives in a powder form.
2. *Ceramic and metal materials*. Drastic difference in sintering temperature and thermal expansion coefficient should be avoided if possible. Possible choices include alloy powder or a mixture of two metal powders for adjustment of CTE to match to that of ceramic.
3. *Master sintering curve and dilatometry*. For understanding sintering kinetics, dilatometry is required. Data collected thereby will allow for generation of mathematical models based on master sinter curve theory; and by incorporating process variables such as time and temperature ramp rate, prediction of sintering shrinkage for relevant inks is possible.[173]

In the context of Robocasting process, future investigations are encouraged to continue in the following aspect:

1. *Ink design.* The overlooked parameter of temperature variation and its effect on certain polymer additives are to be exploited. If successful, the proposed method would allow for larger geometric structures, finer structural definition, and a higher ink solid volume fraction. Robocasting uses weakly flocculated colloidal gels as build materials. Colloidal inks are normally held at a near constant room temperature throughout the wet processing steps. Low yield stress after ink printing (usually around 100 Pa) limits the height of printed structure; and flocs size and interaction strength within the particle network supposedly limit the minimal nozzle size for extrusion and constrains ink solid volume fraction. Temperature induced ink change has benefited other SFF techniques such as FDM and Inkjet Printing, but high concentration organic binder are used in these processes. For Robocasting, it is possible to exploit a thermally induced transition to a low concentration polymer additive such that the low binder colloidal ink has a low yield stress to allow extrusion, but a high yield stress shortly after extrusion to allow continued material addition. Thermal activation of this transition may be achieved by using a temperature controlled oil bath to set oil temperature below or above the transition temperature depending on gelation mechanism and a low vapor pressure hydrocarbon oil at given temperatures; the colloidal ink reservoir is also temperature-controlled, but at a different temperature that inhibits gelation. Possible candidate polymer additives for this purpose include κ-carrageenan, Figure 7.1 and other like ones that demonstrate similar temperature dependant

gelation behavior. κ-carrageenan is essentially a long single chain polysaccharide that is able to form gel work of double helix structure by hydrogen bonding in water when temperature decreases below 34 °C. In this new ink design, less polyelectrolyte flocculant may be used, so that flocs in a hierarchy colloidal gel network before printing will be weaker in strength and smaller in average size to allow extrusion through smaller nozzle diameters; meanwhile, HPMC as viscosifier may no longer be necessary as the proposed additive acts as a viscosifier before extrusion. This ink design promises many research opportunities in chemical engineering, including modeling of fluid dynamics, thermal removal of relevant polymer additive, and heat transfer modeling during the printing process.

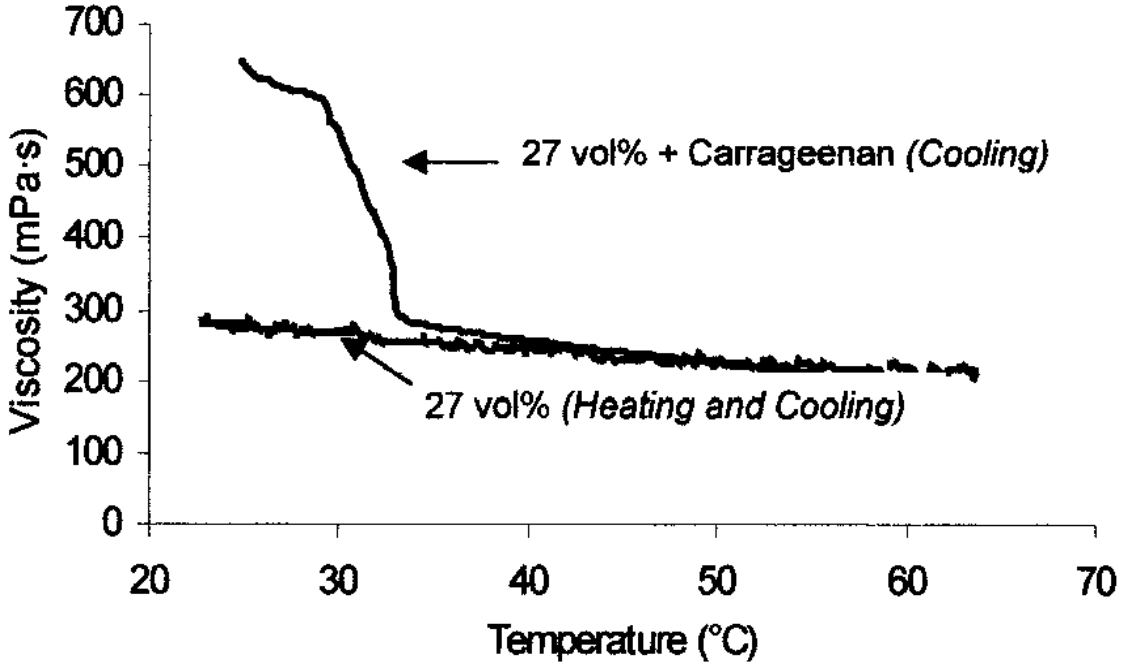

Figure 7.1 Variation of viscosity at 100 s^{-1} as a function of temperature for the an aqueous Ni slurry with and without carrageenan. Gelling point of the slurry containing carrageenan occurs at 34 °C.[138]

REFERENCES

1. Larsson 9301647, 1993.

2. Deckard, C. Method for selective laser sintering with layerwise cross-scanning. 5155324, 1992.

3. Irving, R., Taking a powder: Laser processing. *International Journal of Powder Metallurgy* **2000,** 36, (4), 69-74.

4. Crump, S. S. Modeling apparatus for three-dimensional objects. 5340433, 1994.

5. Cesarano, J. I.; Calvert, P. D. Freeforming objects with low-binder slurry. 6027326, 2000.

6. Smay, J. E.; Cesarano, J.; Tuttle, B. A.; Lewis, J. A., Piezoelectric properties of 3-X periodic Pb(ZrxTi1-x)O-3-polymer composites. *Journal of Applied Physics* **2002,** 92, (10), 6119-6127.

7. Sachs, E.; Cima, M.; Williams, P.; Brancazio, D.; Cornie, J., Three dimensional printing. Rapid Tooling and prototypes directly from a CAD model. *Journal of engineering for industry* **1992,** 114, (4).

8. Friis, L. A.; Smay, J. E., Design, Assembly, and Characterization of Metal-Ceramic Composite Reentrant Structures. In NSF: 2005.

9. Friis, L. A. Surgical Implants Incorporating Re-entrant Material. 5035713, 1991.

10. Darling, E. M.; Athanasiou, K. A., Biomechanical strategies for articular cartilage regeneration. *Annals of Biomedical Engineering* **2003,** 31, (9), 1114-1124.

11. Estes, B. T.; Gimble, J. M.; Guilak, F., Mechanical signals as regulators of stem cell fate. *Stem Cells in Development and Disease* **2004,** 60, 91-126.

12. Beck, B. R.; Qin, Y. X.; McLeod, K. J.; Otter, M. W., On the relationship between streaming potential and strain in an in vivo bone preparation. *Calcified Tissue International* **2002,** 71, (4), 335-343.

13. Becker, R. O., Stimulation of Partial Limb Regeneration in Rats. *Nature* **1972,** 235, (5333), 109-&.

14. Grodzinsky, A. J., Electromechanical and Physicochemical Properties of Connective-Tissue. *Crc Critical Reviews in Biomedical Engineering* **1983,** 9, (2), 133-199.

15. Guzelsu, N.; Walsh, W. R., Streaming Potential of Intact Wet Bone. *Journal of Biomechanics* **1990,** 23, (7), 673-685.

16. Hastings, G. W.; Mahmud, F. A., Electrical Effects in Bone. *Journal of Biomedical Engineering* **1988,** 10, (6), 515-521.

17. Lai, W. M.; Sun, D. D.; Ateshian, G. A.; Guo, X. E.; Mow, V. C., Electrical signals for chondrocytes in cartilage. *Biorheology* **2002,** 39, (1-2), 39-45.

18. Lee, C. R.; Grodzinsky, A. J.; Hsu, H. P.; Martin, S. D.; Spector, M., Effects of harvest and selected cartilage repair procedures on the physical and biochemical properties of articular cartilage in the canine knee. *Journal of Orthopaedic Research* **2000,** 18, (5), 790-799.

19. Legare, A.; Garon, M.; Guardo, R.; Savard, P.; Poole, A. R.; Buschmann, M. D., Detection and analysis of cartilage degeneration by spatially resolved streaming potentials. *Journal of Orthopaedic Research* **2002,** 20, (4), 819-826.

20. Lohmann, C. H.; Schwartz, Z.; Liu, Y.; Li, Z.; Simon, B. J.; Sylvia, V. L.; Dean, D. D.; Bonewald, L. F.; Donahue, H. J.; Boyan, B. D., Pulsed electromagnetic fields affect phenotype and connexin 43 protein expression in MLO-Y4 osteocyte-like cells and ROS 17/2.8 osteoblast-like cells. *Journal of Orthopaedic Research* **2003,** 21, (2), 326-334.

21. Macginitie, L. A.; Gluzband, Y. A.; Grodzinsky, A. J., Electric-Field Stimulation Can Increase Protein-Synthesis in Articular-Cartilage Explants. *Journal of Orthopaedic Research* **1994,** 12, (2), 151-160.

22. Marino, A. A.; Becker, R. O.; Soderhol.Sc, Origin of Piezoelectric Effect in Bone. *Calcified Tissue Research* **1971,** 8, (2), 177-&.

23. Schmidt-Rohlfing, B.; Schneider, U.; Goost, H.; Silny, J., Mechanically induced electrical potentials of articular cartilage. *Journal of Biomechanics* **2002,** 35, (4), 475-482.

24. Wang, C. C. B.; Guo, X. E.; Sun, D. N.; Mow, V. C.; Ateshian, G. A.; Hung, C. T., The functional environment of chondrocytes within cartilage subjected to compressive loading: A theoretical and experimental approach. *Biorheology* **2002,** 39, (1-2), 11-25.

25. Park, J. B.; Recum, A. F. V.; Kenner, G. H.; Kelly, B. J.; Coffeen, W. W.; Grether, M. F., Piezoelectric Ceramic Implants - a Feasibility Study. *Journal of Biomedical Materials Research* **1980,** 14, (3), 269-277.

26. Hull, C. W. Apparatus for production of three-dimensional objects by stereolithography. 4575330 1986.

27. Derby, B.; Reis, N., Inkjet printing of highly loaded particulate suspensions. *Mrs Bulletin* **2003,** 28, (11), 815-818.

28. Khaing, M. W.; Fuh, J. Y. H.; Lu, L., Direct metal laser sintering for rapid tooling: processing and characterisation of EOS parts. *Journal of Materials Processing Technology* **2001,** 113, (1-3), 269-272.

29. Simchi, A.; Petzoldt, F.; Pohl, H., Direct metal laser sintering: Material considerations and mechanisms of particle bonding. *International Journal of Powder Metallurgy* **2001,** 37, (2), 49-61.

30. Smay, J. E.; Cesarano, J.; Lewis, J. A., Colloidal inks for directed assembly of 3-D periodic structures. *Langmuir* **2002,** 18, (14), 5429-5437.

31. Nadkarni, S. Oklahoma State University, Stillwater, 2006.

32. Smay, J. E.; Nadkarni, S. S.; Xu, J., Direct writing of dielectric ceramics and base metal electrodes. *International Journal of Applied Ceramic Technology* **2007,** 4, (1), 47-52.

33. Michna, S.; Wu, W.; Lewis, J. A., Concentrated hydroxyapatite inks for direct-write assembly of 3-D periodic scaffolds. *Biomaterials* **2005,** 26, (28), 5632-5639.

34. Smay, J. E.; Gratson, G. M.; Shepherd, R. F.; Cesarano, J.; Lewis, J. A., Directed colloidal assembly of 3D periodic structures. *Advanced Materials* **2002,** 14, (18), 1279-+.

35. Cesarano, J.; Stuecker, J. N.; Dellinger, J. G.; Jamison, R. D. Method for making a bio-compatible scaffold. 6993406, 2006.

36. Xie, B. J.; Parkhill, R. L.; Warren, W. L.; Smay, J. E., Direct writing of three-dimensional polymer scaffolds using colloidal gels. *Advanced Functional Materials* **2006,** 16, (13), 1685-1693.

37. Ring, T. A., *Fundamentals of Ceramic Powder Processing and Synthesis*. Academic Press: 1996.

38. German, R. M., *Sintering Theory and Practice*. John Wiley & Sons, Inc.: New York, 1996.

39. Kingery, W. D., Densification during Sintering in the Presence of a Liquid Phase .1. Theory. *Journal of Applied Physics* **1959,** 30, (3), 301-306.

40. Igarashi, S.; Achikita, M.; S, M. In *Evolution of Gases and Sintering Behavior in Atomized Iron Powder for Metal Injection Molding*, 1993 powder metallurgy World Congress, Kyoto, Japan, 1993; Bando, Y.; Kosuge, K., Eds. Japan Society Powder and Powder Metallury Kyoto, Japan, 1993; pp 253-256.

41. Berthelot, J.-M., *Composite Materials: Mechanical Behavior and Structural Analysis*. Springer-Verlag: New York, 1998.

42. Chawla, K. K., *Ceramic Matrix Composites*. University Press: Cambridge, UK, 1993.

43. Chou, T.-W., *Structure and Properties of Composites*. VCH Publisher: New York, 1993; Vol. 13.

44. Suresh, S.; Mortensen, A., *Fundamentals of Functionally Graded Materials*. IOM Communications Ltd: London, 1998.

45. Ichikawa, K., *Functionally Graded Materials in the 21st Century*. Kluwer Academic Publishers: Norwell, MA, 2001.

46. Kawasaki, A.; Watanabe, R., Finite-Element Analysis of Thermal-Stress of the Metal Ceramic Multilayer Composites with Controlled Compositional Gradients. *Journal of the Japan Institute of Metals* **1987,** 51, (6), 525-529.

47. Watari, F.; Yokoyama, A.; Omori, M.; Hirai, T.; Kondo, H.; Uo, M.; Kawasaki, T., Biocompatibility of materials and development to functionally graded implant for bio-medical application. *Composites Science and Technology* **2004,** 64, (6), 893-908.

48. Bishop, A.; Lin, C. Y.; Navaratnam, M.; Rawlings, R. D.; Mcshane, H. B., A Functionally Gradient Material Produced by a Powder Metallurgical Process. *Journal of Materials Science Letters* **1993,** 12, (19), 1516-1518.

49. Mizuno, Y.; Kawasaki, A.; Watanabe, R., Measurement of Nonuniform Sintering Shrinkage of Functionally Gradient Material by Digital Image-Processing. *Metallurgical and Materials Transactions B-Process Metallurgy and Materials Processing Science* **1995,** 26B, (1), 75-79.

50. Hirai, T., *Processing of Ceramics*. VCH Publisher: Weinheim, 1996; Vol. 17B.

51. Sogabe, K.; Tanaka, M.; Miura, T.; Tobioka, M. In *Functionally Graded Materials*, Tsukuba, Japan, 1996; Shiota, I.; MIyamoto, Y., Eds. Elsevier: Tsukuba, Japan, 1996; pp 155-158.

52. Tuffe, S.; Marple, B. R., Graded casting: Process control for producing tailored profiles. *Journal of the American Ceramic Society* **1995,** 78, (12), 3297-3303.

53. Dollmeier, K.; Ilschner, B.; Thiele, W. In Third International Symposium on Structural and Functional Graded Materials, Lausanne, Switzerland, 1994; Lausanne, Switzerland, 1994; pp 27-32.

54. Ilschner, B.; Delfosse, D., *Solid State Phenomena* **1989**, (8&9).

55. Lange, F. F.; Atteraas, L.; Zok, F.; Porter, J. R., Deformation Consolidation of Metal Powders Containing Steel Inclusions. *Acta Metallurgica Et Materialia* **1991,** 39, (2), 209-219.

56. Scherer, G. W., Viscous Sintering of Particle-Filled Composites. *American Ceramic Society Bulletin* **1991,** 70, (6), 1059-1063.

57. Delie, F.; Bouvard, D.; Mazille, J. E., Investigation of the Consolidation of Powder Composite by Image-Analysis. *Materials Science and Engineering a-Structural Materials Properties Microstructure and Processing* **1994,** 184, (1), 65-71.

58. Fan, C. L.; Rahaman, M. N., Factors Controlling the Sintering of Ceramic Particulate Composites .1. Conventional Processing. *Journal of the American Ceramic Society* **1992,** 75, (8), 2056-2065.

59. Sudre, O.; Lange, F. F., Effect of Inclusions on Densification .1. Microstructural Development in an Al2o3 Matrix Containing a High-Volume Fraction of Zro2 Inclusions. *Journal of the American Ceramic Society* **1992,** 75, (3), 519-524.

60. Taylor, N.; Dunand, D. C.; Mortensen, A., Initial-Stage Hot-Pressing of Monosized Ti and 90-Percent Ti-10-Percent Tic Powders. *Acta Metallurgica Et Materialia* **1993,** 41, (3), 955-965.

61. Bouvard, D., *Acta Metallurgica Et Materialia* **1993,** 41, 1413-1420.

62. Besson, J.; Evans, A. G., *Acta Metallurgica Et Materialia* **1992,** 40, 2247-2255.

63. Scherer, G. W., *J. Am. Cer. Soc.* **1987,** 70, 719-725.

64. Sudre, O.; Bao, G.; Lange, F. F.; Evans, A. G., *J. Am. Cer. Soc.* **1992,** 75, 525-531.

65. Bouvard, D.; Lange, F. F., *Acta Metallurgica Et Materialia* **1991,** 39, 3083-3090.

66. Kuo, C. H.; Gupta, P. K., *Acta Metallurgica Et Materialia* **1995,** 43, 397-403.

67. Otsuka, A.; Tamazaki, H.; Niiyama, M.; Iwasaki, K., In *Funcitionally Graded Materials* Shiota, I.; Miyamoto, Y., Eds. Elsevier, Amsterdam: Tsukuba, Japan, 1996; pp 251-256.

68. Taya, M. In 9th Ris-International Symposium on Metallurgy and Materials Science, Ris-National Laboratory, Roskilde, Denmark, 1988; Andersen, S. I.; Lilholt, H.; Pedersen, O. B., Eds. Ris-National Laboratory, Roskilde, Denmark: Ris-National Laboratory, Roskilde, Denmark, 1988; pp 201-231.

69. Lin, C. Y.; Mcshane, H. B.; Rawlings, R. D. In Third International Symposium on Structural and Functional Gradient Materials, Lausanne, Switzerland, 1994; Ilschner, B.; Cherradi, N., Eds. Presses Polytechniques et Universitaires Romandes, Lausanne, Switzerland: Lausanne, Switzerland, 1994; pp 327-332.

70. Lin, C. Y.; Mcshane, H. B.; Rawlings, R. D., *Mater. Sci. and Technol.* **1994,** 10, 659-664.

71. Kimura, H.; Kobayashi, S., Fabrication of a Functionally Gradient Material of Tial/Psz System Via Pulse-Electric Discharge Consolidation with Temperature Slope Control Using a Stepped Die. *Journal of the Japan Institute of Metals* **1993,** 57, (11), 1346-1351.

72. Rabin, B. H.; Heaps, R. J. In san Francisco, 1992, 1993; Holt, J. B.; Kiozumi, M.; Hirai, T.; Munir, Z. A., Eds. American Ceramic Society: san Francisco, 1992, 1993; pp 173-180.

73. Hu, C. L.; Rahaman, M. N., Factors Controlling the Sintering of Ceramic Particulate Composites .2. Coated Inclusion Particles. *Journal of the American Ceramic Society* **1992,** 75, (8), 2066-2070.

74. Hatano, T.; Yamaguchi, T.; Sakamoto, W.; Yogo, T.; Kikuta, K.; Yoshida, H.; Tanaka, N.; Hirano, S., Synthesis and characterization of BaTiO3-coated Ni particles. *Journal of the European Ceramic Society* **2004,** 24, (2), 507-510.

75. Matsuzaki, Y. Thermomechanical Behavior of Functionally Graded Material for Scramjet Engine Heat Insulation Structure. Kyoto University, 1994.

76. Watanabe, R., *MRS Bull.* **1995**, (20).

77. Yuan, R. Z.; Zhang, L. M.; Zhang, Q. J.; F., T. X., *J. of Materials Synthesis and Processing* **1993,** 1, 171-179.

78. Rabin, B. H.; Williamson, R. L. In Processing and Fabrication of Advanced Materials III, Warrendale, PA, 1994; Ravi, V. A.; Srivatsan, T. S.; Moore, J. J., Eds. TMS: Warrendale, PA, 1994; pp 145-154.

79. Yuki, M.; Murayama, T.; Irisawa, T.; Kawasaki, A.; Watanabe, R. In *Proc. of the First Int. Symp. on Functionally gradient Materials*, Sendai, Japan, 1990; Yamanouchi, M.; Koizumi, M.; Hirai, T.; Shiota, I., Eds. Functionally Gradient Materials Forum: Sendai, Japan, 1990; pp 203-208.

80. Willert-Porada, M. A.; Borchert, R. In *Functionally Graded Materials*, Tsukuba, Japan, 1996; Shiota, I.; Miyamoto, Y., Eds. Elsevier: Tsukuba, Japan, 1996.

81. Sampath, S.; Herman, H., Plasma Spray Forming Metals, Intermetallics, and Composites. *Jom-Journal of the Minerals Metals & Materials Society* **1993,** 45, (7), 42-49.

82. Srivatsan, T. S.; Lavernia, E. J., Use of Spray Techniques to Synthesize Particulate-Reinforced Metal-Matrix Composites. *Journal of Materials Science* **1992,** 27, (22), 5965-5981.

83. Shiota, I.; Shinohara, Y.; Imai, Y.; Ikeno, S. In the First Int. Symp. on Functionally Gradient Materials, Sendai, Japan, 1990; Yamaguchi, M.; Koizumi, M.; Hirai, T.; Shiota, I., Eds. Functionally Gradient Materials Forum: Sendai, Japan, 1990; pp 219-224.

84. Hirai, T.; Sasaki, M., Vapor-Deposited Functionally Gradient Materials. *Jsme International Journal Series I-Solid Mechanics Strength of Materials* **1991,** 34, (2), 123-129.

85. Chigasaki, M.; Kojima, Y.; Nakashma, S.; Fukuya, Y. In *Proc. of the First International Symo. on Funcitionally Gradient Materials*, Sendai, Japan, 1990; Yamaguchi, M.; Koizumi, M.; Hirai, T.; Shiota, I., Eds. Functionally Gradient Mateirals Forum: Sendai, Japan, 1990; pp 269-272.

86. Kim, B. J.; Lee, S. H.; Lee, J. J., *J. of Mater. Sci. Lett.* **1997**, (16), 1597-1599.

87. Cline, C. F. In Third International Symposium on Structural and Functional Gradient Materials, Lausanne, Switzerland, 1994; Ilschner, B.; Cherradi, N., Eds. Presses Polytechniques et Universitaires Romandes, Lausanne, Switzerland: Lausanne, Switzerland, 1994; p 595.

88. Watanabe, Y.; Nakamura, Y.; Fukui, Y.; Nakanishi, K., A Magnetic-Functionally Graded Material Manufactured with Deformation-Induced Martensitic-Transformation. *Journal of Materials Science Letters* **1993,** 12, (5), 326-328.

89. Carslaw, H. S.; Jaeger, J. C., *Conduction of Heat in Solids*. Second ed.; Clarendon Press: Oxford, 1959.

90. Iida, T.; Guthrie, R. I. L., *The Physical Properties of Liquid Metals*. Clarendon Press: Oxford, 1993.

91. Poirier, D. R.; Geiger, G. H., *Transport Phenomena in Materials Processing*. Second ed.; TMS: Warrendale, PA, 1994.

92. Morissette, S. L.; Lewis, J. A.; Clem, P. G.; Cesarano, J.; Dimos, D. B., Direct-write fabrication of Pb(Nb,Zr,Ti)O(3 d)evices: Influence of paste rheology on print morphology and component properties. *Journal of the American Ceramic Society* **2001,** 84, (11), 2462-2468.

93. Song, J. H.; Edirisinghe, M. J.; Evans, J. R. G., Formulation and multilayer jet printing of ceramic inks. *Journal of the American Ceramic Society* **1999,** 82, (12), 3374-3380.

94. Tuttle, B. A.; Smay, J. E.; Cesarano, J.; Voigt, J. A.; Scofield, T. W.; Olson, W. R.; Lewis, J. A., Robocast Pb(Zr0.95Ti0.05)O-3 ceramic monoliths and composites. *Journal of the American Ceramic Society* **2001,** 84, (4), 872-874.

95. Cesarano, J. I.; Segalman, R. A.; Calvert, P. D., Robocasting: Rapid Prototyping of Ceramic Slurries. *Ceramic Industry* 1998.

96. Seerden, K. A. M.; Reis, N.; Evans, J. R. G.; Grant, P. S.; Halloran, J. W.; Derby, B., Ink-jet printing of wax-based alumina suspensions. *Journal of the American Ceramic Society* **2001,** 84, (11), 2514-2520.

97. Miano, F.; Bailey, A.; Luckham, P. F.; Tadros, T. F., Adsorption of Poly(Ethylene Oxide) Poly(Propylene Oxide) Aba Block Copolymers on Carbon-Black and the Rheology of the Resulting Dispersions. *Colloids and Surfaces* **1992,** 68, (1-2), 9-16.

98. Miano, F.; Bailey, A.; Luckham, P. F.; Tadros, T. F., Adsorption of Nonyl Phenol Propylene-Oxide Ethylene-Oxide Surfactants on Carbon-Black and the Rheology of the Resulting Dispersions. *Colloids and Surfaces* **1992,** 62, (1-2), 111-118.

99. Schaller, C.; Dirnberger, K.; Schauer, T.; Eisenbach, C. D., Stabilization of carbon black with ionic-hydrophobic polyelectrolytes. *Macromolecular Symposia* **2002,** 187, 695-705.

100. Halverson, D. C.; Ewald, K. H.; Munir, Z. A., Influence of Reactant Characteristics on the Microstructures of Combustion-Synthesized Titanium Carbide. *Journal of Materials Science* **1993,** 28, (17), 4583-4594.

101. Kawazoe, M.; Ishida, H., Verification of Selective Adsorption of Polymer on Filler Surface in a Binary Immiscible Polymer Solution Blend Based on Nanoconfinement: Changing the Aggregate Structure and the Surface Character of Carbon Black. *Macromolecules* **2009,** 42, (16), 6175-6180.

102. Zhu, W. Z.; Miser, D. E.; Chan, W. G.; Hajaligol, M. R., HRTEM investigation of some commercially available furnace carbon blacks. *Carbon* **2004,** 42, (8-9), 1841-1845.

103. Chu, B., Structure and Dynamics of Block-Copolymer Colloids. *Langmuir* **1995,** 11, (2), 414-421.

104. Chu, B.; Zhou, Z. K., *Nonionic surfactants: polyoxyalkylene block copolymers*. Marcel Dekker: New York, 1996.

105. Nadkarni, S. S.; Smay, J. E., Concentrated barium titanate colloidal gels prepared by bridging flocculation for use in solid freeform fabrication. *Journal of the American Ceramic Society* **2006,** 89, (1), 96-103.

106. Rueb, C. J.; Zukoski, C. F., Viscoelastic properties of colloidal gels. *Journal of Rheology* **1997,** 41, (2), 197-218.

107. Prestidge, C.; Tadros, T. F., Viscoelastic Properties of Aqueous Concentrated Polystyrene Latex Dispersions Containing Grafted Poly(Ethylene Oxide) Chains. *Journal of Colloid and Interface Science* **1988,** 124, (2), 660-665.

108. Prestidge, C.; Tadros, T. F., Rheological Investigation of Depletion Flocculation of Concentrated Sterically Stabilized Polystyrene Latex Dispersions. *Colloids and Surfaces* **1988,** 31, 325-346.

109. Cesarano, J.; Aksay, I. A., Processing of Highly Concentrated Aqueous Alpha-Alumina Suspensions Stabilized with Poly-Electrolytes. *Journal of the American Ceramic Society* **1988,** 71, (12), 1062-1067.

110. Cesarano, J.; Aksay, I. A.; Bleier, A., Stability of Aqueous Alpha-Al2o3 Suspensions with Poly(Methacrylic Acid) Poly-Electrolyte. *Journal of the American Ceramic Society* **1988,** 71, (4), 250-255.

111. Barnett, K. G.; Cosgrove, T.; Vincent, B.; Burgess, A. N.; Crowley, T. L.; King, T.; Turner, J. D.; Tadros, T. F., Neutron-Scattering, Nuclear Magnetic-Resonance and Photon-Correlation Studies of Polymers Adsorbed at the Solid-Solution Interface. *Polymer* **1981,** 22, (3), 283-285.

112. Sharma, P. K.; Bhatia, S. R., Effect of anti-inflammatories on Pluronic (R) F127: micellar assembly, gelation and partitioning. *International Journal of Pharmaceutics* **2004,** 278, (2), 361-377.

113. Dormidontova, E. E., Role of competitive PEO-water and water-water hydrogen bonding in aqueous solution PEO behavior. *Macromolecules* **2002,** 35, (3), 987-1001.

114. Hammouda, B.; Ho, D.; Kline, S., SANS from poly(ethylene oxide)/water systems. *Macromolecules* **2002,** 35, (22), 8578-8585.

115. Fuller, C. S.; MacRae, R. J.; Walther, M.; Cameron, R. E., Interactions in poly(ethylene oxide)-hydroxypropyl methylcellulose blends. *Polymer* **2001,** 42, (23), 9583-9592.

116. Kondo, T.; Sawatari, C., Intermolecular Hydrogen-Bonding in Cellulose Poly(Ethylene Oxide) Blends - Thermodynamic Examination Using 2,3-Di-O-Methylcelluloses and 6-O-Methylcelluloses as Cellulose Model Compounds. *Polymer* **1994,** 35, (20), 4423-4428.

117. Kondo, T.; Sawatari, C.; Manley, R. S.; Gray, D. G., Characterization of Hydrogen-Bonding in Cellulose Synthetic-Polymer Blend Systems with Regioselectively Substituted Methylcellulose. *Macromolecules* **1994,** 27, (1), 210-215.

118. Turhan, K. N.; Sahbaz, F.; Guner, A., A spectrophotometric study of hydrogen bonding in methylcellulose-based edible films plasticized by polyethylene glycol. *Journal of Food Science* **2001,** 66, (1), 59-62.

119. Tsubokawa, N., Functionalization of Carbon-Black by Surface Grafting of Polymers. *Progress in Polymer Science* **1992,** 17, (3), 417-470.

120. Boehm, H. P., Some Aspects of the Surface-Chemistry of Carbon-Blacks and Other Carbons. *Carbon* **1994,** 32, (5), 759-769.

121. Stanmore, B. R.; Brilhac, J. F.; Gilot, P., The oxidation of soot: a review of experiments, mechanisms and models. *Carbon* **2001,** 39, (15), 2247-2268.

122. Ramirez, A. G.; Sinclair, R.; Harkins, C. G.; Lin, A. R., The effects of slider material on the gasification of carbon. *Journal of Tribology-Transactions of the Asme* **2002,** 124, (4), 771-774.

123. King, B. H.; Dimos, D.; Yang, P.; Morissette, S. L., Direct-write fabrication of integrated, multilayer ceramic components. *Journal of Electroceramics* **1999,** 3, (2), 173-178.

124. Rodriguez, M. A.; Yang, P.; Kotula, P.; Dimos, D., Microstructure and phase development of buried resistors in low temperature Co-fired ceramic. *Journal of Electroceramics* **2000,** 5, (3), 217-223.

125. Venkataraman, N.; Rangarajan, S.; Matthewson, M. J.; Harper, B.; Safari, A.; Danforth, S. C.; Wu, G.; Langrana, N.; Yardimci, A.; Guceri, S. I., *Material property-process relationships in fused deposition of ceramics (FDC) and metals (FDMET)*. American Ceramic Society: 2000; Vol. 108.

126. Venkataraman, N.; Rangarajan, S.; Matthewson, M. J.; Safari, A.; Danforth, S. C.; Yardimci, A.; Guceri, S. I. In *Mechanical and rheological properties of feedstock material for fused deposition of ceramics and metals (FDC and FDMet) and their relationship to process performance*, 1999; University of Texas at Austin: 1999; pp 351-359.

127. Calvert, P., Inkjet printing for materials and devices. *Chemistry of Materials* **2001,** 13, (10), 3299-3305.

128. Calvert, P.; Yoshioka, Y.; Jabbour, G. E., Inkjet printing of biopolymers, conductors and dielectrics. *Abstracts of Papers of the American Chemical Society* **2002,** 224, U56-U57.

129. Magdassi, S.; Ben Moshe, M., Patterning of organic nanoparticles by ink-jet printing of microemulsions. *Langmuir* **2003,** 19, (3), 939-942.

130. Zabetakis, D.; Loschialpo, P.; Smith, D.; Dinderman, M. A.; Dressick, W. J., Direct-Write Patterning Palladium Colloids as a Catalyst for Electroless Metallization for Microwave Composites. *Langmuir* **2009,** 25, (3), 1785-1789.

131. He, G.; Hirschfeld, D. A.; Cesarano, J. I.; Stuecker, J. N. In *Robocasting and Cofiring of Functionally Graded Si3N4-W Materials*, 25th Annual Conference on Composites, Advanced Ceramics, Materials, and Structures: B: Ceramic Engineering and Science Proceedings, 2008; Singh, M.; Jessen, T., Eds. 2008; pp 119-125.

132. Cesarano, J.; Stuecker, J. N.; Dellinger, J. G.; Jamison, R. D. Method for making a bio-compatible scaffold 6993406, 2006.

133. deJesus, J. C.; Pereira, P.; Carrazza, J.; Zaera, F., Influence of argon ion bombardment on the oxidation of nickel surfaces. *Surface Science* **1996,** 369, (1-3), 217-230.

134. Norton, P. R.; Tapping, R. L.; Goodale, J. W., Photoemission Study of Interaction of Ni(100), Ni(110) and Ni(111) Surfaces with Oxygen. *Surface Science* **1977,** 65, (1), 13-36.

135. Hernandez, N.; Moreno, R.; Sanchez-Herencia, A. J.; Fierro, J. L. G., Surface behavior of nickel powders in aqueous suspensions. *Journal of Physical Chemistry B* **2005,** 109, (10), 4470-4474.

136. Hernandez, N.; Sanchez-Herencia, A. J.; Moreno, R., Forming of nickel compacts by a colloidal filtration route. *Acta Materialia* **2005,** 53, (4), 919-925.

137. Im, D. H.; Park, S. Y.; Hyun, S. H.; Lee, B. Y.; Kim, Y. H., Aqueous dispersion stability of nickel powders prepared by a chemical reduction method. *Journal of Materials Science* **2004,** 39, (11), 3629-3633.

138. Sanchez-Herencia, A. J.; Millan, A. J.; Nieto, M. I.; Moreno, R., Gel-forming of nickel powders from aqueous slurries. *Advanced Materials* **2000,** 12, (16), 1192-1195.

139. Sanchez-Herencia, A. J.; Millan, A. J.; Nieto, M. I.; Moreno, R., Aqueous colloidal processing of nickel powder. *Acta Materialia* **2001,** 49, (4), 645-651.

140. Saarinen, T.; Lindfors, L. E.; Fugleberg, S., A review of the precipitation of nickel from salt solutions by hydrogen reduction. *Hydrometallurgy* **1998,** 47, (2-3), 309-324.

141. Mond, L.; Langer, C.; Quincke, F., Action of Carbon-Monoxide on Nickel (Reprinted from J Chem Soc, Vol 57, Pg 749-753, 1890). *Journal of Organometallic Chemistry* **1990,** 383, (1-3), 1-5.

142. Kallay, N.; Torbic, Z.; Golic, M.; Matijevic, E., Determination of the Isoelectric Points of Several Metals by an Adhesion Method. *Journal of Physical Chemistry* **1991,** 95, (18), 7028-7032.

143. Moriwaki, H.; Yoshikawa, Y.; Morimoto, T., Oxide-Films on Iron and Nickel Ultrafine Particles Studied with Zero-Point of Charge Measurements. *Langmuir* **1990,** 6, (4), 847-850.

144. Xiang, L.; Deng, X. Y.; Jin, Y., Experimental study on synthesis of NiO nano-particles. *Scripta Materialia* **2002,** 47, (4), 219-224.

145. Karmhag, R.; Niklasson, G. A.; Nygren, M., Oxidation kinetics of small nickel particles. *Journal of Applied Physics* **1999,** 85, (2), 1186-1191.

146. Kitakatsu, N.; Maurice, V.; Hinnen, C.; Marcus, P., Surface hydroxylation and local structure of NiO thin films formed on Ni(111). *Surface Science* **1998,** 407, (1-3), 36-58.

147. Kitakatsu, N.; Maurice, V.; Marcus, P., Local decomposition of NiO ultra-thin films formed on Ni(111). *Surface Science* **1998,** 411, (1-2), 215-230.

148. Carter, R. E., Kinetic Model for Solid-State Reactions. *Journal of Chemical Physics* **1961,** 34, (6), 2010-&.

149. Fromhold, A. T., Growth-Rate of Low-Space-Charge Oxides on Spherical Metal Particles. *Journal of Physics and Chemistry of Solids* **1988,** 49, (10), 1159-1166.

150. Atkinson, A., Growth of Nio and Sio2 Thin-Films. *Philosophical Magazine B-Physics of Condensed Matter Statistical Mechanics Electronic Optical and Magnetic Properties* **1987,** 55, (6), 637-650.

151. Atkinson, A.; Taylor, R. I., The Diffusion of Ni-63 Along Grain-Boundaries in Nickel-Oxide. *Philosophical Magazine a-Physics of Condensed Matter Structure Defects and Mechanical Properties* **1981,** 43, (4), 979-998.

152. Atkinson, A.; Taylor, R. I.; Goode, P. D., Transport Processes in the Oxidation of Ni Studied Using Tracers in Growing Nio Scales. *Oxidation of Metals* **1979,** 13, (6), 519-543.

153. Atkinson, A.; Taylor, R. I.; Hughes, A. E., A Quantitative Demonstration of the Grain-Boundary Diffusion Mechanism for the Oxidation of Metals. *Philosophical Magazine a-Physics of Condensed Matter Structure Defects and Mechanical Properties* **1982,** 45, (5), 823-833.

154. Cathcart, J. V.; Petersen, G. F.; Sparks, C. J., Structure of Thin Oxide Films Formed on Nickel Crystals. *Journal of the Electrochemical Society* **1969,** 116, (5), 664-&.

155. Khoi, N. N.; Smeltzer, W. W.; Embury, J. D., Growth and Structure of Nickel-Oxide on Nickel Crystal Faces. *Journal of the Electrochemical Society* **1975,** 122, (11), 1495-1503.

156. Mitra, S.; Tatti, S. R.; Stark, J. P., A Spectroscopic Study of Nickel-Oxide Films on Polycrystalline Nickel. *Thin Solid Films* **1989,** 177, 171-180.

157. German, R. M., *Powder Injection Molding*. Metal Powder Industries Federation: Princeton, N.J., 1990.

158. Staller, O.; Holzmann, D.; Gritzner, G.; Diko, P.; Mikolaj, D.; Kovac, F., Textured nickel tapes prepared from commercially available material. *Central European Journal of Chemistry* **2008,** 6, (2), 135-139.

159. Smith; al., e., *Mechanical Engineers' Handbook*. 2006.

160. Alvarez, L.; Guillard, T.; Sauvajol, J. L.; Flamant, G.; Laplaze, D., Growth mechanisms and diameter evolution of single wall carbon nanotubes. *Chemical Physics Letters* **2001,** 342, (1-2), 7-14.

161. Massalski, T. B.; Okamoto, H., In *Binary Alloy Phase Diagrams*, ASM International: 1996.

162. Lewis, J. A., Colloidal processing of ceramics. *Journal of the American Ceramic Society* **2000,** 83, (10), 2341-2359.

163. Vamvakaki, M.; Billingham, N. C.; Armes, S. P.; Watts, J. F.; Greaves, S. J., Controlled structure copolymers for the dispersion of highperformance ceramics in aqueous media. *Journal of Materials Chemistry* **2001,** 11, (10), 2437-2444.

164. Panteny, S.; Bowen, C. R.; Stevens, R., Characterisation of barium titanate-silver composites, part I: Microstructure and mechanical properties. *Journal of Materials Science* **2006,** 41, (12), 3837-3843.

165. Benziada, L.; Ravez, J., Ferroelectric Batio3 Ceramics Sintered at Low-Temperature with the Aid of a Mixture of Caf2 and Lif. *Journal of Fluorine Chemistry* **1995,** 73, (1), 69-71.

166. Feng, Q. Q.; McConville, C. J., Dielectric degradation and microstructures of heterogeneous interfaces in cofired multilayer ceramic capacitors. *Journal of Electroceramics* **2005,** 14, (3), 213-220.

167. Song, T. H.; Randall, C. A., Copper cofire X7R dielectrics and multilayer capacitors based on zinc borate fluxed barium titanate ceramic. *Journal of Electroceramics* **2003,** 10, (1), 39-46.

168. Kirby, G. H.; Harris, D. J.; Li, Q.; Lewis, J. A., Poly(acrylic acid)-poly(ethylene oxide) comb polymer effects on BaTiO3 nanoparticle suspension stability. *Journal of the American Ceramic Society* **2004,** 87, (2), 181-186.

169. Kirby, G. H.; Lewis, J. A., Comb polymer architecture effects on the rheological property evolution of concentrated cement suspensions. *Journal of the American Ceramic Society* **2004,** 87, (9), 1643-1652.

170. Whitby, C. P.; Scales, P. J.; Grieser, F.; Healy, T. W.; Kirby, G.; Lewis, J. A.; Zukoski, C. F., PAA/PEO comb polymer effects on rheological properties and interparticle forces in aqueous silica suspensions. *Journal of Colloid and Interface Science* **2003,** 262, (1), 274-281.

171. Yoshikawa, J.; Lewis, J. A.; Chun, B. W., Comb Polymer Architecture, Ionic Strength, and Particle Size Effects on the BaTiO3 Suspension Stability. *Journal of the American Ceramic Society* **2009,** 92, (1), S42-S49.

172. Poptoshev, E.; Claesson, P. M., Forces between glass surfaces in aqueous polyethylenimine solutions. *Langmuir* **2002,** 18, (7), 2590-2594.

173. Park, S. J.; Suri, P.; Olevsky, E.; German, R. M., Master Sintering Curve Formulated from Constitutive Models. Journal of the American Ceramic Society 2009, 92, (7), 1410-1413.

APPENDICES

A. Mathematical Modeling of Carbon Black Oxidation in Air

The mathematical model is for estimate the oxygen concentration inside the carbon black and the rate of mass loss to carbon black at 650 °C. The following assumptions are made: 1) the ceramic surrounding the carbon black is inert in this process; 2) the permeability of ceramic to related gases is negligible so that gas diffusion only in the direction perpendicular to the carbon black surface is considered, 3) the carbon black support structure is a porous medium and has a large thickness (2L) with regard to the thickness of the reacting layer and oxidation rate, 4) the oxidation process is identical on either side of the carbon black that is open to air. Thus we only need to consider the situation on either side; 5) air flow, if any, is parallel to the carbon black surface; 6) carbon black is of 100% pure carbon without impurities; 7) the oxygen consumption rate is first order with respect to local oxygen concentration; and 8) a quasi-steady state is assumed for the oxidation process. The box shaped carbon black support structure in Figure 3.6a and its model geometry are shown in Figure A.1.

At 650 °C, oxidation of carbon black yields two products CO and CO_2, with a CO2/CO ratio at around 0.85.[A1, A2] The two reactions are:

$$C_{(s)} + O_{2(g)} \rightarrow CO_{2(g)}$$

a)

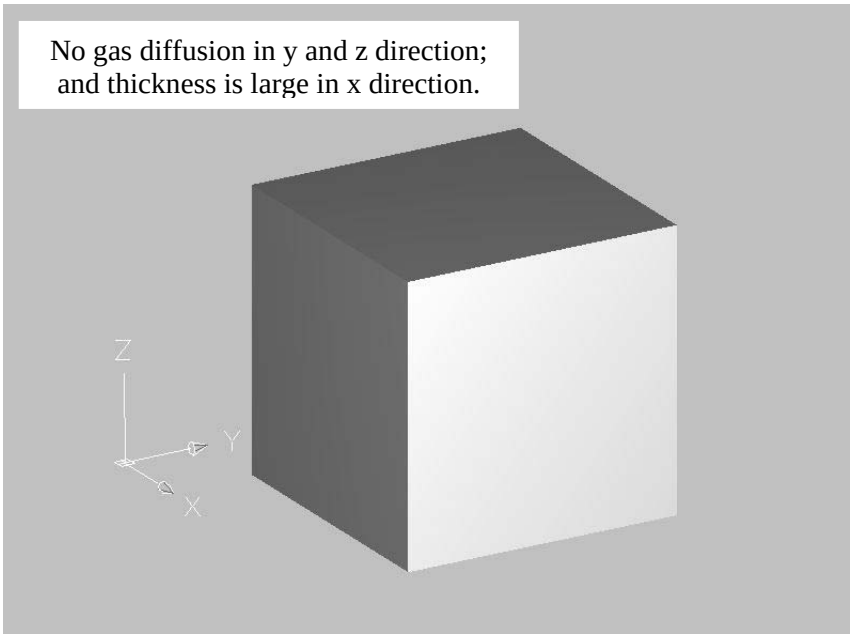

b)

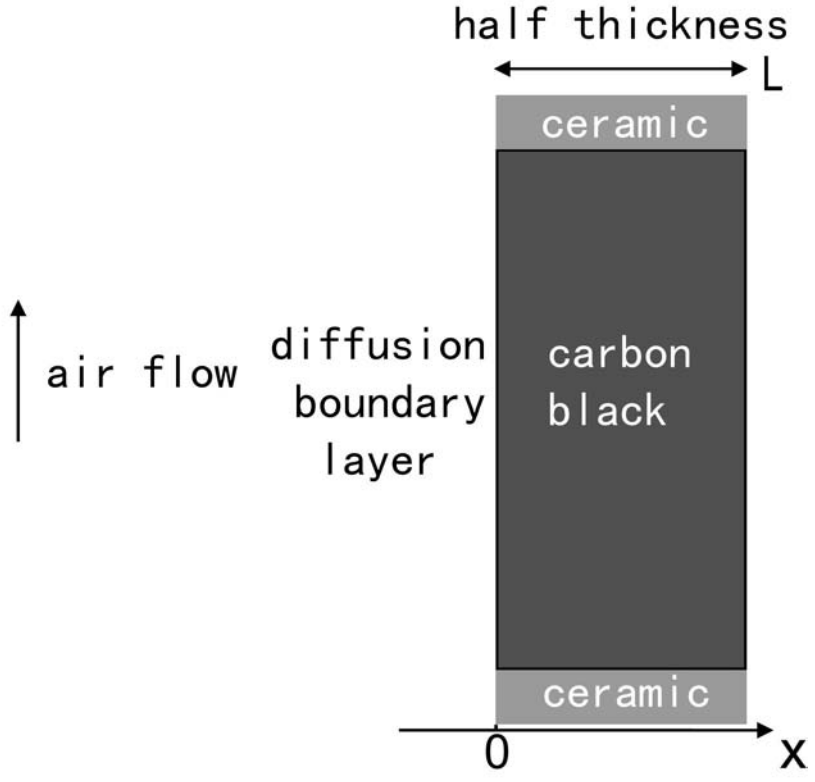

Figure A.1 a) Schematic illustration of the carbon black cube b) model geometry for the oxidation process.

and

$$C_{(s)} + \frac{1}{2} O_{2(g)} \rightarrow CO_{(g)}$$

Assuming for each mole carbon black reacted, α mole carbon generates $CO_{2(g)}$, and $(1-\alpha)$ mole carbon leads to $CO_{(g)}$ $(0 < \alpha < 1)$. Combining this with the above two equations gives:

$$C_{(s)} + \frac{1+\alpha}{2} O_{2(g)} \rightarrow \alpha CO_{2(g)} + (1-\alpha) CO_{(g)} \qquad (A.1)$$

Thus, the mass ratio a between $C_{(s)}$ and $O_{2(g)}$ that are consumed in this oxidation process is:

$$n = \frac{Wt_{O_2}}{Wt_C} = \frac{32 \times \frac{1+\alpha}{2}}{12} = \frac{4}{3}(1+\alpha) \qquad (A.2)$$

Mass balance for oxygen flux inside the carbon black structure:

$$\varepsilon \frac{dJ_{O_2}}{dx} + r_{O_2} = 0 \qquad (A.3)$$

There is a net weight loss to carbon. So the mass balance for total gas flux may be expressed by:

$$\varepsilon \frac{dJ_{gas}}{dx} = \frac{r_{O_2}}{n} \qquad (A.4)$$

The local consumption rate for oxygen at an arbitrary point x inside the carbon black may be expressed by:

$$r_{O_2} = k \rho_g C \qquad (A.5)$$

The oxygen flux J_{O_2} may also be expressed by:

$$J_{O_2} - CJ_{gas} = -\frac{\rho_g D_{O_2}}{\tau}\frac{dC}{dx} \qquad (A.6)$$

The Effective oxygen diffusivity D_{eff} in the porous carbon black is:

$$D_{eff} = \frac{\varepsilon}{\tau} D_{O_2} \qquad (A.7)$$

From Equation A.4 and A.5, we get differential equation as follows:

$$\frac{dJ_{gas}}{dx} = \frac{k\rho_g C}{n\varepsilon} \qquad (A.8)$$

From Equation A.3, A.5 and A.6, we get the following differential equation:

$$\varepsilon\frac{d(CJ_{gas} - \frac{\rho_g D_{O_2}}{\tau}\frac{dC}{dx})}{dx} + k\rho_g C = 0 \qquad (A.9)$$

$$\varepsilon\left(J_{gas}\frac{dC}{dx} + C\frac{dJ_{gas}}{dx} - \frac{\rho_g D_{O_2}}{\tau}\frac{d^2C}{dx^2} - \frac{D_{O_2}}{\tau}\frac{dC}{dx}\frac{d\rho_g}{dx}\right) + k\rho_g C = 0 \qquad (A.10)$$

From Equation A.7, A.8, and A.10, we get:

$$-\rho_g D_{eff}\frac{d^2C}{dx^2} + \varepsilon(J_{gas} - D_{eff}\frac{d\rho_g}{dx})\frac{dC}{dx} + k\rho_g C\left(1 + \frac{C}{n}\right) = 0 \qquad (A.11)$$

Assuming the reacting thickness is very small ($x \to 0$), after evaluation of each term in Equation A.11, a simplified Equation is given as

$$\frac{d^2C}{dx^2} - \frac{k}{D_{eff}}C = 0 \qquad (A.12)$$

Equation A.12 is solved in Maple and the solution is:

$$C(x) = Aexp\left(\sqrt{\frac{k}{D_{eff}}}x\right) + Bexp\left(-\sqrt{\frac{k}{D_{eff}}}x\right) \qquad (A.13)$$

The constants A and B may then be determined using the following boundary conditions:

(i) At the carbon black surface

$$J_{O_2}|_{x=0} = \left(CJ_{gas}\right)|_{x=0} - \left(\frac{\rho_g D_{eff}}{\varepsilon}\frac{dC}{dx}\right)|_{x=0} \qquad (A.14)$$

$$J_{O_2}|_{x=0} = -\rho_g k_d (C|_{x=0} - C_b) \qquad (A.15)$$

Assuming the effluent gas contains no oxygen, i.e. $\left(CJ_{gas}\right)|_{x=0} = 0$, then Equation A.14 and A.15 may be rewritten as:

$$\left(\frac{D_{eff}}{\varepsilon}\frac{dC}{dx}\right)|_{x=0} = k_d (C|_{x=0} - C_b) \qquad (A.16)$$

(ii) At the midpoint of the carbon black, i.e. $x = L$,

$$J_{gas}|_{x=L} = 0 \qquad (A.17)$$

$$\frac{dC}{dx}|_{x=L} = 0 \qquad (A.18)$$

The total carbon consumption rate may be expressed by

$$m = \int_0^L \frac{k\rho_g C}{n}dx = \frac{k\rho_g S}{np}[Aexp(Lp) - Bexp(-Lp) - A + B] \qquad (A.19)$$

where

$$p = \sqrt{\frac{k}{D_{eff}}}$$

Evaluation of D_{eff} The carbon black support structure is assumed to have two degrees of porosity, with the porosity between the aggregates ε_1, and inside the aggregates ε_2. The total porosity ε is roughly around 0.55 based on ink solid volume fraction. For pores inside carbon black aggregates, it is assumed that $\varepsilon_2 \approx 0.5$. Thus ε_1 may be calculated as:

$$\varepsilon_1 = \frac{\varepsilon - \varepsilon_2}{1 - \varepsilon_2} = 0.1$$

The D_{eff} may be calculated as

$$D_{eff} = \frac{2}{\frac{1}{D_1} + \frac{1}{D_2}}$$

with

$$D_i = \frac{\varepsilon_i D_{i1}}{\tau_i}$$

$$i = 1, 2$$

Assuming cylindrical pores of uniform diameter d_1 and d_2,

$$d_1 = \frac{4\varepsilon_1}{\alpha_1 \rho_b}$$

with

$$\alpha_1 = \frac{3}{\rho_b R_{ag}}$$

and

$$d_2 = \frac{4\varepsilon_2}{\alpha \rho_{ag}}$$

with

$$\rho_{ag} = \rho_b \frac{1-\varepsilon}{1-\varepsilon_1}$$

The mean value of R_{ag} is assumed to be around 400 nm, thus $d_1 \approx 100$ nm. and $d_2 \approx 60$ nm. These two values are reasonable since the carbon black network is closely packed. At this temperature, the oxygen mean free path is larger than d_1 and d_2. Hence, the Knudsen diffusivity for oxygen is:

$$D_{i,O_2} = \sqrt{\frac{8RT}{9\pi M}}\, d_i$$

$$i = 1, 2$$

For tortuosity τ_1 and τ_2, a value of 5 may be used for calculation.[A3]

B. Aqueous Colloidal Fugitive Starch Ink

An aqueous colloidal fugitive ink is developed based on a polysaccharide, i.e. rice starch powder. This ink is a rice starch particle filled Pluronic F-127 hydrogel. The main purpose of this study is to find an alternative to carbon black ink that allows for easy thermal removal at a lower temperature and compatible processing with Ni and other potential metal inks.

Materials. A rice starch powder (S7260-500g, SigmaAldrich, St. Louis, MO) is used as the colloidal phase, ABA block polymer Pluronic F-127 (P2443-1KG, SigmaAldrich, St. Louis, MO) is used to form a hydrogel, acrylic polymer latex (Elotex Titan 8100, National Starch. & Chemical, Bridgewater, NJ, USA) is used to assist dispersing rice starch powder in water, formaldehyde 10% by weight solution (Sciencelab, Houston, Texas) is used as an antifungal agent. DI water has a nominal conductivity 5×10^{-4} $(ohm\cdot cm)^{-1}$.

Procedure. Direct blending the following materials yields starch ink: 1) DI water 12.5 g 2) Starch powder 13.5 g, 3) TITAN 8100 1.5 g, 4) Pluronic F-127 3.0 g, and 5) formaldehyde 0.5 g. This ink may be used in Robocasting.

Results. Compared to carbon black ink, this starch ink has the advantages of easier thermal removal and less ash content. But its major flaws include: 1) wet starch powder swells upon heating, and 2) high shrinkage and cracking during drying in air due to low gel strength, Figure A.2a. This starch ink has been used for fabrication of Ni structures that have long spanning features Figure A.2b. The removal of this starch ink in an atmosphere of a 50% CO_2 and 50% H_2 mixture.

a)

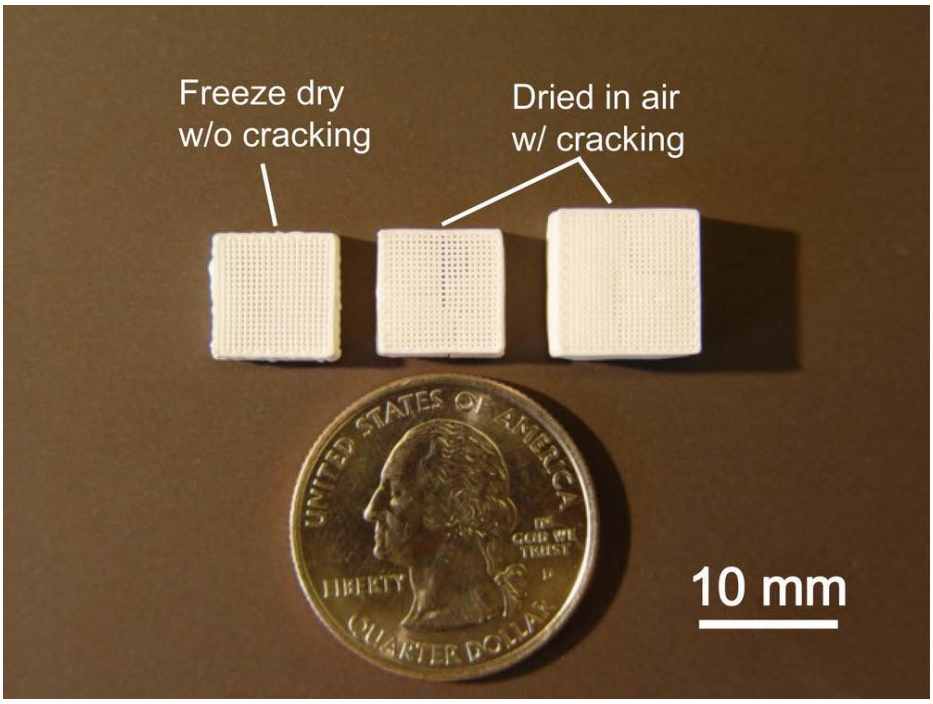

b)

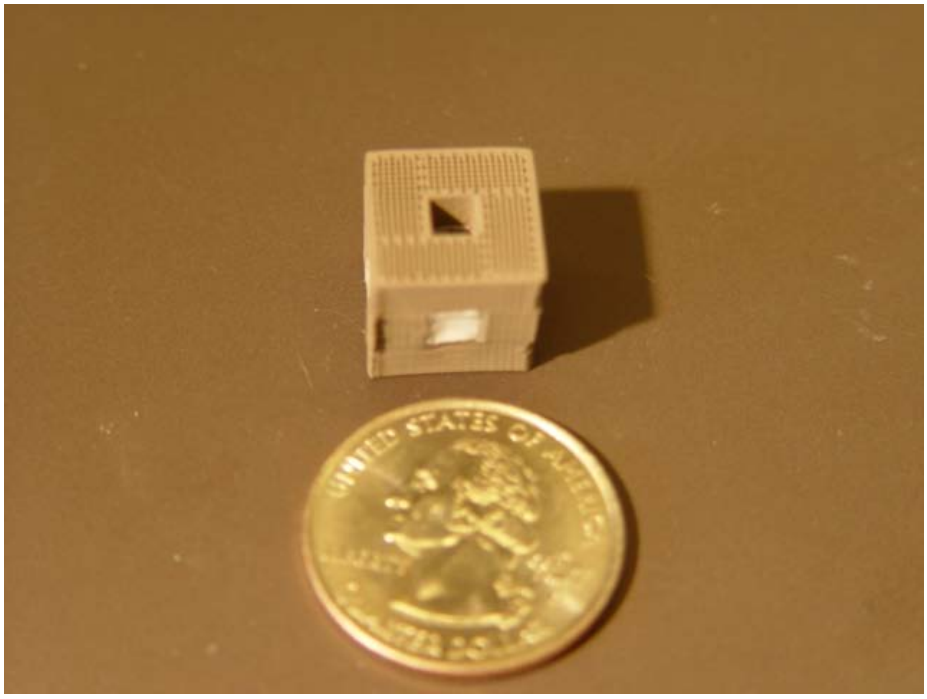

Figure B.1 a) Freeze-dried starch ink lattice compared to those directly dried in air; cracking occurs to the latter due to capillary force and weak gel strength; b) Rice starch in as a fugitive support for a Ni lattice structure.

C. Aqueous Colloidal Cr-Ni Ink

An aqueous colloidal Cr-Ni ink is developed. The Cr powder is supplied by (to be added after coming back to OSU). Table C.1 is a formulation for a 5Cr95Ni (by sold volume fraction) ink. Cr/Ni ratio may be varied for different ink compositions. An SEM image of Cr-Ni lattices is show in Figure A.3. For sintering, a dry non-oxidizing atmosphere, such as N_2 or Ar, is required.

Table C.1 Formulation for a 5Cr95Ni (by solid volume fraction).

Ni Slurry Preparation		
DIW	8.5	g
PEI-50K, 50 wt%,	0.4	g
Ni ENP 800	100.0	g
HPMC, 7.5 wt%	2.2	g
total wt.	111.1	g
Cr Slurry Preparation		
DIW	5.5	g
Adva Flow, 20wt%	0.4	g
Cr powder	33.8	g
HPMC, 7.5 wt%	1.4	g
total wt.	41.1	g
5**Cr95Ni (vol) Composite Ink**		
Ni slurry	111.1	g
Cr slurry	5.258	g
DARVAN 821A	1.058	g
DIW	1.589	g

a) 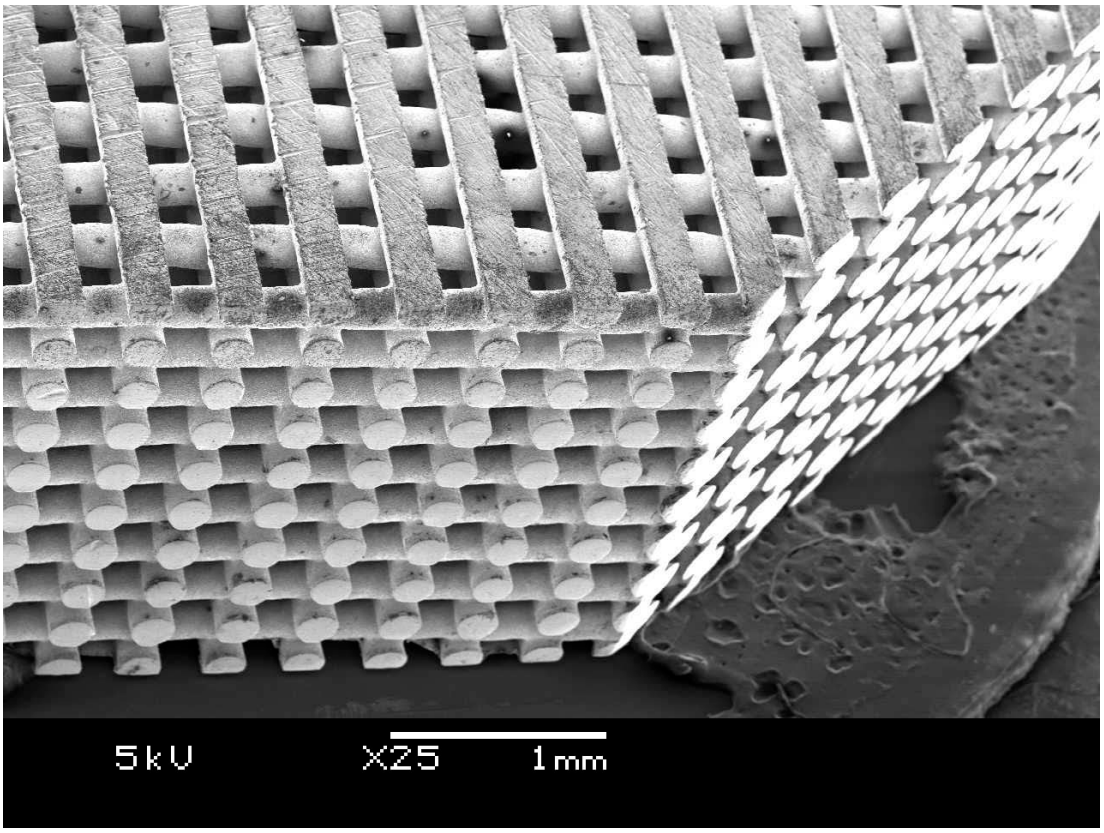

Figure C.1 Cr-Ni lattices of 5Cr95Ni (by solid volume fraction).

D. Oxygen Partial Pressure and Metal Oxidation

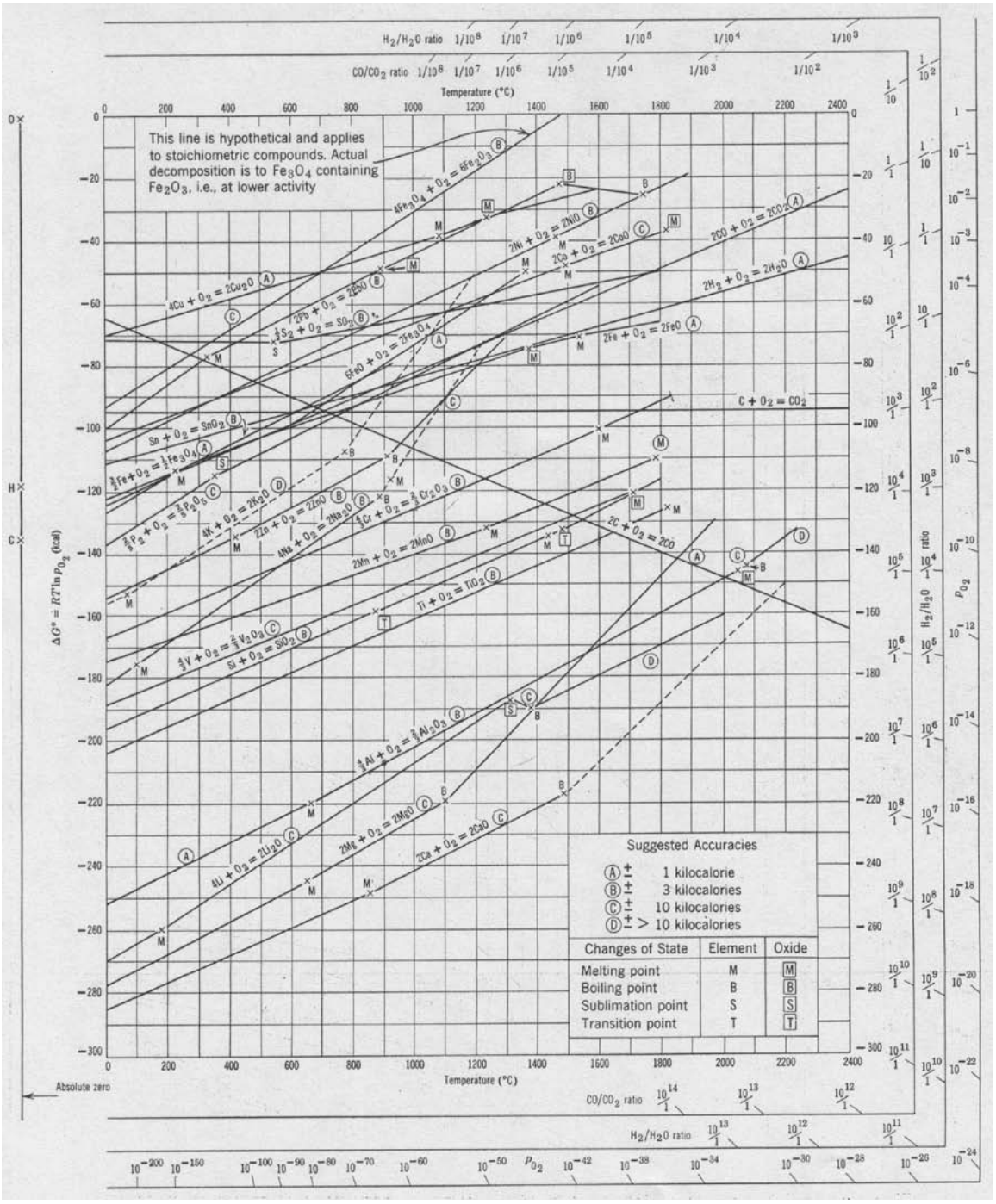

Figure D.1 Standard free energy of formation of oxides as a function of temperature.[A4,A5]

E. Binary Phase Diagram of ZnO-B2O3

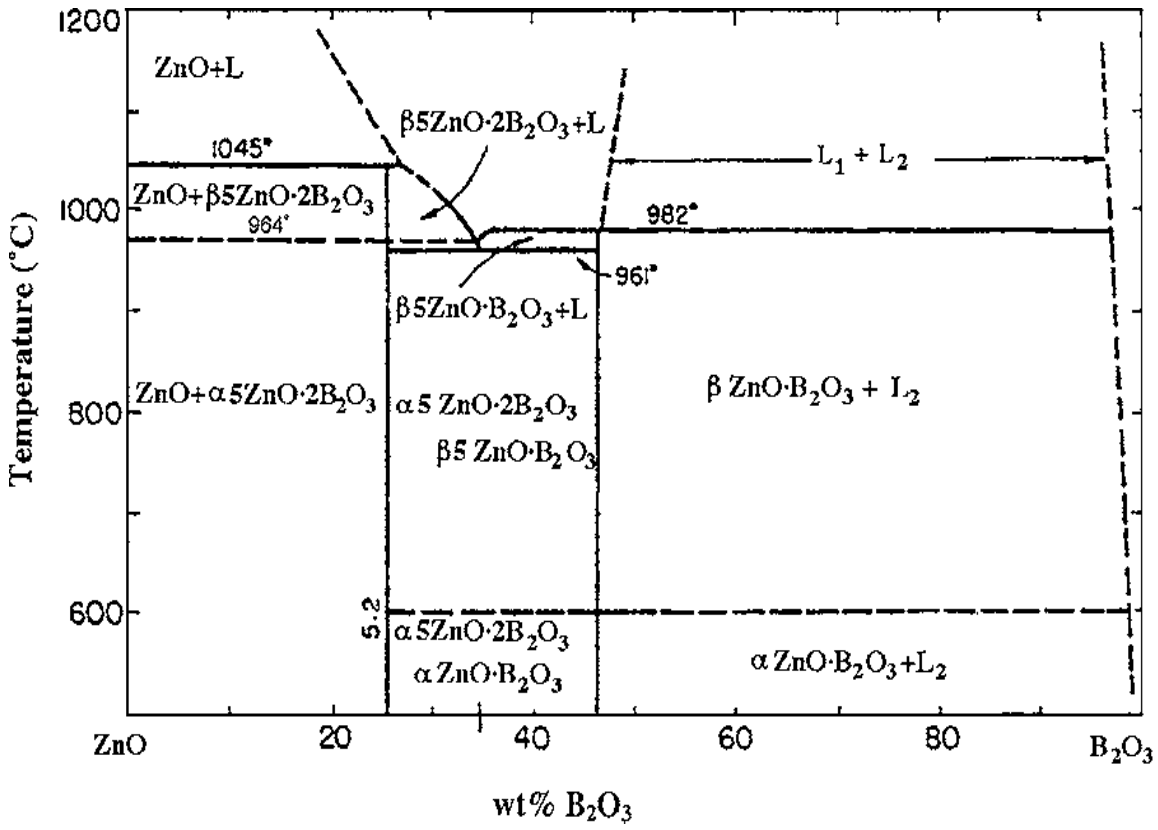

Figure E.1 Binary phase diagram for the ZnO-B_2O_3 system.[A6]

F. Tube Furnace for Sintering Process

Figure F.1 Optical image of the tube furnace for sintering process. Processing gas flows in through the inlet on the left of the horizontal tube, and exits through the outlet on the right. A high purity (>99.8%) alumina tube is used for this furnace.

References

A.1. Du, Z., Sarofim, A. Z., Longwell, J. P., And Tongnotti, L., Fundamental Issues in Control of Carbon Gasification Reactivity, Kluwer, 1991, p. 91

A.2. Du, Z., Ph.D. thesis, Massachusetts Institute of Technology, Cambridge, 1990

A.3. Sharma, R. K., Cresswel, D. L., and Newson, E. J., Ind. Eng. chem. Fund. 30:1428 (1991)

A.4. D. Richardson and J. H. E. Jeffes, J. Iron Steel Inst. 160, 261 (1948).

A.5. L. S. Darken and R. W. Gurry, Physical Chemistry of Metals, McGraw Hill, New York, 1953

A.6. Harrison, D. E.; Hummel, F. A., Phase Equilibria and Fluorescence in the System Zinc Oxide-Boric Oxide. *Journal of the Electrochemical Society* **1956,** 103, (9), 491-49

VITA

Jian Xu

Candidate for the Degree of

Doctor of Philosophy

Thesis: DESIGN, ASSEMBLY AND CHARACTERIZATION OF COMPOSITE STRUCTURES OF BARIUM TITANATE AND NICKEL

Major Field: Chemical Engineering

Biographical:

Personal Data: Jian Xu was born in Feburary 10, 1976 in Zhenjiang, Jiangsu Province, China as the son to Jinlin Xu and Ping Hu.

Education: He attended Central South University, China in 1994 and received Bachelor of Engineering in Chemical Engineering in 1998. After working for three years in the industry, he began his graduate study at Oklahoma State University in 2001. He obtained his Master of Science degree in Chemical Engineering at in December 2004, with a thesis on self-assembly of colloidal particles. Then he continued graduate study and completed the requirements for the Doctor of Philosophy in Chemical Engineering at Oklahoma State University, Stillwater, Oklahoma in May 2010.

Experience: He worked in Gold East Paper (Jiangsu) Co. Ltd. (Asia Pulp & Paper) for one year in Zhenjiang, Jiangsu Province, China. Then he worked for less than two years in a manufacturer plant of SAE Magnetics (HK) Ltd. in Dongguan, Guangdong Province, China

Professional Memberships: He was a student member of Material Advantage program.

Name: Jian Xu Date of Degree: May, 2010

Institution: Oklahoma State University Location: Stillwater, Oklahoma

Title of Study: DESIGN, ASSEMBLY AND CHARACTERIZATION OF COMPOSITE STRUCTURES OF BARIUM TITANATE AND NICKEL

Pages in Study: 241 Candidate for the Degree of Doctor of Philosophy

Major Field: Chemical Engineering

Scope and Method of Study: Three dimensional, heterogeneous, geometrically complex ceramic-metal composite structures are fabricated by assembly of aqueous colloidal gels of barium titanate and nickel, followed by densification of ensembles in controlled atmosphere through sintering. This work focuses on the processing of colloidal gels, assembly of the composite structures, and co-sintering of composite structures. Relevant sintered material properties including oxidation, hardness, microstructure, and electric properties are characterized. Specifically, rheological characterizations are used to determined colloidal gel formulations; sintering shrinkage is used as a function of temperature to determined compatible gel compositions; thermogravimetric analysis is used to characterize thermal degradation and oxidation of polymer additives and carbon black support material, respectively.

Findings and Conclusions: The findings of this study are four folds: 1) a carbon black gel may be used as fugitive materials for assembly of geometrically complex objects; 2) a nickel gel may be used to assemble objects that have >99% density; 3) barium titanate and nickel composite structures that have a low solid volume fraction of nickel may be assembled and consolidated through solid state sintering, and 4) barium titanate and nickel composite structures that have a high solid volume fraction of nickel may be assembled and consolidated through liquid phase sintering. The use of small additions of sintering aids allows successful densification of composite structures that have discrete interface, heterogeneous composition, and intricate geometric design. Low internal stress and plastic deformation of particle network during liquid phase sintering process facilitate the co-sintering of dislike ceramic and metal materials.

ADVISER'S APPROVAL: James. E. Smay